Numerical modelling of an air-helium buoyant jet in a two vented enclosure

Elie Saikali

Sorbonne Université

École doctorale Sciences Mécaniques, Acoustique, Électronique & Robotique

Laboratoire d'Instrumentation et d'Expérimentation en mécanique des Fluides et Thermo-hydraulique (LIEFT, CEA Saclay)

Laboratoire d'Informatique pour la Mécanique et les Sciences de l'Ingénieur (LIMSI-CNRS, UPR3251)

Numerical modelling of an air-helium buoyant jet in a two vented enclosure

Par Elie SAIKALI

Thèse de doctorat de Mécanique des Fluides

Dirigée par Gilles Bernard-Michel, Anne Sergent & Christian Tenaud

Présentée et soutenue publiquement le 8 Mars 2018

Devant un jury composé de :

Bernard-Michel Gilles *(co-encadrant)*	Ingénieur CEA Saclay
Houssin-Agbomson Deborah *(examinatrice)*	Ingénieure de Recherche Air Liquide Paris-Saclay
Lagrée Pierre-Yves *(examinateur)*	Directeur de Recherche CNRS, IJLRA
Le Quéré Patrick *(examinateur)*	Directeur de Recherche CNRS, LIMSI
Malet Jeanne *(rapporteure)*	Ingénieure de Recherche IRSN Saclay
Sergent Anne *(co-encadrante)*	Maître de Conférences Sorbonne Université, LIMSI
Tenaud Christian *(directeur de thèse)*	Directeur de Recherche CNRS, LIMSI
Xin Shihe *(rapporteur)*	Professeur INSA de Lyon, CETHIL

Dedicated to my beloved parents,
Nicolas and Antoinette.

The world is an exciting place when you know CFD
– John Shadid.

Remerciements

Cette thèse est le fruit de mon travail durant mes trois ans de doctorat. Elle a été préparée dans deux laboratoires français: le Laboratoire d'Instrumentation et d'Expérimentation en Mécanique des Fluides et Thermo-Hydrauliques (LIEFT–CEA Saclay DEN / DANS / DM2S / STMF) et le Laboratoire d'Informatique pour la Mécanique et les Sciences de l'Ingénieur (ETCM / LIMSI–CNRS). Je voudrais remercier Jean-Paul Garandet (directeur du LIEFT) et François Yvon (directeur du LIMSI), d'abord pour m'avoir accueilli et donner la possibilité de m'inscrire aux deux laboratoires, puis, de m'avoir fourni les outils nécessaires et un bon environnement de travail pendant ces trois années. Un merci particulier à Jean-Paul pour la relecture des articles de conférence et de ce manuscit.

Je tiens à exprimer ma sincère gratitude à mon directeur de thèse Christian Tenaud et aux encadrants de thèse Anne Sergent et Gilles Bernard-Michel. Je vous remercie tous de m'avoir donné l'opportunité de rejoindre votre groupe de recherche et de m'avoir apporté un soutien continu durant ces trois années. Je vous remercie de votre patience, de vos connaissances, de votre motivation, de vos encouragements et de vos commentaires perspicaces. Vos conseils et vos questions m'ont beaucoup aidé durant les trois années de recherche et lors de la rédaction de ce manuscrit de thèse. Je peux simplement dire que je n'aurais pas pu imaginer avoir de meilleurs directeur et encadrants que vous, pour mon doctorat.

Je tiens également à remercier les membres du jury Jeanne Malet and Xin Shihe pour avoir accepté d'être les rapporteurs de ma dissertation. Je tiens également à remercier Deborah Houssin-Agbomson, Pierre-Yves Lagrée and Patrick Le Quéré pour m'avoir fait le plaisir d'être les examinateurs lors de la soutenance.

Je remercie tous mes collègues de laboratoire au LIEFT et au LIMSI pour leurs discussions stimulantes, les blagues et les pauses café. Merci Jalel Chergui, Marko Pavlov, Can Selçuk, Shreyas Acharya, Raphaël Zanella, Ziad Youssef, Lantao Yu, Andres Castillo Castellanos, Antoine Faugaret, Mebarek Belkadi, Ismail Ben Hassan Saidi, Hugues Faller, Guy Yoslan Cornejo Maceda, Raksmy Nop, Jianfei Song, Roberta Scarpa, Fredric Dabbène, Sonia Benteboula, Constantin Ledier, Etienne Studer, Benjamin Cariteau, Véronique Lechopied et toute la famille LIMSI et LIEFT. J'ai certainement oublié certains d'entre vous parce que la liste est beaucoup plus longue, mais je remercie tous ceux que j'aurais omis de mentionner. Merci également aux stagiaires Loeiz Zamora Medina, Jiaying Bi, Aurore Caquas et Thomas Lozach.

Je suis reconnaissant envers les responsables et les développeurs des codes CFD que j'ai utilisés pendant mon travail pour les discussions fructueuses, leur disponibilité et le partage d'idées. En particulier, je remercie Yann Fraigneau, Gauthier Fauchet, Ulrich Bieder et l'équipe de support CEA-TRUST, Céline Capitaine et Marthe Roux.

Merci beaucoup à mon très cher collocataire et frère Houssein Wehbi (Johnny S.) pour son soutien et ses encouragements de tous jours. Un grand merci particulier à mes chers amis libanais Mustafa et Fatima Al Reda, Dima El Khechen, Tarek et Marwa Zaarour, Najwa Sharaf, Mayla

Selman, Sara Fneich, Oumaya Abou Chabke et José Koussa, Moussa Kafal, Alaa Daher, Mohamad Ayoub, Mohamad Tarhini (toto), Mohamad Bitar, Dali Rashid, Marwa et Zeinab Koumeiha, Houssein Banjak, Mohamad Toufeilli, Mustafa Chehade et Hassan Sleiman. Je vous remercie de votre solidarité et de ces merveilleuses années que nous avons passé ensemble, des moments et des voyages inoubliables. Vous avez été vraiment ma deuxième famille, dans mon deuxième pays, la France. En fait, la liste de mes amis est plus longue. J'aimerais saisir l'occasion de vous remercier tous, un par un et une par une, de votre amitié.

Enfin, je peux dire que tout ce succès n'aurait jamais été possible sans l'amour, le soutien et la confiance de ma famille. Je suis tellement reconnaissant à mon cher père Nicolas et à ma chère mère Antoinette pour leurs encouragements et leur immense amour. Merci de votre patience et de votre soutien continu. Merci d'être toujours là pour moi. Je vous dédie cette thèse à vous deux. Et à vous, ma chère sœur Suzie et mes chers frères, Azar et Naji, et à vos familles (Antoine, Jizelle, Joelle, Jessica, Camelia, Nicole, Nicola, Leanne, Elio, Marlie, Alex), merci pour tous les moments charmants que nous avons passé ensemble.

Acknowledgements

This dissertation is a fruit of my work during three years of Ph.D. and was prepared in the two French laboratories: Laboratory of Instrumentation and Experimentation in Fluid Mechanics and Thermo-Hydraulics (LIEFT–CEA Saclay DEN / DANS / DM2S / STMF) and The Computer Science Laboratory for Mechanics and Engineering Sciences (ETCM / LIMSI–CNRS). I would first like to thank Jean-Paul Garandet (director of the LIEFT) and François Yvon (director of the LIMSI), firstly for hosting and giving me the opportunity to enroll in the two labs and, secondly, for providing me with the necessary materials and good conditions during the three years of work. A special thanks to Jean-Paul for revising the conference proceedings and this manuscript.

I would like to express my sincere gratitude to my thesis director Christian Tenaud and thesis co-directors Anne Sergent and Gilles Bernard-Michel. Thank you all for giving me the opportunity to enroll with your research group and for the continuous support during these three years. Thank you for your patience, immense knowledge, motivation, encouragement and your insightful comments. Your guidance and questions really helped me in the three years of research and in writing this thesis manuscript. I can simply say that I could not have imagined having better advisors than you in my Ph.D. study.

I would like also to thank the jury members Jeanne Malet and Xin Shihe for accepting to be the reviewers of my dissertation. I would like to equally thank Deborah Houssin-Agbomson, Pierre-Yves Lagrée and Patrick Le Quéré for giving me the pleasure and accepting to be the examiners of the Ph.D. defense.

I thank all my colleagues and labmates at the LIEFT and LIMSI for the stimulating discussions, jokes and coffee breaks. Thanks Jalel Chergui, Marko Pavlov, Can Selçuk, Shreyas Acharya, Raphaël Zanella, Ziad Youssef, Lantao Yu, Andres Castillo Castellanos, Antoine Faugaret, Mebarek Belkadi, Ismail Ben Hassan Saidi, Hugues Faller, Guy Yoslan Cornejo Maceda, Raksmy Nop, Jianfei Song, Roberta Scarpa, Fredric Dabbène, Sonia Benteboula, Constantin Ledier, Etienne Studer, Benjamin Cariteau, Véronique Lechopied and all the LIMSI and LIEFT FAMILY. I have surely forgotten some of you because the list is much longer, but I thank all those I might have omitted to mention. Thanks for the interns Loeiz Zamora, Jiaying Bi, Aurore Caquas and Thomas Lozach.

I am grateful to the responsibles and developers of the CFD codes I used during my work for the fruitful discussions, motivations and for sharing ideas. In particular, I take the chance to thank Yann Fraigneau, Gauthier Fauchet and Ulrich Bieder. Special thanks for the amazing CEA TRUST-TrioCFD support team: Céline Capitaine and Marthe Roux.

Big thanks to my dearest room-mate and brother Houssein Wehbi (Johnny S.) for his support and encouragment every day. Special thanks to my beloved Lebanese friends Mustafa and Fatima Al Reda, Dima El Khechen, Tarek and Marwa Zaarour, Najwa Sharaf, Mayla Selman, Sara Fneich, Oumaya Abou Chabke and José Koussa, Moussa Kafal, Alaa Daher, Mohamad

Ayoub, Mohamad Tarhini (toto), Mohamad Bitar, Dali Rashid, Marwa and Zeinab Koumeiha, Houssein Banjak, Mohamad Toufeilli, Mustafa Chehade and Hassan Sleiman. Thank you for your solidarity and for these amazing years we spent together, full of unforgettable moments and travels. You have been really my second family, in my second country, France. In fact, the acknowledgement of the friends list elongates. I would like to catch the opportunity to thank you all, one by one, for your kind friendship.

Last but not least, I can say that all this success would have never been possible without the love, support and trust of my family. I am so grateful to my dear father Nicolas and dear mother Antoinette for their encouragement and immense love. Thanks for your patience and continuous support. Thank you for always being there for me. I dedicate this dissertation to both of you. And to you, my dear sister Suzie and brothers Azar and Naji, and to your families (Antoine, Jizelle, Joelle, Jessica, Camelia, Nicole, Nicola, Leanne, Elio, Marlie, Alex), big thanks for every lovely moment we had together.

Contents

List of Figures

List of Tables

Abbreviations and key words

ACF	*Auto Correlation Function*
CFD	*Computational Fluid Dynamics*
DNS	*Direct Numerical Simulation*
FANS	*Favre Averaged Navier Stokes*
LES	*Large Eddy Simulation*
LMN	*Low Mach Number*
PDE	*Partial Differential Equation*
PIV	*Particle Image Velocimetry*
QUICK	*Quadratic Upstream Interpolation for Convective Kinematics*
RANS	*Reynolds Averaged Navier Stokes*
RK2	*Runge–Kutta second order*
RMS	*Root Mean Square*
RRK2	*Rational Runge–Kutta second order*
SGS	*Sub Grid Scale*
SMAGO	*Smagorinsky*
TKE	*Turbulent Kinetic Energy*
WALE	*Wall Adapting Local Eddy-viscosity*
2D	*Two dimension*
3D	*Three dimension*

Nomenclature

$\mathrm{D}/\mathrm{D}t$	Total derivative operator
Err	statistical error
"amb" or "2"	Denoting the ambient fluid (air in the present work)
"inj" or "1"	Denoting the injected fluid (helium in the present work)
$\mathrm{rms}\{\cdot\}_t$	Root mean square notation
$\overline{}$	Space filter symbol
$\widetilde{}$	Favre filter symbol
$< \cdot >_t$	Time averaging operator
$< \cdot >_t^R$	Reynolds time averaging operator
$< \cdot >_t^F$	Favre time averaging operator
$(\cdot)'$	Fluctuating part (Reynolds)
$(\cdot)''$	Fluctuating part (Favre)
$(\cdot)^{\prime,N}$	Normalized mead fluctuations
$\| \cdot \|$	Norm

Subscripts and notations

Ar	Archimedes number
Fr	Froude number
Gr	Grashof number
Ma	Mach number
Pe	Peclet number
Ra	Rayleigh number
Re	Reynolds number
Ri	Richardson number
Sc	Schmidt number

Dimensionless parameters

Ω	Domain
$\partial\Omega_W$	Wall boundary
$\partial\Omega_i$	Inlet boundary
$\partial\Omega_o$	Outlet boundary
$\partial\Omega_s$	Symmetrical boundary

Computational domain and boundaries

$\mathbf{n}$	Outward unit normal	[-]
$\mathbf{x}$	Space vector	[m]
r	Radial direction	[m]
t	Time	[s]
x	Horizontal direction	[m]
y	Span-wise direction	[m]
z	Vertical or axial direction	[m]
$\mathcal{O}$	Origin of the system	[-]

Coordinate labels

H	Height of the cavity	[m]
H_v	Height of the vent	[m]
L	Span-wise length of the cavity	[m]
L_v	Span-wise length of the vent	[m]
W	Width of the cavity	[m]
W_v	Width of the vent	[m]
d	Diameter of the injection pipe	[m]
h	Height of the injection pipe	[m]
$\mathcal{V}$	Volume of the cavity	[m^3]
Δ	LES filter width	[m]
δ	Mesh step size	[m]
η	Kolmogorov length scale	[m]
λ_B	Batchelor length scale	[m]

Geometrical parameters and length scales

Q	Volumetric flow-rate	[Nl.min^{-1}]
Q_v	Volumetric flow-rate	[m^3.s^{-1}]
q	Mass flow-rate	[Kg.s^{-1}]

Injection conditions

D	Diffusion coefficient	[m^2.s^{-1}]
M	Molar mass	[Kg.mol^{-1}]
M_{mix}	Mixing molar mass	[Kg.mol^{-1}]
P	Hydrodynamic pressure	[Pa]
P_{thm}	Total pressure (thermodynamic)	[Pa]
R	Specific gas constant	[J.K^{-1}.mol^{-1}]
S	Symmetrical strain tensor part	[s^{-1}]
T	Temperature	[K]
V	Volume of the mixture	[m^3]
Y_1	Helium mass fraction	[-]
$\mathbf{g}$	Gravity vector	[m.s^{-2}]
$\mathbf{u}$	Mixture mass velocity vector	[m.s^{-1}]
e	Viscous strain tensor	[s^{-1}]
m	Mass of the mixture	[Kg]
p	Thermodynamic pressure	[Pa]
μ	Dynamic viscosity	[Kg.m^{-1}.s^{-1}]
μ_{SGS}	Modelled SGS dynamic viscosity	[Kg.m^{-1}.s^{-1}]
μ_t	Turbulent dynamic viscosity	[Kg.m^{-1}.s^{-1}]
ν	Kinematic viscosity	[m^2.s^{-1}]
$\overline{\xi}^{\text{SGS}}$	Scalar turbulent flux tensor	[Kg.m^{-3}.s^{-1}]
ρ	Density	[Kg.m^{-3}]
τ	Viscous stress tensor	[Pa]
$\overline{\tau}^{\text{SGS}}$	Reynolds SGS stress tensor	[Pa]

Flow parameters

E_k	Kinetic energy	[$m^2.s^{-2}$]
H_P	Height of the plume	[m]
Q_v^{bot}	Volumetric flow-rate at bottom vent	[$m^3.s^{-1}$]
Q_v^{top}	Volumetric flow-rate at top vent	[$m^3.s^{-1}$]
X_1	Helium volume fraction	[-]
$\|\mathbf{u}\|$	Velocity magnitude	[$m.s^{-1}$]
$\|\mathbf{u}\|_{XZ}$	2D velocity magnitude in xz-plane	[$m.s^{-1}$]
$\|\mathbf{u}\|_{YZ}$	2D velocity magnitude in yz-plane	[$m.s^{-1}$]
f	Frequency	[Hz]
q_{He}^{top}	Helium mass flow-rate at top vent	[$Kg.s^{-1}$]
t_{start}	Starting time of statistics	[s]
$\mathcal{K}_t$	Turbulent Kinetic energy	[$Kg.m^{-1}.s^{-2}$]
$\mathcal{M}_{\text{He}}$	Helium total mass	[Kg]
δt	Time step	[s]
ϵ	Total dissipation rate	[$m^2.s^{-3}$]
λ_f	Taylor micro-scale	[s]

Post-processing quantities

Introduction

The general oriented application of the current work is placed in the frame of security assessment for hydrogen-based systems. These systems are considered one of the important engineering applications that will extensively appear in our every day life over various range of scales; cars fuel cell (figure 1), forklifts in warehouse, power generation stations ... From an environmental point of view, hydrogen is considered as a clean green source of energy, unlike many other sources that release harmful gases into the environment.

Figure 1: Cars fuel cell: International conference on hydrogen safety (ICHS) 2017, Hamburg, Germany (personnel document).

Wide range of hydrogen-based applications require an indoor use (forklifts in warehouse, fuel cells for off-grid or backup applications, refuelling stations, ... [FHAJ$^+$17]). For safety issues, it is often necessary to place the hydrogen system in enclosures (confined environment) to isolate them from the human (user or public) and from material and environmental weather conditions.

The main problematic is with the hydrogen gas which is initially stored inside bottles in a compressed form, where the pressure can be as high as 700 bars for the new developed technologies [EKDB08]. Hydrogen is afterwards distributed through pipes in order to feed the system and to produce energy, after passing by a chemical reaction process (hydrogen plus oxygen giving water and energy). A typical accidental situation (human or technical error) is when hydrogen escapes from the distributing pipes and rises in a form of a plume-jet inside the confinement. In this case, rising light hydrogen gas entrains air from different positions and forms potentially a dangerous-flammable mixture with hazardous consequences. In particular, the danger is due to the concentration accumulation: basically when the hydrogen volume is between 4% – 75 % of the mixture where high flammable conditions are reached. Cariteau et al. in [CT12] present thoroughly the hydrogen problematic in such cases. Regarding all these issues, it can be stated in conclusion that the use of hydrogen as a vector of energy in

a confined medium requires a careful sensitive study devoted to the hazard assessments and the associated risks, before the hydrogen–based systems come into a widespread use in the community [FHAJ$^+$17].

Several international and European non-profit organizations are carrying out a wide number of researches and projects to investigate on the hydrogen release problematic in confined and/or semi–confined enclosures. The international association for hydrogen safety (HySafe) is for example an organization representing 14 countries worldwide and aim to reduce the hydrogen risks to make the indoor use safer. In this framework, HySafe includes a conference committee that organizes every two years the international conference on hydrogen safety (ICHS) so that the international research in this field is presented [KBB$^+$14]. Hyindoor for example, is an European project that includes members from Air Liquide, HFCS, CEA, KIT-G, HSL, JRC, NCSRD, UU and CCS. The aim of the project is to address the issue of safe indoor hydrogen use by developing safety design guidelines and engineering tools to mitigate the hazardous consequence of the hydrogen release problematic [FHAJ$^+$17].

From a physical point of view, the hydrogen release problem is considered as an intrusion of a light fluid into a heavier fluid filling initially the confined environment. According to the classification of Baines and Turner in [BT69], this flow type is referred to as buoyant convection from isolated sources. As a consequence of the continuous intrusion and under specific conditions (mainly dependent on the release characteristics and the effect of the interaction between the fluid inside the confinement and the exterior environment), either homogeneous well mixed layers and/or density/concentration stratification can build-up inside the medium. Such situations are encountered in many technical and engineering applications, say for example jets entering mixing chambers, nuclear or non-nuclear severe accident scenarios, fuel leakage in containments, fire modelling and forced ventilation [MJMB95, SPA04].

Qualifying the concentration regime resulting from different homogeneous and/or stratified mixture situations and its sensitivity to both the release conditions and/or the passive/forced ventilation conditions serves in understanding the concentration accumulation problematic. In particular, such information helps in closing the knowledge gaps to propose finally the desired safety assessments that may be followed to reduce the hydrogen accumulation hazards. For that purpose, quantitative results and data are required to describe the temporal/spatial dynamics of the concentration field. Information regarding the distribution of the concentration and other flow variables (say momentum and pressure for example) could be either predicted from analytical models or from numerical computational fluid dynamics (CFD) approaches, or it could be measured from experiments.

Theoretical models are the fastest and the easiest to employ in safety pre-calculations. These models are initially developed to take into account the release conditions, the geometrical configuration and its corresponding design parameters. For example in vented configurations, the model takes into account the dimensions and the position of the vents. The maximal concentration and pressure values, in addition to the concentration distribution are the main outcomes of the theoretical models. However, these models are usually restricted to academic cases and are limited in situations where the flow is well developed and attains a self-similar behavior along a unique spatial direction; say normal to the release surface. Moreover, all

theoretical models are based on an entrainment assumption where it is initially required to provide information regarding a parameter referred to by the "entrainment coefficient". This issue is itself challenging as far as estimating correctly the entrainment coefficient is not an asy task and is subject of research, mainly in confined configurations.

Numerical CFD approaches are commonly used to study the light fluid release problems where the complete three dimensional (3D) flow equations are solved on a computational grid. Accessing the complete 3D fields, without being intrusive, is the main advantage of the CFD approach and thus breaks the limitations of the theoretical models. Challenges and difficulties mainly rise in specifying a turbulence model to handle the classical closure problem of turbulence. For example, it has been noted in accordance to existing CFD benchmarks that statistical CFD turbulence models, say Reynolds and Favre averaged Navier–Stokes approaches for example, can underestimate in certain configurations the 3D concentration fields and thus are not always recommended in security studies [BMTVG12, BMCN$^+$13]. In such situations, spatial filtered large eddy simulations (LES) or a complete direct numerical simulation (DNS) approaches are rather recommended.

Further difficulties can rise with the CFD approaches: either related to numerical reasons or to the physics of the problem. Numerically speaking, specifying the natural boundary conditions at the inlet/outlet surfaces in semi-confined cavities is not an easy task and remains an open problem of research, especially that a vent can have an opposite flow orientation along its surface at the same time [DCJ$^+$13]. Moreover, the computational cost and the available computing resources are considered as one of the difficulties faced with the CFD approach and thus define its limitation. It is impossible sometimes to obtain a fine resolution prediction in large configurations; say a direct numerical simulation (DNS) of hydrogen leakage from a fuel cell car placed in a large scale garage for example. Physically speaking, it is an extreme challenge for a CFD code to reproduce correctly the natural physics of the release problem: say for example capturing laminar-to-turbulent transitions that are well known to occur within a short distance above the release position, the wide range of time and length scales, the sharp density gradients and thus instabilities, ...

Experimental data are assumed to be a main source of information in describing the flow problem. Depending on the certainty of the measurements, experimental data are generally used in many studies as a reference for validation of both analytical and numerical results, which are used to provide complementary information. An important advantage of the experimental studies is that they can be carried for longer physical time, compared to CFD calculations, which makes the statistical recording more accurate and reliable. However, the disadvantages and the limitations of such approach is usually related to the problem of intrusive measurements where some flow variables can not be always recorded, specially for buoyant flows.

In this dissertation, we show interest in studying the leakage of a light fluid in an atmosphere filled with a heavier one. Thus, we consider a moderate release flow-rate where a buoyant jet is predicted to develop. In such cases, the flow is dominant by momentum in the release vicinity, while by buoyancy forces upstream. We are interested in studying the dynamics of the buoyant jet in a semi-confined cavity subjected to a natural ventilation system. The

enclosure is assumed to have two horizontal vents placed at the top and bottom of the same vertical wall. The entrainment phenomenon that takes place between the heavy and the light fluids, in addition to the concentration distribution and the resultant stratified regime are also points in our interest. According to the theoretical model of Linden et al. in [LLSS90], a homogeneous layer is predicted to develop in a such considered configuration. Due to the reduced size of the configuration which avoids the appearance of self-similar profiles and due to the insufficient knowledge of estimating the entrainment coefficient at present, CFD approaches are used in this study. Comparisons with the theoretical predictions are only presented to compare with the predicted maximal values.

An experimental facility has been already developed at CEA Saclay to study the presented interesting phenomena. Since the use of hydrogen in experiments requires a lot of caution, helium release is considered as far as it has been justified to be a good substitute of hydrogen. Experimental particle image velocimetry (PIV) measurements carried out by Bernard-Michel et al. in [BMSH17] provide some information regarding the velocity distribution in two dimension vertical slices. However, neither concentration nor 3D fields measurements are currently available. We look towards developing a numerical model that mimics the CEA experimental set-up and thus perform numerical simulations to provide complementary 3D information, mainly regarding the helium concentration in the medium. Numerical velocity predictions are compared afterwards with the PIV data for validations.

We look to identify the necessary parameters required to simulate the convenient small flow-rate release problem, both by LES and DNS approaches. First, we aim to propose methodologies to better approach the natural inlet and outlet boundaries. Second, we look towards analyzing the numerical predictions by carrying out a CFD-PIV validation regarding the velocity distribution. And finally, we look to analyse the stratification and mixing-dispersion phenomena that takes place in the vented enclosure. This point is mainly important to provide information regarding the security hazards versus the employed CFD approach on the one hand, and to highlight over the limitations and weak points of the theoretical predictions on the other hand.

The document is organized as follows. The state of the art is presented in chapter 1 at first. Objectives and the modelled configuration are the subject of chapter 2. Flow governing equations and the employed CFD codes are presented respectively in chapters 3 and 4. Numerical results are depicted in the remaining chapters. Preliminary axi-symmetrical simulations are presented in chapter 5. Chapters 6 and 7 are devoted to the LES solutions and the PIV validations. Analysis regarding both the time averaged fields and the turbulence form the heart of chapter 8.

Chapter 1

State of the art

Contents

In this chapter, a simple literature review devoted to the study of buoyant convection flows is presented. Firstly, dimensionless parameters required to identify various buoyant regimes, laminar-turbulent transition, spatial scales and self similarities are discussed. Models and validations based on the entrainment coefficient assumption are presented next for flows in free and limited environments. In the framework of the present work, selected recent numerical–experimental studies of buoyant jets in confined and semi-confined cavities are reviewed. The plan of the thesis and the global work motivation are finally outlined.

1.1 Buoyant convection from isolated sources: intrusion of a fluid into another

Buoyant (or gravitational) convection from isolated sources, according to the definition of Turner in [Tur79], is the motion of a fluid produced by gravity due to the density variation between a source fluid and an ambient one. These flows are identified to occupy a limited region below or above the source, followed by a sharp density interface with the non-buoyant region.

In practice, the phenomenon is described as intruding a fluid, from a source, into another ambient environment, not necessary being at rest. Such flows are not of a rare occurrence to be observed in the field of environmental fluids and human activities, from small sizes to very big scales. Smoke released from a cigar, smoke plumes released from chimneys and industrial smokestacks, waste-water discharged from pipes into lakes and rivers and smoke jets released from volcanic eruption are all examples from our everyday life (see figure 1.1).

(a) (b) (c) (d)

Figure 1.1: Examples of buoyant convection from isolated sources in free environments. (a) smoke rising from a cigar, (b) smoke rising from chimneys, (c) waste water discharge, (d) volcanic smoke release.

The characteristics of the intruded fluid at the source (narrow orifice, nozzle, ...) are used to present a qualitative classification for the flow regime rising in the environment [LC03]. The classification is basically dependent on whether the fluid is intruded with some buoyant and/or momentum (inertia) flux on the one hand, and whether the supply is either continuous or intermittent (discontinuous) on the other hand.

In the present work, we consider only a continuous supply at the source and thus no puffing/thermal phenomena shall be reported. The term **jet** is usually employed for a flow regime rising in an environment due to a continuous intrusion with an inertial flux dominance. However, if the buoyancy flux is dominant at the source, the term **plume** is rather used. **Buoyant jet** is a well known term in such flows and it is referred to the flow regime when both terms, momentum and buoyancy, are important.

Dimensionless parameters are usually used to priory predict the flow regime (plume, jet or buoyant jet) and to characterize main physical phenomena that take place in such flows (laminar, turbulent and/or laminar-to-turbulent transition flows). These parameters are presented

in the sequel of this section.

Physical properties of the source fluid are referred to by the $_{\text{inj}}$ sub-script, while $_{\text{amb}}$ refers to those of the ambient. Assume that a fluid is intruded in a wide bulk with a velocity u_{inj} from a nozzle of diameter d. Let us denote by ρ the density of the fluid, μ the dynamic viscosity, g the gravitational acceleration constant, D the mass diffusion coefficient between the fluids and H the height of the medium where the flow rises.

1.1.1 Injection related parameter: inertia versus buoyancy

Injection **Richardson** number: ratio of potential to kinetic energy at the intrusion surface

$$\text{Ri}_{\text{inj}} = \frac{g(\rho_{\text{amb}} - \rho_{\text{inj}})\ d}{\rho_{\text{inj}} u_{\text{inj}}^2}. \tag{1.1}$$

The value of Ri_{inj} is commonly used to predict a flow regime rising in the medium [CR80a]. Ri_{inj} compares the buoyant-to-inertial strengths at the intrusion location. As far as a continuous intrusion is assumed, comparing the value of Ri_{inj} to unity predicts whether the flow at the source is dominated by inertial and/or buoyancy fluxes. The flow regime prediction versus the variation of Ri_{inj} is sketched in figure 1.2.

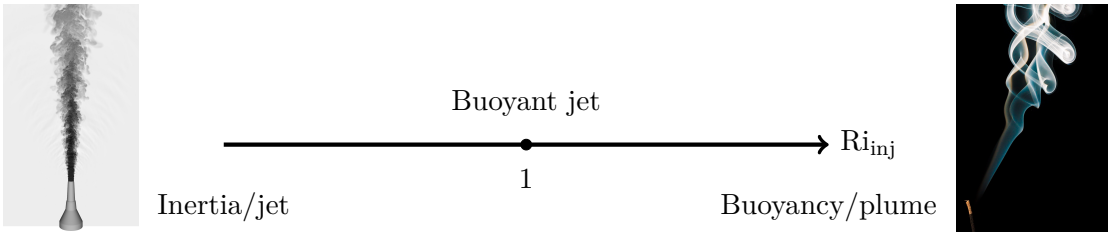

Figure 1.2: Illustration of the predicted flow regime: Buyonancy versus inertial dominant flows.

- When the buoyant forces are dominant, $\text{Ri}_{\text{inj}} \gg 1$ and thus a pure plume regime is predicted (figure 1.2, right).

- If the momentum flux dominates, u_i is basically large resulting in $\text{Ri}_{\text{inj}} \ll 1$ (figure 1.2, left). Thus a pure jet is predicted to rise.

- The buoyant jet is predicted when the importance of both, inertial and buoyant fluxes, are taken into account at the source; Ri_{inj} approaches unity. In such configurations and as the fluid rises in the environment, the momentum effect becomes unimportant and the buoyancy will be the only dominant force exceeding the initial momentum flux at the intrusion surface. In other words, Chen and Rodi in [CR80a] say that a buoyant jet, eventually at a certain distance from the source, is nothing but a pure plume. We focus mainly on this flow regime in the present dissertation.

A schematic representation of a general buoyant jet is illustrated in figure 1.3. The intermediate region is referred to as the zone where the influence of the momentum forces becomes weaker and weaker, compared to those in the non-buoyant region.

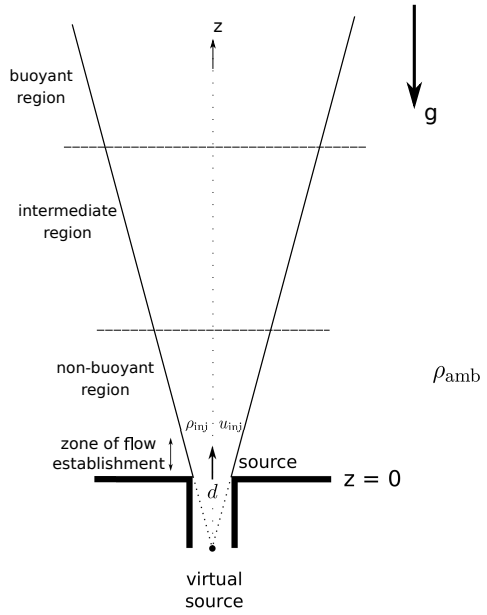

Figure 1.3: Schematic representation of a general buoyant jet in a uniform surrounding: three main identified zones with respect to inertial-buoyant strengths.

1.1.2 Parameters characterizing the laminar to turbulent transition

- Injection **Reynold** number: ratio of inertial to viscous forces at the intrusion surface

$$\mathrm{Re}_{\mathrm{inj}} = \frac{\rho_{\mathrm{inj}} u_{\mathrm{inj}}\, d}{\mu_{\mathrm{inj}}}. \tag{1.2}$$

The value of $\mathrm{Re}_{\mathrm{inj}}$ is a good indicator of the initial intruded fluid's state; basically whether the flow is initially laminar or turbulent in the intrusion surface vicinity. Experimental measurements predict an initial turbulent intrusion starting from $\mathrm{Re}_{\mathrm{inj}} \approx 2 \times 10^3$, as reported in [LC03].

- The dimensionless **Grashof** number measures the ratio of buoyant to viscous forces and is defined locally, at a considered vertical position z above the intrusion surface, as

$$\mathrm{Gr}_{\mathrm{amb},z} = \frac{g \rho_{\mathrm{amb}} (\rho_{\mathrm{amb}} - \rho_{\mathrm{inj}}) z^3}{\mu_{\mathrm{amb}}^2}. \tag{1.3}$$

For an initially starting laminar buoyant jet (small $\mathrm{Re}_{\mathrm{inj}}$), the value of $\mathrm{Gr}_{\mathrm{amb},z}$ is generally used to predict a height z where the flow can take a transition to turbulence (see figure 1.4).

Generally, the value of z is located at small distances above the surface of intrusion [CR80b].

Figure 1.4: Illustration of a laminar to turbulent transition in a buoyant jet flow, M. Masoudian personal contribution, DNS of a turbulent jet [Mas].

Experimental measurements record a wide range of local Grashof numbers ($\mathrm{Gr}_{\mathrm{amb},z}$) depending on the recorded transition height z. However, the accuracy on the recorded values cannot be better than an order of magnitude and thus it is almost impossible to generalize for all problems a unique value. For example, the values of $\mathrm{Gr}_{\mathrm{amb},z}$ can range from 10^6 to 10^9, following the experimental measurements of Bill and Gebhart in [BG75], Forstrom and Sparrow in [FS67] and Railston in [Rai54]. However, to our knowledge, the experimental measurements have been carried out on thermal flows only are thus are not applicable to our density-varying flow problem.

Rouse et al. propose in [RYH52] a different criterion to identify the location of the transition in density-varying buoyant jet configurations. The criterion is based on the dimensionless Richardson number at the intrusion $\mathrm{Ri}_{\mathrm{inj}}$. According to the schematic representation recalled from figure 1.3, the starting and ending point of the transition define the limits of the intermediate region. Obviously, increasing $\mathrm{Ri}_{\mathrm{inj}}$ decreases the size of the non-buoyant region.

Based on the self-similar solutions inside the non-buoyant and buoyant regions, Rouse et al.

suggest in [RYH52] that the limits of the transition satisfy the following correlation

$$0.5 \leq \mathrm{Ri}_{\mathrm{inj}}^{2/3}\left(\frac{\rho_{\mathrm{amb}}}{\rho_{\mathrm{inj}}}\right)^{-1/3}\frac{z}{d} \leq 5. \tag{1.4}$$

We emphasize that the correlation presented in equation (1.4) is applicable for buoyant jets rising in infinite domains and thus may have a limitation when employed in bounded environments. In this context, Ricou and Spalding in [RS61] figured out while considering a jet discharge in a medium with the presence of walls that the position of the transition is not in agreement with the relation presented in equation (1.4).

Although we consider in the present work a buoyant jet rising in a semi-confined cavity, equation (1.4) is served to have an approximate insight on the height of the geometrical configuration required to capture the laminar-to-turbulence transition, and probably turbulence.

1.1.3 Turbulent length scales

Turbulent flows are known to be unsteady and consisting of a wide scale of motion. It is characterized by a complex velocity distribution, greatly varying both in time and space. This distribution consists of rotational flow structures, called eddies. The length scales of the eddies are wide and can range from the width of the flow (integral scale ℓ) to those which are too small (the smallest Kolmogorov length scale η).

The theory behind the turbulence is devoted to the energy distribution, well known by the energy cascade. This theory was introduced by Richardson in [Ric22] while describing how the energy is transferred between the eddies in a turbulent flow. The process takes the following: kinetic energy enters the turbulent flow from the flow structures of size ℓ. The largest eddies break down into smaller and much smaller ones, and in the process transfer the energy to these smaller scales. At the end of the process, basically at the eddies of size η, the viscous effects becomes dominant and the transported energy is completely dissipated (figure 1.5).

In a later work, Kolmogorov illustrated in [Kol41] that the smallest scales are isotropic. In particular, the issue starts with the largest eddies which are dependent of the mean flow. As the scales break down, the directional dependence of the eddies on the mean flow decreases. At the end, Kolmogorov suppose that the smallest eddies are universal and independent on the geometry. Hence, they are similar in all turbulent flows, just differing on the magnitude of the energy transferred to them and on the kinematic viscosity ν. According to the hypothesis of Kolmogorov [Kol41], the energy spectrum (figure 1.5, left) is a mathematical relationship between the energy density per unit wave number (E), the dissipation rate ϵ and the wave number κ, and reads

$$E(\kappa) = C\epsilon^{2/3}\kappa^{-5/3}, \tag{1.5}$$

where $C = 1.4$ is a universal Kolmogorov's constant.

The dependency of the total energy E on ϵ, κ and η can be reviewed from the paper of

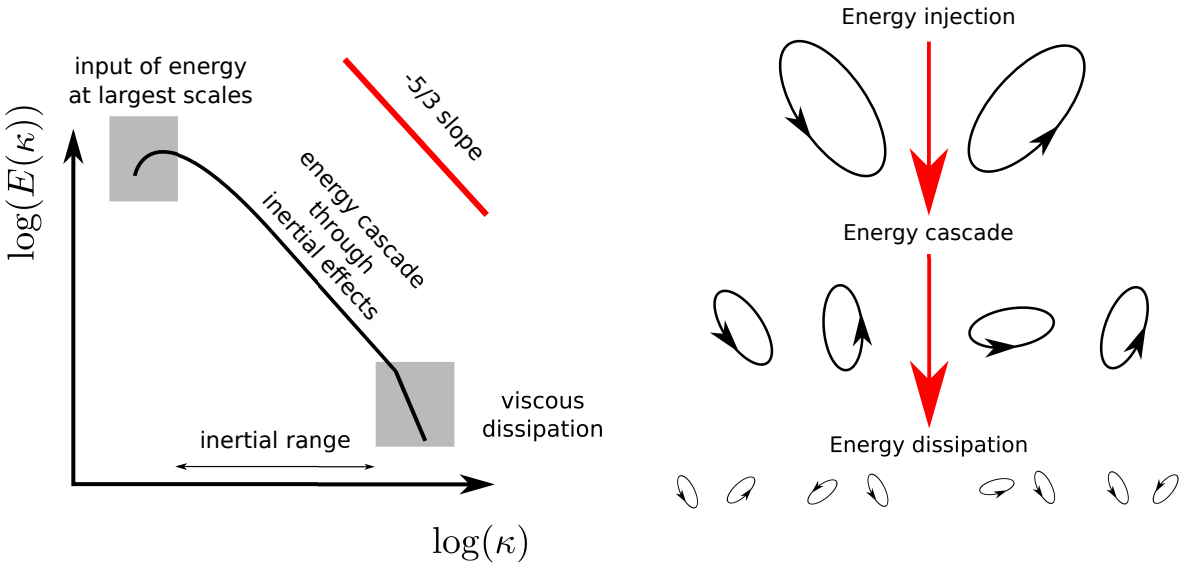

Figure 1.5: A description of the energy cascade phenomenon in a turbulent flow.

Chhabra et al in [CHP06] and thus is expressed as

$$\frac{E(\kappa)}{\nu^{5/4}\epsilon^{1/4}} = \frac{E(\kappa)}{\eta v^2}, \tag{1.6}$$

where $v = (\epsilon\nu)^{1/4}$ is the Kolmogorov's velocity and η defined as

$$\eta = \left(\frac{\nu^3}{\epsilon}\right)^{1/4}, \tag{1.7}$$

the Kolmogorov's length scale.

The center-line energy dissipation rate, for an axi-symmetrical buoyant-jet with center-line velocity u_c, is proposed by Hussein et al. in [HCG94] as

$$\epsilon = \frac{1}{2}\frac{u_c^3}{(z - z_0)}, \tag{1.8}$$

where $z - z_0$ denotes the axial distance away from the virtual source (figure 1.3). Substituting into equation (1.6), the Kolmogorov's length scale can be estimated as

$$\eta = \left(\frac{2\nu^3(z - z_0)}{u_c^3}\right)^{1/4}. \tag{1.9}$$

Batchelor et al in [BHT59] and Corrsin in [Cor51] extended the theory of the spectral cascade to cover the dynamics of species (passive scalars) while advected in a turbulent flow. They focused on identifying spatial scales, known as the Batchelor's scales λ_B, at which the scalars

dissipate and thus defined as

$$\lambda_B = \eta \times \mathrm{Sc}^{-1/2}. \tag{1.10}$$

Here, the **Schmidt** number (Sc) is a dimensionless parameter that measures the ratio of momentum diffusivity (viscosity) to the mass diffusivity, calculated as

$$\mathrm{Sc} = \frac{\nu}{D}. \tag{1.11}$$

1.1.4 Self-preserving solutions and spreading angle

According to the definition presented by Chen and Rodi in [CR80b], a flow regime is said to be self similar (or self preserving) when one velocity, one temperature, one concentration and one length scale are sufficient to present the complete time averaged quantities. Generally, the center-line velocity, temperature and concentration are considered as reference scales. The characteristic length is usually considered as the half width of the buoyant jet.

Experimental measurements on pure plumes and jets rising in infinite media show that the solution is self-similar and all profiles can be scaled to fit a Gaussian distribution [CR80b]. For example, the self-similar Gaussian solution in a round turbulent plume, say for the axial velocity component, can be expressed as

$$\frac{w(r,z)}{w_c(z)} = \exp(-K_w \Upsilon^2), \tag{1.12}$$

where w_c is the vertical center-line velocity. $\Upsilon(r,z)$ is the similarity variable and K_w is an empirical constant defined from scaling laws. Refer to [CR80b] for a complete review and for the values of the constants.

In buoyant jet configurations, the notion of self-similarity needs to be considered separately in the three distinct regions: the non-buoyant, intermediate and buoyant regimes. Clearly, self similar solutions exist in the non-buoyant and buoyant regimes. However, according to Abraham in [Abr65], the self-preserving analysis proves further that inside the intermediate region (transitional regime), the solution can not be self-similar. This is justified as far as the flow changes from a self-similar jet solution to that of a self-similar plume.

Experimental investigations demonstrate that the flow undertakes a linear spreading rate in the regions where the solution is self-similar. In such situations, the spreading rate is usually assumed to follow the exponential e^{-1} width at which the vertical velocity component decrease to 36% of the center-line velocity, for a specific horizontal profile. Generally, the experiments record a spreading angle of 13° in round jets, while about 11.98° for a pure plume as shown in Lee and Chu [LC03].

Both concepts (self-similarity and linear spreading) are rather difficult to employ and/or obtain globally at all positions of a buoyant jet rising in a limited geometrical configuration. Practically, direct interactions between the solid boundaries and the jet destroys the concept

of self-similarity and the linear spreading rate. Thus, solving an appropriate model or system of equations is required to handle such situations.

However, self-similarity analysis and spreading angle measurements can serve at least locally in such problems. In the vicinity of the source where the flow is normally not affected by the geometry, self-similarity analysis can serve to identify approximately the location of the transition and compare with the prediction of equation 1.4, for example. In addition, experimentalists (or numerical engineers) can employ the spreading angle measurements to have a previous insight on the required configuration so that direct interactions between the jet and the lateral boundaries of the domain are avoided.

1.1.5 Notion of entrainment

Entrainment, by definition, is the effect of an ambient fluid mixing another injected one by means of a circular flow structure. More precisely, when a light buoyant jet enters a calm ambient medium, high shearing occurs leading to the formation of eddies. These eddies capture the ambient fluid from the surrounding and remain in the rotational flow to mix with the interior injected fluid and thus form what is called a shearing mixing layer all along the edge of the jet. The ambient-injected fluid mixing is enhanced by the density gradients in very thin structure, and thus by molecular diffusion. All this phenomenon is referred to by the term entrainment and is illustrated in figure 1.6.

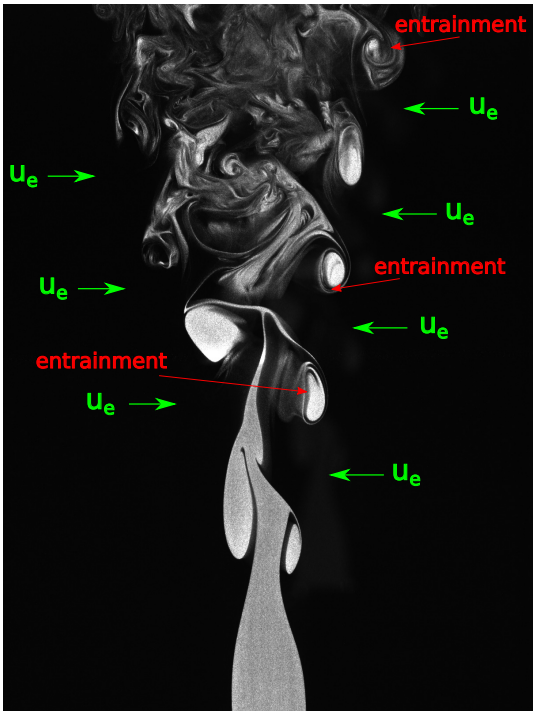

Figure 1.6: Illustration of the entrainment process at the edges of the buoyant jet: CEA private communication.

1.2 Free jet models: entrainment hypothesis

Morton, Taylor and Turner (MTT) in 1956 were the first to present an integral model for flows in infinite media [MTT56]. The model was originally defined for a pure plume flow owing a canonical round structure (system coordinates are r and z with a velocity field $\mathbf{u} = (u, w)$) and relies mainly on three assumptions: Boussinesq approximation (largest local density variations in the field of motion are small compared to a chosen reference density), self-similar solution and the entrainment assumption.

1.2.1 Entrainment modelling

The entrainment assumption of [MTT56] states that the rate of entrainment at the edge of the jet is proportional to a characteristic velocity $\mathcal{W}$ at this height. More precisely, by assuming a top-hat distribution where both the velocity and buoyancy forces are constant inside the buoyant jet and zero outside, the edge-entrainment rate $u_e(z)$ on a considered height z satisfies

$$u_e = \alpha \mathcal{W}, \tag{1.13}$$

where $\mathcal{W}(z)$ is thus the average value of the top-hat profile at the same height of u_e and α is the entrainment constant.

Several experimental studies propose different values for α depending on the flow regime conditions [CR80b]. Assuming a top-hat profile for the vertical velocity component w used to define $\mathcal{W}$, the estimated values of α can be as small as $\alpha^T \approx 0.05$ in pure jets and as big as $\alpha^T \approx 0.16$ for pure plumes [Lin00] (the super-script ^{T} is used to refer to the top-hat profile assumption).

1.2.2 1D conservation equations

The main idea behind the integral model is to relate the flow fluxes, as a function of the height z, together with α; fluxes of mass (mainly volume), momentum and buoyancy. We start by defining the volume flux πQ, the specific buoyancy flux πF and the specific momentum flux πM satisfying

$$Q(z) = \int_0^\infty w(r^2, z) dr^2, \tag{1.14}$$

$$F(z) = \int_0^\infty g'(r^2, z) w(r^2, z) dr^2, \tag{1.15}$$

$$M(z) = \int_0^\infty w^2(r^2, z) dr^2, \tag{1.16}$$

where $g'(r, z) = g(\rho_{\text{amb}} - \rho_p)/\rho_{\text{amb}}$ is the reduced gravity, dependent on the density of the plume $\rho_p(r, z)$ at the considered height.

Following the dimensions of Q [$\text{m}^3.\text{s}^{-1}$] and M [$\text{m}^4.\text{s}^{-2}$], we define the characteristic plume

velocity $\mathcal{W}$ and the characteristic plume radius $\mathcal{B}$ as

$$\mathcal{W}(z) = \frac{M(z)}{Q(z)} \quad \text{and} \quad \mathcal{B}(z) = \frac{Q(z)}{M^{1/2}(z)}, \tag{1.17}$$

Considering the physical balance of mass in the plume, we can easily obtain an ordinary differential equation relating the vertical volume flux variation to the momentum flux and α;

$$\frac{d}{dz}Q = 2\alpha\mathcal{B}\mathcal{W} = 2\alpha M^{1/2}. \tag{1.18}$$

Similarly, an equation for the vertical variation of the buoyancy flux can be obtained by considering the conservation of the buoyancy in the plume, and thus written as

$$\frac{d}{dz}F = -QN^2, \tag{1.19}$$

where $N(z)$ is the buoyancy frequency defined as

$$N^2(z) = -\frac{g}{\rho_{\text{amb}}}\frac{\partial\rho}{\partial z}, \tag{1.20}$$

and $\rho = \rho(z)$ is the density of the stratified layers outside the plume.

A final equation is required for the vertical momentum flux variation dM/dz. Assuming that the flow is steady and incompressible, the conservation of momentum flux equation leads to

$$\frac{d}{dz}M = S(z), \tag{1.21}$$

where S is defined by the following integral

$$S(z) = \int_0^\infty g'(r^2, z)dr^2 = \frac{FQ}{M}. \tag{1.22}$$

Identify $S = FQ/M$ in equation (1.22) is a strong assumption employed in [MTT56]. We carry out further investigations about this issue and its validity in the next section.

As far as α is assumed constant in the problem, the 1D system of equations (1.18), (1.19) and (1.21) is closed and the buoyant jet flow is described in terms of the three plume fluxes, Q, F and M. The quality of the resolution depends on the correct choice of α (based on experimental measurements from the literature) and the validity of the entrainment assumption; $u_e = \alpha\mathcal{W}$

1.2.3 Generalization and profile assumptions

For a matter of completeness, we highlight in this subsection on the simplifications presented in equation (1.22). Employing the similarity assumption of [MTT56], w and g' can be written respectively as

$$w(r^2, z) = \mathcal{W}(z)\mathsf{W}(R^2), \tag{1.23}$$

$$g'(r^2, z) = \mathcal{G}'(z)\mathsf{G}(R^2), \tag{1.24}$$

with $R(r, z) = r/\mathcal{B}$. When the plume's density and vertical velocity admit the same radial structure ($\mathsf{W}(R^2) = \mathsf{G}(R^2)$), equation (1.22) is evidently satisfied. Otherwise, the relation is not satisfied; $SM/FQ \neq 1$.

A simple classical radial structure employed in the literature considers a top-hat (box) profile for both variables, written as

$$w(r^2, z) = \mathcal{W}(z)\mathcal{H}\bigg(1 - \frac{r^2}{\mathcal{B}^2}\bigg), \tag{1.25}$$

$$g'(r^2, z) = \mathcal{G}'_c(z)\mathcal{H}\bigg(1 - \frac{r^2}{\mathcal{B}^2}\bigg), \tag{1.26}$$

where $\mathcal{H}$ denotes the Heaviside step function defined as $\mathcal{H}(l) = 1$ if $l \geq 0$ and 0 otherwise.

However, experimental measurements point very strongly to the fact that the profiles are almost of a Gaussian type and that the density profiles are wider than those of the axial velocity by a varying parameter $\lambda(z)$ [LC03] and thus the Gaussian profiles are defined as

$$w(r^2, z) = \mathcal{W}(z)\exp\bigg(-\frac{r^2}{\mathcal{B}^2}\bigg), \tag{1.27}$$

$$g'(r^2, z) = \mathcal{G}'_c(z)\exp\bigg(-\frac{r^2}{\lambda^2\mathcal{B}^2}\bigg). \tag{1.28}$$

The choice of the profile assumption is clearly reflected on the relation between the fluxes and evidently α. For instant, by considering the integral definitions of Q, M and by employing the super-scripts ^{G} and ^{T} respectively to denote the Gaussian and top-hat profiles, we obtain

$$Q^G = \mathcal{W}\mathcal{B}^2 = Q^T \quad \text{and} \quad M^G = \frac{\mathcal{W}^2\mathcal{B}^2}{2} = \frac{1}{2}M^T. \tag{1.29}$$

Comparing with equation (1.18) for both a top-hat and a Gaussian profile assumptions, it is possible to relate both entrainment coefficients as

$$\alpha^T = \sqrt{2}\ \alpha^G. \tag{1.30}$$

The effect of introducing the parameter λ is reflected on the integral of S, and thus on equation

(1.21) which by using a Gaussian profile modifies to

$$\frac{d}{dz}M = \left(\frac{1+\lambda^2}{2}\right)\frac{FQ}{M}. \tag{1.31}$$

Thus, it is extremely important before employing the model to identify whether the experimental measured value of α is based on a top-hat or on a Gaussian profile assumption for w and g'. Hence, a great attention must be paid on the definition of the fluxes and their relation with the characteristic plume velocity $\mathcal{W}$ and the characteristic plume's radius $\mathcal{B}$ (equation (1.29)).

1.2.4 Validity of the constant entrainment coefficient

It has been figured out later while studying buoyant jet flows that the results obtained from the Morton-Taylor-Turner model [MTT56], if used with a constant α along the height z, contradicts with the experimental measurements. Employing both, similarity solution analysis and experimental measurements, it has been figured by Abraham in [Abr65] and List and Imberger in [LI73] that α takes a non-constant value along the height of the jet and however dependent on the flow structure; basically a local Richardson number. And thus, the model has been modified by employing the new non-uniform definition of α and better comparisons have been reported.

The Modified 1D models are rather difficult to employ in cases of complex stratification, inclined buoyant jets, cross-flows with non-circular structures and mainly flows in limited configurations [CR80b]. This is basically due to the Boussinesq and the self-preserving assumptions that are probably destroyed. Hence, computational fluid dynamics (CFD) approaches are always recommended in such situations and can be employed to perform comparisons versus both, experimental measurements and existing 1D models.

1.3 Models for flows in confined and semi-confined media

It is extremely important in buoyant jet flow models to take into account the studied environment, whether an infinite or a bounded medium. Inside confined/semi-confined bounded environments, the problems are extremely interesting and can appear in security assessment studies for hydrogen based systems, geophysics, fire modellings and ventilations [CT12, BT69, Lin99]. Basically, the main issue in such studies is to understand the mixing-dispersion of the intruded light fluid with the ambient dense fluid (say for example hydrogen-air in fuel cells) inside small chambers with forced or natural ventilations.

1.3.1 Confined cavity with a small hole for de-pressurizing

The first reported theoretical work for buoyant flows in confined cavities is cited for Baines and Turner in [BT69]. The theory was proposed to model a filling box phenomenon by considering the flow of a pure thermal plume inside an enclosure. A schematic description of the filling box phenomenon is illustrated in figure 1.7, where it has been observed that the flow spreads all along the ceiling after the impact. A homogeneous layer is formed at the top of the enclosure due to the flow recirculation near the sides of the enclosure. The layer is separated from the ambient by what is called the filling front, which itself descends with the increase of time.

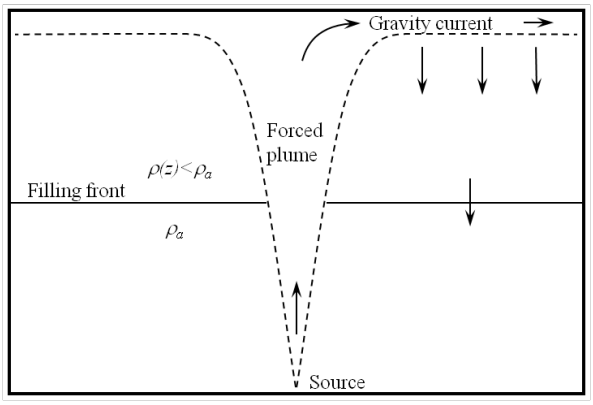

Figure 1.7: Pure plume filling an enclosure without ventilations: filling box phenomenon, Baines and Turner in [BT69].

Analytical expression was proposed in [BT69] to calculate the velocity of the descending filling front and the density distribution once the front reaches the bottom of the cavity. This theory was updated in the next work of Worster and Huppert in [WH83] to describe the time variation of the vertical density profile in the first stage of the front descending. Assuming that the height of the box is H with a cross-section A, Worster and Huppert introduce the normalized length ζ, time τ and density δ respectively as

$$z = H\zeta, \tag{1.32}$$

$$t = t^*\tau, \tag{1.33}$$

$$g\frac{\rho - \rho_{\text{amb}}}{\rho_{\text{amb}}} = \frac{B_0^{2/3}}{4\alpha^{4/3}H^{5/3}}\delta, \tag{1.34}$$

where the reference time $t^* = A/(4\pi^{2/3}\alpha^{4/3}H^{2/3}B_0^{1/3})$. The buoyancy flux at the source B_0 is related to the source mass flux Q_0 as

$$B_0 = g\frac{\rho_{\text{amb}} - \rho_{\text{inj}}}{\rho_{\text{amb}}}Q_0. \tag{1.35}$$

The value the entrainment coefficient α has been assume to be uniform along the height.

However, different used values have been reported in the literature. For a pure plume, Worster and Huppert use $\alpha = 0.1$ in [WH83]. However, the values can be much smaller and can reach up to 0.05 as that employed by Cariteau and Tkatschenko in [CT12], Papanicolaou and List in [PL88] or by Cleaver et al. in [CML94].

Under the iso-bar and iso-thermal conditions, the volume fraction of the injected fluid is defined as

$$X = \frac{\rho_{\text{amb}} - \rho}{\rho_{\text{amb}} - \rho_{\text{inj}}}. \tag{1.36}$$

The normalized density δ can be related to X as

$$X = -X^* \delta, \tag{1.37}$$

where the reference volume fraction of the injected fluid is defined as

$$X^* = \frac{B_0^{2/3} \rho_{\text{amb}}}{4\alpha^{4/3} H^{5/3} g(\rho - \rho_{\text{amb}})} \tag{1.38}$$

Thus, Worster and Huppert express the normalized position of the first front ζ_0 and the density δ respectively as

$$\zeta_0(\tau) = \left\{ 1 + \frac{1}{5} \left(\frac{18}{5} \right)^{1/3} \tau \right\}^{-3/2}, \tag{1.39}$$

and

$$\delta(\zeta, \tau) = \frac{1 - \zeta^{5/3}}{1 - \zeta} 5 \left(\frac{5}{18} \right)^{1/3} \zeta^{-2/3} \left(1 - \frac{10}{39}\zeta - \frac{155}{8112}\zeta^2 \right) - c(\tau), \tag{1.40}$$

where

$$c(\tau) = 5 \left(\frac{5}{18} \right)^{1/3} \left\{ \frac{\zeta_0^{-2/3} - 1}{1 - \zeta_0} + 3 \frac{1 - \zeta_0^{5/3}}{1 - \zeta_0} \left(\frac{1 - \zeta_0^{1/3}}{1 - \zeta_0} - \frac{5}{78} \frac{1 - \zeta_0^{4/3}}{1 - \zeta_0} - \frac{155}{56784} \frac{1 - \zeta_0^{7/3}}{1 - \zeta_0} \right) \right\}. \tag{1.41}$$

In a later work, Cleaver et al. in [CML94] presented a study on the dispersion of natural gas inside an enclosure by a buoyant jet source. They carried out an experimental study which allowed them to propose a theoretical model based on a formation of a homogeneous layer, linked to both the geometry and the momentum flux at the jet source. This homogeneous layer, which is formed at the top of the enclosure, has been predicted almostly by all theoretical models afterwards.

Experimental measurements and observations justifies what causes such a layer formation. Going through the work details of Baines and Turner [BT69], when the ratio of the momentum to buoyancy fluxes in the horizontal gravity current exceeds 0.1 ($M/B \geq 0.1$), the overturning flow creates a homogeneous layer as it reaches the side of the enclosure (figure 1.7). This criterion, being coherent with the correlations introduced by Papanicolaou and List afterwards in [PL88], is based on the ratio of the height of the enclosure H to the horizontal width W (geometrical properties of the domain).

Kaye and Hunt performed in [KH07] similar experimental work on pure salt water plumes inside cylindrical filling box with different aspect ratios. They defined the aspect ratio $\phi = R/z$ (R being the distance from the plume axis to the enclosure's side wall) and observed two flow modes. For great aspect ratio $\phi > 1.5$ (cylinder much wider than its axial height), they noted that the flow spreads calmly along the side wall and then slump down without entraining fresh water (ambient) creating stratified waved density interfaces. In the contrary, when $\phi < 0.66$ (tall thin cylinder), Kaye and Hunt had recorded a rolling back phenomenon (recirculation) which entrains strongly fresh water and create a well mixed homogeneous layer. A schematic representation of the two recorded flow modes is illustrated in figure 1.8. In figures 1.9 and 1.10, we present a series of instantaneous experimental snap-shots presented in [KH07]. The two modes can be clearly seen: calm spreading without overturning (figure 1.9) and spreading with overturning (figure 1.10).

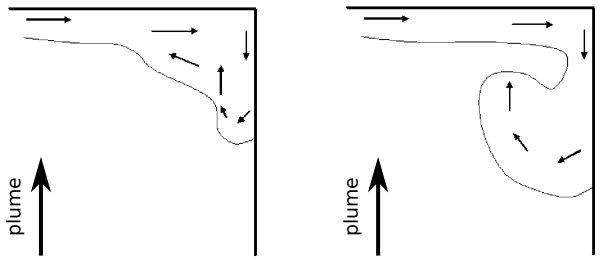

Figure 1.8: Flow modes observed by Kaye and Hunt in [KH07]: filling box phenomenon. Left: no overturning and a slumping mode with stratified density interfaces ($\phi > 1.5$), right: overturning with a rolling mode and strong mixing ($\phi < 0.66$).

Figure 1.9: Instantaneous experimental images from [KH07] with $\phi > 1.5$. Left: outflow from plume, middle: side-wall spreading flow, right: slumping back mode.

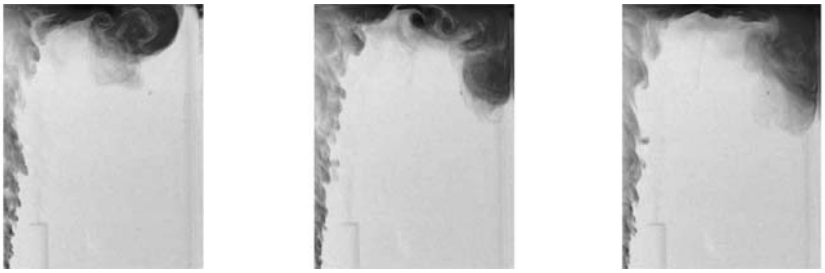

Figure 1.10: Instantaneous experimental images from [KH07] with $\phi < 0.66$. Left: outflow from plume, middle: side-wall spreading flow, right: rolling back mode.

In buoyant jet configurations, overturning occurs regardless of the geometry. Cleaver et al. shows in [CML94] that a homogeneous layer can be formed if the inertial fluxes at the source

are high enough compared to the gravitational effects. More generally, they introduce a dimensionless volume Richardson number

$$\mathrm{Ri_v} = \frac{g(\rho_{\mathrm{amb}} - \rho_{\mathrm{inj}})\ \mathcal{V}^{1/3}}{\rho_{\mathrm{inj}} u_{\mathrm{inj}}^2}, \tag{1.42}$$

where $\mathcal{V}$ is the volume of the enclosure.

In situations where $\mathrm{Ri_v} \ll 1$, overturning occurs and the inertia of the jet is sufficient to mix the entire enclosure and produce a homogeneous mixture. Otherwise, if $\mathrm{Ri_v} \gg 1$, a complied vertical stratified regime is obtained. In a special case where $\mathrm{Ri_v}$ plays around unity, a homogeneous layer is formed at the top of the enclosure and stratification layers follow below. This issue is well illustrated in figure 1.11, for a varying $\mathrm{Ri_v}$.

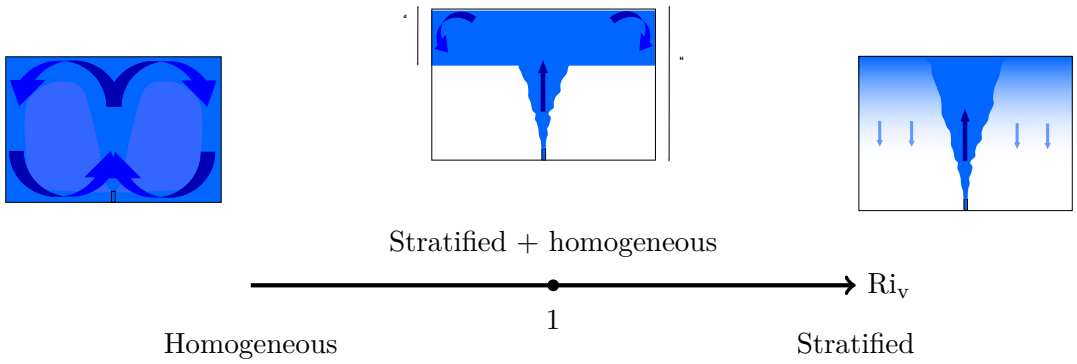

Figure 1.11: Illustration of the predicted flow regime inside confined enclosures: Stratified versus homogeneous mixing phenomena.

In this framework, Cariteau and Tkatschenko performed an experimental work in [CT12] to study the validity and/or limitation of the Worster and Huppert theoretical model [WH83]. A helium release in a nominally unventilated air enclose has been considered, where the cavity satisfies the geometrical conditions of Baines and Turner [BT69]. When a stratified regime without a homogeneous layer builds up in the cavity ($\mathrm{Ri_v} \gg 1$), Cariteau and Tkatschenko observe two type of vertical concentration profiles. The first parabolic profile was in good agreement with the theoretical mode (figure 1.12, left). However, the theoretical model failed to predict the linear concentration profile obtained with a release from a smaller diameter of injection (figure 1.12, right).

No satisfying justifications have been proposed for such a limitation, but one possibility can be always the fact that α must not be considered uniform along the height of the cavity.

1.3.2 Semi-confined cavity

The theoretical work of Baines and Turner was later extended by Linden et al. in [LLSS90] and by Linden in [Lin99] to consider semi-confined cavities; basically to study the emptying

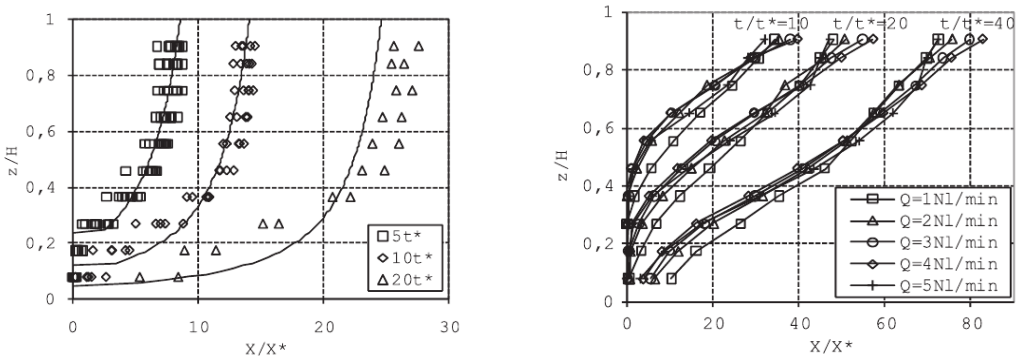

Figure 1.12: Two concentration vertical profiles in a stratified regime without a homogeneous layer. Left: parabolic profile, right: linear profile [CT12].

of a buoyant gaz filling box by forced or natural ventilations. Two main ventilations forms have been considered; mixing ventilation and displacement ventilation.

In the first case, a single vent (window) is considered at the top of the vertical wall, and thus a bidirectional flow takes place. If a light fluid (say hydrogen) is intruded inside the cavity, light mixture exits from the upper part of the vent (where the internal pressure is higher than exterior) while denser fresh fluid enters from the lower part of the vent (external pressure higher). Hence a homogeneous layer is formed at the top of the cavity, separated from below by what is called the neutral plan (the neutral plan is situated at the height where the hydrodynamic pressure inside the cavity is equal to that outside). A theoretical model in such configurations is presented in [LLSS90], where the height of the neutral plan and the top layer concentration are evaluated analytically.

However, two vents situated respectively at the top and the bottom of a vertical wall are considered in the second case. A theoretical model for such configurations is presented in the next subsection.

1.3.3 Two vented cavity

When a light fluid is continuously injected inside a cavity with two vents situated at the top and the bottom of a vertical wall, dense fluid enters from the bottom vent, entrains with the ascending flow and displaces a light mixture throughout the top vent. This behavior forms a simple stratification consisting in two layers separated by a horizontal interface as sketched in figure 1.13.

As we see, the lower layer is of height h and contains pure air (uniform concentration). In the top, Linden et al. [LLSS90] record a uniform homogeneous layer of hight $H - h$ containing a uniform concentration of air-gas mixture, H being the height of the enclosure. The presence of the upper buoyant layer creates a pressure difference across the vents, which results in driving a draining flow. A steady state is assumed to be reached when the draining flow

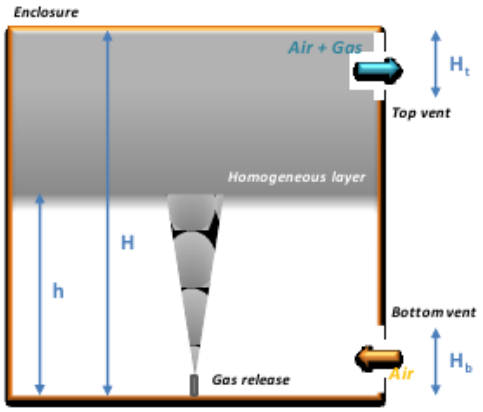

Figure 1.13: Gas-air dispersion phenomenon situated in the displacement ventilation study of Linden et al. in [LLSS90]: case of a gas release in a semi-confined cavity with two vents localized at same side-wall and at different altitudes.

is balanced by the convective buoyant flow. In their theoretical framework, they propose a methodology to calculate for a steady state solution, the concentration of the homogeneous upper layer and the height of the interface.

The height of the interface h is calculated as

$$\frac{S^*}{H^2} = C^{3/2} \left(\frac{\left(\frac{h}{H}\right)^5}{1 - \frac{h}{H}} \right)^{1/2}, \tag{1.43}$$

where S^* is the effective vent area defined as

$$S^* = \frac{\sqrt{C_t} S_t S_b}{\left(0.5 \left(\frac{C_t}{C_b} S_t^2 + S_b^2\right)\right)^{1/2}}, \tag{1.44}$$

with C_t the top vent discharge coefficient, C_b the bottom vent discharge coefficient, S_t the top opening area, S_b the bottom opening area.

The concentration X_f of the upper homogeneous layer is estimated as

$$X_f = \frac{1}{C} \left(\frac{Q^2 h^{-5}}{g'} \right)^{1/3}, \tag{1.45}$$

where Q is the releasing (injecting) gas flow rate, g' is the reduced gravity defines as

$$g' = g \frac{\rho_{\text{amb}} - \rho_{\text{inj}}}{\rho_{\text{amb}}}. \tag{1.46}$$

C is a universal constant given by the plume theory of Morton et al. [MTT56]

$$C = \frac{6}{5}\alpha\left(\frac{9}{10}\alpha\right)^{1/3}\pi^{2/3}, \tag{1.47}$$

where α is the constant entrainment coefficient (from 0.05 to 0.15 for a pure plume).

The discussed approach has been found to be commonly used as an engineering tool for build-up assessment (example in building ventilation [LLSS90]). However, we can easily note that it is limited to a release occurring at the bottom surface as far as it does not allow the height of the release to be considered. A modified model is proposed by Bernard-Michel et al. in [BMSH17], where the parameter H is considered as the altitude separating the upper edge of the top vent from the injection's height. In this case, h has to be considered as the interface's height starting from the injection's height as a reference point. Moreover, the authors propose further improvements to take into account the orientation of the vents and the hypothesis of the varying entrainment coefficient along the buoyant-jet height according to the work of Kaminski et al. in[CKT08].

Another extensively used approach for studying buoyant jet flows in limited (confined or semi-confined) configurations is CFD. This approach is often used to get over the limitations induced by theoretical models and/or the prior knowledge regarding the entrainment coefficient.

1.4 CFD–Experimental benchmarks of buoyant jets in various cavities

In this section, we present some recent numerical–experimental studies of buoyant jets in confined and semi-confined environments. In the framework of this dissertation, the selected studies are devoted to security assessments of systems using hydrogen as energy carrier. The numerical simulations have been performed by several teams [BMTVG12, TSBMLQ13, BMCN$^+$13, GSM$^+$15, PVH$^+$09] and thus comparisons versus experimental measurements are presented. It has been justified that under certain conditions, helium can be a good substitute of hydrogen [SGS98b] and thus air-helium buoyant jets have been considered for experimental security reasons.

We restrict ourselves in presenting benchmarks of air-helium buoyant jet flows in three different types of configurations: confined, one–vented and two–vented cavities. The aim of the review is to see the discrepancies between different employed turbulence models in reproducing the experimental measurements and to analyze the effect on the considered configuration. Results and conclusions of the performed CFD benchmarks are presented in the next subsections.

1.4.1 Case of nominally unventilated enclosure

For an air–helium buoyant jet rising in a confined cavity, Bernard-Michel et al. in [BMTVG12] present a CFD benchmark to evaluate on the capability of numerical simulations to predict the concentration distribution. The performed numerical simulations mimic the experimental set-up GAMELAN, which is a French facility constructed in the framework of the project ANR PANH DIMITRHY at CEA–Saclay [CT12]. Helium is injected, from a pipe situated at the mid-bottom surface, into a 1 m^3 parallelepiped confined cavity (a small opening is assumed at the bottom surface for de-pressurizing). Experiments has been carried out over a wide range of different injection flow-rates where helium concentration has been recorded from employed sensors (katharometers). A schematic representation of the confined-GAMELAN configuration showing the position of the measuring sensors is presented in figure 1.14.

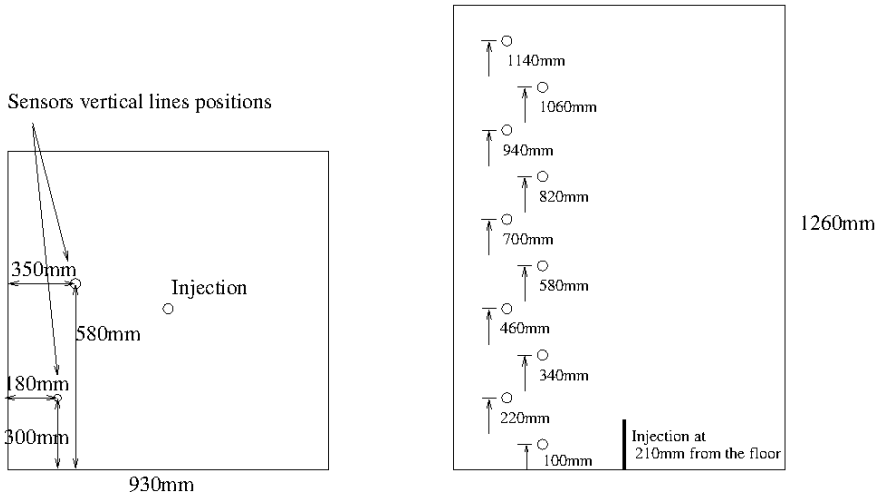

Figure 1.14: Confined–GAMELAN experimental set-up showing the sensors locations. Left: top view, right: side view, [CT12].

Different teams either using large eddy simulations (LES) or Favre averaged Navier-Stokes (FANS) ($k-\epsilon$) simulated the buoyant jet resulting from the helium injection. In cases of high injection volumetric flow-rates, the results obtained by the different teams were satisfactory when compared with the experimental measurements. This is not the case of small injection flow-rates where the differences between experimental measurements and CFD were significant (figure 1.15). The helium concentration was either underestimated or overestimated with CFD up to 30%. The issue behind these discrepancies has been claimed to be due to the employed turbulence models.

In a next work, Tran et al. in [TSBMLQ13] and [Tra13] carried out 2D axi-symmetrical direct numerical simulation (DNS) study on an equivalent configuration with a small injection flow-rate $Q = 4$ Nl.min^{-1} ($\mathrm{Ri}_{\mathrm{inj}} = 22.74$, $\mathrm{Ri}_{\mathrm{v}} = 145$). The numerical results were compared with the experimental measurements and other numerical results in the benchmark of Bernard-Michel et al. [BMCN$^+$13].

In short, the numerical results used in the comparison are either 2D axi-symmetrical or 3D

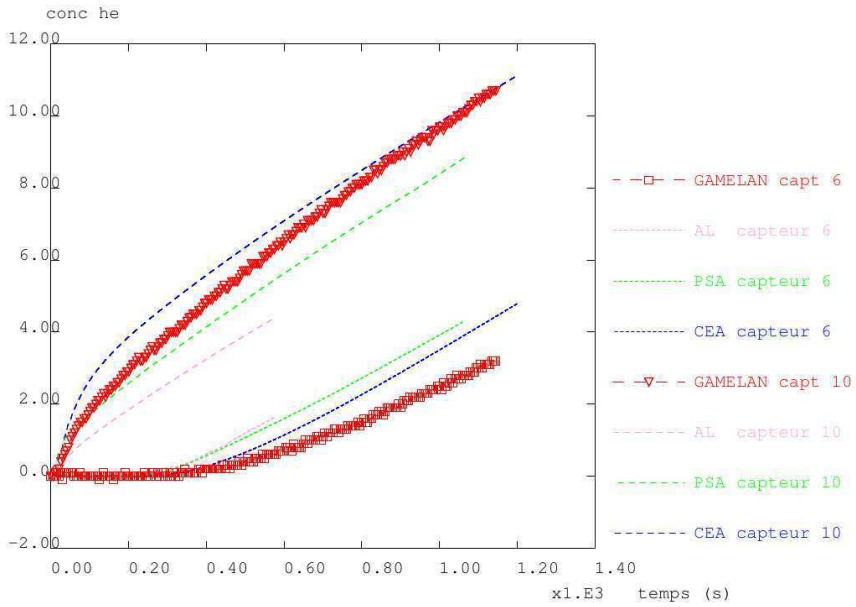

Figure 1.15: Time evolution of the helium concentration at two fixed sensors [BMTVG12]. Experimental measurements are represented with symbols while CFD results with dashed lines.

(two axi-symmetrical simulations performed by DNS and LES, six 3D simulations where 2 are performed with coarse DNS and 4 with FANS). The comparisons are illustrated in figure 1.16 for the instantaneous helium concentration vertical profiles at $t = 275$ seconds.

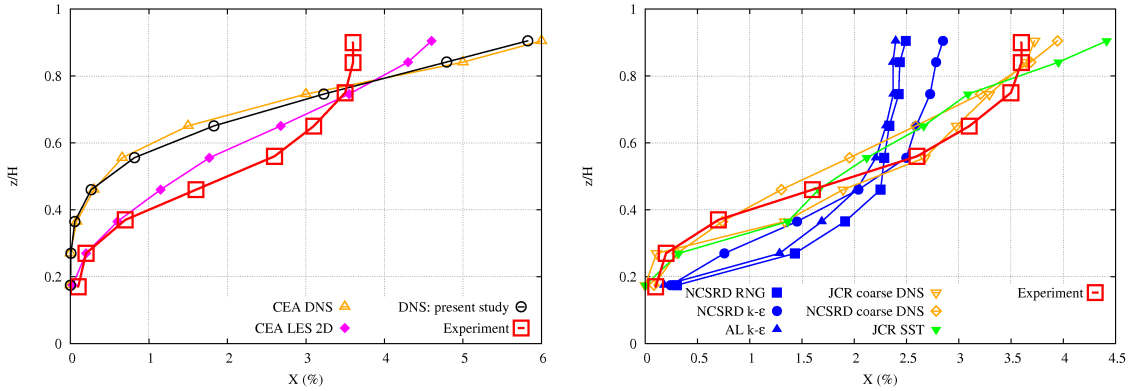

Figure 1.16: Instantaneous helium volume fraction X (concentration) vertical profiles at $t = 275$ seconds [BMCN$^+$13, Tra13]. Left: axi-symmertrical CFD simulation, right: 3D CFD simulations.

Experimental measurements record a maximum helium concentration of 3.6% situated in a top homogeneous layer. In axi-symmetrical configurations, the differences between CFD and the experiment are significant. CFD highly overestimate the maximum concentration (overestimation can reach approximately 60 %) and predict a linear stratification in all cases, although LES (Smagorinsky SGS model) was noted to be more diffusive than DNS.

Regarding the 3D simulations, it was figured out that the FANS results (2 $k-\epsilon$ simulations and one RNG) are very diffusive where they underestimate the maximum helium concentration (underestimation predicted by a $k-\epsilon$ simulation can reach 37.5% approximately) and overestimate the length of the top homogeneous layer (about 60% predicted by NCSRD RNG). Although they do not reproduce the homogeneous layer, the predictions proposed from the two coarse DNS simulations and the SST $k-\omega$ simulation are the closest to the maximum measured concentration at the top of the cavity. However, considerable discrepancies are noted near the mid-height of the cavity.

1.4.2 Case of a one vented cavity

In the framework of HyIndoor project [HyI, FHAJ+17], a CFD benchmark has been proposed by Giannissi et al. in [GSM+15] to compare with the measurements of Cariteau and Tkatschenko on the one-vented GAMELAN experiment [CT13]. A schematic representation of the one-vented GAMELAN configuration showing the position of the vent and the katharometers is presented in figure 1.14.

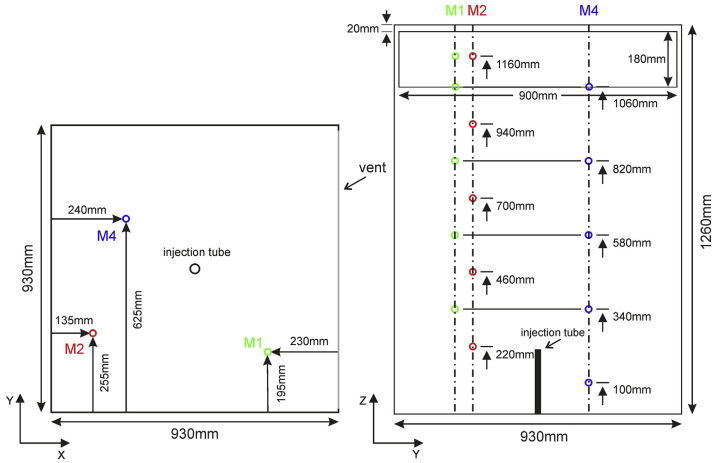

Figure 1.17: One-vented GAMELAN experimental set-up showing the vent and sensors locations. Left: top view, right: side view, [CT13].

The experiment was carried out three times, where three different vent sizes have been examined. In all cases, the vent is located in the middle of the right wall and 2 cm below the top-ceiling. A complete description of the employed vents is summarized in table 1.1.

A high injection flow rate has been considered (60 Nl.min^{-1}, $\mathrm{Ri}_{\mathrm{inj}} = 0.1$). Three HyIndoor partners participated in the benchmark (JRC, NCSRD and UU) using respectively three different CFD softwares (ANSYS Fluent, ADREA-HF and ANSYS CFX) and respectively three turbulence models (FANS transitional SST, FANS $k-\epsilon$ and LES dynamic Smagorinsky).

Both, JRC and NCSRD, impose a symmetry assumption on the mid vertical plane along the y direction and perpendicular to the vents. No symmetrical assumption has been priory made by the UU. All simulations have been carried out by employing an additional meshed zone

	Vent dimension $w \times h$ [cm $\times$ cm]	Vent area [cm^2]
Vent a	90 $\times$ 18	1620
Vent b	18 $\times$ 18	324
Vent c	90 $\times$ 3.5	315

Table 1.1: The three different vents dimensions employed in the one-vented GAMELAN experiment.

outside the vent to move the boundary condition away from the cavity. Fixed outlet pressure condition has been used [GSM$^+$15, MS14].

Cariteau and Tkatschenko identified in [CT13] the influence of the vent size on the dilution phenomenon that takes place inside the cavity, where both the vent's surface area and the vertical extension (h) affect the air dilution. This observation induced another aim of the benchmark [GSM$^+$15] which is to evaluate the capability of CFD to reproduce correctly the effect of the different vent sizes on the interior flow pattern. Satisfactory numerical results have been obtained where the increase of the helium mass respectively from configuration one to three has been predicted by all partners. In what follows, we only present the influence of the employed turbulence model on the predictions obtained from the first configuration, where maximum air dilution takes place in the cavity.

CFD predictions, from all partners, reproduce correctly the formation of a homogeneous mixture (approximately 97% pure air) along the lowest 2/3 of the cavity's height and a stratified layer at the top. This is illustrated by the mean helium volume fraction vertical profiles, measured and simulated, at the steady state along sensors M2 and M4 (figure 1.18, left). However, discrepancies have been recorded on the concentration level predicted by different turbulence models.

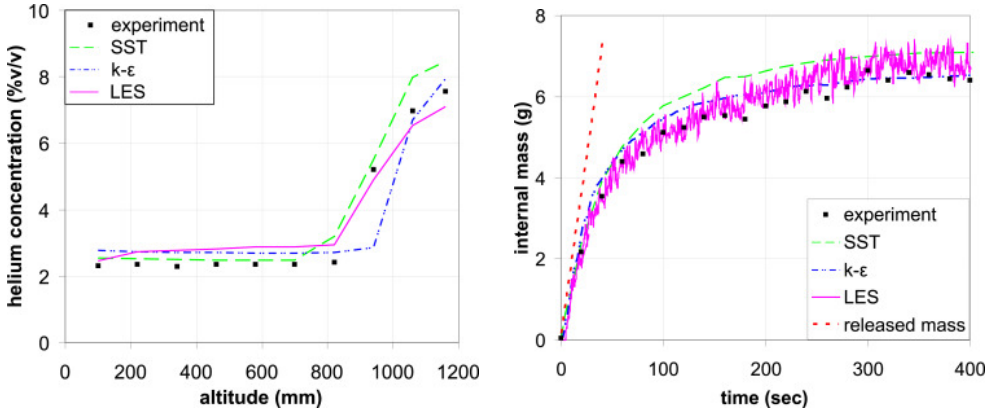

Figure 1.18: CFD predictions versus experimental measurements in configuration one. Left: time averaged helium volume fraction vertical profiles at sensors M2 and M4 in the steady state, right: time evolution of the helium total mass in the cavity, [GSM$^+$15].

In the homogeneous layer at the bottom, both LES and $k-\epsilon$ models overestimate the concentration of helium (by about 36 %), while the predictions of the SST transitional model are in better agreement with the measured values in this region. The concentration overestimation predicted by the $k-\epsilon$ model is probably due to extra turbulent diffusion modeled in this laminar source vicinity. By looking to the details of the performed LES, we note that UU employ a high Courant–Friedrichs–Lewy condition (CFL = 40), and thus a time step of 0.01 s has been used. Moreover, the grid cell size is estimated to be about 0.7 cm per direction, which can be 25 times larger than an estimated Kolmogorov length scale [CHP06]. These issues can justify the LES overestimation due to additional sub-grid scale (SGS) modelled viscosity. UU suggest in [GSM$^+$15] that the LES results could be improved by reducing the time step, however a large step has been used to obtain results in a short time.

At the top of the cavity, SST model overestimates the concentration by about 20 %, while $k-\epsilon$ results underestimates (except for the last sensor, underestimation can reach maximum to 40%). LES results agree better with the experimental measurements except at the highest sensor (6% underestimation). According to JRC, the overestimation of the helium concentration at the top of the cavity predicted by SST model could be probable to the inaccurate prediction of the time and position of the laminar-to-turbulent transition.

For a global comparison, the evolution of the total mass of helium inside the cavity has been calculated (figure 1.18, right). At the transient state, the mass predicted from the LES is in good agreement with the experimental measurement, oppositely to the $k-\epsilon$ prediction which overestimates the value (maximum can reach to 20 %). However, the issue is completely reversed at the steady state where LES slightly the mass ($\approx 13\%$), while $k-\epsilon$ show satisfactory prediction. Predictions presented by the JRC using the SST model always overestimate the mass, probably for the same reason of the inaccurate transition capture (30% at the transient stage and 13% at steady state).

1.4.3 Case of a two vented garage

A benchmark has been carried out by Papanikolaou et al. in [PVH$^+$09] in the framework of HYSAFE SBEP–V20 project to qualify the CFD predictions regarding the hydrogen release scenarios. The numerical results are compared to the experimental measurements of Swain et al. [SGS98a]. The global aim of the work has been devoted to determine the ventilation requirements in car-fuel cells garages and to study the influence of the vent's vertical extension on reducing the concentration accumulation after a release.

Three experiments have been carried in a two vented garage of dimensions 6.4208 x 3.7084 x 2.8067 m^3. The vertical extension of the vents employed in each experimental set-up are respectively 0.064, 0.24 and 0.5 m. In each case, the vents take the complete horizontal width of the door and situated on the same wall (garage door), one at the top and the second at the bottom and both. Helium is injected in the garage with a flow-rate of 120 L.min^{-1} ($\mathrm{Ri}_{\mathrm{inj}} = 514$). Four sensors have been employed to measure the concentration and placed as described in figure 1.19. A complete description regarding the experimental set-up can be

reviewed from [PV05].

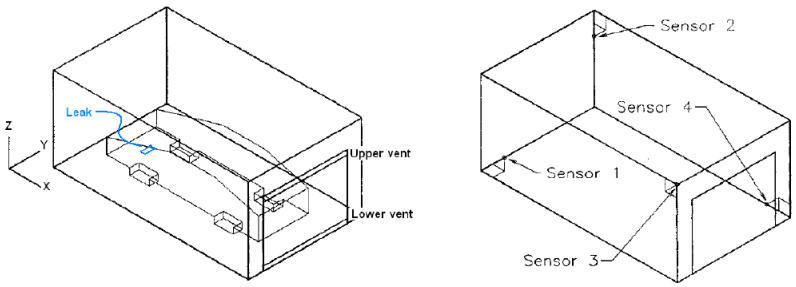

Figure 1.19: Two-vented garage experimental facility showing the vents and sensors positions, [PVH$^+$09].

Five HySAFE partners participated in the benchmark; DNV, JRC, NCSRD, UPM and UU using respectively the CFD codes FLACS9 ($k-\epsilon$), CFX 11 SP1 (laminar + buoyancy effects or SST), ADRA–HF ($k-\epsilon$ + buoyancy effects), FLUENT ($k-\epsilon$) and FLUENT ($k-\epsilon$ + buoyancy effects) [PVH$^+$09]. An exterior domain has been modelled near the vents by all partners and a coarse grid was employed (can reach 38 cm along the span-wise direction). Only NCSRD and UU employ an axi-symmetrical assumption in the half-plane perpendicular to the vents. We review in what follows the results obtained for the last configuration only, where the maximum air-dilution has been recorded in the garage.

The evolution of helium concentration at the four sensors is depicted in figure 1.20, left and middle.

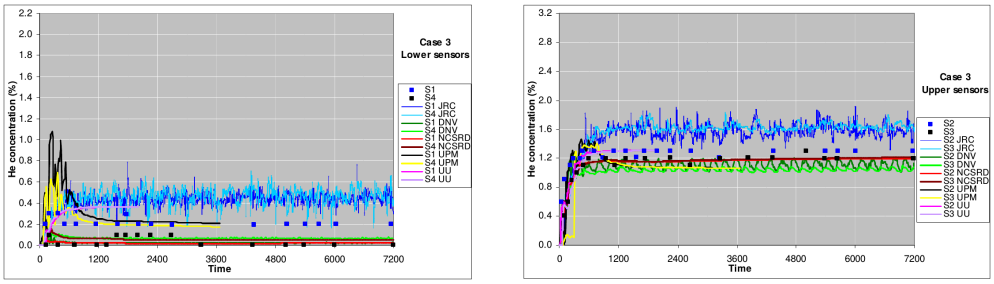

Figure 1.20: Configuration 3. CFD–experimental time evolution of the helium concentration, left: lower sensors, right: upper sensors [PVH$^+$09].

At the lower sensors, UPM prediction rather agrees with the measurement at sensor S1 while DNV and NCSRD predictions rather match the measurements at S4. JRC and UU tend to overestimate the concentration at both bottom sensors (can reach approximately 60%). At the top of the garage, the values recorded by JRC overestimate the measurements at both sensors S2 and S3 (about 35%), UU rather agree with the measured values at S2, while all the remaining partners globally underestimate the concentration (approximately 16 %).

The concentration evolution predicted by JRC show an oscillatory pattern at the four sensors, which has been not predicted by the remaining partners. According to JRC, the oscillations

are probably due to the employment of the laminar turbulence model. In practice, JRC carried out the same simulation using the SST model and recorded weaker oscillations. However, the choice of employing a laminar model is due to the observation of JRC where they note that stagnant flow conditions exists in big regions inside the garage. JRC carried out a grid refinement study, but no improvements have been recorded regarding the oscillations.

DNV report at the higher sensors a periodic-like oscillatory behavior which has been recorded also by reducing the time step of the simulation from 10^{-2} to 10^{-3} seconds. They claim that this particular flow pattern is probably due to an non-physical recirculation of helium from the top to bottom vent, due to reduced size of the exterior region. DNV repeated the simulation with a finer grid, but the same behavior has been reported again.

NCSRD confirm that the oscillations and the periodicity issue are due to the reduced size of the exterior domain employed by DNV and JRC. Basically, NCSRD carried out a sensitivity study on the size of the extended domain and recorded similar oscillations for reduced exterior sizes. They confirm that the influence is also sensitive to the variation of the exterior region, per direction. In fact, the exterior domain employed by NCSRD is the biggest compared to what has been used by other partners.

Globally, the ratio of the predicted concentration to the measured average C_p/C_o at the steady state has been calculated (figure 1.21). The CFD predictions are worse at the lower sensors (C_p predicted by JRC can be about 11 times higher that C_o at S4) while better ratio has been seen for the top sensors (can be bigger by about 0.5 times for JRC). The partners justify this issue to be probably related to experimental uncertainty of the measurements at the low sensors rather than the FANS models, especially that low helium concentration levels take place at the bottom of the garage [PVH$^+$09]. Another justification could be the thermal condition, where different temperatures have been used in different simulations as an initial condition.

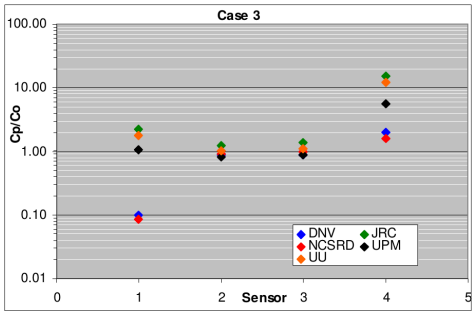

Figure 1.21: Configuration 3. Right: predicted to measured mean concentration, [PVH$^+$09].

1.5 Motivation of the present work

The work carried out in this Ph.D. can be situated in a similar framework of the numerical studies presented in subsections 1.4.1, 1.4.2 and 1.4.3. A motivation on the main numerical

choices taken out in the present work are described in this section.

The issue relies on the difficulty of simulating numerically buoyant jets rising in confined and semi-confined cavities. This difficulty is basically related to the choice of the suitable turbulence CFD model and the discretization parameters.

As far as the present study is a continuation of the PhD work of Tran [Tra13] which was limited to axi-symmetrical configuration, we extend the study to a 3D configuration where we initially look towards performing a DNS calculation. We keep the interest in studying small injection Richardson number case (buoyant jet regime) because it has been showing to be a complex simulation, specially with FANS approaches (section 1.4).

We perform another modification on the studied configuration in [Tra13] where currently a two vented cavity is considered, and that is for two main reasons. Firstly, vented configurations (specially at the top of the cavity) prevent the filling box phenomenon and thus attain a faster steady state solution which makes it possible to perform statistical analysis. Second, as shown in [LLSS90], two vented configurations will prevent a major reversal flow to occur on a specific vent and thus distribute the fresh ambient inflow to take place at the lower vent and mixture to leave from the top.

From our test simulations, we have figured out that the size of the exterior domain influences significantly the predicted results, which is in agreement with the observations of [PVH$^+$09]. Thus, we aim to perform a sensitive convergence study on the size of the employed exterior domain so that we ensure that it does not influence the flow inside the cavity.

Almost all FANS approaches presented in the previous benchmarks of section 1.4 tended to add additional turbulent diffusion in the domain which lead to the underestimation of the concentration. As far as safety recommends overestimating the concentration, no FANS simulations are considered in the present study.

In this context, a first possibility is carrying out a complete DNS calculation to escape from all the problems of modelling. However, it is important to investigate if the case can be simulated with least computational effort. Thus, we consider both LES and DNS approaches in the present work. Moreover, it is important to take into account the influence of the numerical parameters on the quality of the resolution. More precisely, the order of the mesh size must be comparable to the Kolmogorov length scale so that the ratio of modelled to laminar viscosity is acceptable. Hence, we look towards performing a grid sensitivity study before lunching the final LES configuration. In addition, the time step of the simulation, or basically the CFL, must be respected to obtain better predictions and prevent the numerical issues reported in [GSM$^+$15].

Chapter 2

Physical problem and objectives

Contents

In this chapter, the working fluids, employed geometrical configurations and the interesting-challenging key points of the Ph.D. are presented. The organisation of the chapter reads as follows. Firstly, the desired flow regime and corresponding challenges are presented. Secondly, the experimental set-up (configuration, measurement tools, ...) and the numerical configurations are illustrated. And finally, the main objectives of the Ph.D. and the organization of the results are stated.

2.1 Motivation

2.1.1 Studied flow regime

We basically look towards studying a case where the injection Richardson number is slightly less than unity ($\mathrm{Ri}_{\mathrm{inj}} < 1$). We emphasize that in such particular flows, the development of

a buoyant jet is predicted and a transition from an inertial-driven jet into a buoyancy-driven plume occurs in a short distance above the leakage (injection) position [Rod82]. For this issue, we define the injection flow rate Q so that the desired $\mathrm{Ri}_{\mathrm{inj}}$ is treated.

We consider a continuous light fluid release problem in a two vented cavity. According to the theoretical prediction, a simple density (concentration) stratification occurs which separates two homogeneous layers. Thus, qualifying the two homogeneous layers in addition to understanding the mixing-dispersion phenomenon that takes place in the medium are important for the safety studies.

2.1.2 Employed methodologies

The Atomic Energy Commission in France (CEA) shows an interest in such safety problems and thus has been participating in many international and European projects under the theme of reducing hydrogen leakage risks. Experimental studies has been carried out in the Laboratory of Instrumentation and Experimentation in Fluid Mechanics and Thermo-Hydraulics (LIEFT - CEA Saclay).

The usage of hydrogen in experimental studies requires a great caution and thus it is usually replaced with another fluid to avoid accidental situations. As a consequence, the LIEFT experiments consider a helium injection (release) inside closed or vented cavities, covering a wide range of spatial scales and flow rates. Bernard-Michel and Houssin in [BMHA17] prove that helium is considered as a good substitution of hydrogen.

In this dissertation, we limit the study to a specific experimental configuration carried out by Bernard-Michel at the LIEFT [BMSH17]; a helium-air buoyant jet in a two vented cavity. Numerical simulations following both approaches, direct numerical simulations (DNS) and large eddy simulations (LES), are carried out in the present work to investigate if the numerical calculations are able to predict the flow. The numerical results are compared to the particle image velocimetry (PIV) measurements covering almost the whole computational domain. Due the limited size of the configuration, it could not be possible to install concentration-measuring sensors (katharometers) in the cavity. Hence, validations are carried out only for the velocity fields and no CFD–experimental helium concentration comparisons are presented.

2.1.3 Difficulties and key points

Simulating a buoyant jet in a two vented cavity is extremely interesting and challenging for both, physical and numerical reasons.

- Physically, the difficulties in modelling the desired configuration can be stated as follows.

1. Problematic with modelling the significant density-varying mixture which requires a specific approximation choice: Low Mach Number versus Boussinesq approximations.

2. Problematic with modelling the effect of the strong non-stationary and fluctuating flow which requires capturing correctly the wide range of characteristic time and space scales.

3. Problematic with modelling the interaction between the flow inside the cavity and the exterior environment. This difficulty is basically related to the sharp interaction between the exterior heavy fluid entering from the bottom vent and the light rising fluid inside the cavity, where Rayleigh-Taylor instabilities can develop and generate high fluctuations inside the medium [Wil50].

- Numerically, where several issues interfere while studying such a configuration and thus can be summarized as follows.

1. Problematic with the industrial geometry that is generally complex to simulate numerically. In particular, CFD problems require in many cases the employment of immersed solid wall boundaries to mimic the studied configuration. These non-fluid zones introduce a lot of corners in the computational domain and thus induce singularities in the discretized matrix resolution.

2. Problematic with the security hazards where CFD predictions can either underestimate or overestimate the concentration. This issue is basically due to the robustness of the CFD codes where the implemented models and schemes can add artificial diffusion and thus wrongly predict the extreme values. Hence, CFD predictions can not be considered 100 % reliable for security assessments before performing at least benchmarks and validations.

3. Problematic with employing the correct numerical methods and the appropriate turbulence models that are able to capture, both in time and space, the sharp density gradients, the location of the laminar-to-turbulence transition which normally occurs within a small distance above the injection position, in addition to predicting correctly the fluctuating fields.

4. Problematic with boundary condition modelling where there is no clear idea on the correct boundary conditions that can be directly imposed on the vent surfaces and thus representing the true flow. This issue remains an open problem of research and thus more challenging for a two vented configuration, especially that a vent can have an opposite flow orientation at the same time.

2.2 The experimental set-up and physical problem

The experimental set-up has been identified so that the desired flow regime is predicted to develop in the cavity ($\mathrm{Ri}_{\mathrm{inj}} < 1$, two homogeneous separated layers, transitional–fluctuating regime). In what follows, we define the studied configuration at first. The physical problem is then verified by presenting the dimensionless parameters of the simulated regime.

2.2.1 Configuration

The experiment is carried out on a parallelepiped cavity. In order to achieve the steady state solution and to avoid the filling-box phenomenon presented in subsection 1.3, two vents are considered inside the cavity and situated at different altitudes of the same solid wall boundary to the right (see figure 2.1).

Helium is injected with a constant volumetric flow-rate $Q = 5$ Nl.min^{-1} through a cylindrical pipe into the cavity. At the initial state, the pipe and the cavity contain only pure air at rest. The pipe has a diameter of $d = 1$ cm and a sufficiently long enough height of h to ensure that a fully developed Poiseuille velocity profile is attained (10 m flexible pipe connected to a 0.25 m metalic pipe fixed with the cavity).

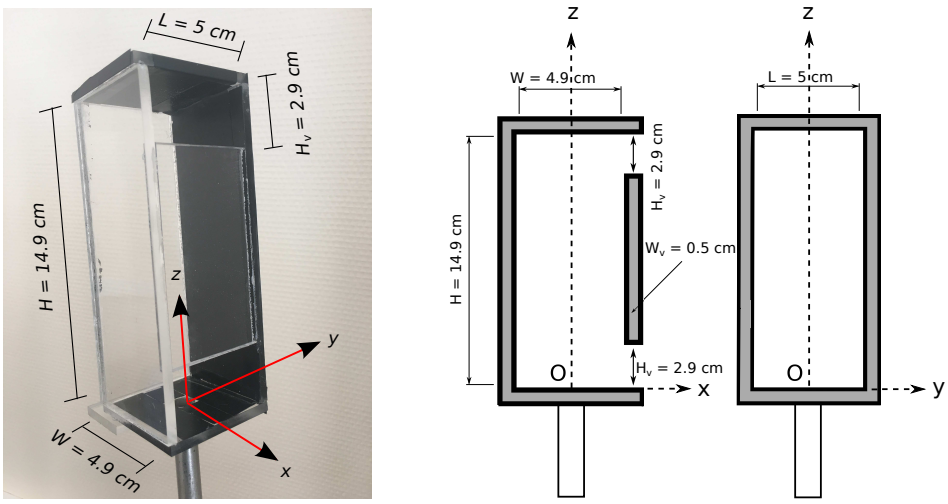

Figure 2.1: CEA-Saclay experimental configuration defined with the cartesian axis orientation. Left: 3D view, middle: 2D section perpendicular to the vents plane and containing the injection pipe, right: 2D section parallel to the vents surfaces and containing the injection pipe.

The height of the cavity $H = 14.9$ cm has been selected for PIV technical reasons. Horizontal and span-wise dimensions are respectively $W = 4.9$ and $L = 5$ cm. The injection flow rate Q and the diameter d have been specified to control $\mathrm{Ri}_{\mathrm{inj}}$ and thus predict the development of a buoyant jet. Such dimensions are in accordance with the literature review of free buoyant jet flows. In particular, according to the experimental data review of Chen and Rodi in [CR80b], the starting of the transition is generally located five diameters ($5d$) above the injection source. In addition, experimental measurements of the jet/plume spreading angle is generally predicted as 11°–12° [KTB$^+$14] from the virtual source. Therefore, the selected height H is enough to obtain a transitional flow regime, while the length L and the width W are enough to prevent any influence between the lateral solid boundaries and the spreading of the buoyant jet.

The two vents are considered to be identical where the first is located at the bottom of the cavity and the second at the top (referred to respectively by the "*bottom vent*" and "*top vent*"). Dimensions are $W_v \times L_v \times H_v = 0.5{\times}5{\times}2.9$ cm^3. W_v denotes the thickness of the plexi-glass used to define the solid wall boundaries. Note that L and W denote respectively the span-wise and horizontal dimensions of the interior domain and do not take into account the thickness of the plexi-glass.

The three dimensional (3D) direct orientation of the cartesian system is shown from figure 2.1. The origin $\mathcal{O}(0,0,0)$ of the cartesian coordinates is placed at the top center of the injection pipe. The axis of abscissas $x'\mathcal{O}x$ is normal to the plane of the vents while the span-wise axis $y'\mathcal{O}y$ orients in the upstream direction parallel to the vents. The vertical $z'\mathcal{O}z$ is situated along the height of the cavity, confounded with the axial axis of the cylindrical tube.

The experiment has been assumed to be carried out at a constant temperature (measured as $T = 25°$ C during the experiment) and a spatially-uniform thermodynamic pressure P_{thm}. For simplicity, we consider that $P_{\text{thm}} = 10^5$ Pa ≈ 0.98 atm.

2.2.2 Physical properties of the working fluids

In order to facilitate the notation of the different working fluids, we refer to the physical properties of the injected helium by the subscript $_{\text{inj}}$ and those of the ambient air by the subscript $_{\text{amb}}$. However, at the stage of the mathematical problem formulation and as far as we consider only two non-reacting fluids, helium is referred to as species 1 (by the $_1$ subscript) while air as the species 2 (by the $_2$ subscript).

Physical properties of the working fluids following the drawn assumptions are summarized in table 2.1.

Fluid	**Density**	**Dynamic viscosity**	**Molar mass**
	[kg.m^{-3}]	[$\times 10^{-5}$ kg.m^{-1}.s^{-1}]	[$\times 10^{-2}$kg.mol^{-1}]
Injected (species 1)	$\rho_{\text{inj}} = 0.16148$	$\mu_{\text{inj}} = 1.918$	$M_{\text{inj}} = 0.4003$
Ambient (species 2)	$\rho_{\text{amb}} = 1.16864$	$\mu_{\text{amb}} = 1.792$	$M_{\text{amb}} = 2.897$

Table 2.1: Physical properties of the working fluids at $T = 25°$ C and $P_{\text{thm}} = 10^5$ Pa.

The density variation in the considered configuration is clearly noted where the injected fluid is approximately 7 times lighter than the ambient air. However, the dynamic viscosity variation is rather comparable.

The diffusion coefficient of the air-helium mixture can be calculated from the Chapman-

Enskog's formula [BSL07]

$$D = 1.8583 \times 10^{-3} \times T^{\frac{3}{2}} \frac{\sqrt{\frac{1}{M_{\text{amb}}} + \frac{1}{M_{\text{inj}}}}}{P_{\text{thm}} \times \sigma_D^2 \times \Omega_D}, \tag{2.1}$$

where $\sigma_D = 0.5(\sigma_{\text{inj}} + \sigma_{\text{amb}}) = 3.0965 \times 10^{-10}$ m is the mean Lennard-Jones collision diameter and Ω_D is the diffusion collision integral, a function of the reduced temperature T_R, evaluated as

$$\Omega_D = \frac{1.06036}{T_R^{0.1561}} + \frac{0.193}{\exp(0.47635\ T_R)} + \frac{1.03587}{\exp(1.52996\ T_R)} + \frac{1.76474}{\exp(3.98411\ T_R)}, \tag{2.2}$$

where

$$T_R = \frac{K_B T}{\epsilon_{\text{mix}}}, \tag{2.3}$$

$K_B = 1.38 \times 10^{-23}$ m^{2}Kg.s^{-2}K^{-1} the Boltzmann constant and ϵ_{mix} the characteristic energy appearing in the Lennard-Jones potential for the helium-air binary pair defined using the characteristic energy of each species in the mixing rule as [NJA72] (see Bird et al. [BSL07] for a complete review)

$$\epsilon_{\text{mix}} = \left(\epsilon_{\text{inj}} \epsilon_{\text{amb}}\right)^{1/2}. \tag{2.4}$$

In iso-thermal and iso-bar cases, and basically for the assumed temperature T and thermodynamic pressure P_{thm}, $\epsilon_{\text{mix}}/K_B \approx 31.45$ K [BSL07]. Finally, the diffusion coefficient is considered approximately constant and uniform in space; basically $D = 6.91 \times 10^{-5}$ m^2.s^{-1} in our case.

2.2.3 Flow characteristics: dimensionless parameters

The equation of state for perfect gases $pV = nRT$ can be used to convert from Nl to m^3, where V is the volume of the fluid, n the mole number and R the perfect gas constant. We recall that 1 Nl is equivalent to the volume of the fluid at 273.15 K and $P_{\text{thm}} = 1$ atm.

For $T = 298.15$ K, $Q = 5$ Nl.min^{-1}, the volumetric injection flow rate Q_v is equivalent to

$$Q_v = Q \times \frac{10^{-3}}{60} \times \frac{298.15}{273.15} \approx 9.096 \times 10^{-5}\ \text{m}^3.\text{s}^{-1}. \tag{2.5}$$

For a pipe of diameter $d = 1$ cm, the injection volumetric flow-rate measures an averaged injection velocity

$$\overline{u}_{\text{inj}} = \frac{Q_v}{\pi(5 \times 10^{-3})^2} \approx 1.158\ \text{m.s}^{-1}. \tag{2.6}$$

Flow physical characteristics are given in terms of some dimensionless parameters.

- Ratio of ambient to injection densities:

$$\frac{\rho_{\text{amb}}}{\rho_{\text{inj}}} \approx 7.2371, \tag{2.7}$$

- Ratio of density difference to injection density

$$\frac{\rho_{\text{amb}} - \rho_{\text{inj}}}{\rho_{\text{inj}}} \approx 6.2371, \tag{2.8}$$

- Ratio of density difference to ambient density

$$\frac{g'}{g} = \frac{\rho_{\text{amb}} - \rho_{\text{inj}}}{\rho_{\text{amb}}} \approx 0.8618, \tag{2.9}$$

where g' is the reduced gravity,

- Injection Reynold's number: ratio of inertial to viscous forces at injection

$$\text{Re}_{\text{inj}} = \frac{\rho_{\text{inj}} u_{\text{inj}}\ d}{\mu_{\text{inj}}} \approx 195, \tag{2.10}$$

- Injection Richardson number: ratio of potential to kinetic energy at injection

$$\text{Ri}_{\text{inj}} = \frac{g(\rho_{\text{amb}} - \rho_{\text{inj}})\ d}{\rho_{\text{inj}} u_{\text{inj}}^2} \approx 0.114 < 1, \tag{2.11}$$

predicting a buoyant jet flow,

- Rayleigh number: ratio of buoyancy to viscous and diffusive forces

$$\text{Ra} = \frac{g(\rho_{\text{amb}} - \rho_{\text{inj}})H^3}{\mu_{\text{amb}} D} \approx 2.64 \times 10^7, \tag{2.12}$$

- Schmidt number: ratio of momentum diffusivity (viscosity) to mass diffusivity at injection and ambient respectively

$$\text{Sc}_{\text{inj}} = \frac{\mu_{\text{inj}}}{D\rho_{\text{inj}}} \approx 1.719, \tag{2.13}$$

$$\text{Sc}_{\text{amb}} = \frac{\mu_{\text{amb}}}{D\rho_{\text{amb}}} \approx 0.222. \tag{2.14}$$

- Grashof number: ratio of buoyant to viscous forces at injection and ambient respectively

$$\text{Gr}_{\text{inj}} = \frac{g\rho_{\text{inj}}(\rho_{\text{amb}} - \rho_{\text{inj}})d^3}{\mu_{\text{inj}}^2} \approx 4.337 \times 10^3, \tag{2.15}$$

$$\text{Gr}_{\text{amb}} = \frac{g\rho_{\text{amb}}(\rho_{\text{amb}} - \rho_{\text{inj}})H^3}{\mu_{\text{amb}}^2} \approx 1.214 \times 10^8. \tag{2.16}$$

2.3 Particle image velocimetry technique

Particle image velocimetry (PIV) measurements have been carried out on the considered helium-air experiment. According to the currently available equipments in our lab, instantaneous velocities are accessible either in the vertical xz or yz-planes.

2.3.1 Two dimensional employed slices

14 vertical two dimensional (2D) slices are considered in the horizontal and span-wise directions, respectively x and y. The slices along the horizontal dimension are denoted by XZ_i, while YZ_j is used for slices along the span-wise direction. Locations of the slices are materialized on subfigure (a) of figure 2.2 from a top view schematic representation, or on subfigure (b) of figure 2.2 for a complete three dimensional (3D) observation. For completeness, a detailed description is reported in table 2.2.

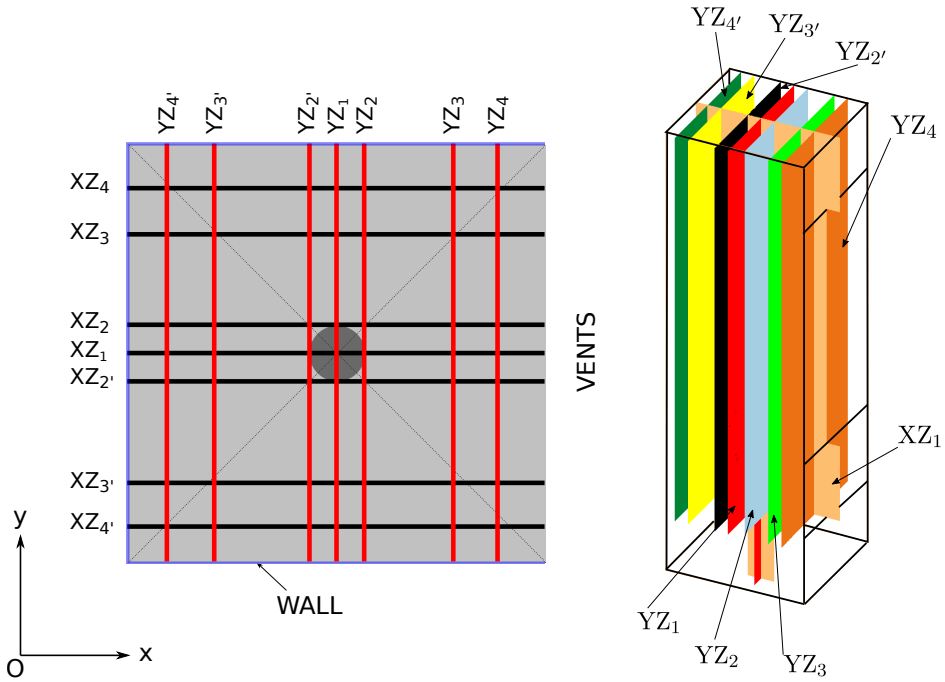

(a) (b)

Figure 2.2: Schematic representation of the vertical slices used in the PIV measurements. Left: 2D top-cavity view, right: 3D representation for some selected slices.

2.3.2 Selected time-averaged results

We present in this subsection some of the results measured by Jiaying Bi in [Bi17] during her intern-ship with the LIEFT, under the supervision of Gilles Bernard-Michel and myself.

xz-planes	**Slice**	y-**position** [cm]
	XZ_1	$y = 0$
	XZ_2	$y = 0.5$
	XZ_3	$y = 1.5$
	XZ_4	$y = 2$
	$XZ_{2'}$	$y = -0.5$
	$XZ_{3'}$	$y = -1.5$
	$XZ_{4'}$	$y = -2$

yz-planes	**Slice**	x-**position** [cm]
	YZ_1	$x = 0$
	YZ_2	$x = 0.5$
	YZ_3	$x = 1.5$
	YZ_4	$x = 2$
	$YZ_{2'}$	$x = -0.5$
	$YZ_{3'}$	$x = -1.5$
	$YZ_{4'}$	$x = -2$

Table 2.2: Position of the PIV studied vertical slices: Left: xz-plane, right: yz-plane.

Selected results are presented to display the main flow pattern inside the treated configuration. We emphasize that all the PIV results presented in this dissertation are based on her measurements during the experimental work. Further experimental results are served in later chapters to validate and compare with the CFD velocity predictions.

A detailed description of the used PIV technique and the measuring algorithm can be reviewed from [BMSH17]. The total simulation time is 10 min with a PIV sampling frequency of $f = 1$ Hz. Statistics are performed in the last 5 min of the experience where a quasi-steady state is recorded. The presented PIV results are obtained with an error smaller than 1.5×10^{-2} m.s^{-1}. Statistical errors on the time averages are about 0.4×10^{-2} m.s^{-1}. The total error is thus below 2×10^{-2} m.s^{-1}.

The flow pattern in the mid-vertical XZ_1-plane is illustrated by the 2D time-averaged velocity magnitude $< |\mathbf{u}|_{XZ} >_t$ iso-contour and vector plots in figure 2.3. We emphasize that the velocities in the vicinity of the injection surface are not provided as far as helium is not seeded with particles during the experiment. In practice, no additional particles have been injected with helium to prevent any creation of artificial turbulence along the jet axis.

From both the velocity magnitude iso-contours and the vector field in the lower part of the cavity, we note that the unique source of fresh air is the bottom vent. The heavy fluid inflow spreads afterwards in an almost divergent way to impact the light buoyant jet axis approximately all along a height of 5 cm. This heavy–light fluid impact causes the buoyant jet axis to bend towards the left wall facing the vents. Afterwards and due to the continuous helium injection and air inflow, the flow remains oriented near the left wall to about a height 12 cm (lower surface of the top vent). Finally, the plume impacts the top ceiling and a flow separation is noted where a first part goes in a circular motion near the top left corner (figure 2.3, right-top). Due to the aspiration from the top vent, the second part leaves the cavity mainly from a thin layer situated at the top right-ceiling.

Moreover, a span-wise recirculating zone is noted near the bottom-left corner (figure 2.3, right-bottom). This flow pattern could be probably justified also by the air inflow that completes

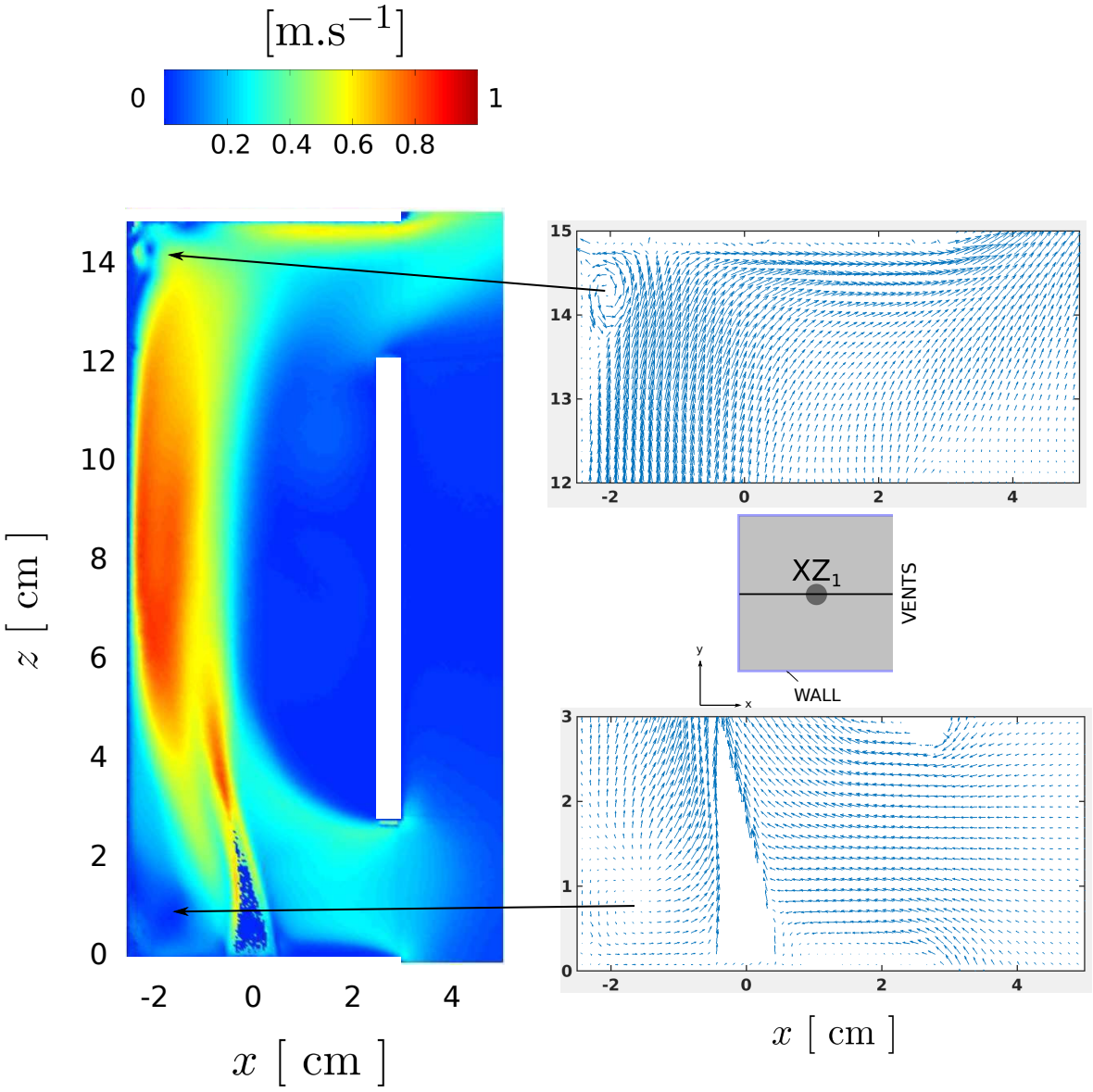

Figure 2.3: PIV measured time averaged flow pattern illustrated by the 2D velocity magnitude $< |\mathbf{u}|_{XZ} >_t$ in the mid-vertical XZ_1-plane. Left: velocity iso-contours [0:0.2:1], right-top: vector field at the top of the cavity, right-bottom: vector field at the bottom of the cavity.

to impact the left wall and thus create a horizontal circulations. This flow pattern is not illustrated by PIV fields at present as far as horizontal slices are not currently measured. However, this issue is well analyzed from the CFD predictions in later chapters.

Next, we consider the flow pattern in the mid-vertical YZ_1-plane which is illustrated by the 2D time-averaged velocity magnitude $< |\mathbf{u}|_{YZ} >_t$ iso-contour and vector plots in figure 2.4. Generally, the velocity magnitude field is almost symmetrical in this plane.

The effect of the jet inclination is firstly noted in the mid-vertical span-wise plane where small

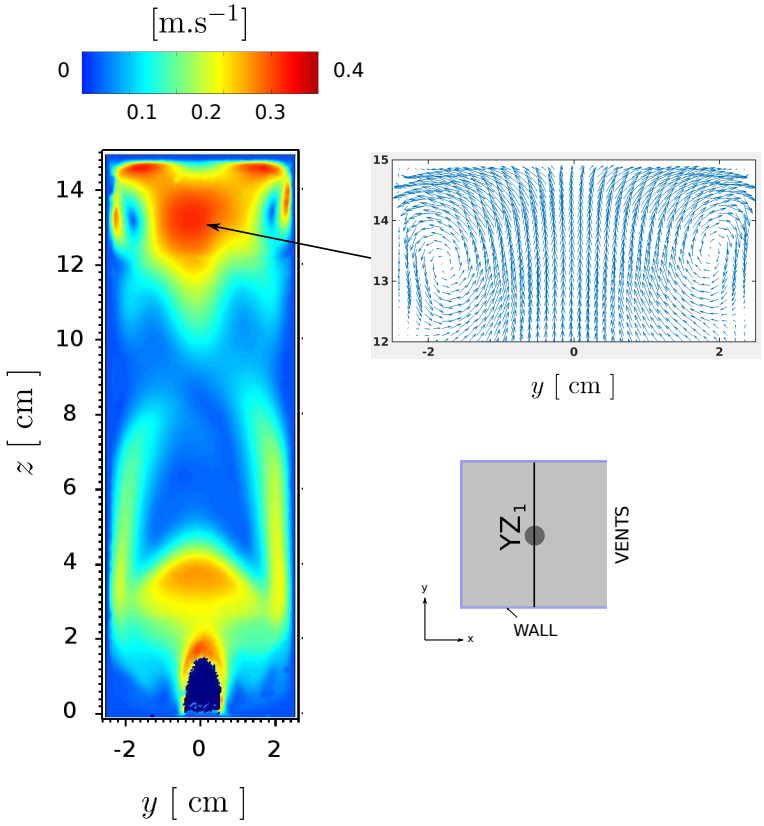

Figure 2.4: PIV measured time averaged flow pattern illustrated by the 2D velocity magnitude $< |\mathbf{u}|_{YZ} >_t$ in the mid-vertical YZ_1-plane. Left: velocity iso-contours [0:0.1:0.4], right: vector field at the top of the cavity.

velocity magnitudes are measured all along a height of about 5 cm in the middle of the plane, compared to higher velocities located in the injection vicinity and in the upper part of the cavity.

We can also identify almost two symmetrical vortices created at the top side walls of the cavity (figure 2.4, right). These counter-rotating vortices play an important role in diluting the air-helium mixture at the top of the cavity where a homogeneous layer is predicted to be formed.

2.4 Objectives and numerical configurations

2.4.1 Objectives

The overall aim of the present thesis is fourfold, discussed in the planned order as follows:

- First, we look towards simulating the industrial problem by a CFD approach; LES and DNS

calculations. To our knowledge, DNS studies of buoyant jets rising in two vented enclosures are not reported in the literature.

- Second, we benefit from the PIV measurements (velocity fields and profiles) to compare with the CFD predictions and thus propose a method to better approach the natural inlet and outlet issues.

- Third, we look towards evaluating the quality of the numerical resolution by performing LES–DNS and also CFD–PIV comparisons to present the validations of both, numerical and turbulence models.

- Finally, analysis on the predicted concentration field are to be carried out to provide information regarding the physical aspect of the problem and the security hazards. At this stage, only the CFD predictions are employed to qualify the air–helium mixing–dispersion, helium stratification levels and the extreme values situated in the homogeneous layer.

2.4.2 Employed numerical configurations

Throughout the work, two different geometries have been simulated; 2D axi-symmetrical and 3D cartesian geometries. 2D axi-symmetrical simulations have been carried out at first as test cases, as far as they require less memory storage and less computational effort than the 3D calculations. The computational domains are described as follows:

- 2D axi-symmetric configurations

Four computational domains are simulated whose schematic representation is depicted in figure 2.5. We emphasize that the simulated cavities in this case do not mimic the experimental configuration presented previously in section 2.2. Further information concerning the cavity's height H, radial dimension R and the pipe will be supplied later in chapter 5.

1. Cavity only (figure 2.5, (a)): the flow equations are simulated inside a one vented cavity only. The inlet and outlet boundaries are imposed directly at the surfaces of the injection and the vent respectively, in contact with the cavity.

2. Meshed pipe and one vented cavity (figure 2.5, (b)): immersed boundaries have been employed to model the injection pipe and the width of the vent in the computational domain. In this type of configuration, the inlet and outlet boundaries are prescribed respectively at the lower surface of the pipe and the exterior surface of the vent.

3. Meshed pipe and two vented cavity without an exterior domain (figure 2.5, (c): the pipe and two vents widths are modelled in the computational domain.

4. Meshed pipe and two vented cavity with an exterior domain (figure 2.5, (d): the flow equations are simulated in the cavity, pipe and in an exterior region directly attached to the right of the vents. The exterior domain takes a chimney-like shape which consists of two openings (top and bottom) and a solid wall boundary. The outlet boundary

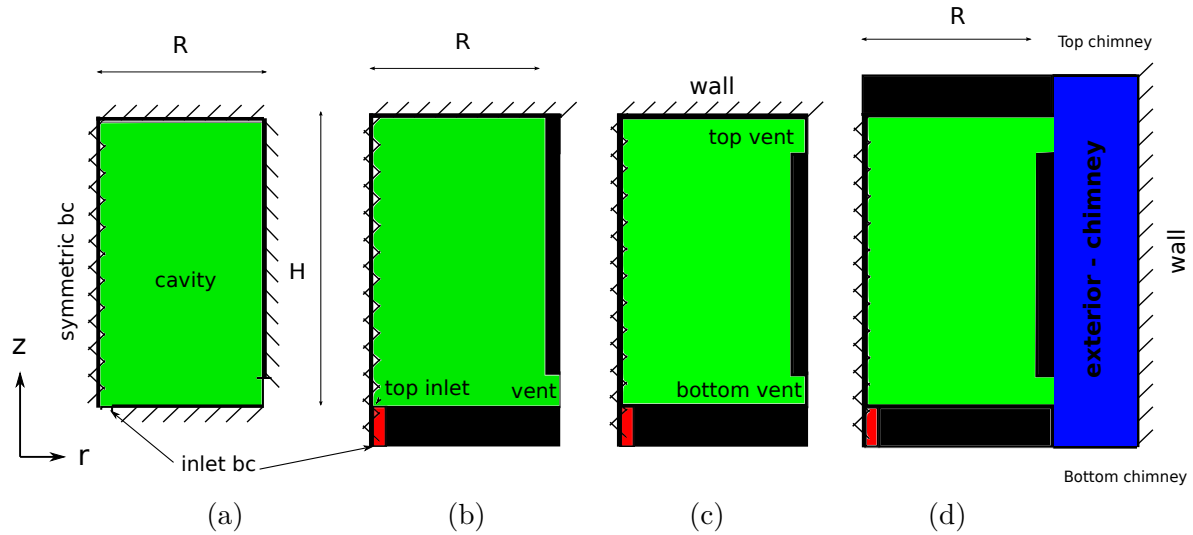

Figure 2.5: Four simulated axi-symmetrical configurations. (a) cavity only, (b) meshed pipe and one vented cavity, (c) meshed pipe and two vented cavity without an exterior domain and (d) meshed pipe and two vented cavity with an exterior domain. Black blocks denote the immersed solid boundaries (non-fluid zones), green color denotes the interior cavity, red denotes the interior of the pipe and blue color denotes the exterior region. Wall boundaries are labelled by dashed ticks, while the symmetrical boundary with the waved dashed labels.

conditions are thus moved away from the cavity and prescribed at the top and the bottom of the chimney openings.

- 3D cartesian configurations

For the complete 3D simulations, two types of computational domains are considered (figure 2.6). In both cases, the injection tube is modelled in the computational domain. We emphasize that the dimensions of the cavity and the vents are preserved and follow the orientation described previously in section 2.2. Further information concerning d and h will be supplied later.

1. Configuration without an exterior domain (figure 2.6, (a)): the flow cartesian equations are simulated inside the pipe and the cavity only. Hence, the fluid influence and exchange with the outer domain is modelled by the effect of the outlet boundary conditions that are applied directly on the vent surfaces (exterior surface), represented by the blue surfaces in figure 2.6.

2. Configuration with an exterior domain (figure 2.6, (b)): where, in addition to the pipe and the cavity, the flow at an exterior region in contact with the wall containing the vents is simulated. Again, the outlet boundary conditions are pushed away from the vents from which we expect a better prediction of the flow inside the cavity. The exterior domain is of horizontal width extension Lx, span-wise length $L + (2 \times Ly)$ and height

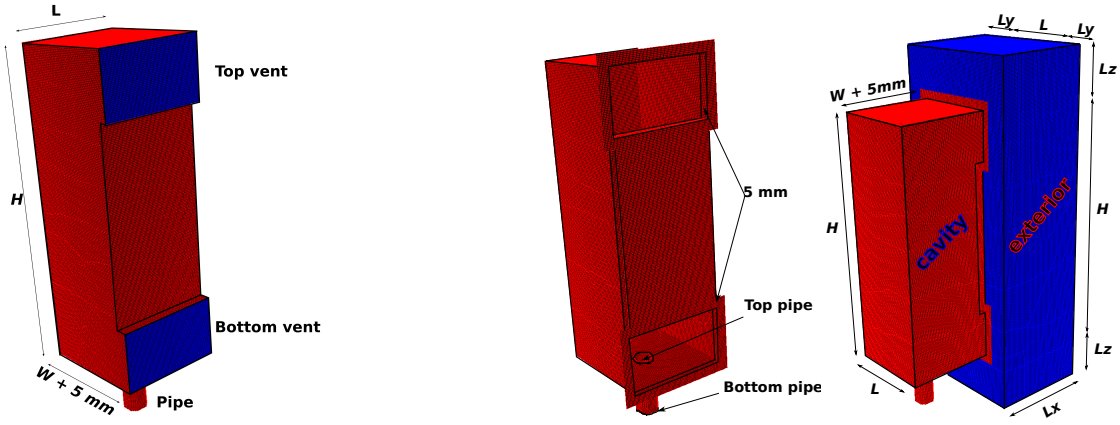

(a) (b)

Figure 2.6: Two types of 3D simulated configurations. (a) configuration without an exterior domain, (b) configurations with an exterior domain. Red surfaces denote the solid wall boundaries while blue surfaces denote the outlet boundaries.

$H + (2 \times Lz)$. The extensions Lx, Ly and Lz are dependent on the simulation aspect and will be stated later in each concerned chapter.

In order to take into account the thickness of the plexi-glass present in the real experiment, we place a layer of 0.5 cm around the vents and thus considered a solid wall layer. The exterior surfaces of the new attached domain far from the cavity are colored with blue in figure 2.6 (b), and are considered as the numerical outlets where the boundary conditions are prescribed. Red surfaces indicate the position of the wall boundaries. The inlet boundary is considered for both types at the bottom surface of the injection pipe.

2.4.3 Organization of the results

In the overcoming chapters, we follow a step-by-step methodology where we move from axi-symmetric configurations towards complete 3D DNS simulations. The road reads as follows.

- Axi-symmetrical simulations

This is the subject of chapter 5, where 2D axi-symmetrical simulations are carried out. The heart of this study is how to treat the inlet boundary condition issue where we show that modelling the pipe in the computational domain is necessary. In this chapter, we highlight also on the influence of modelling an exterior region in the configurations.

- 3D LES study

A 3D convergent LES study is presented in chapter 6. Numerical simulations are performed on the two types of configurations (section 2.4), where a convergence study on the influence of the outer domain is presented. Afterwards, the LES results are compared to the PIV

measurements in chapter 7.

- 3D coarse DNS study

A coarse DNS computation is performed in chapter 8 on the same convergent LES configuration as a final step to provide reference numerical solutions. In this chapter, a statistical post-treatment is also presented to qualify the coarse DNS resolution. The analysis is basically carried out by the turbulent kinetic energy budget. Finally, we define the limits of the buoyant jet regions from the contribution of the gravitational power in producing the turbulent kinetic energy inside the cavity.

Chapter 3

Governing equations

Contents

In this chapter, we present the mathematical formulation of the problem presented in the previous chapter. Basically, the flow is governed by the conservation equations for species (in our case, we consider a transport PDE for helium) and momentum. Under the justified iso-thermal assumption, the resolution of an energy conservation equation is not needed. The density of the air-helium mixture is calculated from an equation of state for binary gas mixtures. The low Mach number (LMN) approximation is valid and justified in this study.

3.1 Conservation equations

We inject helium from a pipe into a two vented cavity filled with air. We recall that helium is referred to by the injected fluid ($_{\text{inj}}$ lower script) and air is referred to by the ambient fluid ($_{\text{amb}}$ lower script).

Let us consider an arbitrary infinitesimally small fluid parcel in an air-helium mixture with volume V and mass m. This parcel is divided into 2 parts: first part consists from helium with mass m_1 and volume v_1, while the second part is devoted to the composition of air with mass m_2 and volume v_2. Hence, we write $m = m_1 + m_2$ and $V = v_1 + v_2$.

The partial mass density of helium ρ_1 with respect to V is defined as $\rho_1 = m_1/V$ (similarly that for air $\rho_2 = m_2/V$), whereas the mass density of the mixture reads $\rho = m/V$.

It can be easily seen that $\rho = \rho_1 + \rho_2$. In the present work, we consider only mass densities so that in the sequel the term "mass" is omitted.

The mass fraction of helium is defined as $Y_1 = m_1/m = \rho_1/\rho$ (similarly mass fraction of air $Y_2 = m_2/m = \rho_2/\rho$). Y_1 gives an indication on how much mass of helium is contained inside the mixture. Note that the mass fraction is always between 0 and 1 and that $Y_1 + Y_2 = 1$.

As far as we are dealing with two species (helium and air), it is thus sufficient to solve only for one species mass fraction equation, say for Y_1. Y_2 is then deduced as

$$Y_2 = 1 - Y_1. \tag{3.1}$$

3.1.1 Species equation

Let $\mathbf{u}_1 = (u_{11}, u_{21}, u_{31})$ denotes the absolute velocity vector of helium with respect to a laboratory frame of reference. The general transport equation of helium is written as

$$\frac{\partial \rho_1}{\partial t} + \frac{\partial}{\partial x_i}(\rho_1 u_{i1}) = \dot{r}, \tag{3.2}$$

where $\partial u_{i1}/\partial x_i$ is the Einstein notation with a summation over the index i, $\dot{r}$ is the rate of production (positive or negative) of helium per unit volume of bulk phase by chemical reaction. We only consider non-reacting species in the present work and thus $\dot{r} = 0$.

Based on the conservation of the total mass flux, we define the mass average velocity

$$\mathbf{u} = (u_i) = \frac{\mathbf{m}_t}{\rho}, \tag{3.3}$$

as the single velocity of the air-helium mixture, where the total mass flux is

$$\mathbf{m}_t = \mathbf{m}_1 + \mathbf{m}_2 = \rho_1 \mathbf{u}_1 + \rho_2 \mathbf{u}_2, \tag{3.4}$$

and $\mathbf{u}_2$ is the absolute velocity vector of air.

From the definition (3.3), the mass average velocity $\mathbf{u}$ is related to the helium and air component absolute velocities as

$$\mathbf{u} = Y_1 \mathbf{u}_1 + Y_2 \mathbf{u}_2. \tag{3.5}$$

To take into account the difference between the mixture's mass average velocity and the absolute velocity of the component, we define the mass diffusion flux of helium and air respectively as

$$\mathbf{j}_1 = \rho_1(\mathbf{u}_1 - \mathbf{u}), \tag{3.6}$$

$$\mathbf{j}_2 = \rho_2(\mathbf{u}_2 - \mathbf{u}). \tag{3.7}$$

Note that $\mathbf{j}_1 + \mathbf{j}_2 = 0$. Substituting $\mathbf{u}_1 = \mathbf{u}_1 - \mathbf{u} + \mathbf{u}$ in equation (3.2), we obtain

$$\frac{\partial \rho_1}{\partial t} + \frac{\partial}{\partial x_i}(\rho_1 u_i) = -\frac{\partial}{\partial x_i}\mathbf{j}_1. \tag{3.8}$$

The mass diffusion flux of helium and air are modeled by Fick's first law saying that the solute moves smoothly from areas of high concentrations to low ones with a magnitude proportional to concentration gradients. Thus we write

$$\mathbf{j}_1 = -D_{12}\rho\frac{\partial Y_1}{\partial x_i}, \tag{3.9}$$

$$\mathbf{j}_2 = -D_{21}\rho\frac{\partial Y_2}{\partial x_i}, \tag{3.10}$$

where D_{12}, D_{21} are respectively the Fick's diffusion coefficient of helium in air and vice versa.

Owing that $\mathbf{j}_1 + \mathbf{j}_2 = 0$ and $Y_1 + Y_2 = 1$, then from equations (3.9) and (3.10) we deduce that $D_{12} = D_{21}$ and a unique diffusion coefficient D is considered (uniform and constant).

Hence, equation (3.8) can be simplified as

$$\frac{\partial \rho Y_1}{\partial t} + \frac{\partial}{\partial x_i}(\rho Y_1 u_i) = \frac{\partial}{\partial x_i}\left(D\rho\frac{\partial Y_1}{\partial x_i}\right), \tag{3.11}$$

well known as the conservation equation of species.

3.1.2 Mass equation

Summing equation (3.11) with a similar one devoted for the evolution of air, we obtain the equation that describes the conservation of the total mass of the mixture

$$\frac{\partial \rho}{\partial t} + \frac{\partial}{\partial x_i}(\rho u_i) = 0. \tag{3.12}$$

Equation (3.12) can be expressed in a different form as

$$\frac{\partial}{\partial x_i}u_i = -\frac{1}{\rho}\frac{\mathrm{D}}{\mathrm{D}t}(\rho), \tag{3.13}$$

where $\mathrm{D}/\mathrm{D}t$ is the total derivative operator defined as

$$\frac{\mathrm{D}}{\mathrm{D}t}(\cdot) = \frac{\partial}{\partial t}(\cdot) + u_i \cdot \frac{\partial}{\partial x_i}(\cdot). \tag{3.14}$$

3.1.3 Momentum equation

Considering the mixture's mass average velocity $\mathbf{u}$, the momentum conservation equation of an air-helium mixture reads

$$\frac{\partial \rho u_j}{\partial t} + \frac{\partial}{\partial x_i}(\rho u_j u_i) = -\frac{\partial P_{\text{thm}}}{\partial x_j} + \frac{\partial \tau_{ij}}{\partial x_i} + \rho g_j, \tag{3.15}$$

where P_{thm} is the thermodynamic pressure, τ is the viscous stress tensor. $\mathbf{g}$ is the gravitational vector directed in the direction of the gravitational acceleration, along the downward vertical direction in our case; basically $\mathbf{g} = (0, 0, -g)$.

Air-helium mixture is a Newtonian fluid. Thus, the viscous stress depends linearly on the velocity gradients. In practice, we write

$$\tau_{ij} = \mu \left(\frac{\partial u_j}{\partial x_i} + \frac{\partial u_i}{\partial x_j} \right) + \lambda \delta_{ij} \frac{\partial u_k}{\partial x_k}. \tag{3.16}$$

μ is the dynamic viscosity of the mixture, λ is the coefficient of the bulk viscosity and δ_{ij} is the Kronecker-Delta symbol. We consider the Stoke's hypothesis (see book of Hirsch for more details [Hir07]) where the following relation is valid

$$\lambda + \frac{2}{3}\mu = 0. \tag{3.17}$$

For a compact notation, we write $\tau_{ij} = 2\mu e_{ij}$, where

$$e_{ij} = \frac{1}{2} \left(\frac{\partial u_j}{\partial x_i} + \frac{\partial u_i}{\partial x_j} \right) - \frac{1}{3} \delta_{ij} \frac{\partial u_k}{\partial x_k}, \tag{3.18}$$

denotes the strain rate tensor. The symmetrical part of e_{ij} is defined as

$$S_{ij} = \frac{1}{2} \left(\frac{\partial u_j}{\partial x_i} + \frac{\partial u_i}{\partial x_j} \right). \tag{3.19}$$

3.2 Equation of state

The density of the air-helium mixture ρ can be estimated explicitly from the equation of state which is expressed in terms of the thermodynamic quantities. For a binary gas mixture, the equation of state is dependent of the two species mass fractions (see book of Williams [Wil65]) where the mixing molar mass is defined as

$$M_{\text{mix}} = \left(\frac{Y_1}{M_{\text{inj}}} + \frac{Y_2}{M_{\text{amb}}} \right)^{-1}. \tag{3.20}$$

Thus, the mixture's density ρ is evaluated as

$$\rho = \frac{P_{\text{thm}} M_{\text{mix}}}{RT}, \tag{3.21}$$

where $R = 8.314$ J.K^{-1}.mol^{-1} is the specific gas constant.

As far as the problem is placed within a justified iso-thermal assumption, it is not necessary to solve for an additional energy conservation equation. Hence, the binary species flow problem is governed by the conservation equations (3.11), (3.12), (3.15) and the state equation (3.21).

3.3 Low Mach Number approximation

The Mach number Ma $= \mathbf{u}/c$ measures the ratio of the bulk velocity to the local speed of sound. Typically for Ma < 0.1, the compressibility effects can be neglected and the physical problem may be reduced by using a low Mach number formulation.

In the present study, we consider a small flow velocity (Ma $\approx 7 \times 10^{-3} \ll 0.1$) which makes the aspect of the problem oriented towards simulating a mass variation rather than capturing and solving for the acoustic waves. This is basically the main hypothesis of a LMN approximation where all acoustic waves are filtered out.

Indeed, the second reason behind using the LMN approximation in our case is due to the significant density variations that take place in our problem. In figure 3.1, the variation of ρ versus the helium mass fraction Y_1 with $P_{\text{thm}} = 10^5$ Pa and $T = 298.15$ K is depicted.

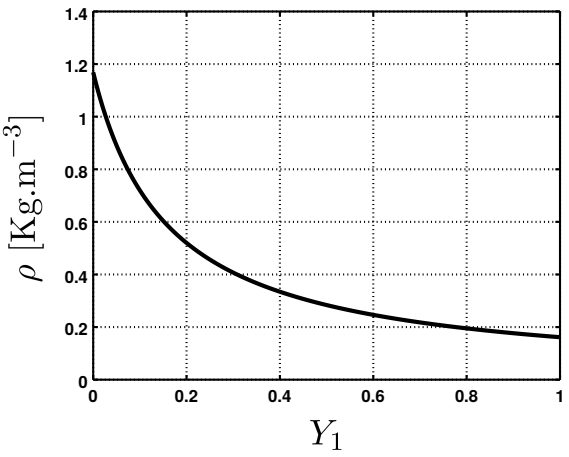

Figure 3.1: Variation of the mixture's density ρ versus the helium mass fraction Y_1: $P_{\text{thm}} = 10^5$ Pa and $T = 298.15$ K.

We can clearly note that the mixture density ρ can vary with a factor 6, and those variations can occur locally for example around the boundary of the jet. Such a significant density variation makes the use of a Boussinesq approximation not valid [GG76].

Following a single scale asymptotic analysis referring to the Mach number, the zero Mach-order equations are considered where the total pressure P_{thm} is decomposed into a thermodynamic pressure $p(t)$, uniform in space, and a hydrodynamic pressure $P(\mathbf{x}, t)$ that fluctuates in an order of $\widetilde{\text{Ma}}^2$ (refer to appendix A for complete details). Here, $\widetilde{\text{Ma}}$ is a modified Mach number defined for a reference velocity $\mathbf{u}_r$ and a reference density ρ_r as

$$\widetilde{\text{Ma}} = \sqrt{\frac{\rho_r}{p}}\mathbf{u}_r = \sqrt{\gamma}\ \text{Ma}, \tag{3.22}$$

where γ is the ratio of the specific heats [Mül99].

In conclusion, the LMN pressure decomposition reads

$$P_{\text{thm}}(\mathbf{x}, t) = p(t) + \widetilde{\text{Ma}}^2 P(\mathbf{x}, t). \tag{3.23}$$

P is much smaller than p. P alone is used in the momentum equation because p is uniform, while p is used in the equation of state. In our case, p is constant with time as far as the iso-thermal assumption holds.

3.3.1 LMN dimensional equations

The dimensional system of governing equations under the LMN approximation read

$$\frac{\partial \rho}{\partial t} + \frac{\partial}{\partial x_i}(\rho u_i) = 0, \tag{3.24}$$

$$\frac{\partial \rho u_j}{\partial t} + \frac{\partial}{\partial x_i}(\rho u_j u_i) = -\frac{\partial P}{\partial x_j} + \frac{\partial \tau_{ij}}{\partial x_i} + \rho g_j, \tag{3.25}$$

$$\frac{\partial \rho Y_1}{\partial t} + \frac{\partial}{\partial x_i}(\rho Y_1 u_i) = \frac{\partial}{\partial x_i}\left(D\rho\frac{\partial Y_1}{\partial x_i}\right), \tag{3.26}$$

$$\rho = \frac{p}{RT}\left(\frac{Y_1}{M_{\text{inj}}} + \frac{Y_2}{M_{\text{amb}}}\right)^{-1}. \tag{3.27}$$

- A formulation for the velocity divergence constraint

For numerical reasons, we present alternative formulation of the velocity divergence constraint dependent on the mass fraction of helium Y_1 and which is equivalent to the mass conservation equation (3.24).

Applying the chain rule on equation (3.27) and recalling the iso-bar and iso-thermal assumptions, the total variation of the air-helium density reads

$$\frac{\mathrm{D}}{\mathrm{D}t}(\rho) = \frac{\mathrm{D}}{\mathrm{D}Y_1}(\rho)\frac{\mathrm{D}}{\mathrm{D}t}(Y_1) + \frac{\mathrm{D}}{\mathrm{D}Y_2}(\rho)\frac{\mathrm{D}}{\mathrm{D}t}(Y_2), \tag{3.28}$$

with

$$\frac{\mathrm{D}}{\mathrm{D}Y_1}(\rho) = -\frac{pM_{\mathrm{mix}}^2}{RTM_{\mathrm{inj}}} \quad \text{and} \quad \frac{\mathrm{D}}{\mathrm{D}Y_2}(\rho) = -\frac{pM_{\mathrm{mix}}^2}{RTM_{\mathrm{amb}}}. \tag{3.29}$$

The total variation of Y_1 follows from equation (3.26) using the product rule of partial differentiation and equation (3.24),

$$\frac{\mathrm{D}}{\mathrm{D}t}(Y_1) = \frac{1}{\rho}\frac{\partial}{\partial x_i}\left(D\rho\frac{\partial Y_1}{\partial x_i}\right). \tag{3.30}$$

Note that as far as $Y_1 + Y_2 = 1$, we have

$$\frac{\mathrm{D}}{\mathrm{D}t}(Y_2) = -\frac{\mathrm{D}}{\mathrm{D}t}(Y_1). \tag{3.31}$$

Substituting the relations in equations (3.28) and (3.13), a divergence constraint on the velocity field can be expressed in terms of Y_1 as

$$\frac{\partial}{\partial x_i}u_i = \xi\frac{\partial}{\partial x_i}\left(D\rho\frac{\partial Y_1}{\partial x_i}\right), \tag{3.32}$$

with the constant

$$\xi = \frac{RT}{p}\left(\frac{1}{M_{\mathrm{inj}}} - \frac{1}{M_{\mathrm{amb}}}\right). \tag{3.33}$$

We just emphasize that, unlike the incompressible fluid cases, the velocity field in the formulation (3.32) is not divergence free but reflects the volume variation of the fluid.

3.4 Mixture dynamic viscosity versus the mass fractions

Being widely used in the literature, the dynamic viscosity of the air-helium mixture μ is calculated using the Wilke's gas mixtures viscosity formula [Wil50] as follows

$$\mu = \frac{Y_1\mu_1}{Y_1\phi_{11} + Y_2\phi_{12}} + \frac{Y_2\mu_2}{Y_1\phi_{21} + Y_2\phi_{22}}, \tag{3.34}$$

where ϕ_{ij} is a set of dimensionless constants calculated as

$$\phi_{ij} = \frac{\left[1 + \left(\frac{\mu_i}{\mu_j}\right)^{1/2}\left(\frac{M_j}{M_i}\right)^{1/4}\right]^2}{\left[8\left(1 + \frac{M_i}{M_j}\right)\right]^{1/2}} \quad : \quad i,j = \{1,2\}. \tag{3.35}$$

The variation of the dynamic and kinematic viscosities ($\nu = \mu/\rho$) as a function of helium

mass fraction Y_1 is seen in figure 3.2.

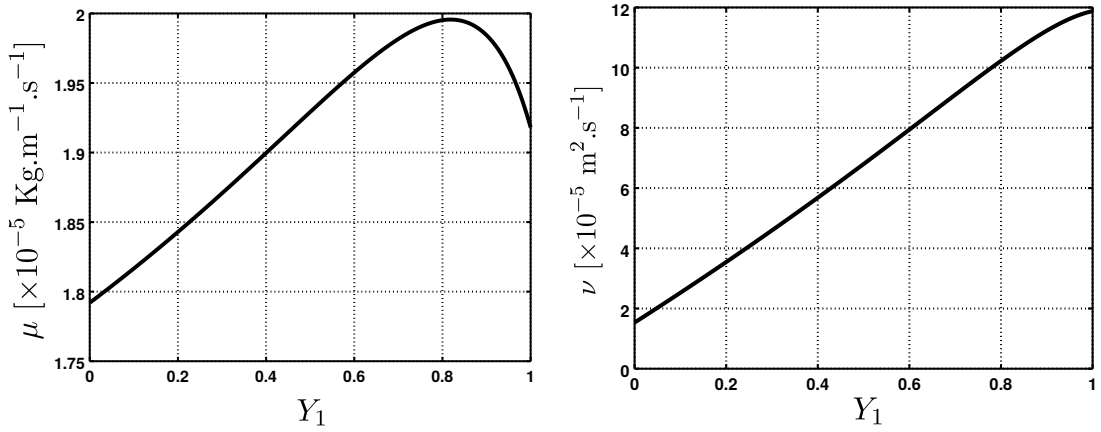

Figure 3.2: Variation of the mixture's dynamic viscosity μ (left) and kinematic viscosity ν (right) versus the helium mass fraction Y_1: $p = 10^5$ Pa and $T = 298.15$ K.

We can clearly note that the variation of μ is not as significant as the density variation (figure 3.2) and thus the variation of ν. More precisely, the maximum variation of the dynamic viscosity can reach to 11% in the injection vicinity. However, the maximum variation inside the plume region can reach a maximum of 3% approximately (figure 3.2, left). This is not the case with ν where variations can be as big as 100% near the injection and up to 50% upstream (figure 3.2, right).

In the present work, numerical simulations have been carried out with both DNS and LES approaches. In the DNS calculations, the system of equation presented in subsection 3.3.1 is discretized and solved without any turbulence model. In the next section, the LES formulation and the employed model are presented.

3.5 LES filtered equations

The LES formulation is obtained by applying a spatial filter to the system of equations presented in subsection 3.3.1 (refer to appendix B for complete details). We denote the spatially averaged quantities by the over-bar symbol ($\overline{\ }$). Since in the LMN system of equations the density is variable and the equations are written in the conservative formulation, a density weighted Favre averaging is required, referred to by a tilde symbol ($\widetilde{\ }$). The definition of the Favre average is recalled, for a considered density dependent flow quantity φ, as

$$\widetilde{\varphi} = \frac{\overline{\rho\varphi}}{\overline{\rho}}. \tag{3.36}$$

The filtered LES system of equations reads

$$\frac{\partial \overline{\rho}}{\partial t} + \frac{\partial}{\partial x_i}(\overline{\rho}\widetilde{u}_i) = 0, \tag{3.37}$$

$$\frac{\partial \overline{\rho}\widetilde{u}_j}{\partial t} + \frac{\partial}{\partial x_i}(\overline{\rho}\widetilde{u}_j\widetilde{u}_i) = -\frac{\partial \overline{P}}{\partial x_j} + \frac{\partial \overline{\tau}_{ij}}{\partial x_i} - \frac{\partial \overline{\tau}_{ij}^{\mathrm{SGS}}}{\partial x_i} + \overline{\rho} g_j, \tag{3.38}$$

$$\frac{\partial \overline{\rho}\widetilde{Y}_1}{\partial t} + \frac{\partial}{\partial x_i}(\overline{\rho}\widetilde{u}_i\widetilde{Y}_1) = \frac{\partial}{\partial x_i}\left(D\overline{\rho}\frac{\partial \widetilde{Y}_1}{\partial x_i}\right) - \frac{\partial \overline{\xi}_i^{\mathrm{SGS}}}{\partial x_i}, \tag{3.39}$$

$$\overline{\rho} = \frac{p}{RT}\left(\frac{\widetilde{Y}_1}{M_{\mathrm{inj}}} + \frac{\widetilde{Y}_2}{M_{\mathrm{amb}}}\right)^{-1}, \tag{3.40}$$

where

$$\overline{\tau}_{ij} = \widetilde{\mu}\left(\frac{\partial \widetilde{u}_i}{\partial x_j} + \frac{\partial \widetilde{u}_j}{\partial x_i}\right) - \frac{2}{3}\widetilde{\mu}\delta_{ij}\frac{\partial \widetilde{u}_k}{\partial x_k}, \tag{3.41}$$

$$\overline{\tau}_{ij}^{\mathrm{SGS}} = -\overline{\rho}(\widetilde{u}_i\widetilde{u}_j - \widetilde{u_i u_j}), \tag{3.42}$$

$$\overline{\xi}_i^{\mathrm{SGS}} = -\overline{\rho}(\widetilde{u}_i\widetilde{Y}_1 - \widetilde{u_i Y_1}). \tag{3.43}$$

$\overline{\tau}_{ij}^{\mathrm{SGS}}$ and $\overline{\xi}_i^{\mathrm{SGS}}$ are respectively the sub-grid scale (SGS) Reynolds stress and turbulent scalar flux tensors and thus require suitable models so that the LES system of equations is closed.

3.5.1 Reynolds stress tensor models

In the present work, two models have been employed to model the SGS $\overline{\tau}_{ij}^{\mathrm{SGS}}$ tensor: the classical Smagorinsky model [Sma63] and the Wall-Adapting Local Eddy-Viscosity (WALE) model [ND99a]. Both SGS models are based on an eddy-viscosity assumption where the components of $\overline{\tau}_{ij}^{\mathrm{SGS}}$ are expressed following:

$$\overline{\tau}_{ij}^{\mathrm{SGS}} - \frac{1}{3}\overline{\tau}_{kk}^{\mathrm{SGS}}\delta_{ij} = -2\mu_{\mathrm{SGS}}\overline{S}_{ij}, \tag{3.44}$$

with

$$\overline{S}_{ij} = \frac{1}{2}\left(\frac{\partial \widetilde{u}_j}{\partial x_i} + \frac{\partial \widetilde{u}_i}{\partial x_j}\right). \tag{3.45}$$

- Classical Smagorinsky SGS model:

The SGS dynamic viscosity μ_{SGS} is calculated as

$$\mu_{\mathrm{SGS}} = \overline{\rho}(C_s\Delta)^2\sqrt{2\ \overline{S}_{ij}\overline{S}_{ij}}. \tag{3.46}$$

Δ is the filter width taken to be equal to the cell volume $(\delta_x\delta_y\delta_z)^{1/3}$, with δ_x, δ_y and δ_z the effective mesh spacing. The Smagorinsky coefficient is considered constant and uniform

throughout the whole domain; $C_s = 0.18$.

- WALE SGS model:

The SGS dynamic viscosity μ_{SGS} is calculated as

$$\mu_{\text{SGS}} = \overline{\rho}(C_w\Delta)^2 \frac{(\mathcal{S}^d_{ij}\mathcal{S}^d_{ij})^{3/2}}{(\overline{S}_{ij}\overline{S}_{ij})^{5/2} + (\mathcal{S}^d_{ij}\mathcal{S}^d_{ij})^{5/4}}. \tag{3.47}$$

$\mathcal{S}^d_{ij}$ is the traceless symmetrical part of the square of the velocity gradient tensor defined as

$$\mathcal{S}^d_{ij} = \frac{1}{2}\left(\overline{g}^2_{ij} + \overline{g}^2_{ji}\right) - \frac{1}{3}\delta_{ij}\overline{g}^2_{kk}, \tag{3.48}$$

where $\overline{g}_{ij} = \partial\widetilde{u}_i/\partial x_j$ and $\overline{g}^2_{ij} = \overline{g}_{ik}\overline{g}_{kj}$.

The WALE coefficient is considered constant and uniform throughout the whole domain; $C_w = 0.325$.

3.5.2 Turbulent scalar flux model

The unresolved turbulent scalar flux $\overline{\xi}_i^{\text{SGS}}$ is modeled by using a classic Fourier's law as:

$$\overline{\xi}_i^{\text{SGS}} = -\frac{\mu_{\text{SGS}}}{Sc_{\text{SGS}}}\frac{\partial\widetilde{Y}_1}{\partial x_i}. \tag{3.49}$$

The SGS Schmidt number is considered constant and uniform throughout the whole domain; $Sc_{\text{SGS}} = 0.7$ (to compare with $\text{Sc}_{\text{inj}} \approx 1.719$ and $\text{Sc}_{\text{amb}} \approx 0.222$).

For a matter of simplifying the notations, we remove all filter symbols when dealing with LES solutions.

Chapter 4

Numerical methods and CFD codes

Contents

In this chapter, we present the numerical methods and the tools implemented in the two codes "**S**imulations of **UN**steady **FL**ows **U**nder **I**ncompressible and **D**ilatable **H**ypothesis" (SUNFLUIDH) and "**TR**io_**U** **S**oftware for **T**hermohydraulics" (CEA TRUST-TrioCFD) which we employ for the numerical resolution of the time dependent system of equations already presented in chapter 3.

The chapter is organized as follows. First, we present a general overview and the performance of both CFD softwares. Secondly, the resolution algorithm is described where the main differences between both codes are stated. Thirdly, the numerical approximations of the spatial and temporal integrations are presented. After, the initial and boundary conditions are discussed according to the different employed geometries. Finally, the stability criteria of the numerical schemes are stated.

4.1 Employed CFD codes

4.1.1 SUNFLUIDH

SUNFLUIDH has been developed in the year 2011 (to present) by Yann FRAIGNEAU [Fra13a, Fra13b] at the "**L**aboratoire d'**I**nformatique pour la **M**écanique et les **S**ciences de

l'**I**ngénieur" (LIMSI–CNRS). SUNFLUIDH is used to perform numerical simulations, either by LES or DNS approaches, incompressible and/or dilatable flows under the LMN hypothesis. This code, being efficiently parallelized (OpenMP, MPI, hybrid), is useful to simulate several types of problems (natural convection, forced flows, ...) in cartesian or cylindrical coordinates. It offers the possibility of employing immersed bodies with different forms in the domain in order to handle complex geometries. The software is a closed source and written in the Fortran 90 language, with a wide usage of derived type variables.

A cartesian structured mesh is the starting key point in SUNFLUIDH. The MPI domain decomposition algorithm is defined by a cartesian topological technique (equal cell sized aligned sub-domains). Several numerical schemes are already implemented in the code and the choice is kept as an option for the code user. In all cases, the spatial discretization is performed by a finite volume (FV) approach on a staggered mesh of type Marker-And-Cell MAC. A detailed description can be reviewed from [Fra13a]. In our work, a purely explicit scheme based on the paper of Yu et al. in [YYB12] is employed.

SUNFLUIDH was executed for an axi-symmetrical configuration on a local cluster of LIMSI–CNRS (Intel Xeon, X5675, 3.07 GHz, 148 Go memory per node and standard ethernet 1 Gbit.s^{-1}). The OpenMP option has been specified for the parallel computation over 6 shared-memory threads, where the total mesh corresponds to 4.7872×10^5 cells. The code performance report reads as follows:

- Total process CPU time = 535.22 hours $\Rightarrow$ total wall-time 89.2 hours per thread ($\approx$ 3.7 days),
- Number of carried out iterations = 6×10^5,
- Poisson resolution takes about 85% of the computational time,
- Performance = 6.708×10^{-6} seconds/cell/time-step (wall-time).

4.1.2 CEA TRUST-TrioCFD

CEA TRUST-TrioCFD has been initially developed for about more than 20 years (to present) at the "**D**irection de l'**É**nergie **N**ucléaire" (DEN) of the "**C**ommissariat à l'**É**nergie **A**tomique" (CEA) [DC]. The code is capable to simulate a wide range of problems, such as turbulent flows, fluid/solid coupling, mono or multi-phase flows, mono or multi-species flows, ... [ABF15]. The domains of applications of CEA TRUST-TrioCFD are mainly related to the nuclear industry, which makes it able to treat easily complex and coupled geometries. In practice, the code reads a non-structural mesh with an MPI decomposition technique based of a graphical topology (Metis).

The code is written in the C++ language; object oriented with more than 1500 classes. The source is open and latest downloadable versions are always up to date on the site [DC]. Several choices of implemented numerical schemes are kept as an option for the code user.

In addition, the flow equations are discretized either by a finite element (FE) method or by a finite difference volume (VDF) method; the discretization of each term is performed by integrating over a control volume where the diffusion gradient terms are approximated by a linear difference equation. The discretization method is always kept as an option of the user. In our work, we specify the VDF option where a semi-explicit scheme has been employed. A non-structured hexahedral mesh is used and the spatial discretization is performed also on a staggered grid.

CEA TRUST-TrioCFD has been executed for a 3D LES on a local cluster of CEA–SACLAY (Intel Xeon, E5-2680 V2, 2.8 GHz, 128 Go memory per node and infiniband QDR 40 Gbit.s^{-1}). MPI option has been specified for the parallel computation over 100 communicating processors, where the total mesh corresponds to 6.108484×10^6 cells. The code performance report reads as follows.

- Total process wall-time time = 47 hours per MPI processor,
- Number of carried out iterations = 30197,
- Poisson resolution takes 63% of the computational time,
- 95 times the "MPI_Allreduce" is used per time-step,
- Performance = 9.17×10^{-7} seconds/cell/time-step (wall-time).

4.2 The resolution algorithm

In this section, the numerical algorithm implemented in both codes is presented. Two equations are mainly discretized: the species conservation equation (3.26) and the momentum conservation equation (3.25).

Equation (3.26) is always treated in a non-conservative formulation

$$\rho \frac{\partial Y_1}{\partial t} + C_{Y_1} = D_{Y_1}, \tag{4.1}$$

where $C_{Y_1} = \rho u_i \cdot \frac{\partial}{\partial x_i} Y_1$ and $D_{Y_1} = \frac{\partial}{\partial x_i}\left(D\rho \frac{\partial Y_1}{\partial x_i}\right)$ are respectively the species convective and molecular diffusion terms.

Equation (3.25) is discretized in both codes following a conservative formulation. However, the pressure term is treated differently in both softwares: SUNFLUIDH solves for the reduced pressure $\pi = P + \rho_{\text{amb}} g z$, while CEA TRUST-TrioCFD solves for the hydrodynamic pressure P. Thus, the momentum equation is written as

$$\frac{\partial \rho u_j}{\partial t} + C_{\mathbf{u}} = D_{\mathbf{u}} + S_{\mathbf{u}}, \tag{4.2}$$

where $C_{\mathbf{u}} = \frac{\partial}{\partial x_i}(\rho u_j u_i)$ and $D_{\mathbf{u}} = \frac{\partial \tau_{ij}}{\partial x_i}$ denote respectively the convective and the viscous terms. $S_{\mathbf{u}}$ is a source term containing both the buoyant and the pressure gradient terms. It is rather dependent on the employed code and defined in table 4.1.

	SUNFLUIDH	CEA TRUST-TrioCFD
$S_{\mathbf{u}}$	$-\frac{\partial \pi}{\partial x_j} + (\rho - \rho_{\text{amb}})g_j$	$-\frac{\partial P}{\partial x_j} + \rho g_j$

Table 4.1: The momentum source term defined in the softwares SUNFLUIDH and CEA TRUST-TrioCFD.

In both CFD softwares, the numerical resolution is carried out in a sequential way. Three variables are considered in each time iteration as the main unknowns; respectively Y_1, $\mathbf{u}$ and π or P. The density of the mixture ρ is simply estimated from the state equation (3.27). The remaining unknowns (Y_2, μ, ...) are easily deduced from the resolved fields, and that is by simple substitution following their definition.

Suppose that the flow variables are known from the previous time iteration t^n. The resolution algorithm employed for calculating the flow variables at the next time increment t^{n+1} is described in the schematic representation illustrated in figure 4.1 and more detailed in the coming subsection.

4.2.1 Species and state equations resolution

The species conservation equation, expressed in its non-conservative formulation (equation (4.1)), is treated in both codes firstly. Following the employed numerical scheme (either purely explicit or semi-implicit) and using the fields ρ^n, $\mathbf{u}^n$, the field Y_1^{n+1} is evaluated.

The mass fraction of air is deduced from that of helium, at each scalar node, using the relation

$$Y_2^{n+1} = 1 - Y_1^{n+1}. \tag{4.3}$$

From the values of Y_1^{n+1}, Y_2^{n+1} and using the gas mixture viscosity equation (3.34), the mixture dynamic viscosity μ^{n+1} is updated.

Next, the equation of state (3.27) is considered. From the mass fraction fields at t^{n+1}, the density of the mixture ρ^{n+1} is evaluated at each scalar node in the computational grid as follows

$$\rho^{n+1} = \frac{p}{RT}\left(\frac{Y_1^{n+1}}{M_{\text{inj}}} + \frac{Y_2^{n+1}}{M_{\text{amb}}}\right)^{-1}. \tag{4.4}$$

Next, we move to the momentum equation (4.2) resolution. Here, we describe the procedure depending on the employed software.

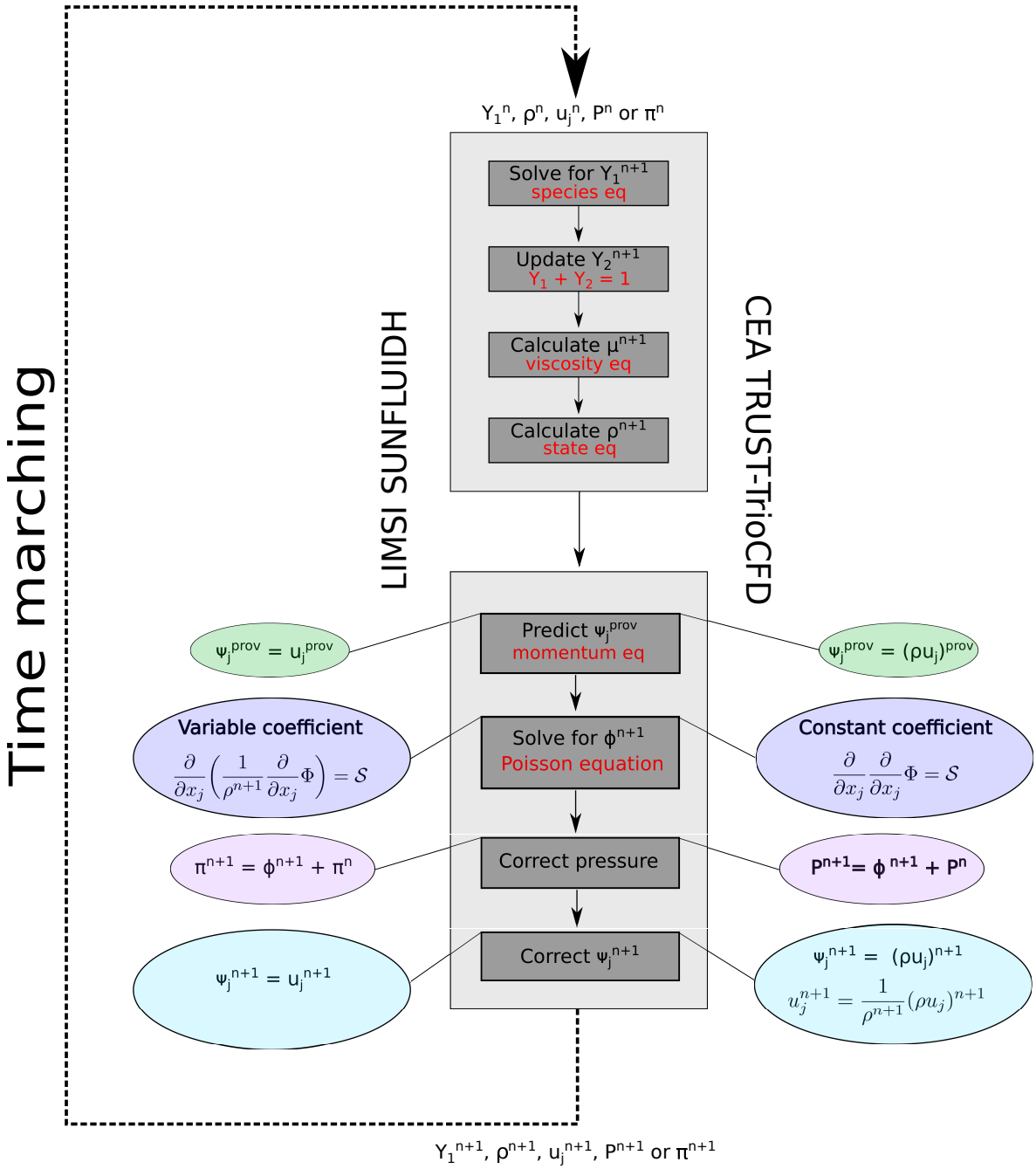

Figure 4.1: An overall algorithm overview: sequential resolution, SUNFLUIDH and CEA TRUST-TrioCFD codes.

4.2.2 Momentum and Poisson equations resolution

To handle the problem of the velocity-pressure coupling, an incremental prediction–projection method is employed in both codes [GMS06]. This basically follows a three step procedure: a prediction step at first, resolution of an elliptic pressure Poisson equation at second and

finally a correction step is performed to satisfy the conservation of mass or volume in the domain (depending on the followed approach in each CFD software). We emphasize that the heart of this procedure is in solving the Poisson equation as it takes mainly 3/4 of the computational time. The three step procedures can be summarized as follows:

- Step one: prediction of the velocity or momentum

The pressure gradient term is treated explicitly at first and a provisional field ψ_j^{prov} is calculated by solving the momentum equation (4.2). The discretized equation is expressed as

$$\begin{cases} \text{SUNFLUIDH} & : \quad \rho^{n+1}\dfrac{\partial \psi_j}{\partial t} + \mathcal{A}^*_{\mathbf{u}} = -\dfrac{\partial \pi^n}{\partial x_j} + D^n_{\mathbf{u}}, \\ \\ \text{CEA TRUST-TrioCFD} & : \quad \dfrac{\partial \psi_j}{\partial t} + C^n_{\mathbf{u}} = D^{n+1}_{\mathbf{u}} + S^n_{\mathbf{u}}, \end{cases} \tag{4.5}$$

where

$$\begin{cases} \text{SUNFLUIDH} & : \quad \psi_j = u_j \text{ (velocity)}, \ \mathcal{A}^*_{\mathbf{u}} = \dfrac{3}{2}\mathcal{A}^n_{\mathbf{u}} - \dfrac{1}{2}\mathcal{A}^{n-1}_{\mathbf{u}}, \\ & \quad \mathcal{A}^n_{\mathbf{u}} = C^n_{\mathbf{u}} - (\rho^n - \rho_{\text{amb}})g_j, \ C^n_{\mathbf{u}} = \dfrac{\partial}{\partial x_i}(\rho^n u_j^n u_i^n), \\ & \quad D^n_{\mathbf{u}} = \dfrac{\partial}{\partial x_i}(2\mu^n e_{ij}^n), \\ \\ \text{CEA TRUST-TrioCFD} & : \quad \psi_j = \rho u_j \text{ (momentum)}, \ C^n_{\mathbf{u}} = \dfrac{\partial}{\partial x_i}\Big[(\rho u_j)^n u_i^n\Big], \\ & \quad D^{n+1}_{\mathbf{u}} = \dfrac{\partial}{\partial x_i}(2\mu^{n+1} e_{ij}^{n+1}), \ S^n_{\mathbf{u}} = -\dfrac{\partial P^n}{\partial x_j} + \rho^n g_j, \\ & \quad e_{ij}^{n+1} = \dfrac{1}{2}\left[\dfrac{\partial}{\partial x_i}\left(\dfrac{(\rho u_j)^{n+1}}{\rho^{n+1}}\right) + \dfrac{\partial}{\partial x_j}\left(\dfrac{(\rho u_i)^{n+1}}{\rho^{n+1}}\right)\right] \\ & \qquad\qquad - \dfrac{1}{3}\delta_{ij}\dfrac{\partial}{\partial x_k}\left(\dfrac{(\rho u_k)^{n+1}}{\rho^{n+1}}\right), \end{cases} \tag{4.6}$$

The temporal integration of system (4.5) is performed from t^n to a provisional time t^{prov}. Note that provisional field ψ_j^{prov} do not satisfy the conservation of volume or mass equations; volume conservation derived from equation (3.13) and (3.28) (SUNFLUIDH) or mass conservation presented in equation (3.24) (CEA TRUST-TrioCFD).

- Step two: resolution of the Poisson equation

The contribution of the pressure gradient term is treated implicitly for t^{n+1}. In fact, we are looking for solving the momentum equation under the final form where the temporal integration is carried out over the whole time increment $[t^n, t^{n+1}]$ and thus the equation is

discretized as

$$\begin{cases} \text{SUNFLUIDH} & : \quad \rho^{n+1}\dfrac{\partial \psi_j}{\partial t} + \mathcal{A}^*_{\mathbf{u}} = D^n_{\mathbf{u}} - \dfrac{\partial \pi^{n+1}}{\partial x_j}, \\ \\ \text{CEA TRUST-TrioCFD} & : \quad \dfrac{\partial \psi_j}{\partial t} + C^n_{\mathbf{u}} = D^{n+1}_{\mathbf{u}} - \dfrac{\partial P^{n+1}}{\partial x_j} + \rho^n g_j. \end{cases} \tag{4.7}$$

Subtracting equation (4.7) from equation (4.5) and taking afterwards the divergence on both sides, the elliptic Poisson equation of the pressure increment Φ is obtained and thus written as

$$\frac{\partial}{\partial x_j}\left(\frac{1}{\alpha^{n+1}}\frac{\partial}{\partial x_j}\Phi\right) = \mathcal{S}, \tag{4.8}$$

where

$$\mathcal{S} = \frac{1}{\delta t}\left(\frac{\partial}{\partial x_j}\psi_j^{\text{prov}} - \frac{\partial}{\partial x_j}\psi_j^{n+1}\right), \tag{4.9}$$

and

$$\begin{cases} \text{SUNFLUIDH} & : \quad \alpha = \rho, \ \Phi = \pi^{n+1} - \pi^n, \\ \\ \text{CEA TRUST-TrioCFD} & : \quad \alpha = 1, \ \Phi = P^{n+1} - P^n. \end{cases} \tag{4.10}$$

$\delta t = t^{n+1} - t^n$ is the time integration step. The divergence $\partial/\partial x_j(\psi_j^{n+1})$ appearing in the source term $\mathcal{S}$ of the Poisson equation (4.8) is the correct field that satisfies the volume or mass equations [1]

$$\begin{cases} \text{SUNFLUIDH} & : \quad \dfrac{\partial}{\partial x_j}\psi_j = \displaystyle\sum_{i=1}^{2} \frac{1}{M_i}\left(\frac{Y_1}{M_1} + \frac{Y_2}{M_2}\right)^{-1} \frac{\mathrm{D}}{\mathrm{D}t}(Y_i), \\ \\ \text{CEA TRUST-TrioCFD} & : \quad \dfrac{\partial}{\partial x_j}\psi_j = -\dfrac{\partial \rho}{\partial t}. \end{cases} \tag{4.11}$$

and thus is discretized as follows

$$\begin{cases} \text{SUNFLUIDH} & : \quad \dfrac{\partial}{\partial x_j}\psi_j^{n+1} = \displaystyle\sum_{i=1}^{2} \frac{1}{M_i}\left(\frac{Y_1^{n+1}}{M_1} + \frac{Y_2^{n+1}}{M_2}\right)^{-1} \times \\ & \qquad \left\{ \dfrac{3}{2}\left[\dfrac{Y_i^{n+1} - Y_i^n}{\delta t} - \dfrac{3}{2}C^n_{Y_i} + \dfrac{1}{2}C^{n-1}_{Y_i}\right] - \right. \\ & \qquad \left. \dfrac{1}{2}\left[\dfrac{Y_i^{n} - Y_i^{n-1}}{\delta t} - \dfrac{3}{2}C^{n-1}_{Y_i} + \dfrac{1}{2}C^{n-2}_{Y_i}\right] \right\}, \\ \\ \text{CEA TRUST-TrioCFD} & : \quad \dfrac{\partial}{\partial x_j}\psi_j^{n+1} = -\dfrac{\rho^{n+1} - \rho^n}{\delta t}. \end{cases} \tag{4.12}$$

[1] The divergence constraint on the velocity field implemented in SUNFLUIDH is related to the total variation of the species mass fractions expressed in equation (3.28).

We note at this stage two basic key points. At first, we emphasize that the species and the state equations are treated before the momentum equation in the resolution algorithm in order to employ the updated fields and ensure at each time iteration the balance equation (4.12).

The second point that we like to highlight on is the difference between the two CFD codes. SUNFLUIDH ensure the volumetric balance by the velocity field (u_j), while CEA TRUST-TrioCFD ensure the mass balance by the momentum field (ρu_j).

Φ, the solution of the Poisson equation (4.8), is obtained in both codes by employing an iterative solver; SUNFLUIDH: V-cycle multi-grid algorithm with a successive over relaxation (SOR) iterative solver, CEA TRUST-TrioCFD: symmetrical successive over relaxation (SSOR) iterative solver (algorithms are thoroughly discussed in [Wes95] and [Saa03]).

From the values of Φ evaluated at each scalar node, the local pressure values of π^{n+1} (SUNFLUIDH) or P^{n+1} (CEA TRUST-TrioCFD) are deduced.

- Step three: correction of the velocity or momentum (projection)

Finally, the projection method takes place where the field ψ is updated using the projection (correction) formula

$$\psi_j^{n+1} = \psi_j^n - \frac{\delta t}{\alpha^{n+1}} \frac{\partial}{\partial x_j} \Phi. \tag{4.13}$$

ψ_j^{n+1} satisfies the mass conservation described in the divergence formulation of equation (4.11). Again, we emphasize the difference between the two softwares on the corrected field that satisfies the divergence constraint (velocity u_j^{n+1} in SUNFLUIDH, while momentum $(\rho u_j)^{n+1}$ in CEA TRUST-TrioCFD).

In the case where CEA TRUST-TrioCFD is employed, a supplementary step is performed to calculate the velocity field. Assuming that $(\rho u_j)^{n+1} \approx \rho^{n+1} u_j^{n+1}$, the correct velocity field along the direction of j is approximated as

$$u_j^{n+1} = \frac{1}{\rho^{n+1}} (\rho u_j)^{n+1}. \tag{4.14}$$

However, it is important to note that the corrected velocity field u_j^{n+1} in CEA TRUST-TrioCFD may not satisfy explicitly the velocity divergence constraint.

At this stage, all the fields are up to date and thus a new time iteration is considered where the sequential resolution presented in subsections 4.2.1 and 4.2.2 is performed again.

4.3 Numerical approximations

4.3.1 Spatial discretization

Spatial discretization is performed by both codes on a staggered grid of type MAC. On such grid, the flow variables are stored at different geometrical positions. More precisely, the scalars (pressure, density and mass fraction, ...) are stored at the center of the control volumes, whereas the velocity components are defined on the center-faces of the control volumes [HW65]. A 2D description of a non-uniform staggered grid is illustrated in figure 4.2.

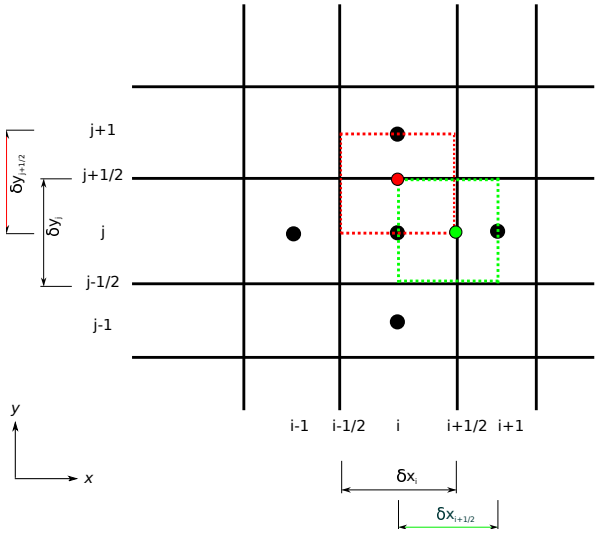

Figure 4.2: 2D staggered grid description: scalars stored at the center of the main black cell (black point •), $x-$horizontal velocity component at the horizontal faces of the main black cell (green point •), $y-$horizontal velocity component at the vertical faces of the main black cell (red point •). Green and red dotted control volumes are used to solve the horizontal (green) and vertical (red) velocity components equations.

In accordance with the staggered grid, all the terms of equation (4.1) are always stored at the center of the control volumes while those of equation (4.2) at the faces, where the velocities are initially stored. In SUNFLUIDH, the spatial discretization is always handled by a second order central scheme that employs a linear interpolation between two known points respectively from the up and down streams [VM07].

When the numerical simulations are performed with the CEA TRUST-TrioCFD code, we specify two numerical schemes (as an option) to handle the spatial disretization. For all the spatial terms defined in equations (4.1) and (4.2), a second order central scheme is employed except for the species convective term C_{Y_1}, where a quadratic upstream interpolation for convective kinematics (QUICK) scheme is specified.

QUICK is a third order accurate scheme, initially introduced by Leonard in [Leo79]. Depending on the orientation of the flow, an upstream (or downstream) quadratic interpolation is

performed to obtain the approximations [NSC11]. We emphasize that QUICK scheme, as any upwind scheme, induces some numerical diffusion that can reduce the oscillations of the helium mass fraction (oscillations can mainly develop in the regions where a sharp Y_1 gradients take place; jet boundary and in the vicinity of the injection). Moreover, it is monotonic and bounded which ensures that the mass fraction is always within the range 0 and 1 [VM07].

4.3.2 Temporal discretization

The time advancement of equations (4.1) and (4.2) is treated by an appropriate temporal scheme in order to approximate the time derivative (transient) term. However, the employed temporal schemes are not unique for both codes and are thus discussed in what follows.

- SUNFLUIDH:

The pure explicit scheme presented by Yu et al. in [YYB12] is originally implemented based on the work of Knio et al . in [KNW99] to simulate reactive species, where the temporal integration of the diffusion and reaction terms is performed by an operator-splitting technique; the Strang's splitting method. However, as far as we consider non-reactive species in the present study, only a second order two-stage Runge-Kutta (RK2) scheme is used.

The convective and source terms are incorporated directly in the Strang operator splitting algorithm. In practice, the convective and source terms are extrapolated from two previous time instants by a second order Adam-Bashforth (AB2) scheme and thus the values are merged with the diffusion term to enter each RK2 stage integration.

- CEA TRUST-TrioCFD:

A two stage second order Rational Runge-Kutta scheme (RRK2) is employed for the temporal discretization. RRK2 scheme was first introduced by Wambecq in [Wam78] to simulate steady flows and showed to be accurate, second order and A_0 stable. Angrand et al. in [ABD$^+$85] show that RRK2 is more efficient than the first order Euler method, especially in cases where a central spacial scheme is considered.

4.4 Initial and boundary conditions

As far as we consider a time marching problem, appropriate initial and boundary conditions are to be imposed. For all the simulations and independently of the employed code, the fluid is considered to be at rest ($\mathbf{u} = 0$) in the initial state everywhere in the domain except at the inlet boundary. The configuration is filled everywhere with pure air ($Y_1 = 0$) excluding the pipe where, when modelled in the computational domain, it is initialized with a smooth vertical helium mass fraction profile that decreases from 1 (pure helium) at the bottom of the pipe where the inlet boundary condition is prescribed, to 0 (pure air) while approaching the top of the pipe. In the horizontal sections of the pipe, the distribution is uniform. An

example of an initial pipe distribution for a simulation with a 10 cm pipe height is illustrated in figure 4.3. The smooth distribution is considered to reduce the stiff concentration gradients at the first iterations of the simulation.

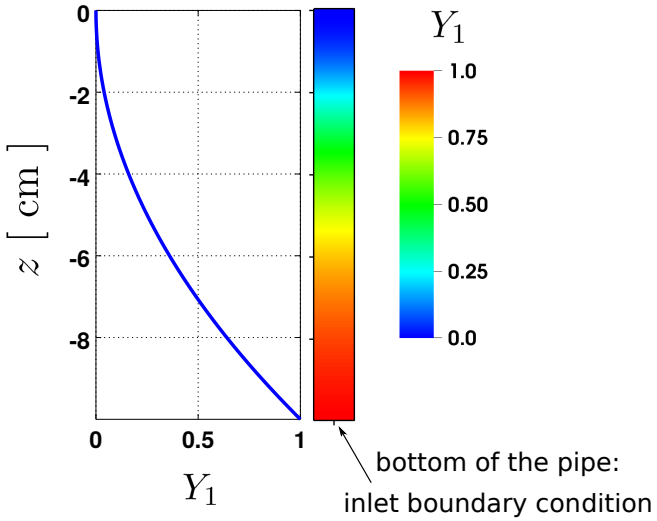

Figure 4.3: Helium mass fraction Y_1 vertical profile inside the tube at the initial state: case of a simulation carried out by CEA TRUST-TrioCFD for a pipe of height $h = 10$ cm; $Y_1(z) = (1/h)z^2 + z(h^2 - 2)/(2h)$. Left: Y_1 distribution along the vertical axis, right: Y_1 iso-contour plot in the mid-vertical XZ_1 plane ($y = 0$).

We present in the remaining of this section the implemented boundary conditions depending on the employed CFD software. As far as we simulate mainly two different geometries (axi-symmetric and 3D configurations), two decompositions of the boundary surfaces are thus considered.

In the 3D geometrical configurations (CEA TRUST-TrioCFD), the boundaries of the complete domain Ω can be classified into three distinct types: solid wall boundaries ($\partial\Omega_W$) reproducing the plexi-glass in the real experiment, inlet boundary ($\partial\Omega_i$) representing the surface where pure helium is injected and the outlet boundaries ($\partial\Omega_o$) where the exchange between the interior and exterior environments are modelled (see figure 4.4). We particularly consider the following decomposition

$$\partial\Omega = \partial\Omega_W \cup \partial\Omega_i \cup \partial\Omega_o. \tag{4.15}$$

In cases of axi-symmetrical simulations (SUNFLUIDH), the boundary decomposition reads as

$$\partial\Omega = \partial\Omega_W \cup \partial\Omega_i \cup \partial\Omega_o \cup \partial\Omega_s, \tag{4.16}$$

where $\partial\Omega_s$ represents the symmetrical boundary situated along the jet axis (see figure 4.5). This condition is defined as a zero gradient homogeneous Neumann condition for all variables except the velocity component normal to the axis of symmetry, which is placed to zero. We assume in our case that the axis of symmetry is along the z-direction and thus the conditions

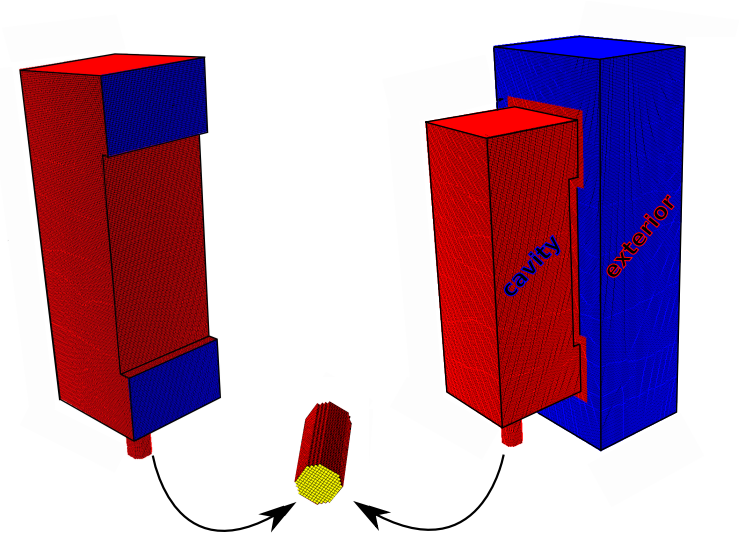

Figure 4.4: Locations of the prescribed boundary conditions for 3D computational domains: $\partial\Omega_W$ on red surfaces, $\partial\Omega_i$ on yellow surface and $\partial\Omega_o$ on blue surfaces. Left: configuration without an exterior domain, right: configuration with an exterior domain.

at $\partial\Omega_s$ are described as

$$\begin{cases} \dfrac{\partial \varphi}{\partial r} = 0 \quad : \quad \varphi = \{\pi, \rho, Y_1\}, \\ \dfrac{\partial u_z}{\partial r} = 0, \\ u_r = 0. \end{cases} \tag{4.17}$$

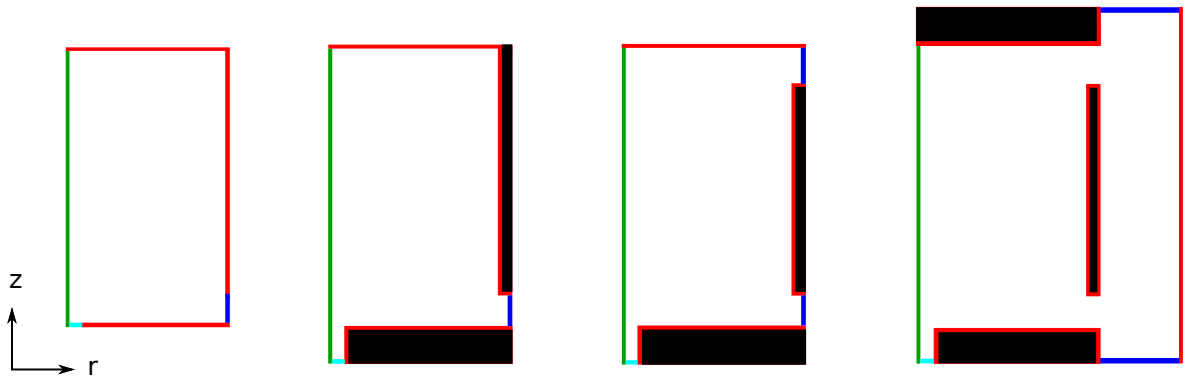

(a) (b) (c) (d)

Figure 4.5: Locations of the prescribed boundary conditions for 2D axi-symmetrical computational domains: $\partial\Omega_W$ on red boundaries, $\partial\Omega_i$ on cyan boundaries, $\partial\Omega_s$ on green boundaries and $\partial\Omega_o$ on blue boundaries. Left to right: (a) cavity only, (b) meshed pipe and one vented cavity, (c) meshed pipe and two vented cavity without an exterior domain and (d) meshed pipe and two vented cavity with an exterior domain. Black blocks denote the immersed solid boundaries (non-fluid zones).

Similar inlet and wall boundary conditions are implemented in both codes, and thus prescribed at the corresponding surfaces. They are defined as follows.

- The wall boundary conditions prescribed at $\partial\Omega_W$ are the easiest and the extensively used ones. For the velocity field, a no-slip condition is considered ($\mathbf{u}$=0), while a homogeneous Neumann condition is imposed for other variables

$$\frac{\partial \varphi}{\partial(\mathbf{x}\cdot\mathbf{n})} = 0 \quad : \quad \varphi = \{P \text{ or } \pi, \rho, Y_1\}, \tag{4.18}$$

  where $\mathbf{n}$ denotes the outward unit normal at the considered boundary surface and $\mathbf{x}$ is the space coordinate vector; $\mathbf{x} = (x, y, z)$ in the 3D cartesian geometry and $\mathbf{x} = (r, z)$ for the axi-symmetrical configurations.

- At the bottom boundary of the pipe $\partial\Omega_i$, we prescribe a constant injection mass flux $\rho_{\text{inj}} Q_v$ as far as the diffusive contribution is cutted off (set to zero). A parabolic velocity profile is imposed for $\mathbf{u}$ so that the velocity vector is oriented along the z-direction. The distribution is rather dependent of the geometry and thus defined as follows

$$\begin{cases} \text{SUNFLUIDH} & : \quad u_z = 2\ \overline{u}_{\text{inj}} \times \left(1 - \dfrac{4r^2}{d^2}\right), \\ \\ \text{CEA TRUST-TrioCFD} & : \quad u_3 = \epsilon_Q \times u_{3_*}, \end{cases} \tag{4.19}$$

  where d is the diameter of the pipe, $u_{3_*} = d^2/4 - (x^2 + y^2)$ and ϵ_Q is a correction parameter used to ensure the volumetric flow-rate conservation and calculated as

$$\epsilon_Q = \frac{Q_v}{\displaystyle\iint_{\partial\Omega_i} u_{3_*} dxdy}. \tag{4.20}$$

  Constant flat uniform profiles are prescribed for the mixture's density and helium mass fraction with

$$\rho = \rho_{\text{inj}} \quad \text{and} \quad Y_1 = 1. \tag{4.21}$$

  For the hydrodynamic pressure P, a homogeneous Neumann condition is implemented.

The conditions at the outlet boundary $\partial\Omega_o$ are the most difficult to impose. It is impossible to have a prior information on the flow profiles traversing the outlet boundaries and consequently, the volumetric and mass flow rates are impossible to priory estimate. All what we hope is that the conservative property of the finite volume approach balances the total flow rates in the domain; basically the volumetric one. In addition, a reversal flow can probably occur making the physical outlet boundary a numerical inlet and outlet boundary at the same time.

The conditions prescribed at $\partial\Omega_o$ are dependent on the employed software and thus summarized in what follows:

- SUNFLUIDH:

- **Case of a unique outlet boundary**

  In such cases, the employed boundary condition preserves the inlet/outlet volumetric flow-rate balance by performing a global explicit correction at each time the momentum equation is treated. In particular, the velocity field normal to the vent's boundary (u_r in our case) is first prescribed with a homogeneous Neumann condition as

$$\frac{\partial u_r}{\partial r} = 0. \tag{4.22}$$

  Afterwards, u_r is corrected all along $\partial\Omega_o$ so that the injection volumetric flow-rate Q_v is equal to the volumetric flow-rate at the outlet Q_v^{out} which is defined as

$$Q_v^{\text{out}} = \pi d \int_{\partial\Omega_o} u_r dz. \tag{4.23}$$

  A homogeneous Neumann condition is assumed for the tangential velocity component at the outlet boundary (u_z in our case) and thus written as

$$\frac{\partial u_z}{\partial r} = 0. \tag{4.24}$$

  Regarding the other scalar flow variables, a homogeneous Neumann condition is prescribed;

$$\frac{\partial \varphi}{\partial r} = 0 \quad : \quad \varphi = \{\rho, Y_1, \pi\}. \tag{4.25}$$

- **Case of two outlet boundaries**

  In such cases, a fixed reduced pressure boundary condition is implemented ($\pi = 0$) all along the outlet boundaries. However, a homogeneous Neumann condition is considered for the remaining flow variables

$$\frac{\partial \varphi}{\partial (\mathbf{x} \cdot \mathbf{n})} = 0 \quad : \quad \varphi = \{\mathbf{u}, \rho, Y_1\}, \tag{4.26}$$

- CEA TRUST-TrioCFD:

We employ while using this software an ambient-equilibrium hydrostatic pressure condition all along the outlet surfaces. The approximation of the pressure at the outlet is supposed to be dependent on the height z, defined as

$$P = -\rho_{\text{amb}} g z, \tag{4.27}$$

and thus fixed (per outlet cell) during the whole simulation (Dirichlet condition). It can be stated that this pressure boundary condition is identical to imposing $\pi = 0$ in SUNFLUIDH (cases of two vents).

For the remaining variables, a fluid–orientation test is performed. In particular, if the fluid

enters the domain ($\mathbf{u} \cdot \mathbf{n} < 0$), a pure air is assumed at the outlet surfaces where

$$Y_1 = 0 \quad \text{and} \quad \rho = \rho_{\text{amb}}. \tag{4.28}$$

Otherwise, if the fluid exits the domain ($\mathbf{u} \cdot \mathbf{n} \geq 0$), a zero gradient homogeneous Neumann condition is employed as expressed in equation (4.26).

We emphasize that this is basically the main difference between the outlet boundary condition implemented in CEA TRUST-TrioCFD and that in SUNFLUIDH (case of two outlet boundaries). More precisely, we ensure in CEA TRUST-TrioCFD that fresh air enters from the outside whenever an inflow takes place at $\partial\Omega_o$. This is not the case in SUNFLUIDH where a mixture inflow is considered.

4.5 Stability criteria

In this subsection, we present the choice of the time step δt in our simulations so that stable convergent results are obtained. This is generally known as the stability criteria and thus presented depending on the used CFD software as follows:

- SUNFLUIDH:

We recall that a pure explicit scheme is employed. In this case, the choice of δt is dependent on the convective stability criterion (Courant-Friedrich-Lewy CFL condition), diffusive and viscous stability criteria (Von Neumann condition).

Thus, we select

$$\delta_t = \min\{\delta t_c, \delta t_d, \delta t_\nu\}, \tag{4.29}$$

where δt_c is the convective time step, δt_d is the diffusive time step and δt_ν is the viscous time step defined respectively as

$$\delta t_c = \tau_c \times \text{CFL}, \tag{4.30}$$

$$\delta t_d = \tau_d \times \mathcal{R}_{VN}, \tag{4.31}$$

$$\delta t_\nu = \tau_\nu \times \mathcal{R}_{VN}, \tag{4.32}$$

where the CFL and the Von Neumann $\mathcal{R}_{VN}$ numbers are defined in SUNFLUIDH for a problem of dimension dim as

$$\text{CFL} = 0.5^{\text{dim}} \quad \text{and} \quad \mathcal{R}_{VN} = 0.5^{\text{dim}+1}, \tag{4.33}$$

and for characteristic time scales defined locally at each control volume as

$$\tau_c = \frac{1}{\max\left\{ \dfrac{u_{r_{i+1/2,k}}}{\delta_{r_{i+1/2}}}, \dfrac{u_{z_{i,k+1/2}}}{\delta_{z_{k+1/2}}} \right\}}, \tag{4.34}$$

$$\tau_d = \frac{1}{\max\left\{D \times \left[\left(\frac{1}{\delta_{r_i}}\right)^2, \left(\frac{1}{\delta_{z_k}}\right)^2\right]\right\}}, \tag{4.35}$$

$$\tau_\nu = \frac{1}{\max\left\{\nu_{i,k} \times \left[\left(\frac{1}{\delta_{r_i}}\right)^2, \left(\frac{1}{\delta_{z_k}}\right)^2\right]\right\}}. \tag{4.36}$$

- CEA TRUST-TrioCFD:

We recall that a semi-implicit scheme is employed where the convective terms are treated explicitly at each time iteration, while the diffusion and viscous terms are implicitly solved. This scheme has the advantage of restricting the choice of δt to the convective criterion only. Thus, smaller time steps required for the diffusive and viscous contributions are successfully prevented (note that being dependent on the square of the mesh size, the viscous and diffusive time steps are generally smaller than the convective time step δt_c).

Therefore, the time step is defined at each iteration from the convective contribution only and is calculated in CEA TRUST-TrioCFD as

$$\delta t = \delta t_c = \min\left(\frac{V_{\text{cell}}}{\zeta_{\text{cell}}}\right), \tag{4.37}$$

where ζ_{cell} [$\text{m}^3.\text{s}^{-1}$] corresponds to the volumetric flux entering at each arbitrary control volume (cell) of volume V_{cell}. This is basically equivalent to a CFL = 1, which means that a fluid particle does not cross more than one mesh cell per time step.

Chapter 5

Axi-symmetrical investigations

Contents

In this chapter, we present the first test cases performed by the code SUNFLUIDH. The simulations are carried out on axi-symmetric geometrical configurations. The expanded flow equations, in a general cylindrical system frame, can be reviewed from the book of Bird et al. in [BSL07].

As far as the simulations do not require high computational effort compared to 3D cases, the numerical configuration has been selected with bigger dimensions than the real experimental one. Practically, the idea behind simulating such test cases is to illustrate on the boundary condition issues, rather than validating to PIV measurements and recording statistics, which will be kept for the 3D simulations.

The chapter is organized as follows. At first, the code is validated and the numerical parameters are identified from a simple geometry with one vent. Secondly, we focus on the inlet boundary condition issue and the requirement of modelling the injection pipe in the computational domain. Finally, the influence of taking into account an exterior domain in the simulations is presented for a two vented cavity. All the post-treatment values throughout this chapter are defined in appendix C.

5.1 Code validation and grid convergence: case of a laminar starting plume

A simple one vented cavity (configuration AX1), of height $H = 50$ cm and radial width $R = 25$ cm, is firstly considered. The outlet (vent) is of height $z_{o_{\mathrm{AX1}}} = 2.1$ cm, situated at the bottom right wall. Helium is injected through an opening situated at the left bottom surface, corresponding to a cylindrical pipe of diameter $d_i = 2.1$ cm. The computational domain is illustrated in figure 5.1. Inlet and outlet boundary conditions are directly applied at the bottom opening and the vent surface respectively.

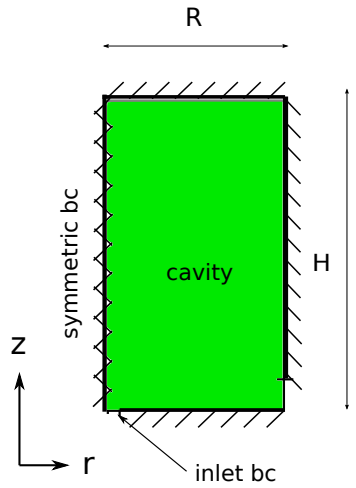

Figure 5.1: Schematic representation of the one vented cavity: configuration AX1.

A constant injection flow-rate $Q = 2$ Nl.min^{-1} is considered. Q, in a pipe of diameter $d_i = 2.1$ cm, is equivalent to an averaged injection velocity $\overline{u}_{\mathrm{inj}} \approx 0.103$ m.s^{-1} of pure helium. A parabolic profile for the axial velocity is employed at the inlet. The injection dimensionless parameters are $\mathrm{Re}_{\mathrm{inj}}$=19 and $\mathrm{Ri}_{\mathrm{inj}} = 120 \gg 1$ (pure plume predicted).

Simulations have been performed on four grids in order to identify the mesh size required for a good numerical resolution and convergence. In all cases, the mesh is structured and globally non-uniform. In practice, constant grid spacing are considered per direction in blocks aligned with the borders of the inlet and outlet. However, elsewhere in the cavity, the nodes are distributed by a hyperbolic tangent function

$$\mathrm{node}(n) = \mathcal{D} \left\{ \frac{F(n)}{\dfrac{\mathcal{D}}{N \times h} + \left(1 - \dfrac{\mathcal{D}}{N \times h}\right) F(n)} \right\}, \tag{5.1}$$

with

$$F(n) = \frac{1}{2}\left\{1 + \frac{\tanh\left[\dfrac{\mathcal{D}}{N \times h}\left(\dfrac{n-1}{N} - \dfrac{1}{2}\right)\right]}{\tanh\left(\dfrac{1}{2}\dfrac{\mathcal{D}}{N \times h}\right)}\right\}. \tag{5.2}$$

$\mathcal{D}$ denotes the distance along a considered direction, h is the desired step size (equal at the extremities of the distribution), $n = \{2, 3, \ldots, N\}$ where N is the total number of the required nodes. The size of the four employed meshes are summarized in table 5.1.

Mesh	$\min \delta r$ [cm]	$\max \delta r$ [cm]	$\min \delta z$ [cm]	$\max \delta z$ [cm]	**Cell number**
1	1.05×10^{-1}	2.7×10^{-1}	1.05×10^{-1}	2.7×10^{-1}	130 x 260 = 33,800
2	7×10^{-2}	1.8×10^{-1}	7×10^{-2}	1.8×10^{-1}	195 x 390 = 76,050
3	5.5×10^{-2}	1.35×10^{-1}	5.5×10^{-2}	1.35×10^{-1}	260 x 520 = 135,200
4	4.2×10^{-2}	1.08×10^{-1}	4.2×10^{-2}	1.08×10^{-1}	325 x 650 = 211,250

Table 5.1: Employed meshes for configuration AX1.

Considering only a vent at the bottom of the cavity places the problem in the framework of a **filling box** phenomenon, where the time required to obtain a steady state solution is rather long (obtained after filling the complete entire box). An instantaneous flow pattern showing the behavior of a filling box phenomenon is illustrated in figure 5.2.

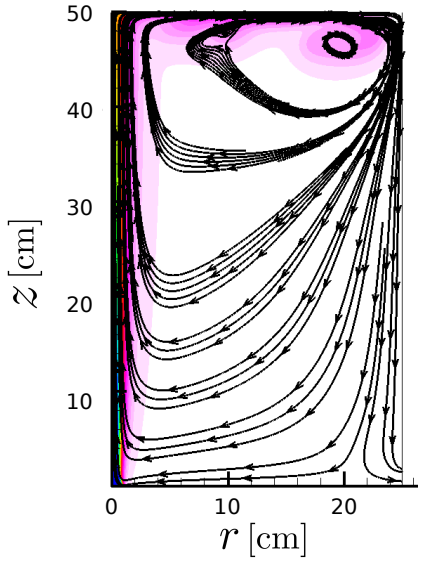

Figure 5.2: Filling box phenomenon, configuration AX1, fine grid: flow circulation illustrated by instantaneous velocity stream lines at $t = 5$ seconds.

As far as the complete flow is laminar and since the solution is not yet steady, convergence study is carried out on the plume characteristics before impacting the top ceiling; basically the

plume's height evolution. This evolution is well known as the behavior of laminar starting plume before impact and is thoroughly discussed in the previous Ph.D. work of Tran in [Tra13].

The height of the plume H_P has been determined using three different criteria. The first two methodologies (threshold and stagnation point criteria) already exist in the literature, while the third one (inflection point criterion) is based on our observations and has been currently proposed in this work. Thus, the aim of using the three methods is twofold. First, to test the validity of the new proposed criterion and second, to study the grid influence by comparing H_P obtained with different criteria. In what follows, we present the different methodologies employed to predict H_P.

- **Threshold criterion:**

  We consider the same procedure carried out in [Tra13]. A threshold ε_{Y_1} is used to determine whether a point is inside the plume or outside (inside if the mass fraction $Y_1 > \varepsilon_{Y_1}$). It is clear that the choice of ε_{Y_1} is not obvious and can change the predicted H_P.

  In this framework, we have carried out a parametric study by changing the value of ε_{Y_1} from 0.002 to 0.0052 (6 values have been considered). At a fixed time instant and before the impact with the top ceiling ($t = 0.99$ s), the contour line corresponding to $Y_1 = \varepsilon_{Y_1}$ is depicted in figure 5.3, left.

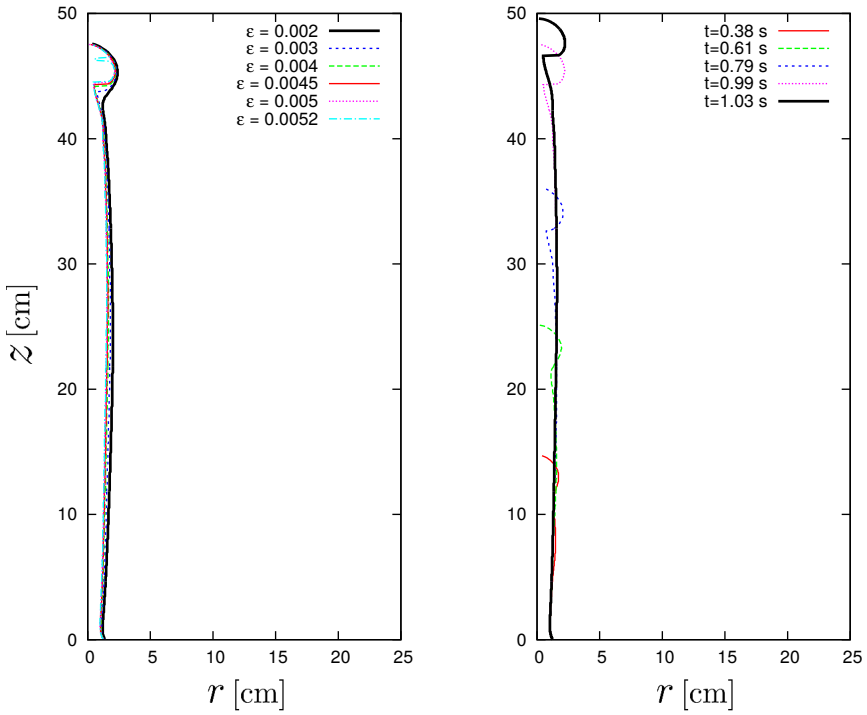

Figure 5.3: Plume's height estimation with the finest mesh (211,250 cells): threshold criterion ε_{Y_1}. Left: parametric study, right: plume time evolution with $\varepsilon_{Y_1} = 0.0045$.

From the contour lines, the boundaries of the plume are clearly identified (conduit and plume's head as described in [RM09]). We can note that varying the threshold parameter ε_{Y_1} modifies slightly the shape of the conduit (in maximum of 3%), while affects significantly the shape of the head. In particular, a part of the head is lost with the largest considered parameter $\varepsilon_{Y_1} = 0.0052$, while seems to be more diffusive with the smallest $\varepsilon_{Y_1} = 0.002$ (figure 5.3, left).

Three contour lines devoted to $\varepsilon_{Y_1} = 0.004, 0.0045$ and 0.005 show to be almost superposed with a well identified shape of the head. Thus, $\varepsilon_{Y_1} = 0.0045$ has been selected and the evolution of the plume before impacting the top ceiling is illustrated by the line contours in figure 5.3, right (Mesh 4). In this case, the plume-top ceiling impact has been predicted to occur at $t = 1.06$ s.

- **Stagnation point criterion:**

In a second approach, we follow the work of Davaille et al. in [DLT+11] where H_P is defined to be the axial position of the maximum radial derivative of u_r (stagnation point), that is

$$H_p = \text{vertical position } z \text{ of } \left\{ \max \left(\frac{du_r}{dr}\bigg|_{r=0} \right) \right\}. \tag{5.3}$$

The axial position of the stagnation point compared to H_P is illustrated for two time instants $t = 0.72$ and 0.9 seconds in figure 5.4 (mesh 4).

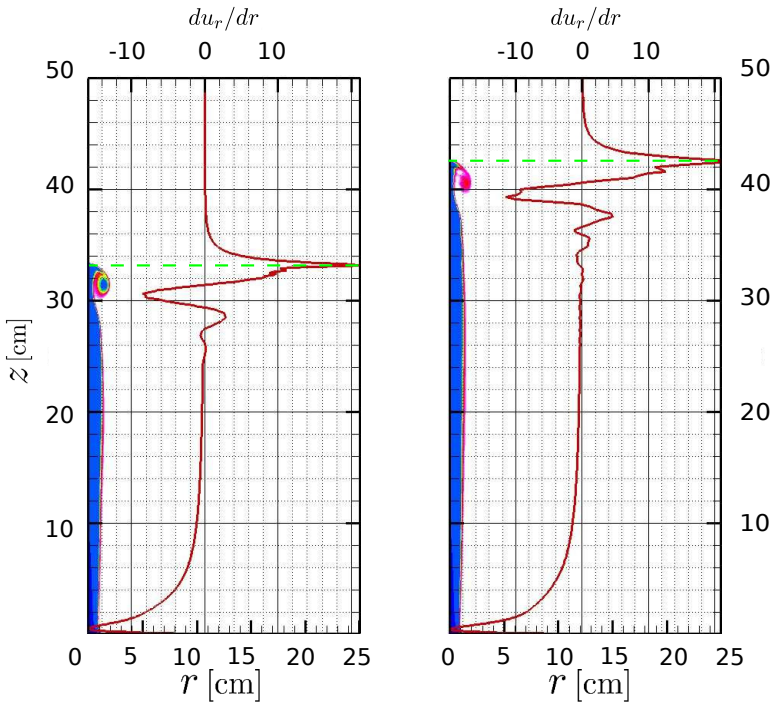

Figure 5.4: Plume's height estimation: stagnation point criterion, (Mesh 4). 2D iso-contour of the helium mass fraction superposed under the axial profile of du_r/dr. Left: $t = 0.72$ s, right: $t = 0.9$ s.

We can clearly note that the axial position of the maximum du_r/dr is situated a the same height with the top-head of the plume (green dashed line)

- **Inflection point criterion:**

We propose this criterion following the behavior of the u_z axial profile (along the jet axis). In fact, an inflection point is always observed just before the velocity profile decays smoothly to zero and before the plume impacts the top ceiling. This issue is illustrated in figure 5.5 by considering 4 instantaneous axial profiles before the plume-ceiling impact (respectively at times $t = 0.3$, 0.5, 0.7 and 0.9 seconds, mesh 4).

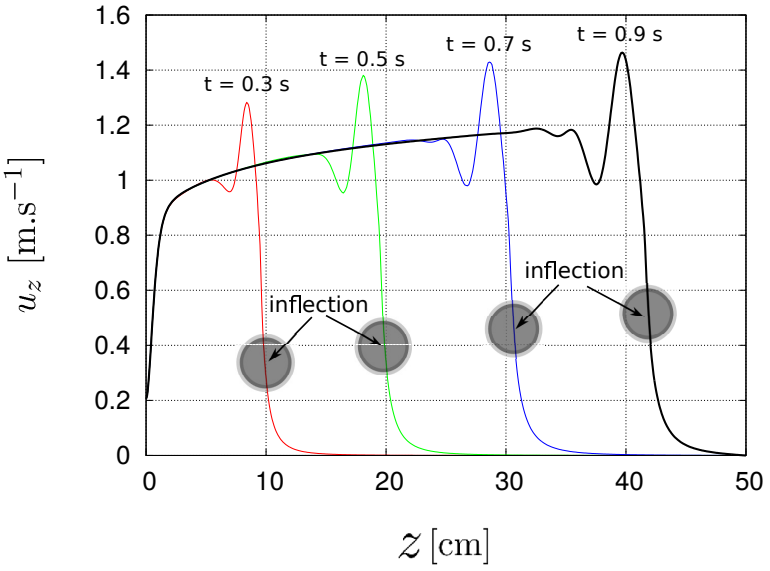

Figure 5.5: Illustration of the predicted inflection point on the axial velocity profiles at four time instants respectively $t = 0.3$, 0.5, 0.7 and 0.9 seconds (mesh 4).

We claim that H_P is equivalent to the axial position of the inflection point and thus expressed mathematically as

$$H_p = \text{vertical position } z \text{ of } \left\{ \left. \frac{d^2 u_z}{dz^2} \right|_{r=0} = 0 \right\}. \tag{5.4}$$

To illustrate on this issue, we consider the axial variation of du_z/dz superposed over the iso-contour plot of helium mass fraction at two time instants $t = 0.72$ and 0.9 seconds on a simulation performed with mesh 4 (figure 5.6).

We can clearly note that the axial position of the top-plume's head is in good agreement with the algebraic minimum of the du_z/dz axial profile. This position is thus the position of the observed inflection point.

At this stage, we can say that the first aim is reached as far as the inflection point criterion is pointing on the axial position of the plume's top-head. We then move towards reaching the

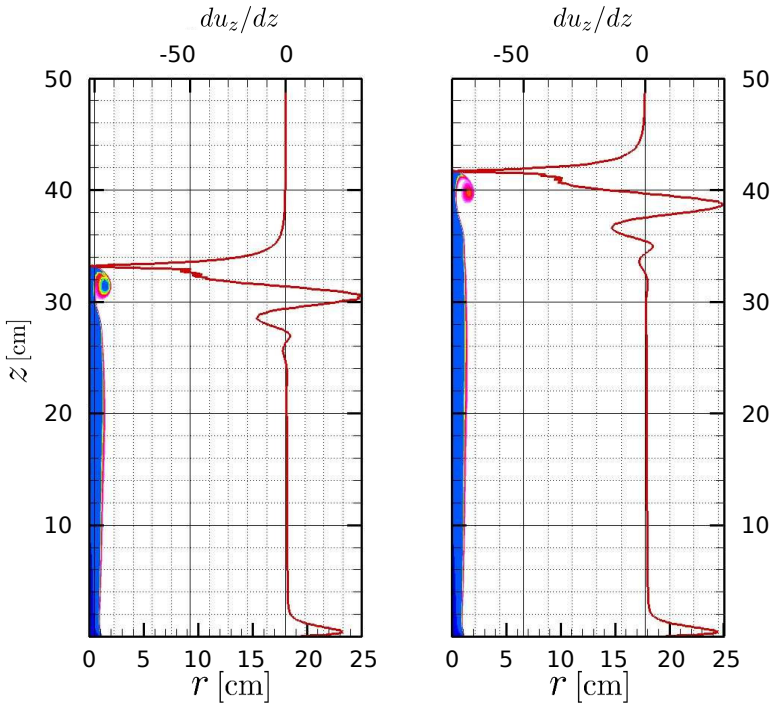

Figure 5.6: Plume's height estimation: inflection point criterion, (Mesh 4). 2D iso-contour of the helium mass fraction superposed under the axial profile of du_z/dz. Left: $t = 0.72$ s, right: $t = 0.9$ s.

second goal where we apply the three criteria over the four meshes to study the grid influence (convergence).

5.1.1 Grid influence

The plume's height H_P, defined by the three criteria, has been evaluated at different time instants and with the four meshes. The results are summarized in table 5.2.

We can clearly note that the values obtained with both stagnation and inflection points criteria are almost identical for meshes 3 and 4. It is important to emphasize at this stage that a first order linear interpolation has been employed to predict the axial position defined from equations (5.3) and (5.4). This is not the case with the first methodology (threshold criterion) where the value of H_P denotes the axial position of the control volume center where $Y_1 = \varepsilon_{Y_1}$.

However, it can be stated that the values of H_P predicted by all criteria show satisfactory convergent results at mesh 3. This is illustrated in figure 5.7 by the H_P error evolution, relative to the finest mesh (mesh 4), at $t = 0.998$ s.

The curve devoted to the threshold criterion decays from about 1.7% (mesh 1) to 0.25% (mesh

		Time t [s]	Plume's height H_P [cm]		
			Threshold	**Stagnation**	**Inflection**
Mesh 1	**130 x 260**	0.384	14.9249156	14.6933834	14.4629800
		0.600	25.3801900	25.3802156	25.1124452
		0.792	36.7068615	36.7065039	36.7065034
		0.998	48.3312440	48.3308424	48.3308430
		1.032	49.9475000	49.8414193	49.7342514
Mesh 2	**195 x 390**	0.384	14.7400130	14.4330798	14.4330791
		0.600	25.2470310	25.0687207	25.0687211
		0.792	36.4230086	36.2644751	36.2644759
		0.998	47.8311824	47.7421383	47.7421380
		1.032	49.7521238	49.7519627	49.7519622
Mesh 3	**260 x 520**	0.384	14.7635178	14.4181852	14.4181852
		0.600	25.1805553	24.9132605	24.9132608
		0.792	36.1613601	36.0418300	36.0418305
		0.998	47.6393167	47.5031985	47.5031985
		1.032	49.6522678	49.5973219	49.5973217
Mesh 4	**325 x 650**	0.384	14.6851588	14.4181853	14.4181852
		0.600	25.1407034	24.9132606	24.9132607
		0.792	36.0993084	36.0418302	36.0418300
		0.998	47.5224616	47.5031984	47.5031987
		1.032	49.5916558	49.5973217	49.5973218

Table 5.2: Comparison of the approximated plume height H_p at different time instants with the three different criteria.

3). However, the two other curves devoted to the stagnation and inflection points criteria are rather superposed and decay from 1.7% (mesh 1) to converge finally with mesh 3.

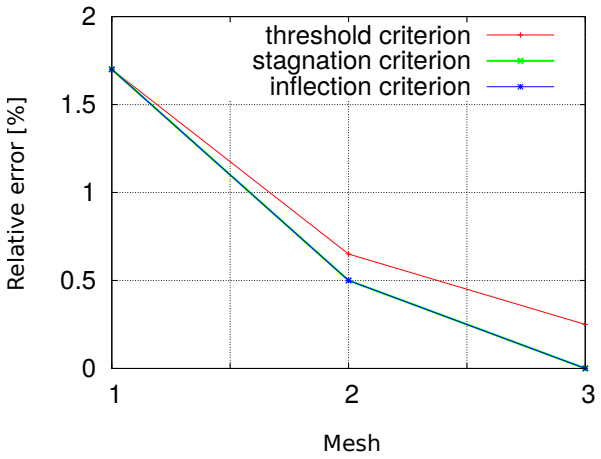

Figure 5.7: Instantaneous error convergence of H_P relative to mesh 4 ($t = 0.998$ s): comparisons with the three criteria.

And here we can say that the second goal is reached. Mesh 3 is required to converge on the plume's internal characteristics in its laminar starting flow (before the top ceiling impact). This convergence has been justified by the three criteria.

At the end of this convergence study, it can be stated that the new proposed methodology is in good agreement with existing stagnation point criterion from [DLT+11]. From the evolution of H_P predicted with these two criteria, the plume is assumed to impact the top ceiling at $t = 1.034$ s (compared to 1.06 s with the threshold criterion).

Mesh 3 is sufficient for attaining convergence on H_P in its laminar rising stage. However, the mesh refinement (mesh 4) can give a slight improvement of the spatial approximation inside the plume's head. This is illustrated in figure 5.8 by the instantaneous helium volume fraction X_1 iso-contours ($X_1 = \rho Y_1/\rho_{\text{inj}}$) for a zoomed portion of the domain at $t = 0.71$ s.

Thus, mesh 4 is selected as a reference mesh which is necessary for reproducing convergent results.

5.1.2 Flow description

In the first stage of the plume rise and before the top impact, a laminar starting plume is observed where its characteristics (well developed conduit and a head) are clearly visualized. A detailed study of laminar starting plumes can be reviewed from a paper of Rogers and Morris in [RM09]. The results of [RM09] were was also reproduced by Tran [Tra13].

We illustrate the flow pattern at different time snapshots by the helium volume fraction X_1 in figure 5.9. In figure 5.10, we can clearly see the orientation of the flow developed in a vortex ring. This recirculation is responsible for the head shape creation.

Afterwards, the plume impacts and starts to spread along the top ceiling. Before impacting

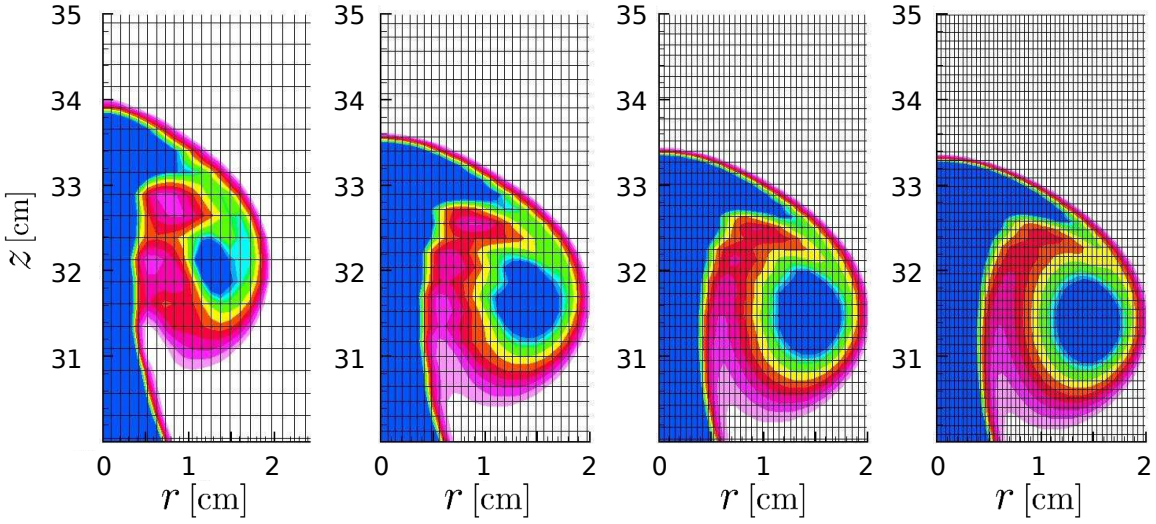

Figure 5.8: Numerical resolution quality in a zoomed region at a fixed time instant $t = 0.71$ s: plume's head illustrated by the helium volume fraction X_1 iso-contours. Left to right: respectively mesh 1 to mesh 4.

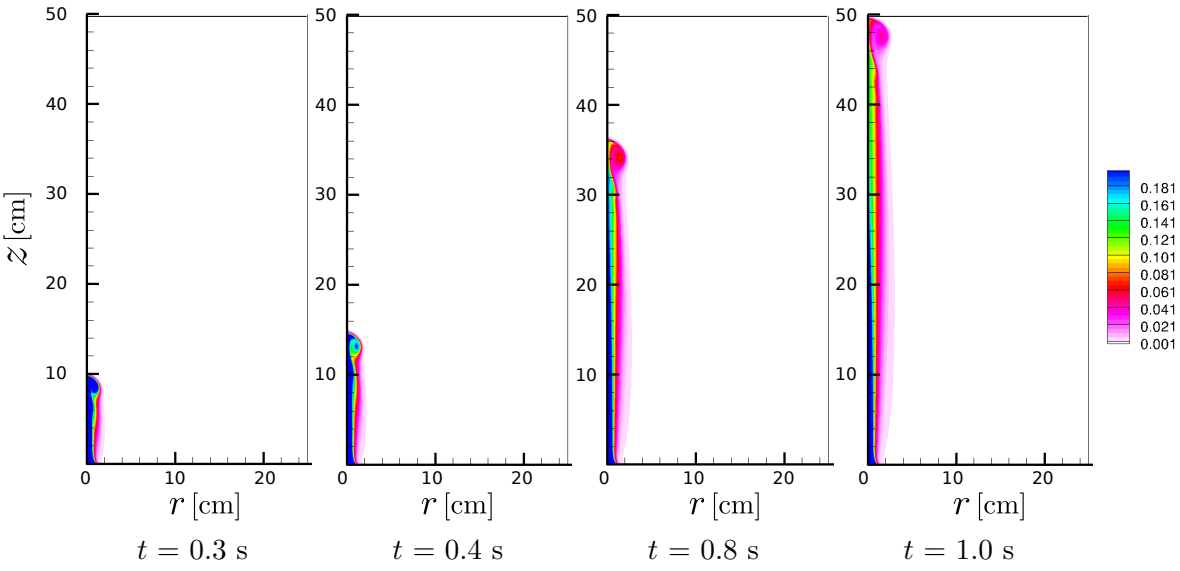

Figure 5.9: Instantaneous helium volume fraction X_1 time evolution before the ceiling-impact: configuration AX1, mesh 4.

again the right wall from the top, a recursive phenomenon is observed. Each rotating flow forms a dipole at the extremity that entrains ambient fluid inside the spreading layer and a new dipole is formed. This issue is illustrated in figure 5.11 by instantaneous helium volume fraction X_1 iso-contours at four different time instants where the dipole formation is noted.

The simulation carried out on mesh 4 have been performed for physical time $t = 40$ s. As time advances, the representation of the filling box phenomenon is clearly seen. We plot in

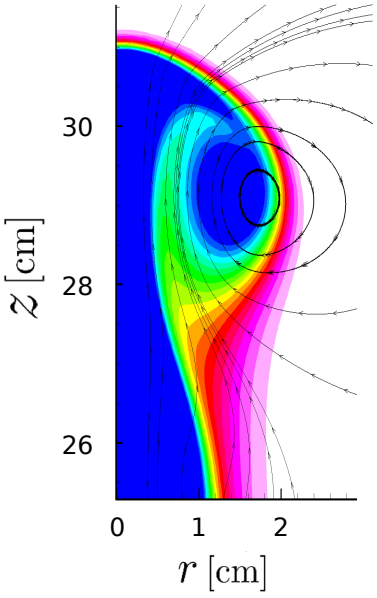

Figure 5.10: Flow orientation responsible in the development of the head (vortex ring): instantaneous helium volume fraction X_1 with velocity streamlines at $t = 0.65$ s, configuration AX1, mesh 4.

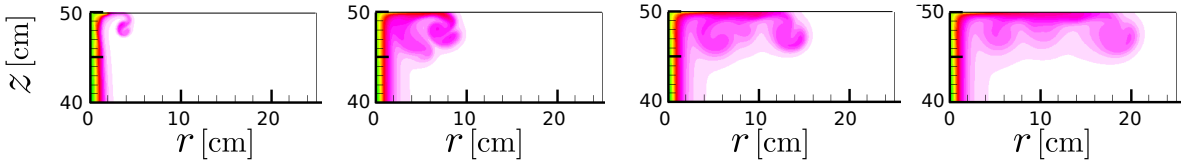

Figure 5.11: Time evolution of the instantaneous helium volume fraction X_1 iso-contours near the top ceiling after the impact: configuration AX1, mesh 4. Left to right: respectively $t =$ 1.14, 2, 3 and 4.1 seconds.

figure 5.12 the contour lines of X_1 to illustrate on the thickening helium stratified layer.

5.1.3 Global mass validation

To validate the results and to illustrate on the accuracy of the resolution, the evolution of the total mass of helium $\mathcal{M}_{\text{He}}$ in the first 5 physical seconds is plotted on the same graph with the mass injected and that leaving the cavity from the vent (figure 5.13).

As expected, we can clearly note the linear evolution of $\mathcal{M}_{\text{He}}$. As far as we are placed in a filling box phenomenon, helium requires a lot of time to reach the bottom vent. This is illustrated by the null values of helium mass leaving the cavity from one side, and the accordance between the injected and total mass on the other hand. This behavior has been

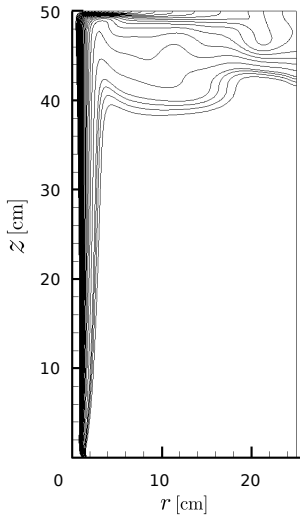

Figure 5.12: Layers of helium stratification at an instantaneous time instant: X_1 contour lines [0.01:0.003:0.1], configuration AX1, mesh 4.

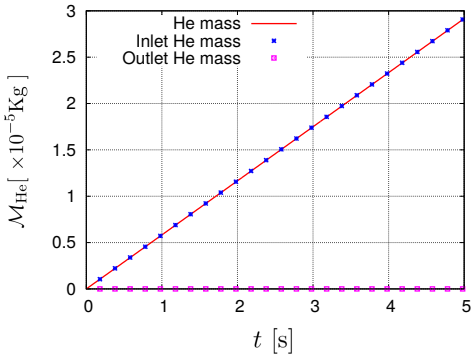

Figure 5.13: Global He mass evolution in the first 5 seconds as a function of He entering and leaving the cavity: configuration AX1, mesh 4.

well recorded in [Tra13].

The balance of the integrated species conservation equation is presented in figure 5.14, where a trapizoidal rule has been employed for the time integration. Global mass flux balance is of order 10^{-9}, which is rather small.

5.2 Inlet boundary investigations

Configuration AX1 coupled with the prescribed boundary conditions is able to predict well the desired flow as we observed in subsection 5.1.2. We have tried to increase successively the injection flow-rate Q but unfortunately the numerical problems rise where the Poisson equation poorly converges, although from the first time iterations. We claim that this issue rises due to both, numerical and/or physical problems.

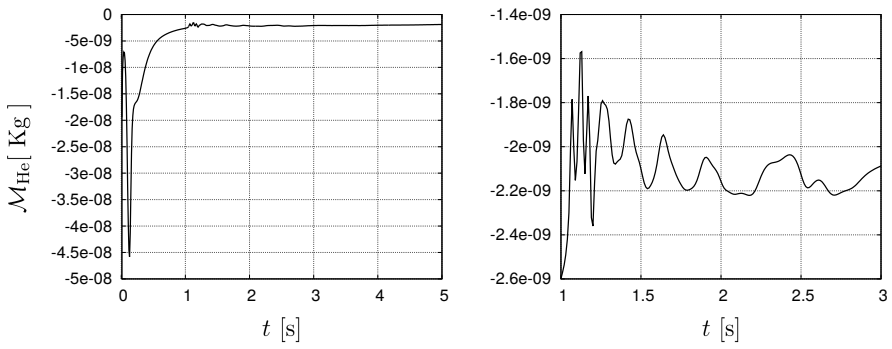

Figure 5.14: Integrated helium conservation equation balance for configuration AX1, mesh 4. Left: first 5 seconds, right: zoomed between 1 and 3 seconds.

Numerically speaking, the high and stiff gradient of the axial velocity u_z just at the first cell above the inlet boundary $\partial\Omega_i$ can cause this algorithm divergence (failure). With small injection velocities as the previous convergent case, the velocity gradients are small and the flow is basically generated by the concentration gradients (diffusion), without problems with the Poisson convergence.

From a second point of view, let us consider the species conservation equation (3.26) integrated over the complete domain Ω

$$\underbrace{\int_\Omega \frac{\partial \rho Y_1}{\partial t} d\Omega}_{\text{helium mass variation}} \underbrace{- \int_{\partial\Omega_i} \rho Y_1 u_z d\partial\Omega_i}_{\text{inlet convective flux}} + \underbrace{\int_{\partial\Omega_o} \rho Y_1 u_r d\partial\Omega_o}_{\text{outlet convective flux}} = \underbrace{- \int_{\partial\Omega_i} D\rho \frac{\partial Y_1}{\partial z} d\partial\Omega_i}_{\text{inlet diffusive flux}}. \tag{5.5}$$

Note that there is no contribution of the outlet diffusion flux in equation (5.5) as far as a homogeneous Neumann boundary condition has been prescribed on $\partial\Omega_o$.

In fact, equation (5.5) defines the balance in the domain between what is injected on the one hand and between both, the mass variation and what leaves the domain on the second hand. We concentrate at this level on the injection contributions.

Pure helium is injected from $\partial\Omega_i$ with a fixed flow rate. Defining the injection convective and diffusive fluxes respectively as

$$\mathscr{F}_C = \int_{\partial\Omega_i} \rho u_z Y_1 d\partial\Omega_i \quad \text{and} \quad \mathscr{F}_D = - \int_{\partial\Omega_i} \rho D \frac{\partial Y_1}{\partial z} d\partial\Omega_i, \tag{5.6}$$

the constant fixed total injection mass flux $\mathscr{F}$ can be decomposed as

$$\mathscr{F} = \mathscr{F}_C + \mathscr{F}_D, \tag{5.7}$$

which is in balance with outlet flux and the helium mass variation in the entire domain Ω.

The balance formulation expressed in equation (5.7) is valid **globally** by integrating along the whole injection surface. However, let us look more locally at the surface of injection. On

the axial position, the concentration gradient is almost null and thus the flux is dominant by convection with the greatest positive velocity value. Besides, on the extremities of pipe, the concentration gradient $\partial Y_1/\partial z$ can be significantly dominant. Imposing a constant $\mathscr{F}$ may requires negative velocity values in order to balance the fluxes.

In the numerical simulations, the flow at the inlet surface $\partial\Omega_i$ where helium is injected into the cavity is only subjected to a fixed convective flux, as far as the diffusion is cut off by imposing numerically a zero diffusion coefficient at the first cell. Thus, the velocities at this surface are always positive (parabolic distribution) and thus, pure helium leaves exits pipe all along the injection surface. From the previous demonstration, it can be stated that this issue is not completely physical since it does not take into account probable negative velocity values at the pipe extremities due to the diffusion attribution from this region.

5.2.1 Modified inlet velocity

As a first approach, we look toward imposing an inlet velocity profile which is able to balance the total mass flux $\mathscr{F}$ within the system.

Assume that helium is injected from a mass point source S_m by pure convective flux (D=0) into a pipe as sketched in figure 5.15 and denoted by Ω_p. The boundary of the pipe domain Ω_p can be expressed as

$$\partial\Omega_p = \partial\Omega_i \cup \partial S_m \cup W_{r_1} \cup W_{r_2}, \tag{5.8}$$

where W_{r_1} and W_{r_2} are solid walls.

By integrating over Ω_p the velocity constraint presented in equation (3.32), we can obtain the correct velocity field which satisfies the volume balance and when imposed at the boundary $\partial\Omega_i$, it takes into account both $\mathscr{F}_C$ and $\mathscr{F}_D$.

At the walls, a no slip-boundary condition with zero diffusion is imposed. Thus, no contribution of these boundaries is attributed when the integration is performed. We assume that $d\partial\Omega_i = d\partial S_m = 2\pi r\ dr$.

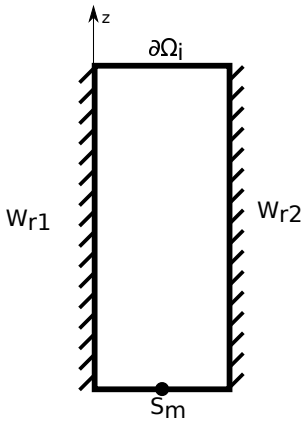

Figure 5.15: Pipe boundaries.

The integration follows

$$\int_{\Omega_p} \frac{\partial}{\partial x_i} u_i d\Omega_p = \xi \int_{\Omega_p} \frac{\partial}{\partial x_i} \left(D\rho \frac{\partial Y_1}{\partial x_i} \right) d\Omega_p, \tag{5.9}$$

with the constant ξ defined in equation (3.33).

Applying the Green-Ostrogradsky's (divergence) theorem and using the decomposition (5.8),

we obtain

$$\int_{\partial\Omega_i} u_z(r,t)d\partial\Omega_i - \int_{\partial S_m} \overline{u}_{\text{inj}} d\partial S_m = \xi \int_{\partial\Omega_i} \rho D \frac{\partial Y_1}{\partial z} d\partial\Omega_i, \tag{5.10}$$

which leads to

$$2\pi \int_0^R \Big(u_z(r,t) - \overline{u}_{\text{inj}}\Big) r dr = 2\pi\xi \int_0^R \rho D \frac{\partial Y_1}{\partial z} r dr, \tag{5.11}$$

where R is the radius of the injection pipe. For simplicity, we assume that a top-hat constant profile u_z^T is to be imposed at $\partial\Omega_i$. Thus equation (5.11) simplifies to

$$u_z^T(t) = \overline{u}_{\text{inj}} + \frac{2\xi}{R^2} \int_0^R \rho D \frac{\partial Y_1}{\partial z} r dr. \tag{5.12}$$

A parabolic profile is finally prescribed at $\partial\Omega_i$ using $u_z^T(t)$ as

$$u_z^P(r,t) = u_z^T(t)\Big(- \frac{2r^2}{R^2} + 2\Big). \tag{5.13}$$

The new velocity profile has been prescribed at the inlet boundary of configuration AX1, mesh4. At the end of each iteration, the gradient of the helium mass fraction is calculated and thus the velocity is updated (equation (5.13)). At the end of 500 consecutive iterations ($t \approx 0.05$ s), the profile converges due to the constant gradient at the inlet. We illustrate in figure 5.16 the evolution of the imposed velocity profile at $\partial\Omega_i$.

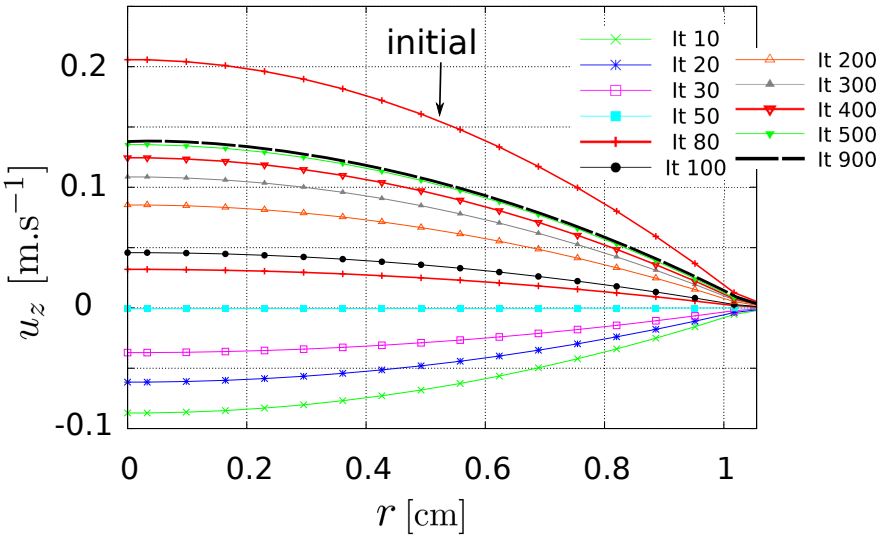

Figure 5.16: Prescribed injection velocity profile at $\partial\Omega_i$ versus the iteration number It: convection-diffusion fluxes attributes, configuration AX1, mesh 4.

We can observe from the evolution of u_z that the values in the first iterations (till iteration It = 50) are negative. This means that the diffusion flux $\mathscr{F}_D$ is more significant than $\mathscr{F}_C$ at this time, which is logical due to the stiff Y_1 gradients. At It = 50, the velocity is almost null

due to the balance of the convective-diffusive flow-rates.

The magnitude of the velocities increase gradually with time until obtaining a convergent profile (dashed black line, figure 5.16).

An important key point at this level is to know if the modified injection velocity is physically consistent and corresponds to the real solution. From the evolution of the velocity profile (figure 5.16), we see that the convergent values remain smaller to what has been initially imposed; maximum value reached at the plume axis is 0.14 m.s^{-1} compared initially to 0.206 m.s^{-1}. This discrepancy is due to the global (integral) treatment in the formulation (5.12) without taking into account the local balance. Thus, the effect of the stiff concentration gradients $\partial Y_1/\partial z$ at the extremities of the pipe is reduced by integrating with the null concentration gradients in the axial vicinity.

To reduce these discrepancies, we carried out a local modification on the injection profile by integrating equation (3.32) over each control volume of the inlet, taking into account the concentration diffusion in the radial direction. However, it has been figured out that the resultant profiles do not preserve the constant injection flow-rate from one iteration to another and thus require more detailed investigations. We thus follow a second approach from which we expect to reproduce the real physical behavior and obtain a velocity profile as a result from the resolution of the coupled system.

5.2.2 Meshed injection pipe

Basically, we consider to model the injection pipe in the computational domain (figure 5.3, left). Thus, a new computational domain (configuration AX2) is constructed. Using a horizontal immersed boundary (IB), a pipe of height $h = 5$ cm is modelled in the domain. Another vertical IB has been introduced to model the flow within the borders of the vent, whose height was chosen to be $z_{o_{\mathrm{AX2}}} = 5$ cm and placed at the bottom right wall (figure 5.3, right). The height and radial width of the interior cavity have been kept identical to those identified in configuration AX1; $H = 50$ cm and $R = 25$ cm.

Again, the injection flow-rate considered is $Q = 2$ Nl.min^{-1}. In order to reduce the sharp gradients of Y_1 at the boundary, the pipe has been filled with helium at the initial state following a smooth decreasing function, similar to the profile presented in figure 4.3. In the numerical simulation, the inlet boundary condition is prescribed at the bottom of the pipe (bottom inlet). The outlet boundary condition is prescribed at the outer surface of the vent to model the exchange between the cavity flow and the exterior. Injected fluid enters the cavity from the top of the pipe and thus the corresponding profiles at this level are obtained as a part of the solution. A mesh of same cell size order as mesh 4 has been generated. Again, the distribution of the nodes is uniformed along the pipe and the vent. The distribution is generated by a hyperbolic tangent function elsewhere (equation (5.1)).

The simulation converges and an expected regime is observed where helium stratification layers builds up. We focus our interest on the top inlet. We observe that approximately for

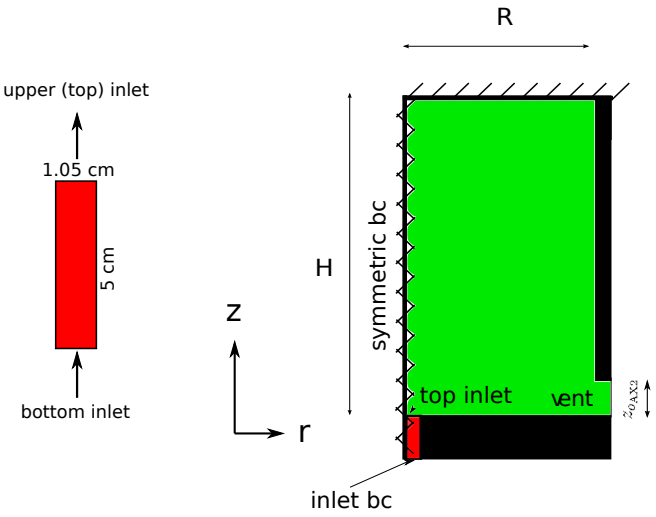

Figure 5.17: Left: meshed pipe description, right: schematic representation of the one vented cavity with a meshed injection pipe: configuration AX2. Green color is used to denote the cavity while the red color denotes the injection pipe. Black areas correspond to the employed immersed boundaries (IB) (non-fluid zones).

$t \approx 3$ s, a steady state solution in the pipe is attained and negative velocities are recorded at the extremity of the pipe. In accordance with the negative velocities, concentration gradients are more significant at the edge of the pipe than in the vicinity of the axis (figure 5.18).

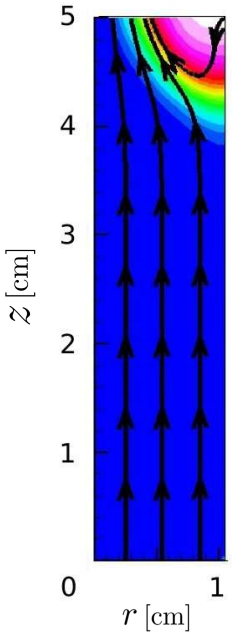

Figure 5.18: A pipe steady state solution: helium volume fraction X_1 iso-contours [0:0.1:1] with velocity streamlines, $Q = 2$ Nl.min^{-1}, configuration AX2.

The evolution of the velocity u_z profiles along the upper inlet in the radial direction is plotted

as a function of the iteration number It in figure 5.19. We note clearly that negative velocities are required in the first iterations (figure 5.19,left). However the distribution is not parabolic, compared to what we prescribed in subsection 5.2.1.

Marching in time, the velocity magnitude increase and the profiles starts to take a similar form with maximum velocity of 0.58 m.s^{-1} situated at the axial axis. Negative velocities appear at the extremity of the tube surface, until convergence (figure 5.19, right). On the same figure, we plot the converged parabolic velocity distribution obtained by the first approach; modified inlet velocity to take into account both convective and diffusive contributions (thick dashed black line). Two basic differences are noted: the profile distribution (positive and negative velocities) and the magnitude of the maximum velocity. We claim obviously that the results obtained by modelling the tube in the computational domain are more physical and this approach is to be followed in the sequel of the thesis.

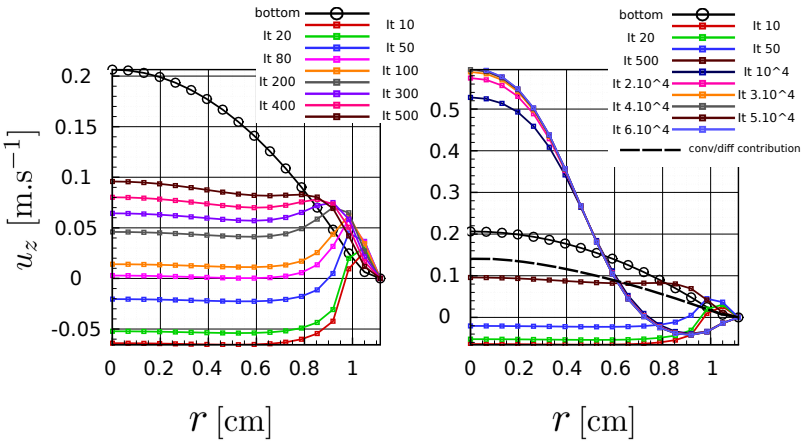

Figure 5.19: Evolution of the axial velocity u_z at the top of the injection pipe as a function of the iteration number (It), $Q = 2$ Nl.min^{-1}, configuration AX2. Left: pipe transient solution, right: variation until achieving a steady state solution. Thick black dashed line corresponds to the converged velocity profile obtained by the approach presented in subsection 5.2.1.

Similarly, the evolution of the helium X_1 profiles is illustrated in figure 5.20. We note that imposing a flat profile at the bottom inlet leads to a convergent profile at the top in several iterations. The observed X_1 values at this position take almost a Gaussian bell distribution.

Several numerical simulations have been carried out for successively increasing flow-rates to approach a jet configuration. No numerical issues have been recorded and the algorithm perfectly converge. Numerical results for a case of $Q = 6$ Nl.min^{-1} will be presented in the next section.

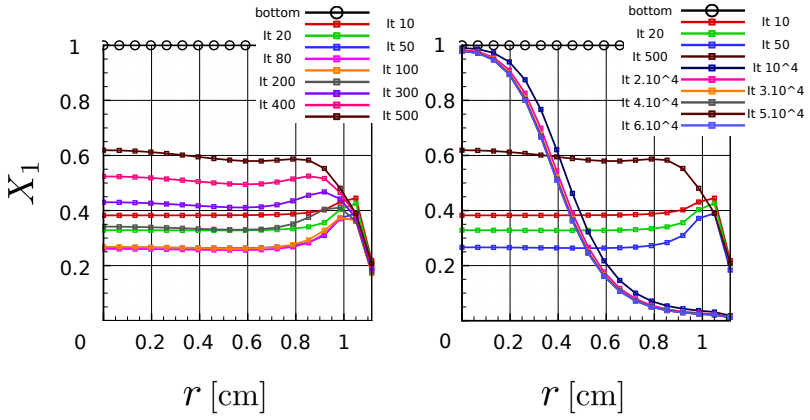

Figure 5.20: Evolution of helium volume fraction X_1 at the top of the injection pipe as a function of the iteration number (It), $Q = 2$ Nl.min^{-1}, configuration AX2. Left: pipe transient solution, right: variation until achieving a steady state solution.

5.3 Influence of modelling an exterior domain in the computations

At this level, we move to focus on our main objective: flows in two vented cavities. We consider two computational domains, respectively configurations AX3 and AX4.

The two vents in configuration AX3 are of same height $z_{o_{\mathrm{AX3}}} = 5$ cm and are placed on the same wall to the right top and bottom. Similar to AX2, two IB's are employed to model the pipe and flow inside the width of the vent within the computational domain (figure 5.21, left).

AX4 is proposed to study the influence of modelling an exterior region, situated at the right of the vents, in the computational domain. We look basically to simulate, in addition to the pipe and cavity , the flow in the exterior region so that the outlet boundary conditions are moved away from the vents. The interior cavity is identical to that of AX3. The exterior domain takes the form of a chimney with two openings respectively at the bottom and top, with a solid wall to the right. The radial dimension of the chimney is L_r and the axial vertical height is $H + 2L_z$ (figure 5.21, right).

The key point is that the outlet boundary conditions are prescribed directly at the exterior vent surface in configuration AX3, while at the openings of the chimney in AX4. A complete numerical description of both configurations are summarized in table 5.3.

In the common region, the mesh employed for AX3 and AX4 is identical. At the interior of the cavity, the order of the mesh cell size reads the same as that produced by mesh 4. However, in order to avoid long simulations, the size of the cells along the pipe and vents have been relaxed, as far as the flow is completely laminar in these regions. The quality of the mesh employed in configuration AX4 is illustrated in figure 5.22.

Two injection flow-rates are considered; $Q = 2$ and 6 Nl.min^{-1}. In the second case ($Q = 6$

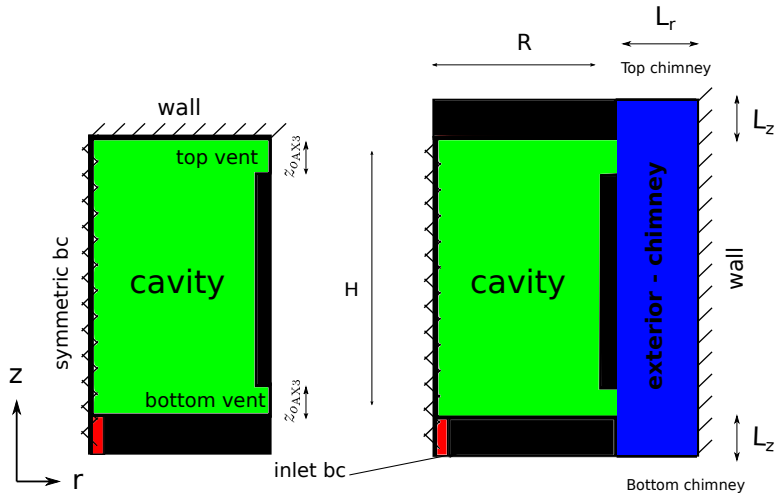

Configuration AX3 Configuration AX4

Figure 5.21: Schematic representation of the two vented cavities: configurations AX3 and AX4. Green color is used to denote the cavity while, red color denotes the injection pipe and blue denotes the exterior domain. Black areas correspond to the employed immersed boundaries (IB) (non-fluid zones).

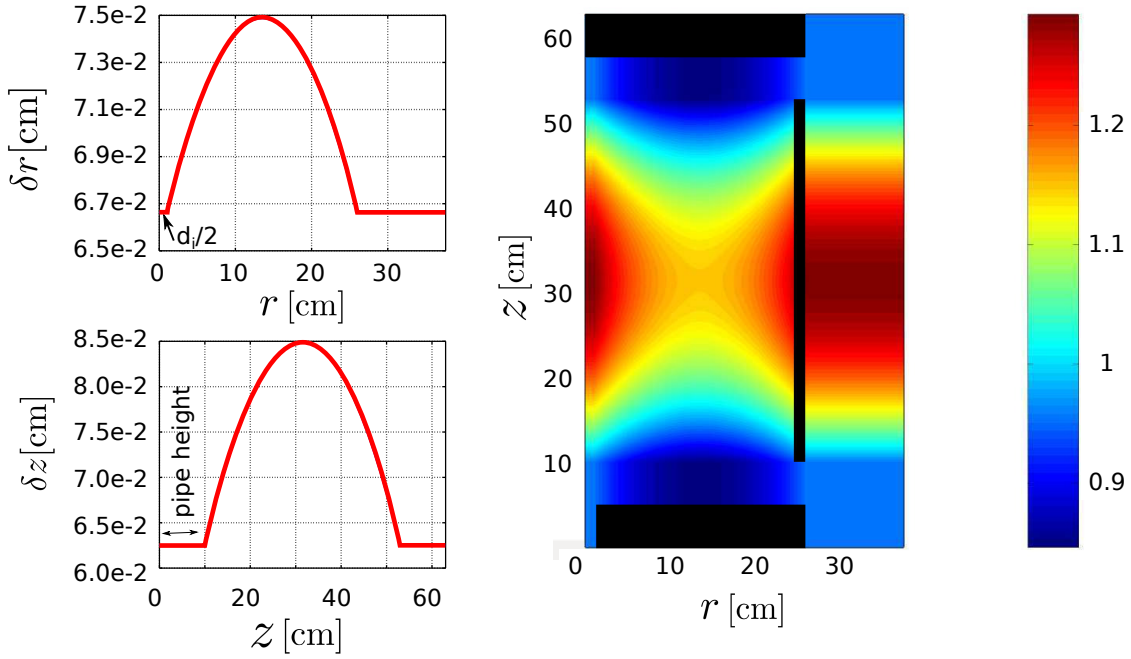

Figure 5.22: Non-uniform mesh quality, configuration AX4. Left-top: radial step δr, left-bottom: axial step δz, right: aspect ratio $\delta z/\delta r$.

Nl.min^{-1}), the averaged injection velocity $\overline{u}_{\text{inj}}$ with the same pipe injection surface area is equivalent to ≈ 0.306 m.s^{-1}. Thus, the injection dimensionless parameters read as Re_{inj}=56 and $\text{Ri}_{\text{inj}} = 13$ (approaching a buoyant jet configuration).

Configuration	H [cm]	R [cm]	IB [$r_{\mathrm{IB}} \times z_{\mathrm{IB}}$ cm^2]	Lr [cm]	Lz [cm]	**Cell number**
AX3	53	26.05	**bottom:** 26.05 x 5 **vertical:** 1.05 x 43			384 x 800 = 307,200
AX4	53	26.05	**bottom:** 26.05 x 5 **vertical:** 1.05 x 43 **top:** 27.1 x 5	10.5	5	544 x 880 = 478,720

Table 5.3: Configurations Ax3 and AX4 numerical set-up: dimensions and mesh size.

A time step $\delta t = 5 \times 10^{-5}$ s is imposed during the simulation. Its value has been identified from the minimum values of the previous simulations where both convective and diffusive stability criteria are satisfied. 210 seconds of physical time has been performed for configuration AX3 while 150 seconds only for AX4. The simulations have been carried out on the LIMSI–CNRS local cluster with 6 openMP shared threads. Computational cost per thread is about 11 days for AX3 , while 18 days for configuration AX4.

5.3.1 In-dependency of the injection and jet axis

The flow inside the tube converges towards a steady state solution approximately in the first 3 physical seconds. It has not been observed any influence of the different configurations AX3 and AX4 on the profiles at the top of the inlet pipe. The profiles are only dependent on the injection flow-rate Q, which is expected as far as the properties change from those of a pure plume towards a buoyant jet. In figures 5.23, 5.24 and 5.25 , the steady state profiles of Y_1, ρ, u_z at the top inlet are respectively depicted.

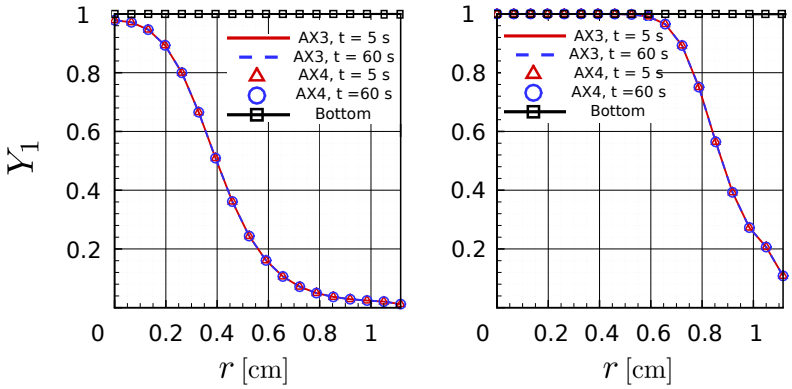

Figure 5.23: Steady state Y_1 profiles at the top inlet for configurations AX3 and AX4. Left: $Q = 2$ Nl.min^{-1}, right: $Q = 6$ Nl.min^{-1}.

From the profiles of the helium mass fraction Y_1 (confirmed by the profiles of ρ), we see that increasing the injection flow-rate changes the profiles at the top inlet from a Gaussian to an almost flat profile in a great portion of the tube. These profiles are well reported in the literature and are situated in the zone of flow establishment (ZFE), basically in the potential core of plumes and jets as described by Lee and Chu in [LC03].

Regarding the axial velocity profile, we note that increasing the volumetric flow-rate decreases the magnitude of negative velocities as far as it reduces the vertical concentration gradients and the flow becomes more dominant by inertia. However, it is important to ensure that after integrating along the meshed pipe, the resultant mass flow-rate is satisfied in all cases.

Similarly, the flow along the jet axis establish a steady state solution in all cases at the end of the first 4 seconds. The steady state solution is illustrated by the axial Y_1 profile in figure 5.26. Again, the profiles show that the solution along plume axis is independent of the employed

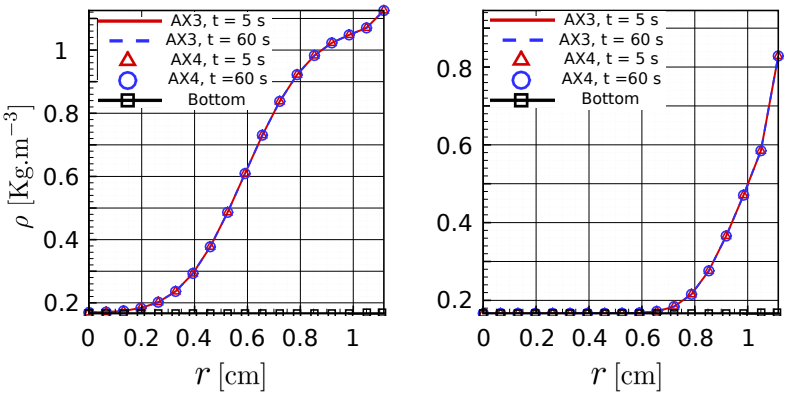

Figure 5.24: Steady state mixture density ρ profiles at the top inlet for configurations AX3 and AX4. Left: $Q = 2$ Nl.min^{-1}, right: $Q = 6$ Nl.min^{-1}.

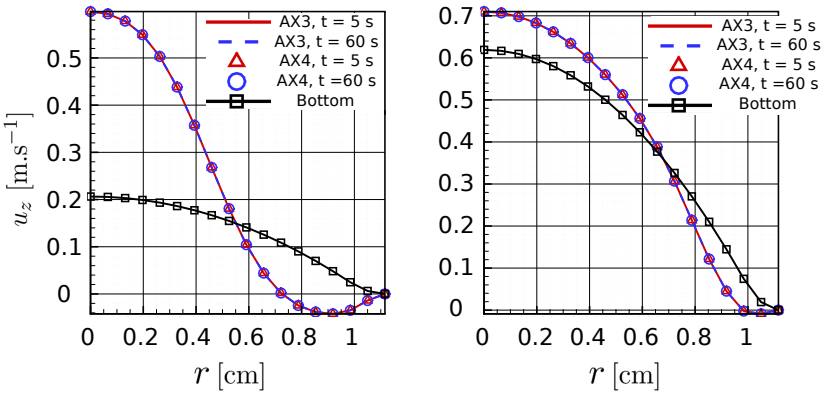

Figure 5.25: Steady state axial velocity u_z profiles at the top inlet for configurations AX3 and AX4. Left: $Q = 2$ Nl.min^{-1}, right: $Q = 6$ Nl.min^{-1}.

configuration and is however only dependent on the considered Q. The bigger the injection flow-rate is, the smaller the concentration gradients along the axis are.

In what follows, we present the influence of taking into account an exterior domain. We present firstly the influence on the general flow pattern inside the cavity.

5.3.2 The influence on the flow pattern inside the cavity

An instantaneous flow pattern ($t = 110$ s) visualized in both configurations is illustrated in figures 5.27 and 5.28 for both flow-rates. The velocity streamlines have been superposed over the iso-contours of the helium volume fraction to illustrate on the orientation of the flow. The employed configuration is the major parameter that influences the flow.

In configuration AX3 (figure 5.27), air enters from the bottom vent and entrains with the

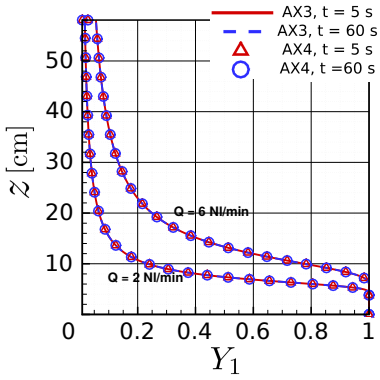

Figure 5.26: Steady state helium mass fraction Y_1 axial profile along the plume's axis for configurations AX3 and AX4.

mixture inside the cavity. With the help of the buoyant forces, the significant mixing phenomenon occurs at the top of the cavity, from which a part of the mixture leaves from a thin layer situated at the top of the upper vent. A reversal flow is noted at the top vent where exterior fluid enters from the lower part of the vent and leaves again from the top as a mixture. The descending stratification layers of X_1 covers approximately two times the height of the vent $z_{o_{\mathrm{AX3}}}$ (recall figure 5.21).

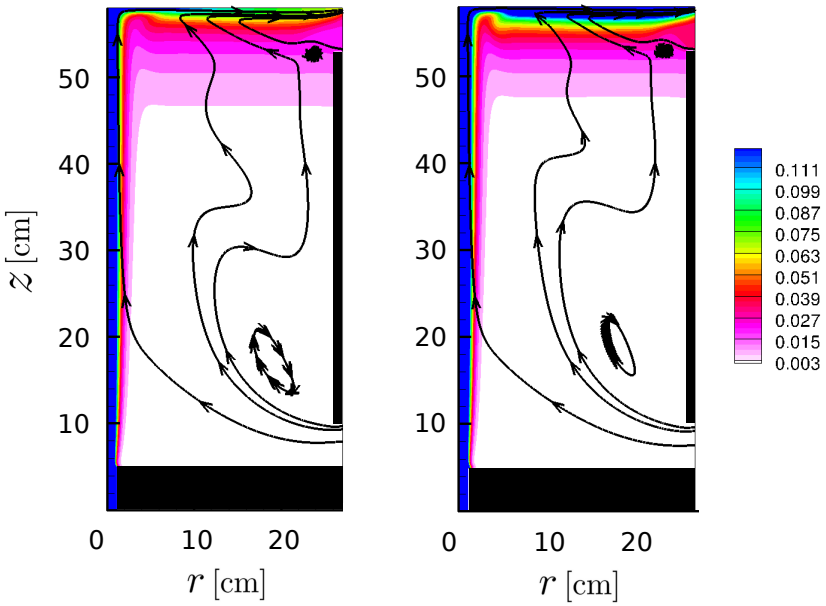

Figure 5.27: Instantaneous flow pattern by the X_1 iso-contours and velocity streamlines at $t = 110$ s for configuration AX3. Left: $Q = 2$ Nl.min^{-1}, right: $Q = 6$ Nl.min^{-1}.

The flow pattern in the lower part of configuration AX4 (figure 5.28) is almost similar to that of AX3 where air enters from outside and entrains with the mixture. However, significant discrepancies are reported in the uppert part of the cavity, when compared with the flow

pattern of configuration AX3. Although the mixed fluid leaves also from a thin layer at the top, the level of the descending stratification layers reaches almost the mid-height of the cavity and thus affects the flow pattern in the region near the top vent.

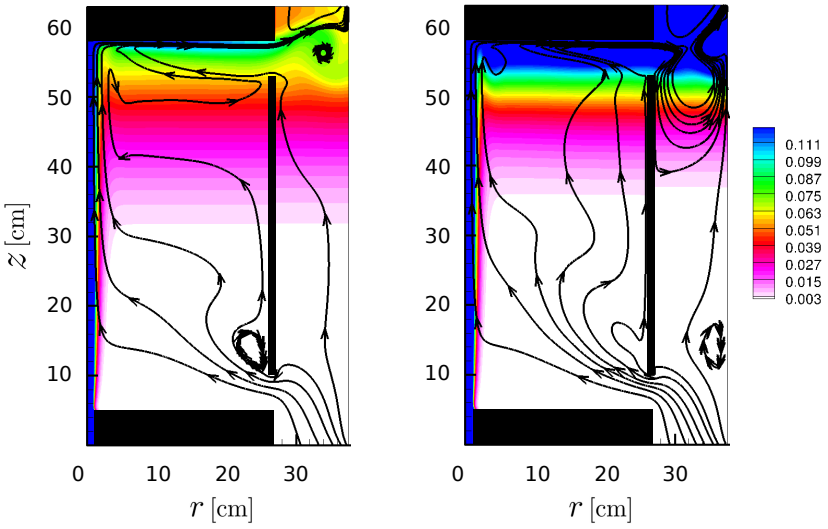

Figure 5.28: Instantaneous flow pattern by the X_1 iso-contours and velocity streamlines at $t = 110$ s for configuration AX4. Left: $Q = 2$ Nl.min^{-1}, right: $Q = 6$ Nl.min^{-1}.

The flow pattern in the region near the top vent suggests that the chimney configuration (with a wall at the right) is probably blocking the exiting flow. It seems that the buoyancy forces at the top opening of the chimney are not strong enough to aspire the mixture outside the domain, where we note that the mixture is blocked inside the cavity and the exterior domain to build a stratified regime. The profiles of u_z along the bottom and top opening are presented in figure 5.29. For $Q = 2$ Nl.min^{-1}, the mixture leaves from a thin layer at the end of the top chimney's opening, while a different behavior is reported for the injection second flow-rate.

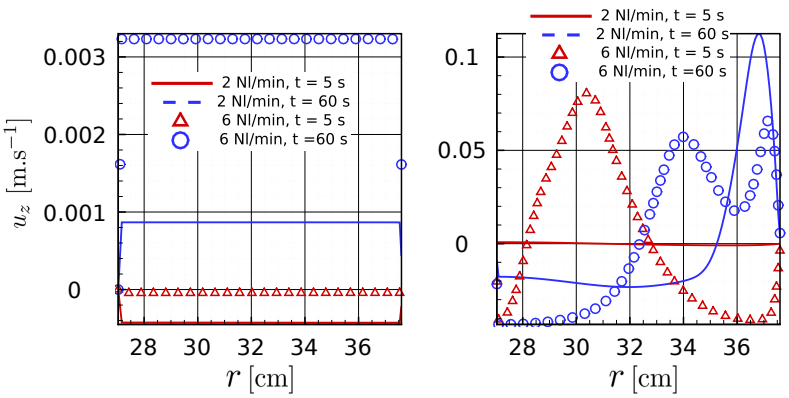

Figure 5.29: Radial profiles of the axial velocity u_z for configuration AX4 at $t = 5$ and 60 s. Left: bottom chimney opening, right: top chimney opening.

Several justifications on such observations can be drawn. A first probable reason is the reduced width of the chimney. In practice, as the fluid mixture approaches the top vent, it accelerates and an impact-jet phenomenon is observed with the chimney's wall at the right. In figure 5.30, we illustrate by X_1 iso-contours instantaneous snapshots the jet-impact behavior.

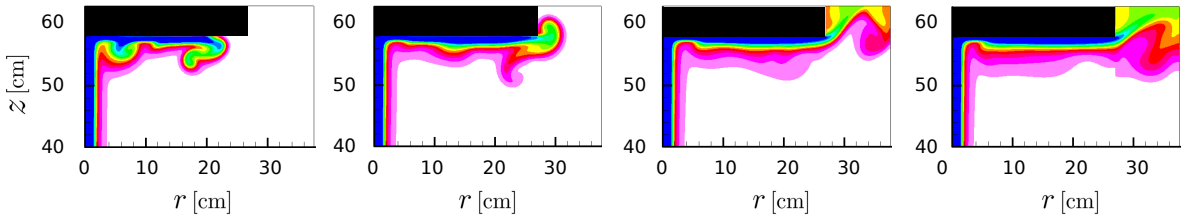

Figure 5.30: Evolution of the jet before impacting the solid wall of the chimney illustrated bu X_1 iso-contours: $Q = 6$ Nl.min^{-1}. Left to right: $t = 2$, 4, 6 and 8 seconds.

Before reaching the top vent, the flow pattern is similar to that described in the filling box phenomenon; formation of dipoles that entrain ambient fluid and spread all over the ceiling. As time advances, the plume approaches the vent, accelerates due to the aspiration phenomenon and tries to leave the domain from the top chimney opening ($t = 2$ and 4 seconds). To the reason of the reduced width of the chimney L_r, the plume impacts the chimney's right wall as seen at time $t = 6$ s (known as the jet-impact phenomenon). Afterwards, a recirculation zone is induced which blocks the exiting flow, and thus the mixture starts to form a stratified layer as seen at $t = 8$ s .

Another probable justification remains the issue of the physically good outlet boundary condition and the influence of the modelled configuration. This issue require further investigations.

For a global comparison, we calculate the total mass of helium inside the cavity. The time evolution of $\mathcal{M}_{\text{He}}$ is presented in figure 5.31 for all cases.

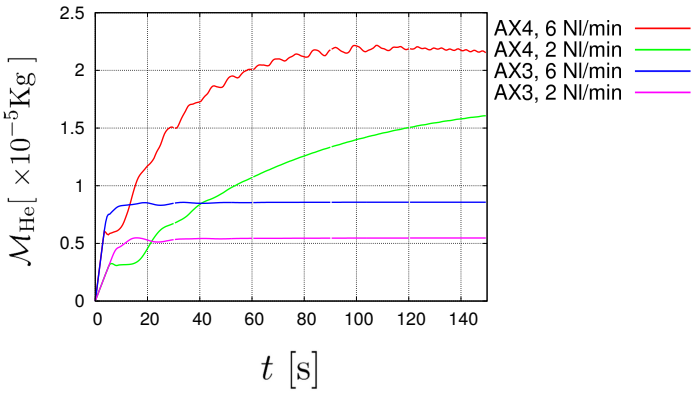

Figure 5.31: Time evolution of helium mass $\mathcal{M}_{\text{He}}$ inside the cavities of configurations AX3 and AX4 for both flow-rates.

In both cases, the greatest values of $\mathcal{M}_{\text{He}}$ are recorded with the greatest injection flow-rate $Q = 6$ Nl.min^{-1}. However, the profiles differs significantly with the different configurations. For both values of Q and without modelling an exterior region in the computational domain

(AX3), the mass increases almost linearly at first, enters in a short transition from which afterwards takes an almost fixed value (plateau). On the contrary, although we record a linear increase in the first evolution, no plateau is reached in configuration AX4. In a short time, the linear evolution is followed by a smooth increase in the case of $Q = 2$ Nl.min^{-1}. A sharper increase is observed when $Q = 6$ Nl.min^{-1} where a maximal value ($\approx 2.25 \times 10^{-5}$ Kg) is reached approximately at $t = 100$ s, followed by a slight decrease afterwards. However, we can clearly note that the evolution is not smooth and follows an oscillatory behavior.

From figure 5.31, we can clearly note that a steady solution is attained in configuration AX3 with both flow-rates approximately in the first 30 physical seconds of the simulation. This is not the case in configuration AX4 where the steady state solution is not established yet. In addition, we can not emphasize whether the solution will converge towards a stationary state or not.

Considering a fixed injection flow-rate and comparing both configurations, we note that the same mass is recorded during the first linear evolution. For a short time period later (transitional region of AX3), the mass predicted with configuration AX3 overestimates that predicted by AX4. Afterwards, the issue is reversed where the bigger helium mass is recorded in the configuration that takes into account an exterior domain. This confirms well the visualized stratification in AX4 at a long time instant and maybe, the blockage phenomenon in the top vent vicinity.

5.3.3 The influence on the flow traversing both vents

The profiles of the radial velocity u_r passing along the inner surface of the bottom vent are plotted in figure 5.32, for both injection flow rates and at two time instants $t = 5$ and 60 s. Independent of the value of Q, fresh air enters completely from outside in configuration AX4. On the contrary, two different flow-orientations takes place in configuration AX3. Ambient fluid enters from the upper part of the vent, while a mixture exits the cavity from its lower part. We emphasize here that both the ambient and the mixture in the bottom vent vicinity are basically pure air as far as no helium reaches the far field of the bottom cavity. At $t = 60$ s, the maximum inlet velocity traversing the bottom vent is recorded in configuration AX3, where the velocity of fresh air entering the cavity strengthen at the top of the vent, whatever the value of Q is.

In figure 5.33, u_r profiles of the fluid traversing the top vent are presented. At $t = 60$ s, the profiles in all cases take almost a similar form: light mixture leaves the cavity in a layer at the top and a heavy fluid enters from outside through the lower part of the top vent. We can note that the highest velocity values of the exiting fluid are recorded for configuration AX3 which does not take into account an exterior domain.

For a global comparison, the volumetric flow rates entering and leaving respectively from the bottom and top vent have been calculated and their corresponding time evolution is presented in figure 5.34. At the inner surface of the bottom vent and for $t > 30$ s, we note for a fixed Q that the configuration that does not take into account an exterior domain overestimates the

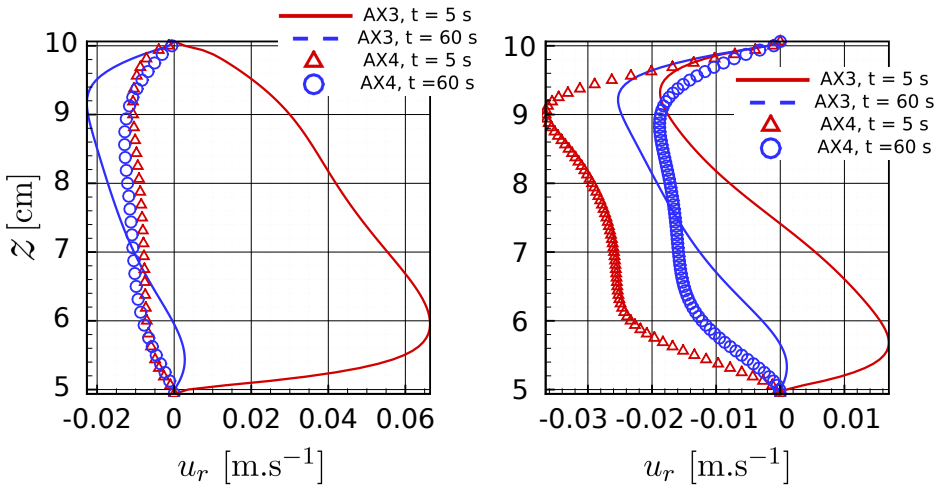

Figure 5.32: Instantaneous radial velocity u_r profiles along the inner surface of the bottom vent for configurations AX3 and AX4 at $t = 5$ and 60 s. Left: $Q = 2$ Nl.min^{-1}, right: $Q = 6$ Nl.min^{-1}.

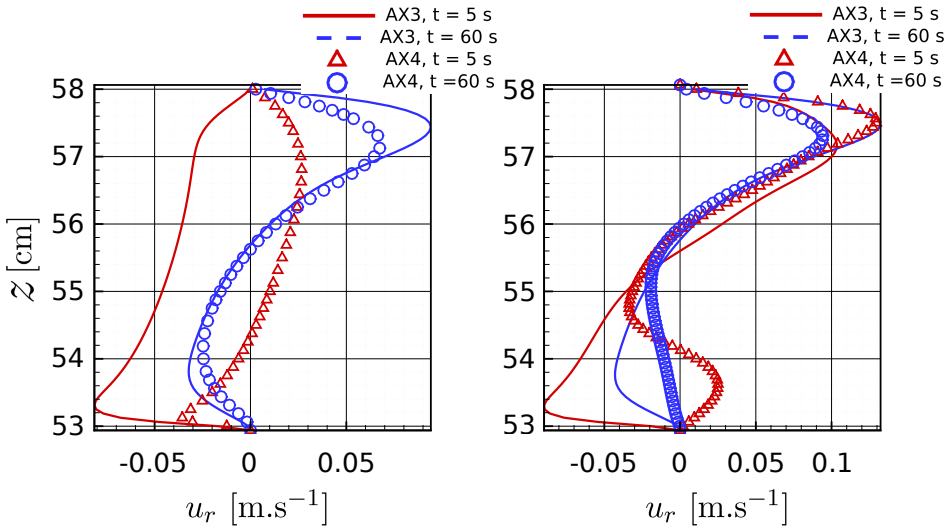

Figure 5.33: Instantaneous radial velocity u_r profiles along the inner surface of the top vent for configurations AX3 and AX4 at $t = 5$ and 60 s. Left: $Q = 2$ Nl.min^{-1}, right: $Q = 6$ Nl.min^{-1}.

absolute value of the inlet volumetric flow rate Q_v^{bot} predicted with the second configuration (can reach 50% as seen in figure 5.34, left). Similar is the case at the inner surface of the top vent where we see that the highest Q_v^{top} are recorded for configuration AX3 for a fixed Q (figure 5.34, right). This accordance is well justified by the conservation principle as far as a constant helium injection is considered. Moreover, this issue is also confirmed by fixing the configuration and comparing for different Q where we see that Q_v^{bot} and Q_v^{top} increase with Q.

For further confirmation regarding the helium stratification near the top vent region, the

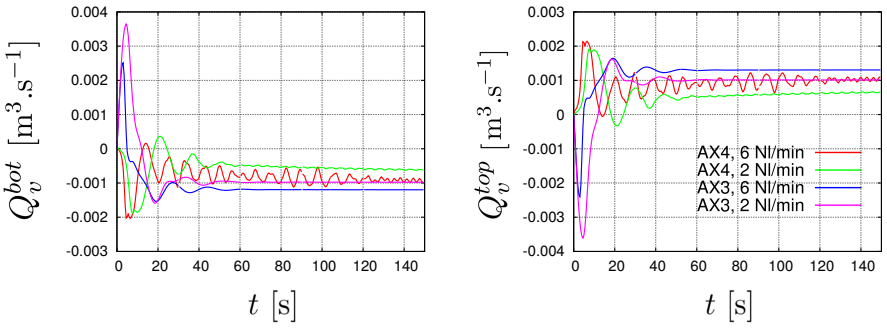

Figure 5.34: Instantaneous volumetric flow-rates evolution for configurations AX3 and AX4 with both injection flow-rates. Left: inner surface of the bottom vent, right: inner surface of the top vent .

mass flow-rate of helium q_{He}^{top} leaving the top vent has been calculated and the evolution is illustrated in figure 5.35.

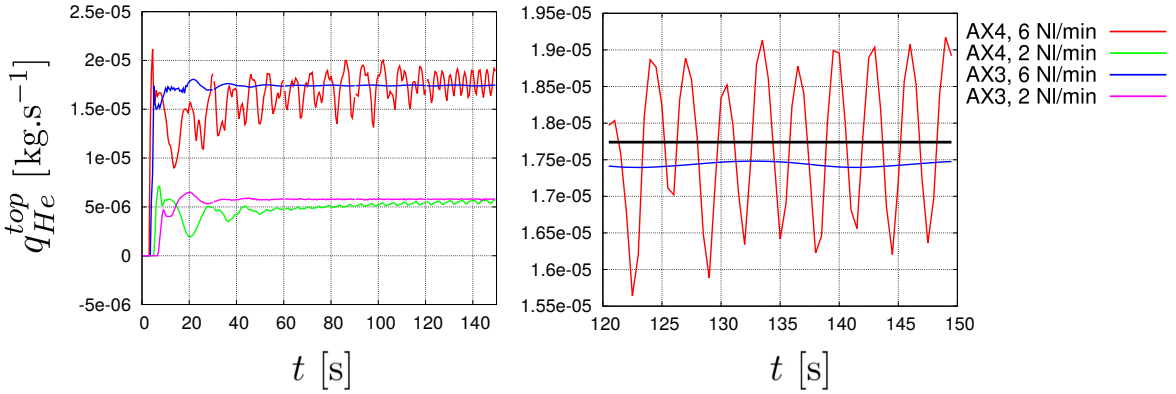

Figure 5.35: Instantaneous evolution of the helium mass flow-rates at the inner surface of the top vent for configurations AX3 and AX4. Left: both injection flow-rates over 150 s, right: zoomed time interval with $Q = 6$ Nl.min^{-1}. Thick black line denotes the mean value for AX4 over 30 s.

For $Q = 2$ Nl.min^{-1}, we note that the configuration that takes into account an exterior domain underestimates q_{He}^{top} predicted with AX3 until about 120 seconds (can reach 20%), and thus confirms the overestimation of helium total mass inside the cavity. However, the underestimation issue is solved as time advances where we note that the two graphs approach each other at $t = 150$ s.

It is rather not trivial to confirm the situation for $Q = 6$ Nl.min^{-1} as far as the values of q_{He}^{top} are highly fluctuating. However, during the observed time period where $\mathcal{M}_{\mathrm{He}}$ increase stiffly (up to 100 seconds), it is clear that AX4 underestimates q_{He}^{top} predicted with AX3 (in average, figure 5.35, left). Afterwards, during the decay of the mass ($t > 100$ s), the mean value of q_{He}^{top} for AX4 overestimates that of AX3.

Up to present, we do not have any reference solution to compare with and conclude if the

flow is better represented by AX3, AX4 or even by neither configuration. All what we can say is that the flow inside the cavity is highly influenced by the modelled configuration.

5.4 Concluding remarks

The performed study can be divided into three parts. In the first part, a laminar starting plume in a one vented cavity has been employed to identify the size of the mesh required for obtaining stable converged results. We have proposed a new criterion to predict the height of the plume H_p before the top ceiling impact using the axial velocity distribution along the plume axis. The comparisons with existing approaches from the literature are satisfactory and thus convergent.

In the next part of this axi-symmetrical study, we considered the treatment of inlet boundary condition issues which arise when the injection flow-rate is increased gradually. Numerical results show that modelling a pipe in the computational domain is required so that the fluid entering the cavity is influenced by both, convective and diffusive contributions.

Finally, two geometrical configurations were considered to simulate flows in two vented cavities: configuration without or with (chimney with a wall at the right) an exterior domain. The direct interaction between the exterior and the interior environment (cavity), in both cases, influences extremely the flow and thus induces significant discrepancies in the mixture dilution phenomenon. However, in the case of the configuration that models an exterior domain, a convergence study on the width of the chimney is recommended to reduce the effect of the jet impacting the side wall.

Therefore, we show interest in simulating the flow in configurations that take an exterior region into account. In spite of conducting a convergence study on the size of the exterior domain on axi-symmetrical configurations, we prefer to perform it on the real 3D configuration where experimental measurements are available for comparisons. Moreover, we consider the exterior domain in the 3D cases to be opened from all directions, and that is to avoid any impact jet phenomenon.

Chapter 6

Setting up the numerical configuration by the use of LES

Contents

In this chapter, we present 3D LES results performed on the numerical configurations presented in chapter 2. The closure problem is handled by the classical Smagorinsky sub-grid scale model (SMAGO SGS). Following the axi-symmetrical investigations, the injection pipe is always modelled within the computational domain. Moreover, exterior regions of different sizes are considered and a convergence study is presented. No solid wall boundaries are considered in the exterior region and thus six surfaces are prescribed with a pressure outlet boundary condition.

The 3D computational domains features a complex geometry which contain large parts of non-fluid zones that does not require any resolution. Thus, the use of a non-structural mesh is recommended to prevent situations of having non-working processors which contains the non-fluid zones only. The CEA TRUST-TrioCFD code is used in the parallel MPI matis version (geometrical topology).

The chapter is organized as follows. First, the numerical schemes and the LES parameters are identified. The influence of modelling an exterior region in the computational domain is presented next, where basically a convergence study along the horizontal width of the additional domain is carried out. Analysis of the mixing-dispersion phenomenon in addition to a 3D flow description are finally presented.

Variables employed in the post-treatment throughout the chapter are all defined in appendix C. We fix from now on the helium injection flow-rate to that used in the CEA experiment; $Q = 5$ Nl.min^{-1}.

6.1 Defining the LES configuration

Several points are required to be identified before starting the numerical resolution of the problem. In the following subsections, the road followed to identify the LES configuration is described. Firstly, the choice of the employed numerical schemes is presented so that the physical phenomena are well reproduced. Next, we identify the size of the mesh required for obtaining converged LES results, and that is basically by performing statistical grid convergence study. Finally, the choice of the SGS model in the rest of the work is justified.

In this section, the numerical configuration presented in figure 2.6 (a) (no exterior domain) is considered. The flow equations are simulated only inside the cavity and the pipe where the outlet boundary conditions are directly prescribed at each vent surface. A pipe of diameter $d = 1$ cm and height $h = 3$ cm is employed with a Poiseuille velocity inlet profile, prescribed at the bottom pipe inlet boundary.

6.1.1 Choice of the numerical schemes

The generated mesh for which we test different schemes is a parallelepiped, uniform-by-block mesh with a size, per direction, approximately 9.1×10^{-2} cm. We emphasize that the mesh is defined in terms of blocks to ensure that the control volumes boundaries are aligned with the boundaries of the pipe and the vents (4 blocks along the x-horizontal direction, 3 blocks along the y span-wise direction and 4 blocks along the z-vertical direction).

6.1.1.1 Temporal scheme

Two time integration schemes have been tested: the first order upwind Euler [VM07] and the second order RRK2 schemes. When coupled with a spatial second order central scheme, it has been observed that the Euler integration scheme produce numerical instabilities which are not reproduced by the RRK2 simulation. We illustrate in figure 6.1 the numerical instabilities by an instantaneous velocity magnitude iso-contour plot in the vertical mid XZ_1 plane at $t = 4s$.

As expected, the instabilities induced by Euler's scheme are easily viewed along the jet axis

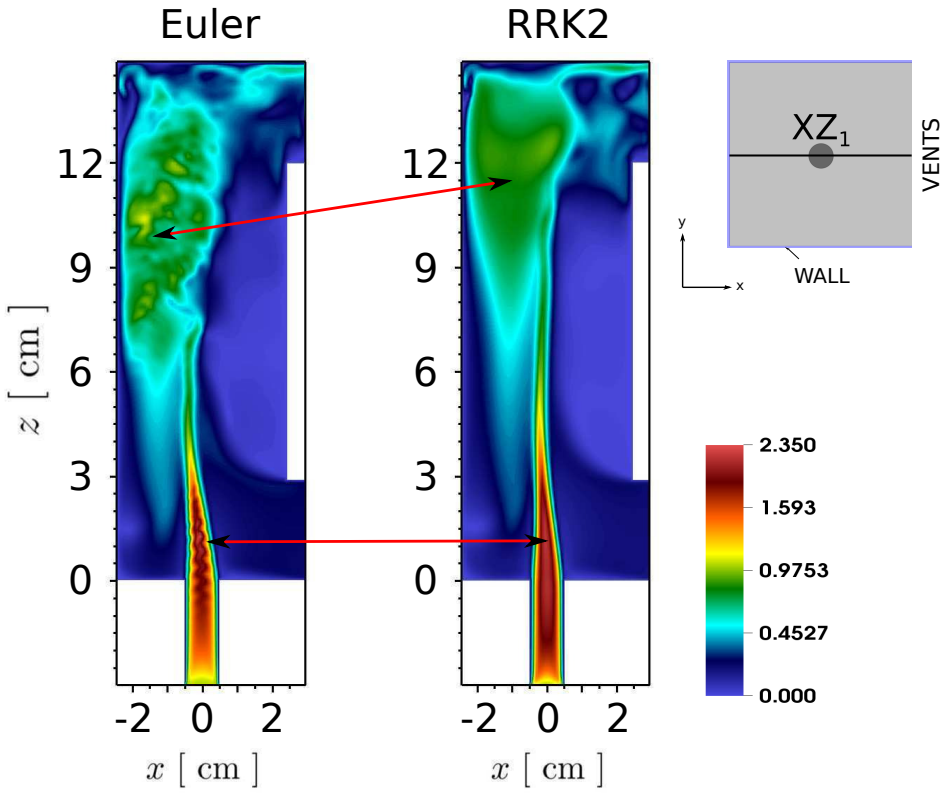

Figure 6.1: Instantaneous velocity magnitude $|\mathbf{u}|$ [m.s^{-1}] iso-contour plot at $t = 4$ s in the vertical mid XZ_1 plane showing the influence of the temporal scheme and the induced numerical instabilities. Left: first order Euler, second order RRK2.

in the vicinity of the pipe, in addition to a big portion of the domain situated at the top-left of the cavity (figure 6.1, left). In contrary, a continuous distribution is recorded by the RRK2 scheme (figure 6.1, right).

We emphasize that the instabilities are numerical rather than physical as far as they are also recorded inside the pipe where the flow is completely laminar ($\mathrm{Re_{inj}} \approx 195$). As a consequence, the RRK2 scheme is employed in the rest of the work for the temporal integration.

6.1.1.2 Spatial scheme

Several numerical schemes have been tested to perform the spatial discretization for the **convective terms** of the momentum and species conservation equations. When a second order central scheme is employed, the resolution algorithm did not converge in all the simulations. We justify the scheme failure due to the maximum cell Reynolds and Peclet numbers defined as

$$\mathrm{Re_{cell}} = \frac{|\mathbf{u}| \times \Delta}{\nu + \nu^{\mathrm{SGS}}} \quad \text{and} \quad \mathrm{Pe_{cell}} = \frac{|\mathbf{u}| \times \Delta}{D + D^{\mathrm{SGS}}}, \tag{6.1}$$

where both can range from an order of 10 to 10^2 (depending on the used mesh size). $\Delta = (\delta_x \delta_y \delta_z)^{1/3}$, ν^{SGS} and D^{SGS} are respectively the SGS viscosity and diffusivity, related together by the SGS Schmidt number ($\mathrm{Sc}^{\mathrm{SGS}} = 0.7$ in our case) by the relation

$$\mathrm{Sc}^{\mathrm{SGS}} = \frac{\nu^{\mathrm{SGS}}}{D^{\mathrm{SGS}}}. \tag{6.2}$$

Second order central schemes for convective terms are known from the literature to fail with high $\mathrm{Re}_{\mathrm{cell}}$ and $\mathrm{Pe}_{\mathrm{cell}}$ (see the book [VM07] for details). In particular, the two dimensionless numbers are recommended to take at most a value 2 as a sufficient condition with an explicit scheme.

The issue of high $\mathrm{Re}_{\mathrm{cell}}$ and $\mathrm{Pe}_{\mathrm{cell}}$ can be resolved be a further mesh refinment. However, using smaller values of Δ induces stiffer mass fraction Y_1 gradients which leads to further numerical problems if a second order scheme is employed for the convective term of the species equation [Tra13].

In a second trial, the first order upwind scheme [VM07] has been employed for both convective terms. The solution converges and a fast steady solution is obtained (about approximately 4 s of physical time). However, it has been figured out during the results post-treatment that the obtained regime is completely laminar everywhere. This is illustrated in figure 6.2 (left) by the time evolution of the velocity magnitude $|\mathbf{u}|$ at a fixed probe in the top vent ($x = 2.45$ cm, $y = 0$, $z = 14$ cm).

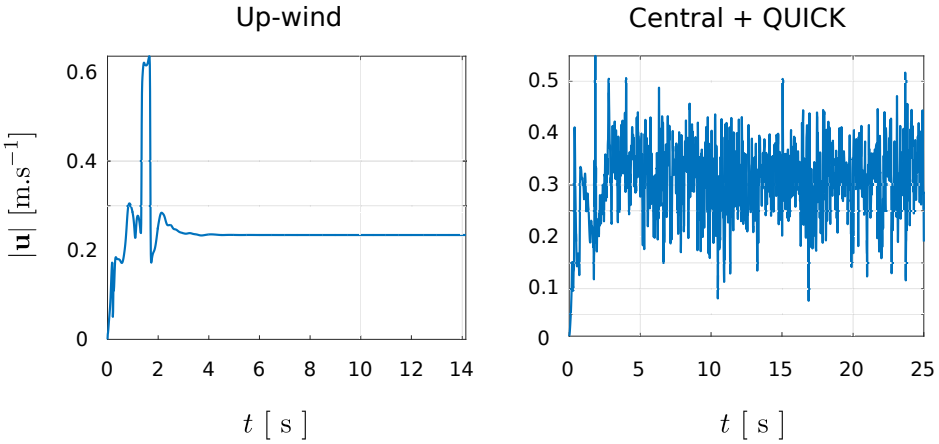

Figure 6.2: Instantaneous velocity magnitude $|\mathbf{u}|$ [m.s^{-1}] evolution at a fixed probe in the top vent ($x = 2.45$ cm, $y = 0$, $z = 14$ cm) showing the influence of the spatial scheme on the flow regime. Left: first order upwind scheme, right: second order central scheme for the momentum convective term and third order QUICK scheme for the species convective term.

The evolution of $|\mathbf{u}|$ in figure 6.2 (left) shows no fluctuations. This result is not surprising as far as the the upwind scheme, being dependent on the direction of the flow, induces artificial numerical diffusion and thus laminarize the flow [VM07]. We note the same behavior when a third order QUICK scheme is employed for both convective terms of the momentum and Y_1

equations.

In a last trial, we consider the following: convective term of the momentum equation is approximated by a second order central scheme and a third order QUICK scheme is employed to discretize the species convective term. By employing a QUICK scheme, we ensure that the values of Y_1 are always bounded between 0 and 1 as far as this scheme holds the boundedness property [VM07].

We emphasize that employing the central and QUICK schemes simultaneously in a coupled system, respectively for convective terms of momentum and species equations, has been already used by Tran in [Tra13] and Blanquart and Pitsch in [BP08] in their simulations of buoyant plumes.

In figure 6.2 (right), the instantaneous evolution of $|\mathbf{u}|$ at the same probe ($x = 2.45$ cm, $y = 0$, $z = 14$ cm) is illustrated when the central (momentum convective term) and the QUICK (species convective term) schemes are simultaneously used. The order of fluctuations clearly justifies that the regime is not laminar and that we will study the quasi-steady state solution obtained.

6.1.1.3 Diffusion/viscous implicit scheme

Two numerical schemes have been initially considered: either a pure explicit scheme or a diffusion/viscous implicit scheme which solves explicitly for the convective terms and implicitly for the diffusion and viscous ones (semi-implicit).

It has been noted that the diffusive and viscous time steps δt_d and δt_ν related to the Von Neumann stability criteria can be as 3–4 times smaller than a convective time step δt_c satisfying the CFL stability condition (refer to section 4.5). To prevent having a time step smaller than δt_c, we fix the choice on employing a semi-implicit scheme in all the 3D computations.

As a consequence of the semi-implicit treatment of equations (4.1) and (4.2), we require to solve at each time iteration a linear system of the form

$$AX = B, \tag{6.3}$$

to calculate the flow variables at t^{n+1}. X is a vector containing the unknowns Y_1^{n+1} or ρu_j^{n+1} defined at the discrete spatial positions and A is the coefficient matrix of the Helmholtz operator. The vector B contains the explicitly treated terms from t_n. A conjugate gradient (CG) method is employed to solve the linear system (6.3) resolution (the algorithm can be reviewed from the book [Saa03]).

We emphasize that a gain of factor 2 has been recorded in the computational cost while using a semi-implicit scheme rather than a fully explicit scheme. This gain takes into account the time cost required for the resolution of system (6.3).

6.1.2 Grid effect

In this subsection, we aim to highlight over the grid influence in our LES calculations. From this study, the size of the mesh required to converge the LES statistical fields is identified.

Again, the mesh is almost uniform per block (a slight variation is reported in the injection tube due to the limited size and the fact of the cells-boundaries alignment). Seven grids labelled respectively as mesh A, mesh B, ..., mesh G are used and thus described in table 6.1. A 2D representative description of the grid and the cell aspect ratio (mesh E) in the vertical mid XZ_1 plane is illustrated in figure 6.3.

Mesh	**Cell size** [cm]	**Cell numbers**	**MPI procs**	$\delta t_{\min}$ [$\times 10^{-4}$ s]	$\delta t_{\max}$ [$\times 10^{-4}$ s]
A	2×10^{-1}	50,125	1	5	7.9
B	1.54×10^{-1}	110,250	3	3.2	6.7
C	1.18×10^{-1}	233,928	6	3.1	5.1
D	9.1×10^{-2}	502,777	12	2.9	3.8
E	7×10^{-2}	1,117,204	24	1.8	3
F	5.39×10^{-2}	2,452,175	48	1.4	2.3
G	4.14×10^{-2}	5,334,048	96	0.9	1.7

Table 6.1: Description of the seven 3D computational uniform grids employed for the LES grid convergence study. The cell size successively decrease with a geometric ratio $q \approx 1.3$ from $\delta = 2 \times 10^{-1}$ to 4.14×10^{-2} cm. The minimum and maximum recorded time-steps are also presented.

A specific procedure has been carried out inside the injection tube where a stair-type mesh is employed to mimic the cylindrical pipe. The stair-type mesh (mesh G) is illustrated at the surface of the bottom injection (inlet boundary) in figure 6.4. u_3 iso-contours are employed to illustrate on the parabolic profile distribution at the injection.

The simulations have been carried out for a physical time of 40 seconds. The minimum and maximum time-steps recorded with each mesh are presented in table 6.1. The time evolution of the mixture's density at the point ($x = 2.45$ cm, $y = 0$, $z = 14$ cm), situated in the top vent, is depicted in figure 6.5 for the seven simulations. A quasi-steady state solution is seen to be reached at the end of the first 5 s. Statistical fields are recorded with a frequency $f_{\text{stat}} = 1/\delta t$ Hz starting from $t_{\text{start}} = 5$ s.

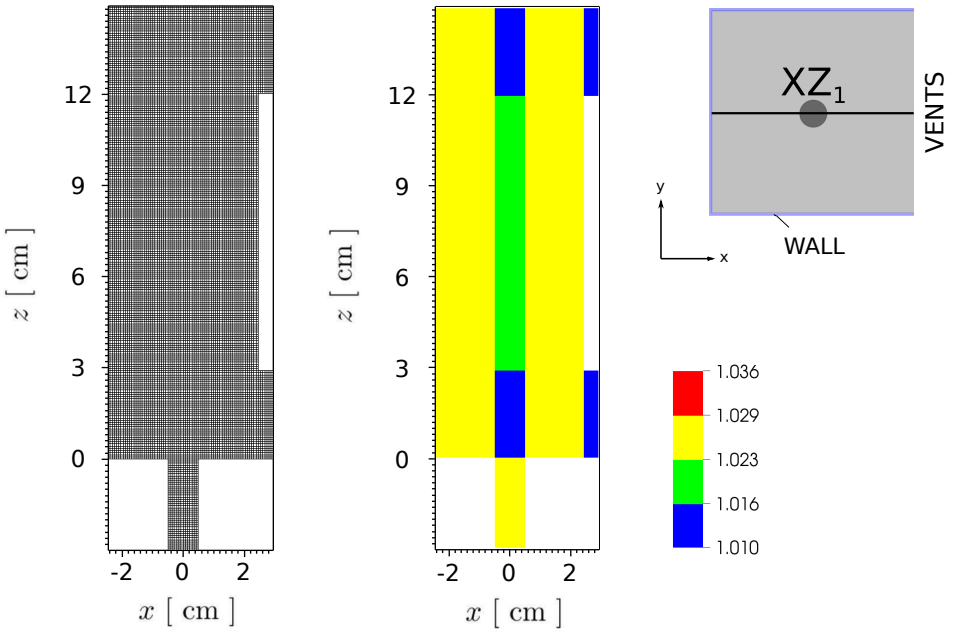

Figure 6.3: Mesh E description in the vertical mid xz-plane (XZ_1). Left: configuration 1, right: cell aspect ratio $\delta z/\delta x$. White rectangles denote the zones outside the computational domain.

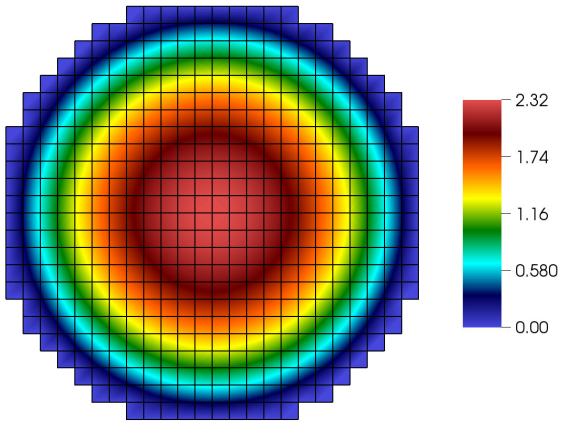

Figure 6.4: Mesh E description at the bottom of the injection pipe overlying the prescribed vertical velocity u_3 parabolic profile.

6.1.2.1 Mesh sensitivity: flow pattern

Generally speaking, it has been figured out that the visualized flow pattern is similar in the seven simulations, and that is without taking into account the quality of the numerical resolution and the statistical error. In figure 6.6, we show the flow behavior inside the cavity illustrated by an instantaneous helium volume fraction X_1 iso-contours and the velocity stream lines in the XZ_1 and YZ_1 mid vertical planes (only for mesh E).

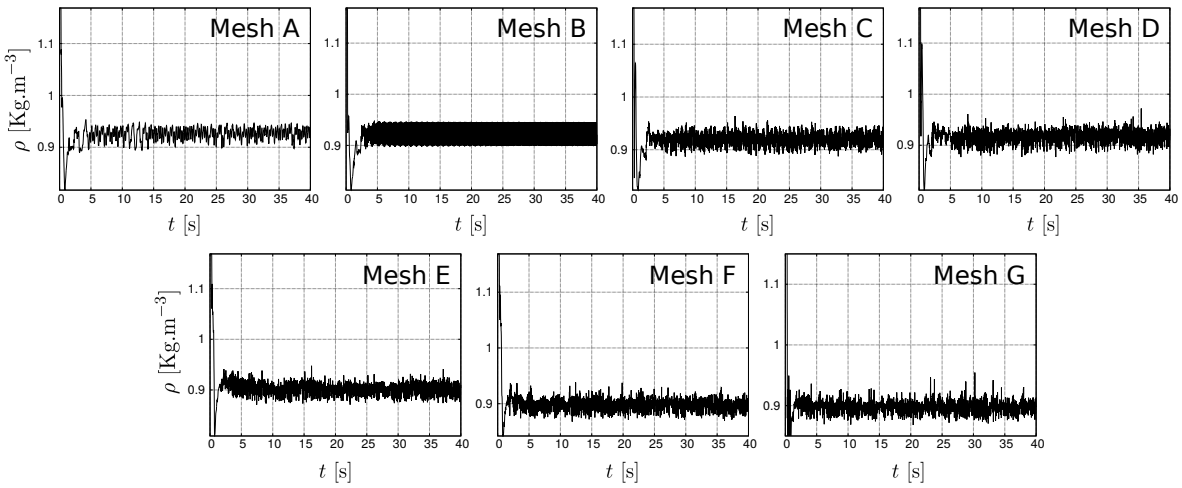

Figure 6.5: Evolution of the mixture density ρ as a function of time at a point in the top vent of configuration 1 ($x = 2.45, y = 0, z = 14$) cm. Top to bottom, left to right: mesh A to G.

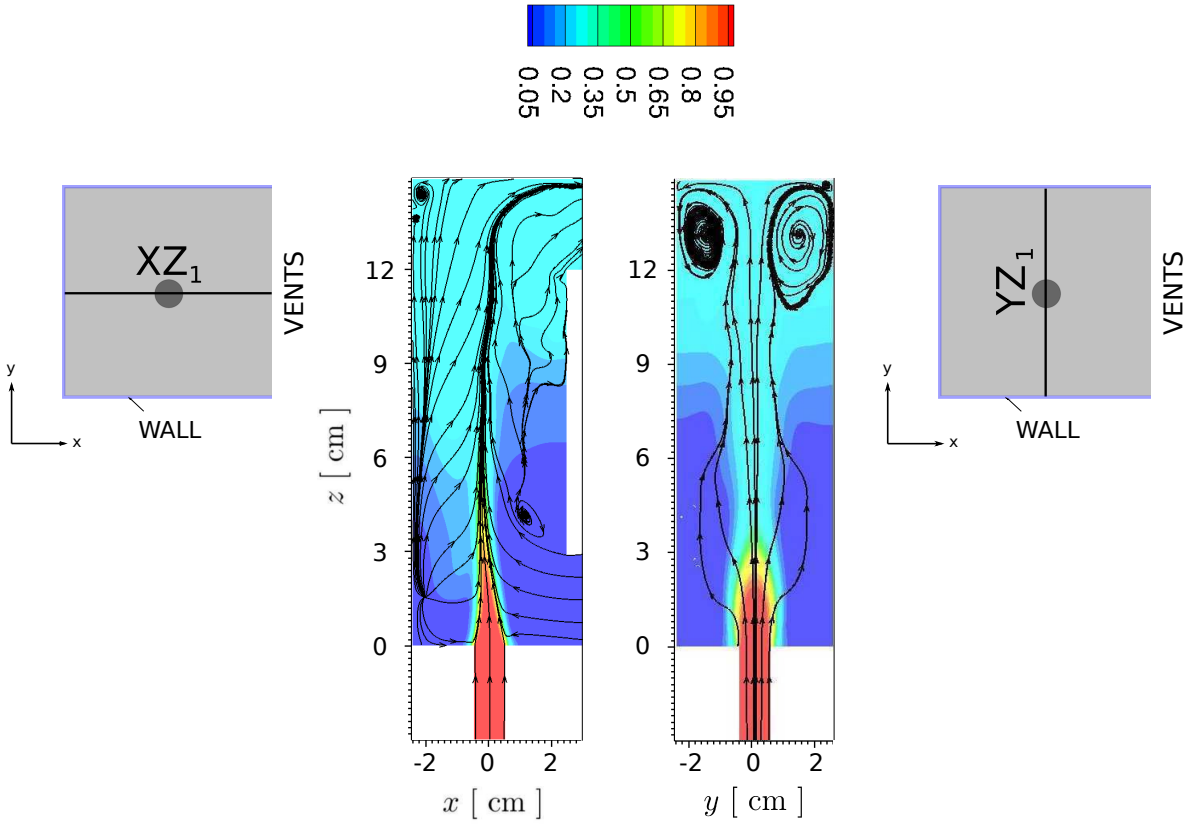

Figure 6.6: Instantaneous X_1 iso-contours superposed by velocity streamlines ($t = 35$ s), mesh E, configuration 1. Left: mid-vertical XZ_1 plane, right: and mid-vertical YZ_1 plane.

We record three basic circulation zones. Due to the jet's top-ceiling impact and the presence of the solid vertical boundaries, a zone in the corner facing the top vent is observed (figure

6.6, left) and two along the corners of the facing walls (figure 6.6, right).

At the corners facing the bottom vent, a similar span-wise reversal flow takes place in all simulations, as a result of the cross-flow effect [LC03]. In practice, fresh air coming with the inflow impacts the jet axis. After this impact, the flow spreads symmetrically with respect to the jet axis in two parts. In each part, two opposite vortices are created: one continues to recirculate near the corner of the cavity and the other one circumvents the jet axis until it collides with the one symmetrically coming from the other side of the jet. When these two counter-rotating vortices collide, they form a dipole that accelerates and enters within the jet axis causing a deformation of the initial circular structure. This behavior can be illustrated by the time averaged (denoted by $< \cdot >_t$) velocity stream lines and helium volume fraction $< X_1 >_t$ in the horizontal xy-plane ($z = 2$ cm, mesh E, figure 6.7). Finally, the dipole is convected upward and an other dipole forms repeating the same mechanism.

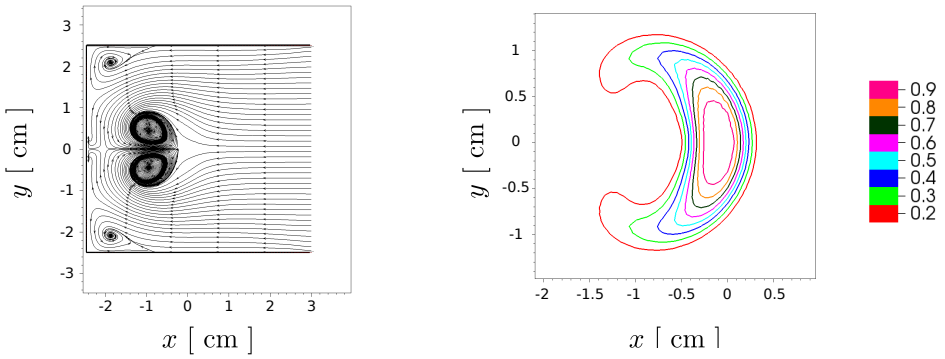

Figure 6.7: Time averaged flow pattern in the horizontal xy-plane ($z = 2$ cm), mesh E. Left: stream lines of $< \mathbf{u} >_t$, line contours of the time averaged volume fraction $< X_1 >_t$.

6.1.2.2 Mesh sensitivity: SGS viscosity distributions

In order to test the response of the LES Smagorinsky's model on the different employed mesh sizes, we consider the instantaneous SGS to laminar (molecular) viscosity ratio ν_{SGS}/ν in the vertical mid XZ_1-plane at the quasi-steady state temporal interval (figure 6.8). The scale variation is clearly noted while moving from mesh A towards mesh G.

From the iso-contours of ν_{SGS}/ν, we note that the modelled viscosity ν_{SGS} is located along the jet axis, near the top and left walls. Recalling equation (3.46), the Smagorinsky's SGS viscosity model reads

$$\nu_{\text{SGS}} = (C_s\Delta)^2\sqrt{2\ \overline{e}_{ij}\overline{e}_{ij}}, \tag{6.4}$$

where Δ is the filter width taken as $(\delta_x\delta_y\delta_z)^{1/3}$ and C_s a constant. It is clear that the model is mainly dependent on the velocity gradients and the square of the cell size, which verify the variation in the figure 6.8. The effect of the cell size is recorded on the maximum of the ratio which decrease from 1.314 (mesh A) to 0.2581 (mesh G). Moreover, the distribution of ν_{SGS} in the domain corresponds to the positions of the big velocity gradients that are situated along

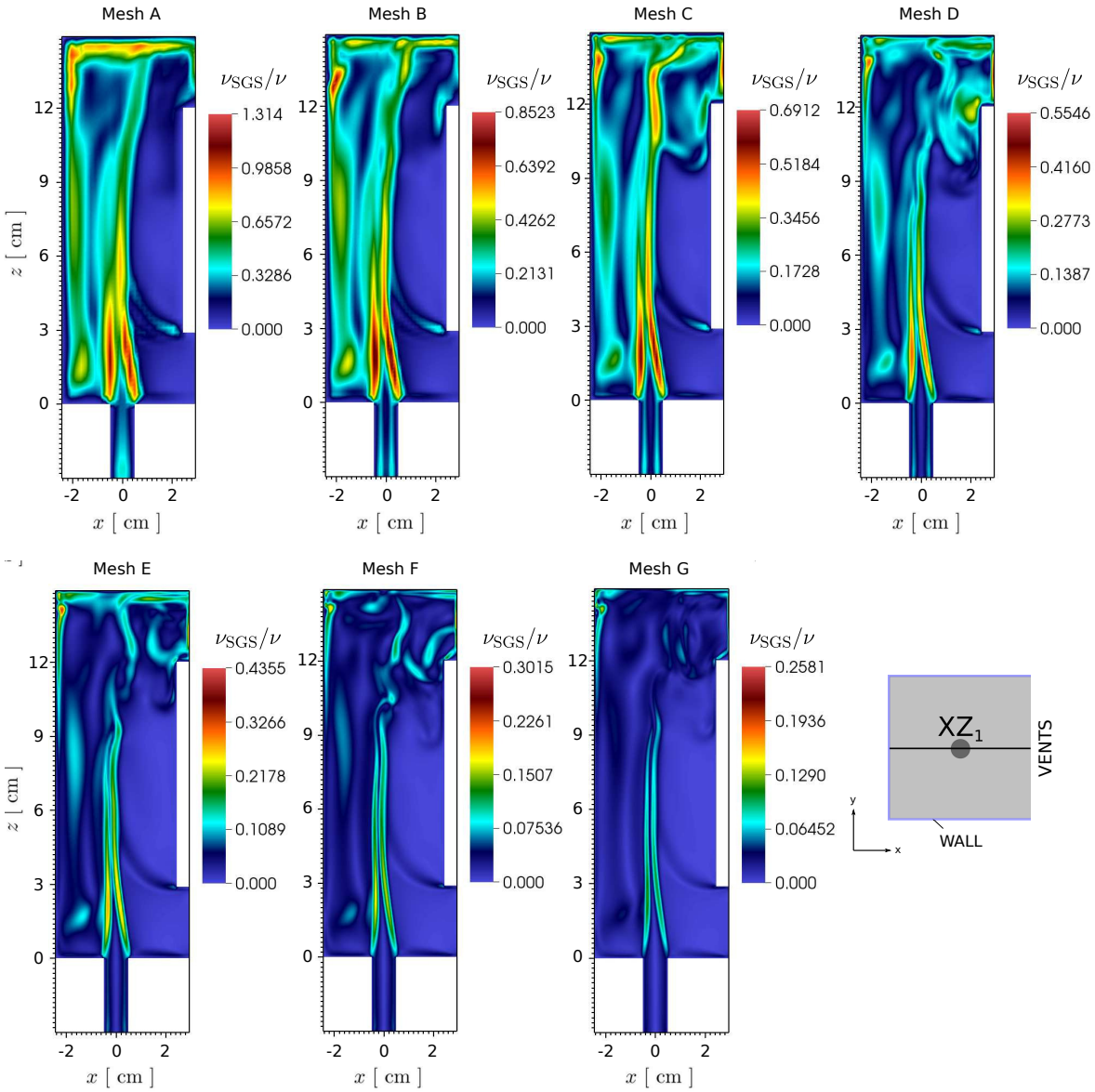

Figure 6.8: Instantaneous SGS to laminar viscosity ratio iso-contours in the vertical mid xz-plane (XZ_1). Top to bottom, left to right: mesh A to G.

the jet axis and in the recirculating zones which is consistent with the definition presented in equation (6.4).

It should be noted that the ratio ν_{SGS}/ν decreases with the mesh refinement. However, the ratio recorded in all cases is small in the framework of LES. Therefore, it can be stated that the global model tends towards the DNS solution.

We emphasize that the seven simulations have been performed again but with employing the wall adaptive local eddy-viscosity (WALE) SGS model [ND99b] to test the influence of the SGS model. No significant discrepancies have been noted and almost a similar flow pattern

is predicted. Hence, the Smagorinsky SGS model has been always employed in the present work as far as it is cheaper in computational cost compared to WALE.

6.1.2.3 Convergence

In a final step, we look towards a sufficient mesh for obtaining a convergent LES results. We present now the grid convergence study. Only convergent statistical fields are currently used, basically the mean and rms fields of the helium mass fraction and velocity magnitude.

In each simulation, we record the evolution of Y_1 and $|\mathbf{u}|$ at 14,161 fixed probes inside the cavity, with a frequency of 100 Hz. More precisely, the probes are equidistant and cover the entire cavity (17 x 17 x 49, equal space along each direction). At each fixed point, the mean and the rms at the quasi-steady state solution are evaluated.

The error for each mesh is calculated as follows. At each probe, the difference between the time-averaged field (or rms) and that calculated on a reference mesh (chosen as the finest mesh G) is evaluated. A spatial norm is then calculated (equation (C.15)) on the obtained 14,161 sized field. The relative error (say on the time-average of Y_1) thus reads

$$\frac{\| < Y_1 >_t - < Y_1 >_t^{\mathrm{G}} \|}{\| < Y_1 >_t^{\mathrm{G}} \|}. \tag{6.5}$$

The evolution of the rms and time-average relative errors are illustrated respectively for Y_1 and $|\mathbf{u}|$ in figures 6.9 and 6.10. It can be stated that the mean (time-averaged) values of Y_1 and $|\mathbf{u}|$ show satisfactory converged LES results starting from mesh E. We note that the convergence of the rms is much slower but acceptable converged values have however been reached.

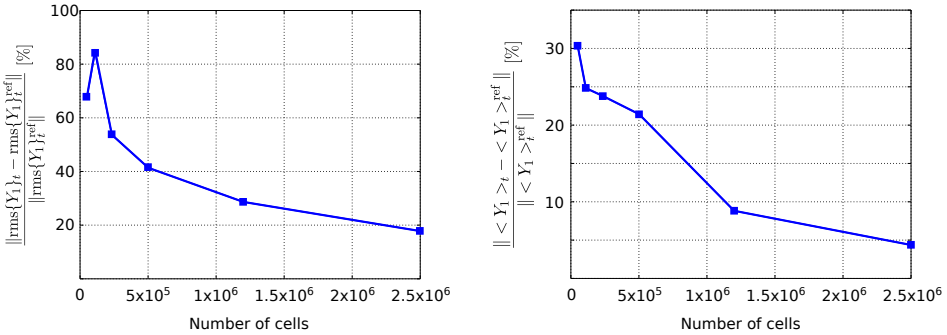

Figure 6.9: Evolution of the helium mass fraction relative error, Smagorinsky SGS model. Left: $\mathrm{rms}\{Y_1\}_t$, right: $< Y_1 >_t$.

In conclusion and otherwise stated in the sequel, all the LES results are obtained with a mesh of cell size $\delta = 7 \times 10^{-4}$ m (Mesh E). We keep in mind that the relative error for such a mesh is about 8% for the mean Y_1 and 12% for the mean of $|\mathbf{u}|$.

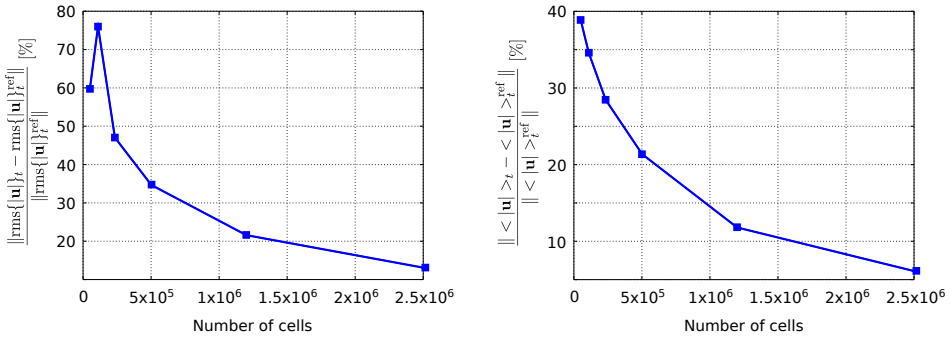

Figure 6.10: Evolution of the velocity magnitude relative error, Smagorinsky SGS model. Left: $\mathrm{rms}\{|\mathbf{u}|\}_t$, right: $< |\mathbf{u}| >_t$.

6.2 Influence of the configurations that take into account an exterior domain

Numerical simulations have peen performed on six different geometrical configurations referred to as configurations 0_x, 1_x, 2_x, 3_x, 4_x and 5_x.

Configuration 0_x is similar to the computational domain used in section 6.1 (no exterior domain), where the flow is simulated inside the pipe and the cavity. In this case, the outlet boundary conditions are applied just at the exterior vents surfaces to model the exchange between the cavity and the exterior environment. However, this is not the case for the remaining 5 configurations where an exterior domain of different dimensions, is directly attached to the outer vent surfaces and therefore moving the outlet boundary condition away from the cavity (recall section 2.4 of chapter 2). A schematic representation of the computational domains is illustrated in figure 6.11.

We aim to perform a convergence study on the influence of taking into account an exterior region in the computational domain. The study is carried out along the $x-$horizontal direction only. Extensions in the span-wise and vertical directions are kept constants throughout the work; $Ly = Lz = 2$ cm. The horizontal extension Lx of configurations 1_x to 5_x varies from 2 cm to 10.125, in a geometrical sequence of ratio $q = 1.5$. A detailed description of the six configurations is presented in table 6.2.

In order to verify the injection conditions at the top surface of the injection pipe and to reproduce well the experimental injection profile, the pipe of height $h = 10$ cm is employed. The value of h is selected to assure that it is long enough to obtain a well developed flow which is independent of the prescribed velocity profile at the bottom inlet. This is well illustrated in figure 6.12 where we see that the maximum vertical velocity is uniquely attained at 8 cm above the bottom inlet, whatever a flat or a parabolic profile is initially prescribed. The diameter of the pipe d is always kept to 1 cm.

The mesh generated for the six configurations is again unstructured and uniform by block. Following the previous grid convergence study, the size of the cells, per direction, is $\delta =$

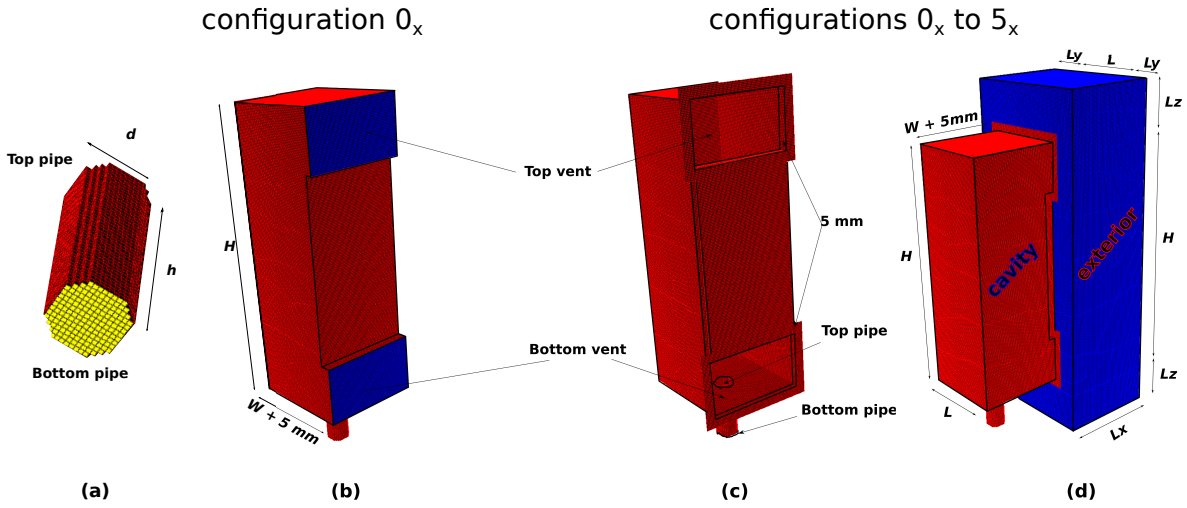

Figure 6.11: 3D sketch of the computational domains: $\partial\Omega_w$ on red surfaces, $\partial\Omega_{in}$ on yellow surface and $\partial\Omega_{out}$ on blue surfaces. (a) pipe for all configurations, (b) configuration 0_x, (c) and (d) for configurations 1_x to 5_x.

Configuration	Lx [cm]	**Cell numbers**	**MPI procs**
$\mathbf{0}_x$		1,134,404	20
$\mathbf{1}_x$	2	2,129,220	40
$\mathbf{2}_x$	3	2,609,476	40
$\mathbf{3}_x$	4.5	3,329,860	60
$\mathbf{4}_x$	6.75	4,427,588	80
$\mathbf{5}_x$	10.125	6,108,484	100

Table 6.2: 3D computational domains description: Reference LES, influence convergence study.

7×10^{-4} m (mesh E). A zoomed part of the computational domain 4_x showing the position of the different boundaries is presented in figure 6.13.

Six simulations covering 110 seconds of physical time have been performed. The choice of the time steps has been relaxed in accordance with the temporal scheme and a minimum recorded convective time step is $\delta t_{\min} = 3.3 \times 10^{-4}$ s, compared to a $\delta t_{\max} = 4.51 \times 10^{-4}$ seconds employed at maximum.

The time evolution of $|\mathbf{u}|$ at a probe in the middle of the top vent ($x = 2.45$, $y = 0$ and $z = 13.5$ cm) is illustrated in figure 6.14. To make sure that the large fluctuations and the transitional regime are finished, a quasi-steady state solution is assumed to be reached at $t = 70$ s. Therefore, statistical fields have been recorded over a unique window ($[70, 110]$ seconds) with a frequency of $1/\delta t$ Hz.

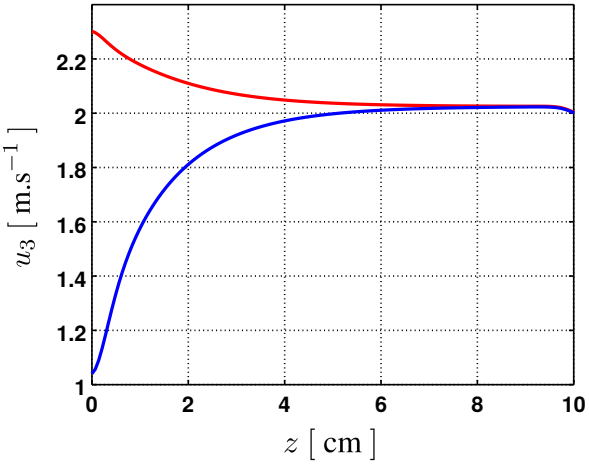

Figure 6.12: Vertical velocity establishment inside the injection tube along vertical axis ($\mathcal{O}z$). Red line denotes the profile established with a Poiseuille velocity profile at the bottom inlet. Blue line denotes the profile obtained with a prescribed flat velocity profile.

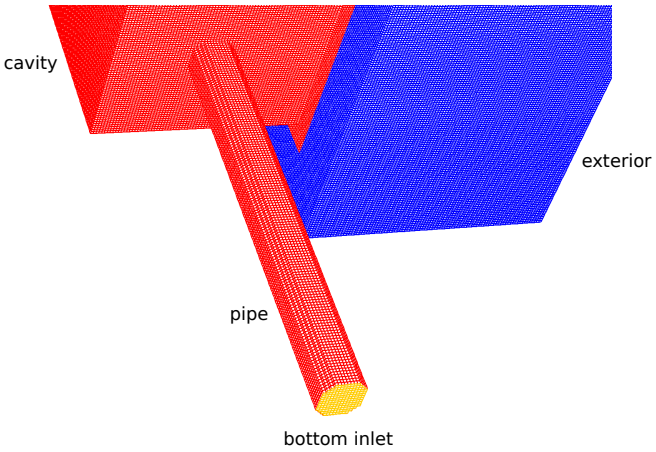

Figure 6.13: A zoomed part of the computational domain configuration 4_x showing the mesh and the position of the three boundary conditions: $\partial\Omega_W$ on red surfaces, $\partial\Omega_o$ on blue surfaces. The bottom inlet denoting the $\partial\Omega_i$ is colored by yellow.

It is important to note that the time required to establish a quasi-steady state solution with configurations that take an exterior region into account is much longer than configuration 0_x (70 s compared with 5 s in section 6.1). This issue is well discussed in [SBMS$^+$17].

6.2.1 Flow pattern: cavity

Firstly, the influence of the configuration is illustrated by visualizing the time averaged flow pattern. The iso-contours of the time averaged velocity magnitude $< |\mathbf{u}| >_t$ in the vertical XZ_1 and $YZ_{3'}$ planes are respectively presented for all cases in figures 6.15 and 6.16.

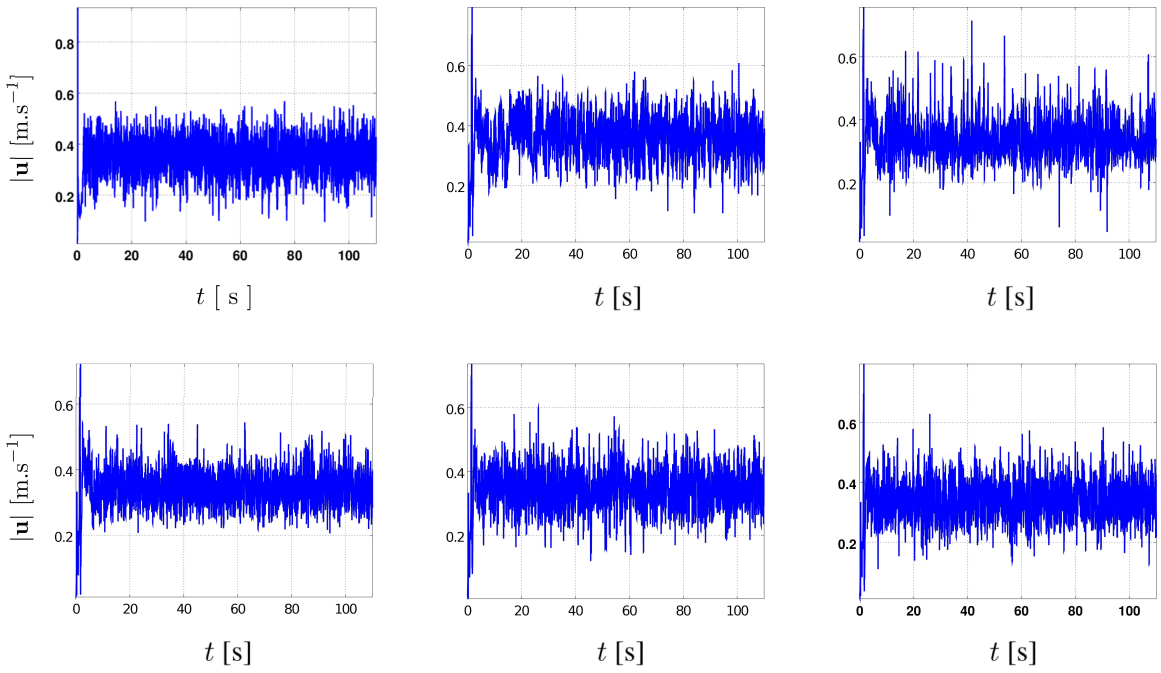

Figure 6.14: Time evolution of the velocity magnitude $|\mathbf{u}|$ at a probe in the middle of the top vent ($x = 2.45$, $y = 0$ and $z = 13.5$ cm). Left to right, top to bottom: configurations 0_x to 5_x.

The flow pattern shows a lot of similarities in the mid-vertical XZ_1 plane (figure 6.15). In all cases, fresh air enters the cavity from the bottom vent, impacts the jet and causes a deviation of the axis towards the wall facing the vents. After that, a mixture is convected upward with the help of buoyancy forces to dilute an air-helium mixture at the top of the cavity. A part of this mixture follows a recirculating motion at the left corner while a second part leaves from a thin layer at the highest position of the top vent. Moreover, we note in all cases that the velocity magnitude, equivalently the kinetic energy, is mainly concentrated inside the bottom jet axis and in a more diffuse way at a large part near the wall facing the vents where the buoyancy forces are dominant.

However, we note that the inclination of the jet axis towards the left wall is much sharper in configurations that employ an exterior domain and that it is strengthened by increasing Lx (configurations 1_x to 5_x).

Another significant influence is seen on the structure of the plume region situated in the top left part of the cavity. Although in all cases the plume is reoriented from the mid height towards the vents wall due to the aspiration from the top vent, the buoyant zone seems to be wider in the configuration that does not employ an exterior domain (configuration 0_x). This is in contrary to the remaining configurations where the iso-contours illustrate that the plume width is reduced by increasing the size of Lx and thus takes a larger size in height. In practice, the velocity magnitude increase in this region and consequently the recirculating flow near the left wall descends further so that the plume occupies a long portion of the

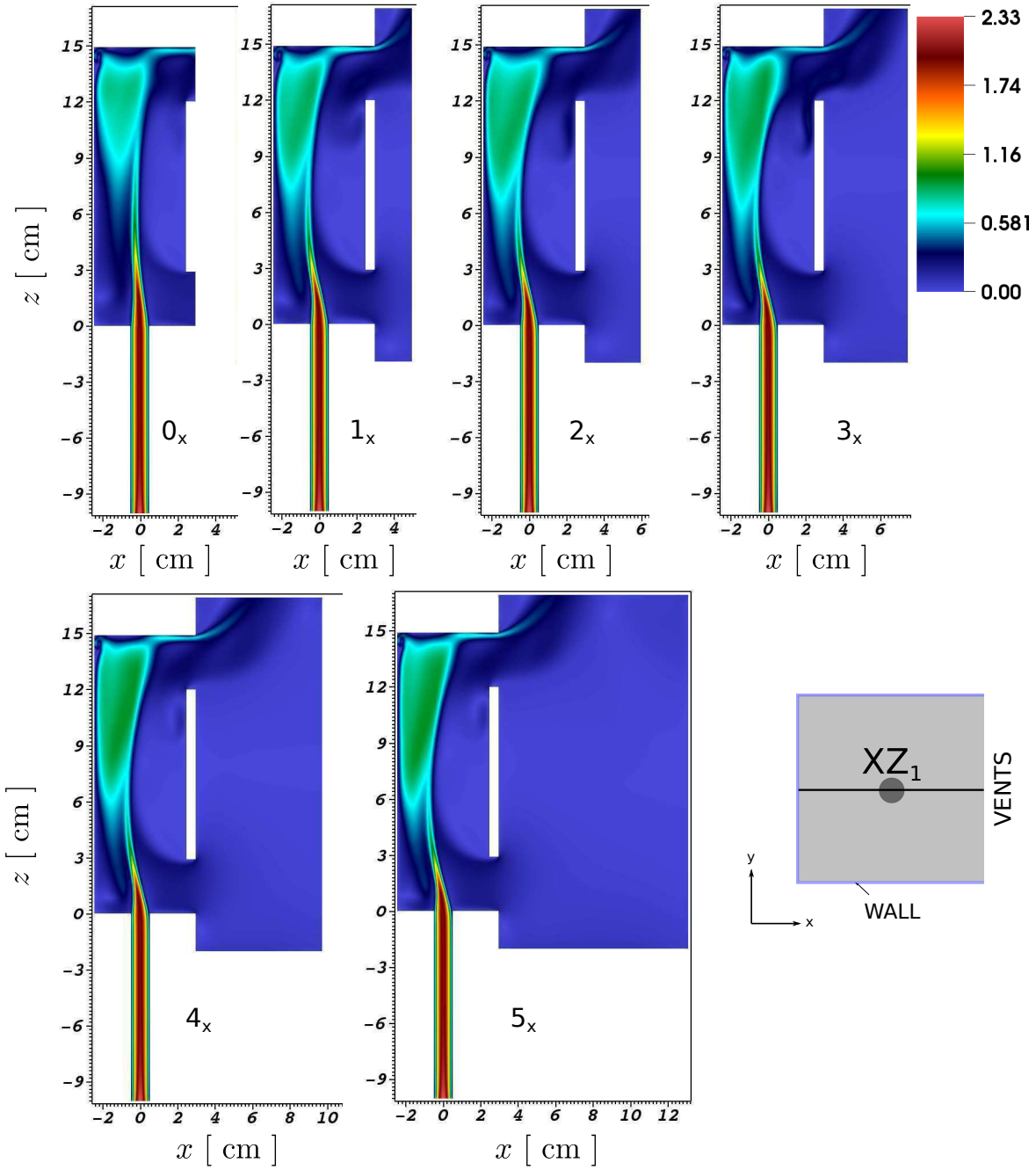

Figure 6.15: Time averaged flow pattern illustrated by the velocity magnitude $< |\mathbf{u}| >_t$ [m.s^{-1}] iso-contours in the mid vertical XZ_1 plane. Left to right, top to bottom: configurations 0_x to 5_x.

cavity's height. However, almost no change is reported in the last two configurations.

Next, we consider the vertical $YZ_{3'}$ plane where almost a similar flow pattern is recorded in all cases (figure 6.16). Two counter-oriented circular flow are observed at the top corners,

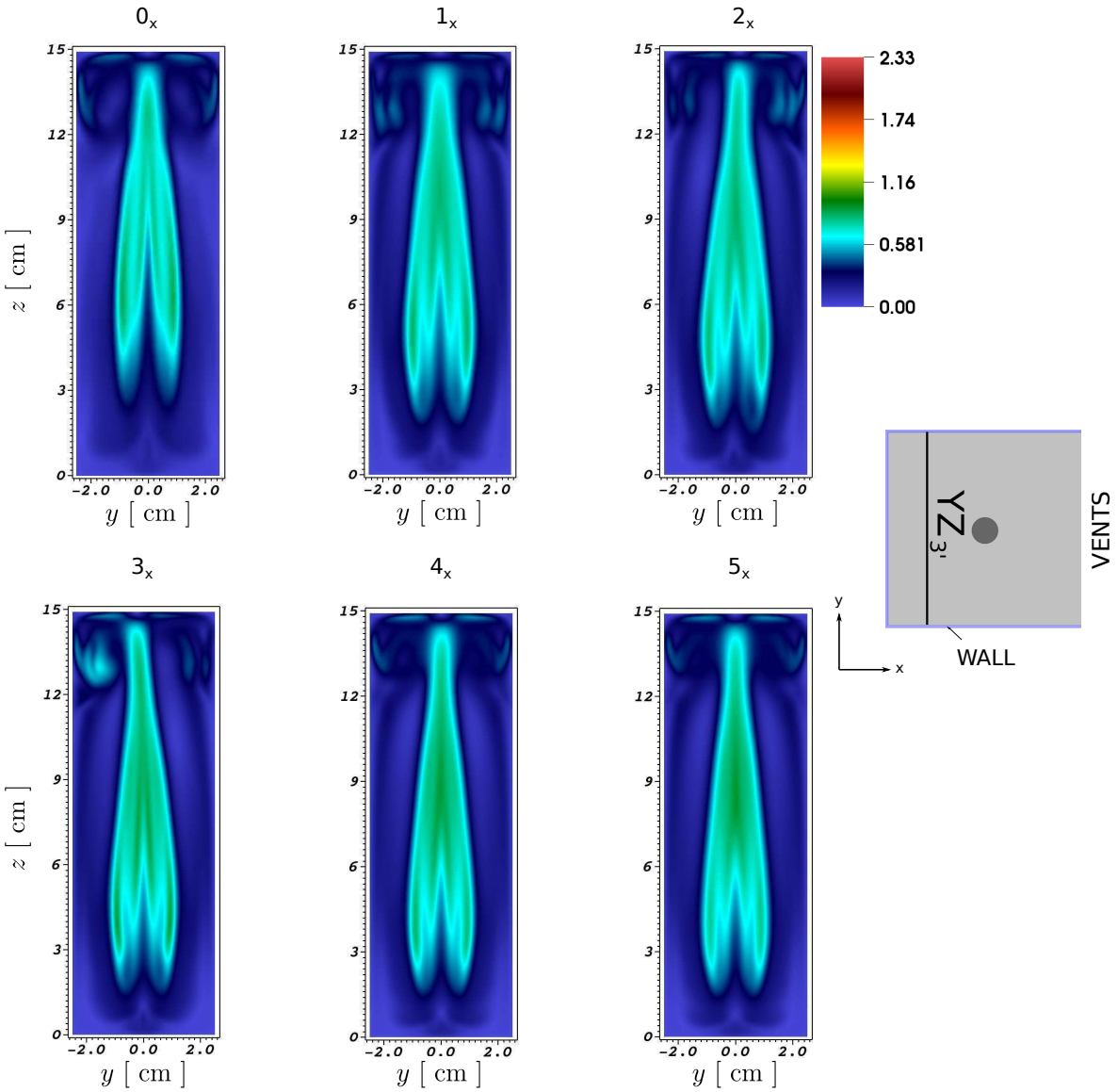

Figure 6.16: Time averaged flow pattern illustrated by the velocity magnitude $< |\mathbf{u}| >_t$ [m.s^{-1}] iso-contours in the vertical $YZ_{3'}$ plane. Left to right, top to bottom: configurations 0_x to 5_x.

although the corresponding velocity magnitude is more significant for the configurations that employs an exterior domain. The variation of the velocity magnitude is justified both by the inclination of the jet towards the left wall (which it is stiffer in this plane for configurations 1_x to 5_x) and by the structure of the plume region near the top left wall. However, we can note a slight non-symmetrical behavior in configurations 2_x and 3_x compared to an almost symmetrical distribution in the remaining cases.

In addition, the effect of the air cross-flow and the jet axis deformation, which has been already described in section 6.1.2.1, is reported for all cases in the lower part of the jet axis.

The effect of the strengthened jet inclination in configurations 4_x and 5_x is reflected on the velocity magnitude at the middle part of plane $YZ_{3'}$, where the values are higher than other cases. However, again there is almost no significant change of the behavior in these two configurations (4_x and 5_x).

The most significant comparison is shown with the rms iso-contours of the velocity magnitude $\text{rms}\{|\mathbf{u}|\}_t$ in same vertical planes (figures 6.17 and 6.18).

In the plane XZ_1, we note that the rms reaches its maximum near the top-vent region in all cases (figure 6.17). However, the global field in this plane is modified by the configuration. In configuration 0_x, the velocity oscillations are mainly recorded along the jet axis, the recirculating flow at the top-left corner and near the top vent. This is not the case of the configurations that take into account an exterior region (except configuration 3_x), where additional oscillations are recorded in the recirculating zones near the left wall and the bottom left corner. However, excluding the configuration 3_x, we note that the velocity mean-deviations increase with the extension length Lx until the last two configurations, where the distribution is rather the same.

Similarly in the vertical plane $YZ_{3'}$ (figure 6.18), the rms distribution is dependent on the simulated configuration. In the first configuration 0_x, the rms is mainly significant at the top in the two counter recirculating zones, to the contrary of the remaining configurations (except configuration 3_x) which record additional oscillations along and near the jet axis. However, we note that the rms values increase successively as we move from configuration 1_x to 2_x and from 4_x to 5_x. In this plane, the rms distribution is not trivially similar in the last two cases, which is justified as far as the convergence of the deviated quantities is usually the slowest.

The significant rms production on the lower part of the jet axis is noted in the configurations that consider an exterior domain (except configuration 3_x). This is clearly the effect of the fresh air inflow from the bottom vent that impacts the light helium buoyant jet in the injection vicinity. We can predict at this stage a significant influence of this phenomenon (air inflow) between configuration 0_x and the remaining cases (except configuration 3_x) as far as almost no rms production is recorded in the same position of configuration 0_x.

The behavior of $\text{rms}\{|\mathbf{u}|\}_t$ in configuration 3_x is rather difficult to interpret. All what we can say is that for sure the specific extension size Lx used in this configuration influences significantly the interior flow, compared with other configurations that employ an exterior domain.

6.2.2 Flow pattern: bottom vent region

Here, we consider the influence of the configuration in the lower part of the cavity; specially near the bottom vent region.

The flow pattern in the lower part of the cavity is influenced by the fact if an exterior domain is taken into account or not. Qualitatively speaking, the general flow pattern in the lower part

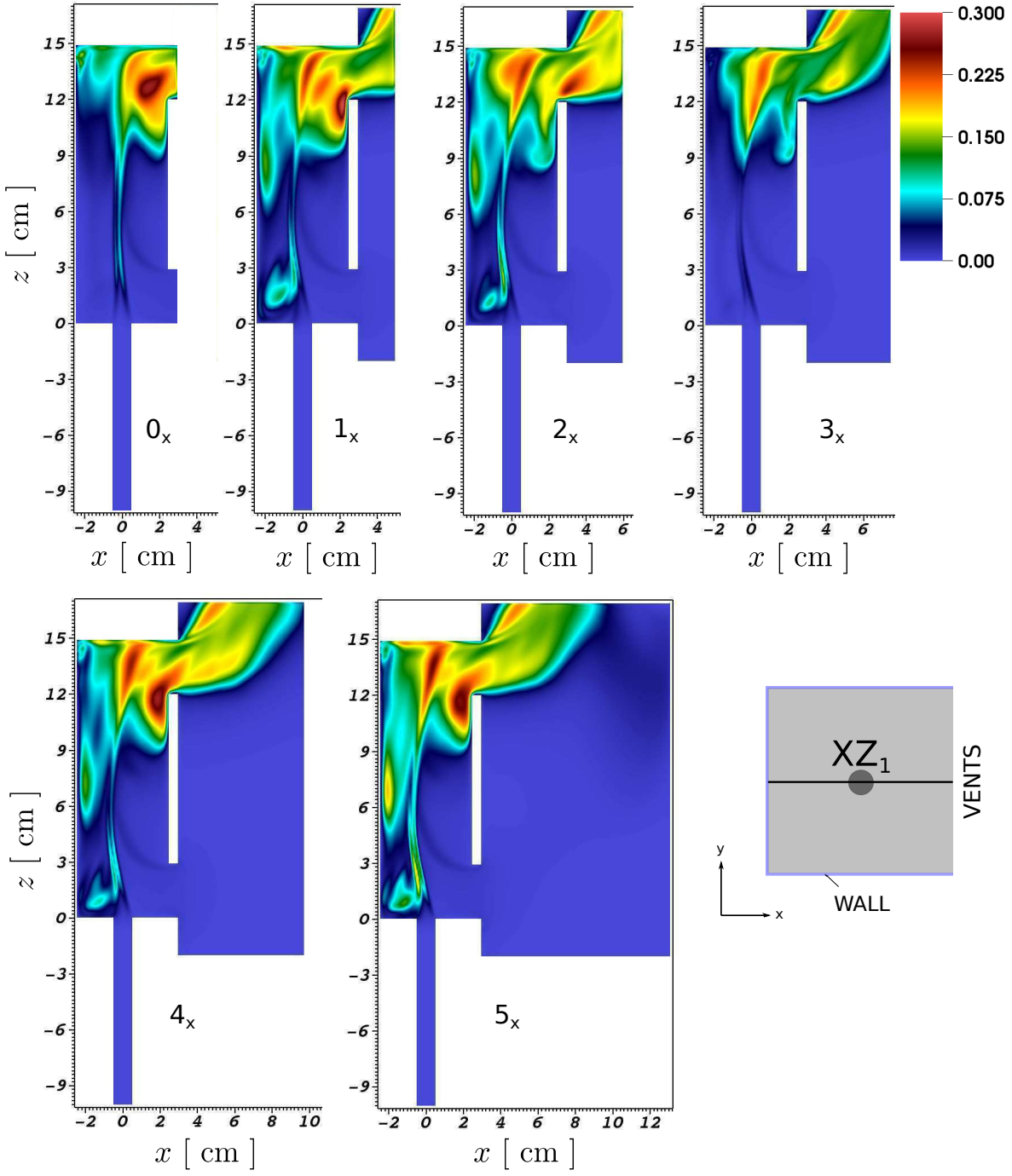

Figure 6.17: RMS iso-contours of the velocity magnitude $\text{rms}\{|\mathbf{u}|\}_t$ [m.s^{-1}] in the mid vertical XZ_1 plane. Left to right, top to bottom: configurations 0_x to 5_x.

of the cavity is rather similar for configurations 1_x to 5_x and thus independent of the extension L_x. This flow pattern is however completely different than that observed in configuration 0_x. We illustrate in figure 6.19, using the time averaged velocity streamlines in a zoomed region situated at the lower part of the vertical mid plane XZ_1, the influence of modelling an exterior

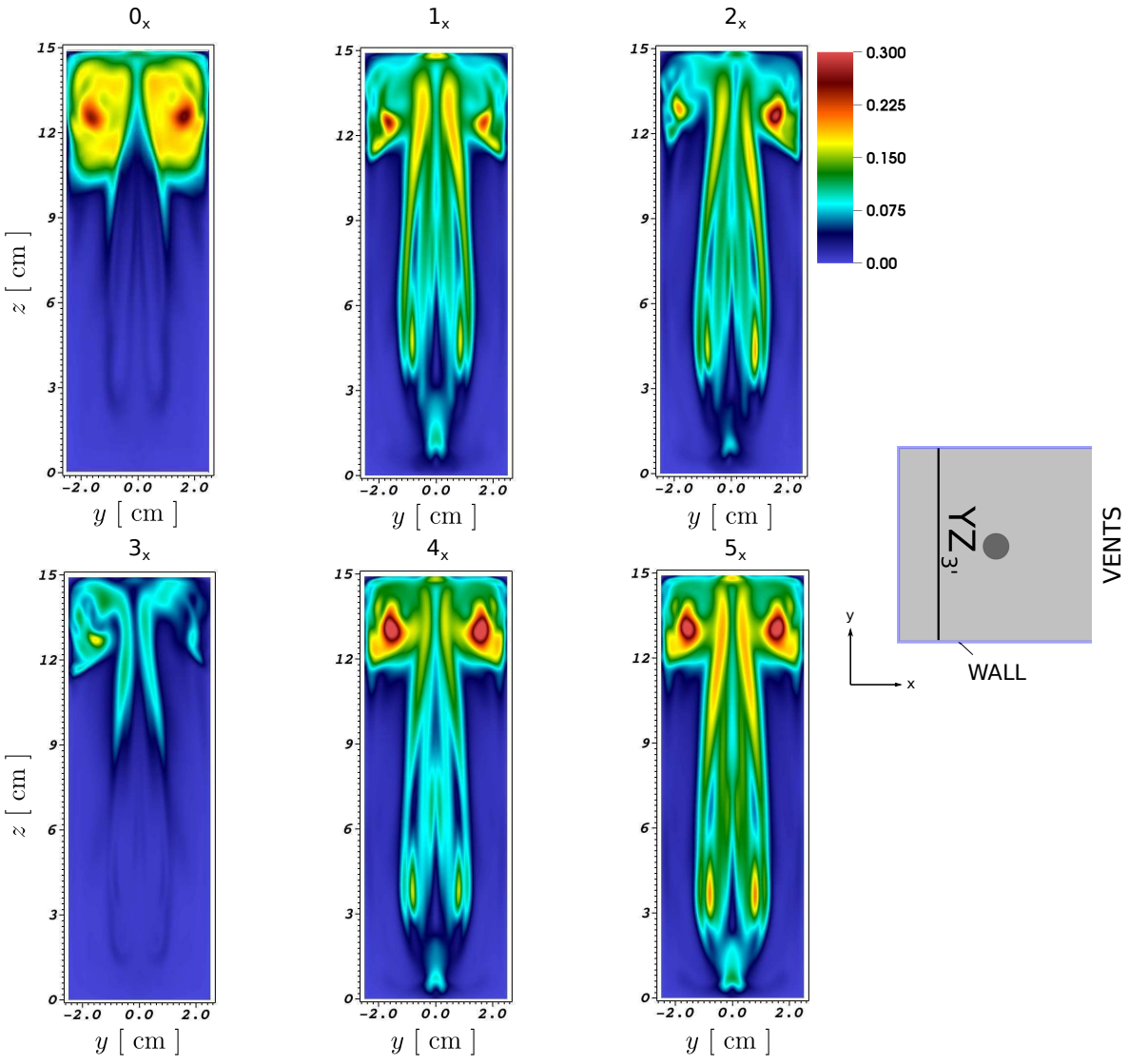

Figure 6.18: RMS iso-contours of the velocity magnitude rms$\{|\mathbf{u}|\}_t$ [m.s^{-1}] in the vertical $YZ_{3'}$ plane. Left to right, top to bottom: configurations 0_x to 5_x.

region in the computational domain.

Basically, we note that fresh air enters configuration 0_x in almost a uniform parallel way and with absolute velocities smaller than those compared to other configurations. However, the behavior of the air inflow in the configurations that takes into account an exterior domain is different where we note that the flow is not completely parallel and that the velocity magnitude is strengthened near the extremities of the vent. The effect of the different inflow velocities on the jet inclination is clearly noted; slight inclination versus strengthened inclination (figure 6.19 left versus right).

For a quantitative comparison, we consider the time averaged velocity $< u_1 >_t$ vertical profiles along the exterior surface of the bottom vent (figure 6.20).

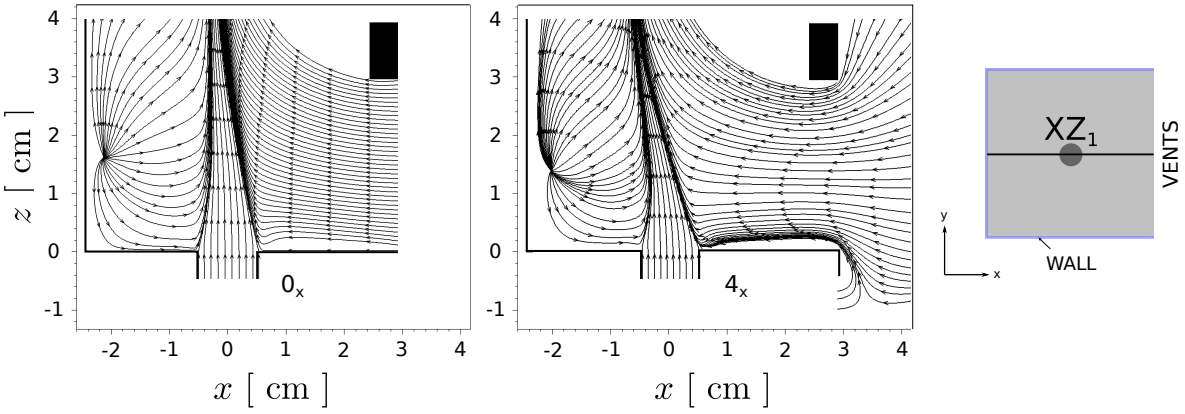

Figure 6.19: Time averaged flow pattern illustrated by $< \mathbf{u} >_t$ stream-lines in a zoomed part of the bottom cavity situated in the mid-vertical XZ_1 plane. Left: configuration 0_x, right: configuration 4_x.

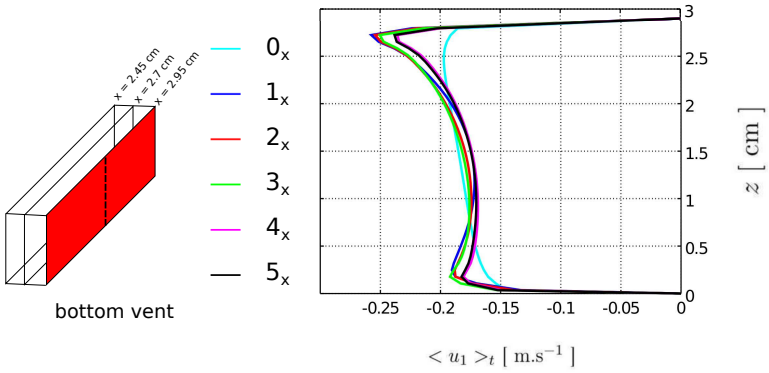

Figure 6.20: Time averaged $< u_1 >_t$ mid-vertical profiles ($y = 0$) in the vertical yz-plane ($x = 2.95$ cm) at the bottom vent for configurations 0_x to 5_x.

The influence of the configuration on the vertical $< u_1 >_t$ profiles is clear. An almost linear distribution is recorded along about 1/2 of the vent's height in the configuration that does not take into account an exterior domain. However, the profiles for the remaining configurations are rather the same, taking almost an inverted parabola distribution with maximum absolute values situated at the extremities of the vent. We note that the profiles are slightly modified by the variation of L_x and that they are almost superposed for the last two configurations.

6.2.3 Flow pattern: top vent region

In this subsection, we consider the influence of the configuration in the upper part of the cavity; basically near the top vent region.

The flow pattern at the top vent is illustrated for all configurations in figure 6.21, where the

iso-contours of time averaged horizontal velocity component $< u_1 >_t$ are presented.

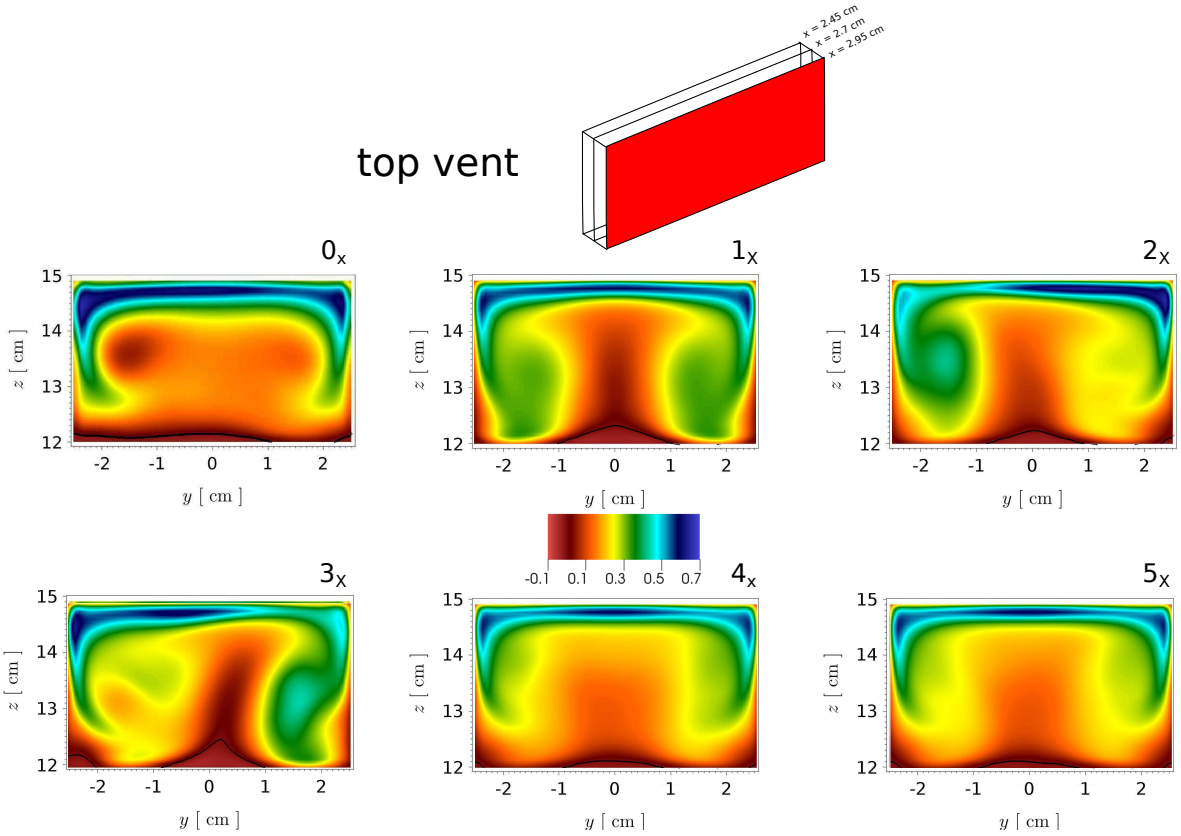

Figure 6.21: Time averaged flow pattern in the vertical yz-plane ($x = 2.95$ cm) at the top vent surface: $< u_1 >_t$ [m.s^{-1}] x-horizontal velocity component iso-contours. Thick black lines of the contour plots denotes the zero contour line indicating the limit of the back flow. Left to right, top to bottom: configurations 0_x to 5_x.

In all cases, the mixture leaves the cavity with the highest velocity $< u_1 >_t \approx 0.65$ m.s^{-1} from a thin layer situated at the top of the vent. However, the $< u_1 >_t$ distribution is highly influenced by the employed configuration.

When the flow is simulated without modelling an exterior region within the computational domain, the distribution of $< u_1 >_t$ at the top vent surface is almost symmetrical, with a small inflow along the whole vent's width at the bottom. However, the distribution is rather different when an exterior domain is taken into account. As the extension Lx increases, a non-symmetrical distribution is induced where we see that the mixture leaves more intensively at a specific corner (configuration 1_x compared to configurations 2_x and 3_x). This issue is resolved starting from configuration 4_x, and definitely 5_x. Again, a small inflow takes place at the bottom of the vent but not along the complete width as in configuration 0_x. We can clearly note that in the last two configurations (4_x and 5_x), the iso-contours of $< u_1 >_t$ are rather similar and both almost symmetrical with respect to the vertical dimension.

A quantitative comparison regarding the influence of the exterior region is illustrated by the

considering the mid-vertical profiles of $< u_1 >_t$ at the top vent exterior surface (figure 6.22).

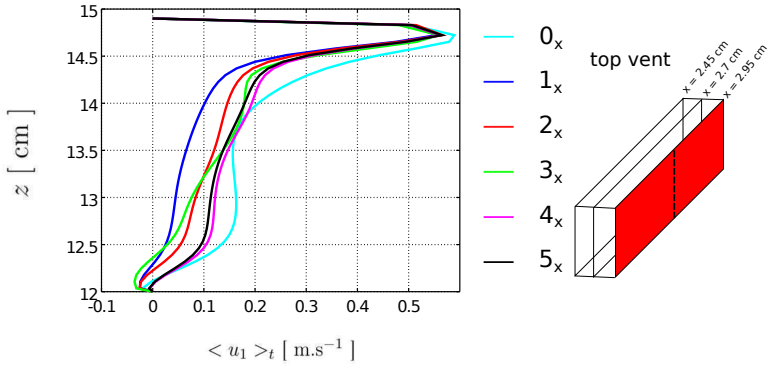

Figure 6.22: Time averaged $< u_1 >_t$ mid-vertical profiles ($y = 0$) in the vertical yz-plane ($x = 2.95$ cm) at the top vent for configurations 0_x to 5_x.

Almost all profiles are confounded in the thin layer at the upper part of the top vent where the maximum velocity value is recorded, except that of configuration 0_x where the maximal $< u_1 >_t$ value is overestimated by about 4% compared to configurations 1_x to 5_x. Significant discrepancies are noted below this layer where we note clearly the influence of the configuration. In configuration 0_x, the velocity increases sharply along the height of the vent to attain about 0.15 m.s^{-1}. Then, the velocity remains constant for about 1.5 cm to increase after rapidly and take the maximum value. To the contrary, the distribution in the remaining cases is almost linear for about 2 cm where the velocity increase after rapidly to attain the maximum. However, the profiles are modified with the value of Lx for configurations 1_x to 3_x. Regarding configurations 4_x and 5_x, the distribution is rather similar with slight discrepancies.

6.2.4 Helium distribution

We present in this section the influence of the employed configuration on the helium distribution inside the cavity. The distribution is illustrated by the time averaged contour lines of the helium volume fraction $< X_1 >_t$ in the vertical XZ_1 and $YZ_{3'}$ planes (respectively in figures 6.23 and 6.24).

In the mid-vertical plane XZ_1 (figure 6.23), we can note that in all cases, helium stratification layers are predicted to form at the left and right regions of the cavity. In addition, the layers at the left descend more than those at the right, which is justified by the low pressure region in the vicinity of the lower–left corner (lower layers) and the mixture that is aspired continuously from the top vent (higher layers).

However, significant discrepancies are noted with the different configurations, both on the position of the stratification layers and on the distribution in the exterior domain (near the top vent of configurations 1_x to 5_x).

In the left of the cavity, the time-averaged helium stratified layers are spatially situated higher

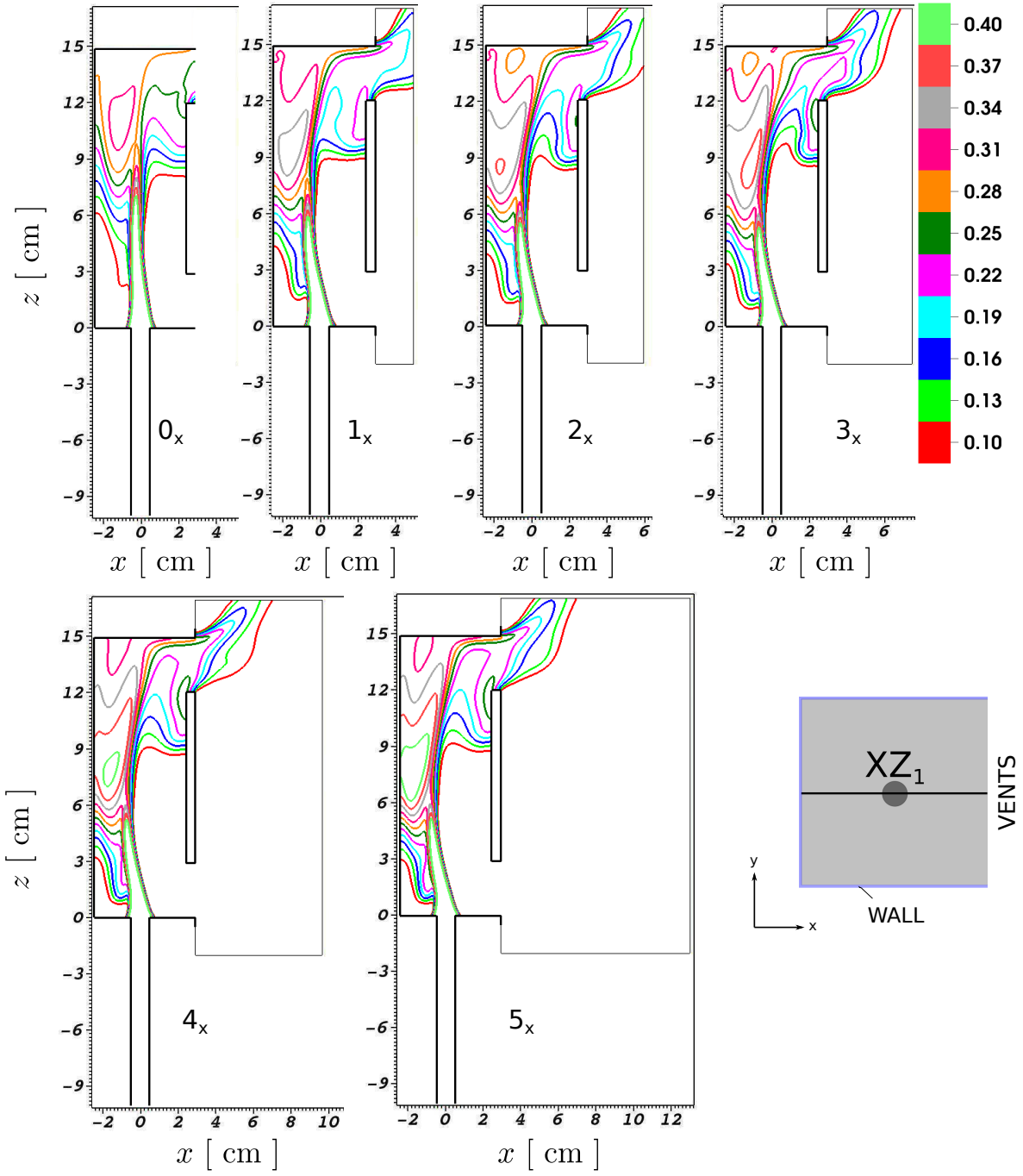

Figure 6.23: Time averaged helium volume fraction $< X_1 >_t$ contour lines in the mid vertical XZ_1 plane. Left to right, top to bottom: configurations 0_x to 5_x.

in configuration 0_x compared to other cases (configurations 1_x to 5_x) where we note that the layers are more approaching the bottom of the cavity. It can be noted in the later case that the layers–descending phenomenon is strengthened by increasing Lx (configurations 1_x to 4_x). Almost no discrepancies are reported on the helium stratification layer in the left lower part

of the last two configurations. However, the slight variations are seen in the upper left part mainly on the contour-lines devoted for 31 to 40% of pure helium.

The behavior is completely different near the right wall (vents wall) where the height of the stratification layers is reduced if an exterior domain is taken into account. Moreover, different shapes of the contour lines are viewed in this region (basically on the lines corresponding to 19 and 22% of helium) due to the different structure of the vortex created near the lower position of the top vent. However, the distribution in the last two configurations 4_x and 5_x is almost the same.

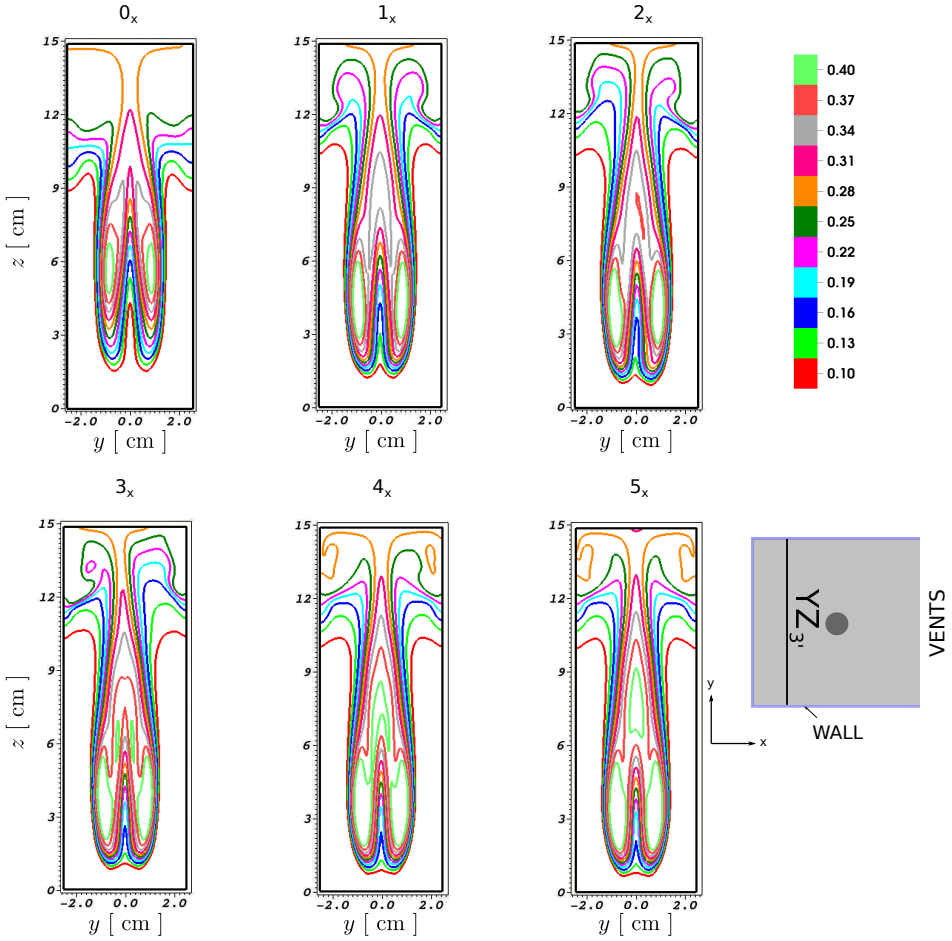

Figure 6.24: Time averaged helium volume fraction $< X_1 >_t$ contour lines in the vertical $YZ_{3'}$ plane. Left to right, top to bottom: configurations 0_x to 5_x.

For configurations 1_x to 5_x, it has been noted that the helium distribution in the top vent vicinity is influenced by the size of the horizontal extension Lx. More precisely, the reduced size of Lx can induce helium stratification in the exterior region as seen in configurations 1_x and 2_x. This issue is improved in the remaining configurations (3_x to 5_x) where the mixture leaves freely from the top outlet boundary with the help of buoyancy.

In the vertical $YZ_{3'}$-plane (figure 6.24), the effect of the air cross-flow and the jet axis defor-

mation is viewed in all cases in the middle–lower part of the cavity. Moreover, similar helium stratification levels are reported outside the buoyant jet in all cases.

However, significant discrepancies take place in this plane. First, the deformation of the axis in this plane remains to higher altitudes in configuration 0_x compared to the remaining cases where the height of this deformation is reduced by increasing Lx (1_x to 4_x). This issue can be justified by the jet inclination that is strengthened in the configurations that employ an exterior domain. Almost no differences are noted in the last two cases.

Second, the stratified layers at the top of the cavity (mainly corresponding to 10, 13 and 16% of helium) are predicted to descend more in the configuration that does not employ an exterior domain (for example the layer corresponding to 10% of helium is situated about a height 9 cm in 0_x which is approximately 1.5 cm higher in other cases).

The issue of the non-symmetrical distribution which has been already reported with configurations 2_x and 3_x is also depicted with the $< X_1 >_t$ contour lines at the top of the plane $YZ_{3'}$. We emphasize again that this is due to the influence of the exterior domain sizes in these particular configurations as far as the distribution reattains its almost symmetrical behavior starting from configuration 4_x.

We present next the influence of the configuration on the rms field (illustrated by iso-contours plots) of the helium mass fraction $\text{rms}\{Y_1\}_t$ in same vertical planes (figures 6.25 and 6.26).

In the plane XZ_1 (figure 6.25), the rms reaches its maximum at the jet axis in all cases (lower part of the cavity) due to the heavy air impacting the ascending light helium which induces stiff concentration gradients. However, the rms field in this plane is modified by the configuration where oscillations are specially recorded near the left wall in the configurations that employ an exterior domain (except configuration 3_x). These oscillations, which are not recorded in configuration 0_x, increase when Lx increases.

Similarly in the vertical plane $YZ_{3'}$ (figure 6.26), the rms distribution is dependent on the simulated configuration. We note basically that the rms is only significant (in this particular plane) in the configurations that employ an exterior region in the computational domain (except for configuration 3_x). The significant values are again located in the position of the heavy-light fluid impact and are strengthened by increasing the horizontal length Lx.

It can be stated that in both plane, unlike the time-averaged fields, the rms distribution is not trivially similar in the last two cases (configurations 4_x and 5_x). This can be justified again by the fact that the convergence of the deviated quantities is usually the slowest (recall the error evolution depicted in figures 6.9 and 6.10).

As stated previously when considering the rms of the velocity magnitude $|\mathbf{u}|$ (recall figures 6.17 and 6.18), the behavior of $\text{rms}\{Y_1\}_t$ in configuration 3_x is not easy to explain and is just related to the specific extension size Lx used in this computational domain.

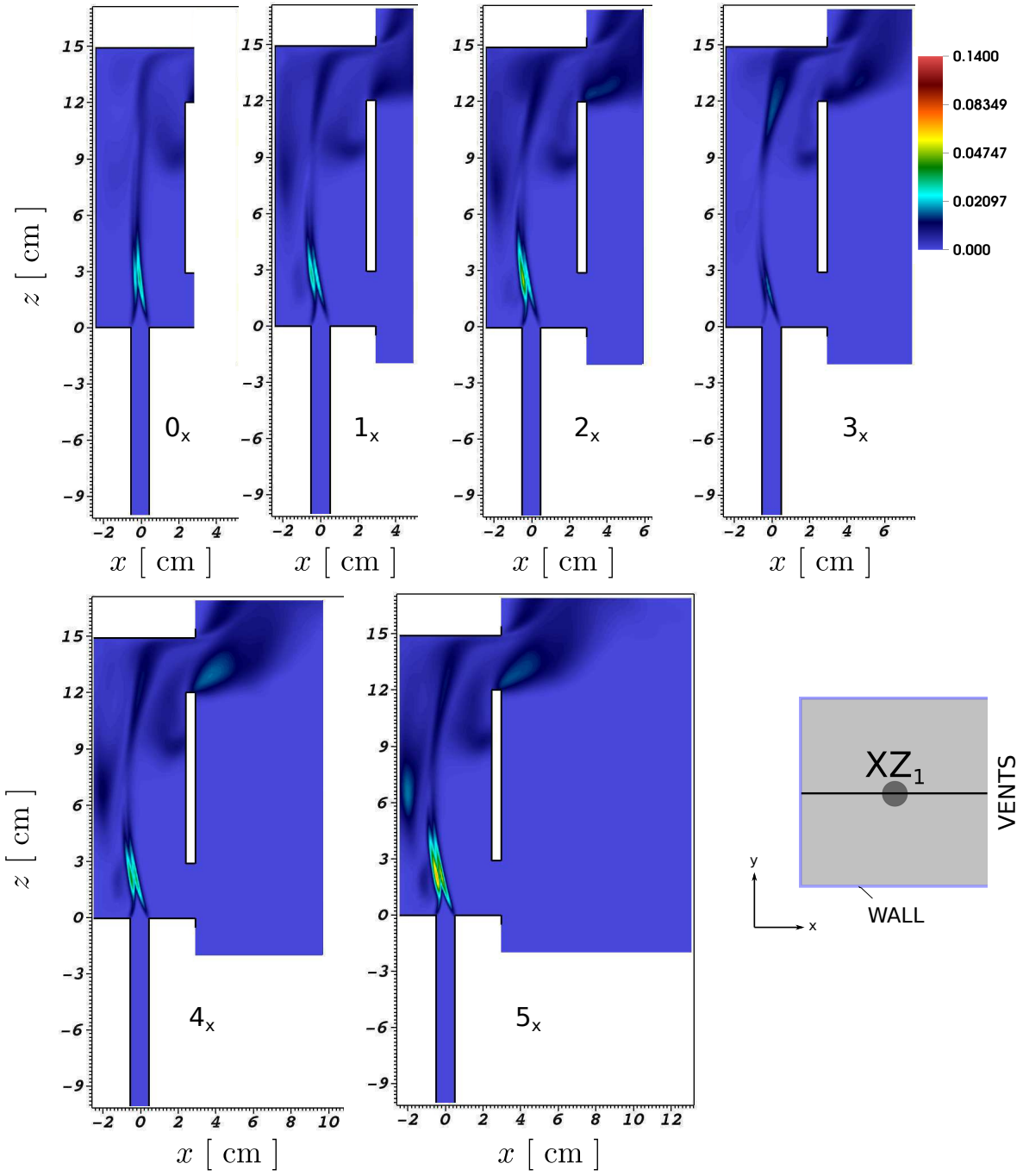

Figure 6.25: RMS iso-contours of the helium mass fraction rms$\{Y_1\}_t$ in the mid vertical XZ_1 plane. Left to right, top to bottom: configurations 0_x to 5_x.

6.2.5 Global quantitative comparison: helium mass and flow-rates

In order to perform a global comparison on the influence of configurations that take or not an exterior domain into account, we calculate the time-averaged total mass of helium $< \mathcal{M}_{He} >_t$

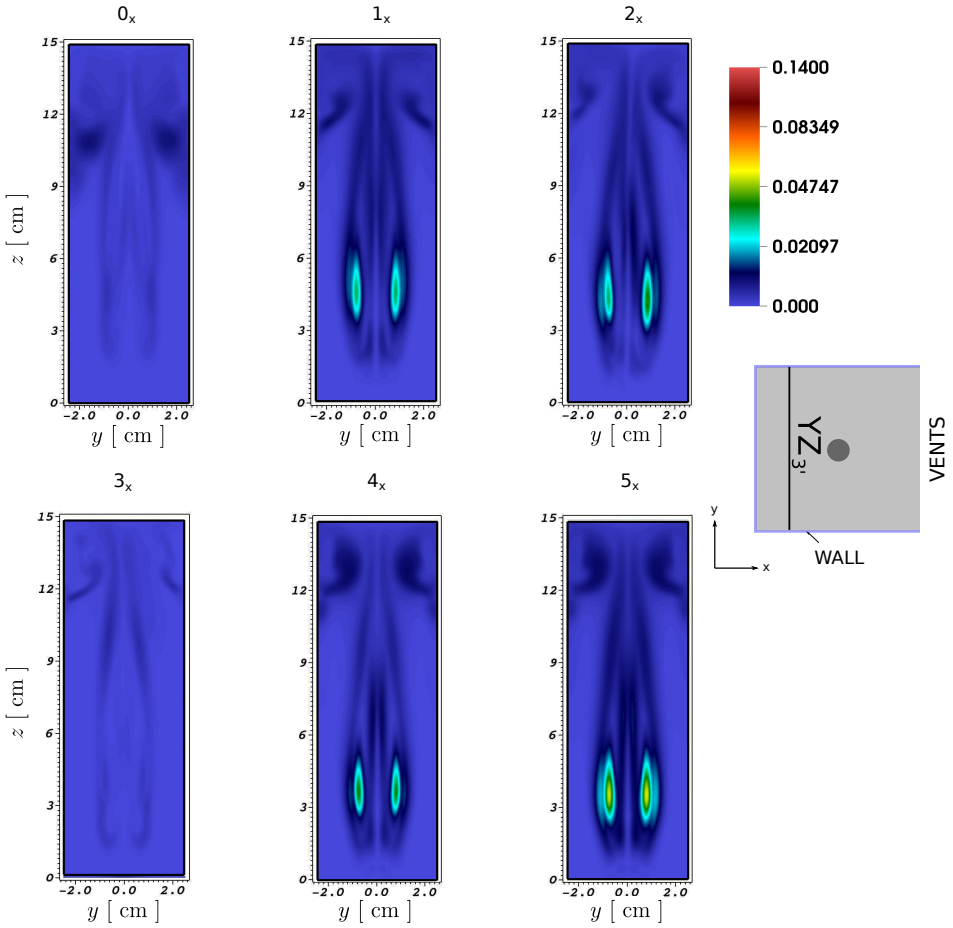

Figure 6.26: RMS iso-contours of the helium mass fraction rms$\{Y_1\}_t$ in the vertical $YZ_{3'}$ plane. Left to right, top to bottom: configurations 0_x to 5_x.

(inside the cavity), helium mass flow-rate leaving the top vent $< q_{He}^{top} >_t$, volumetric flow-rate of air entering the bottom vent $< Q_v^{bot} >_t$ and that of the mixture leaving from the top $< Q_v^{top} >_t$. The values are summarized in table 6.3.

We can clearly note that the configuration that does not take into account an exterior region overestimates the mass of helium $< \mathcal{M}_{He} >_t$ inside the cavity, compared to the remaining configurations. This is justified by the values of the volumetric flow-rates entering and leaving the cavity, respectively $< Q_v^{bot} >_t$ and $< Q_v^{top} >_t$, which are lower in configuration 0_x.

Regarding the configurations that employ an exterior region in the computational domain, we can not generalize any rule to relate the global variation with the increase of Lx. All what we can say is that the values of the total mass are sensitive to Lx and that they are always in agreement with the helium mass flow-rate leaving the top vent ($< q_{He}^{top} >_t$) and the volumetric flow-rates $< Q_v^{bot} >_t$ and $< Q_v^{top} >_t$. Among them, the cavity of configuration 4_x contains the greatest mass of helium and record the smallest values for $< q_{He}^{top} >_t$, $< Q_v^{bot} >_t$ and $< Q_v^{top} >_t$. However, almost convergent values are recorded in the last two configurations.

Configuration	$< \mathcal{M}_{He} >_t$ [$\times 10^{-6}$ kg]	$< q_{He}^{top} >_t$ [$\times 10^{-5}$ kg.s^{-1}]	$< Q_v^{bot} >_t$ [$\times 10^{-4}$ m^3.s^{-1}]	$< Q_v^{top} >_t$ [$\times 10^{-4}$ m^3.s^{-1}]
$\mathbf{0}_x$	9.02033	1.41644	-2.57013	3.47496
$\mathbf{1}_x$	8.10638	1.42059	-2.81147	3.71449
$\mathbf{2}_x$	8.30408	1.40970	-2.80676	3.70839
$\mathbf{3}_x$	8.20663	1.42378	-2.77233	3.67504
$\mathbf{4}_x$	8.47855	1.39376	-2.60348	3.49892
$\mathbf{5}_x$	8.45375	1.39996	-2.60436	3.50027

Table 6.3: Global time averaged quantities for configurations 0_x to 5_x: helium total mass ($< \mathcal{M}_{He} >_t$), mass and volumetric flow-rates.

For instance, selecting the helium mass obtained in configuration 5_x as a reference value, the relative error of $< \mathcal{M}_{He} >_t$ estimated in configuration 4_x reads 0.3%.

6.2.6 Convergence on the size of the exterior domain

In this subsection, we present a convergence study on the size of the exterior domain; basically on the x-horizontal extension Lx. Thus only the five configurations, where an exterior domain is modelled, are considered. From this study, the minimum extension value required so that the flow inside the cavity becomes independent from increasing Lx is identified.

The mean and rms quantities calculated at the same 14,161 probes of configuration 5_x have been chosen as the reference values. The evolution of the relative error versus configurations 1_x to 4_x is graphed in figures 6.27 and 6.28.

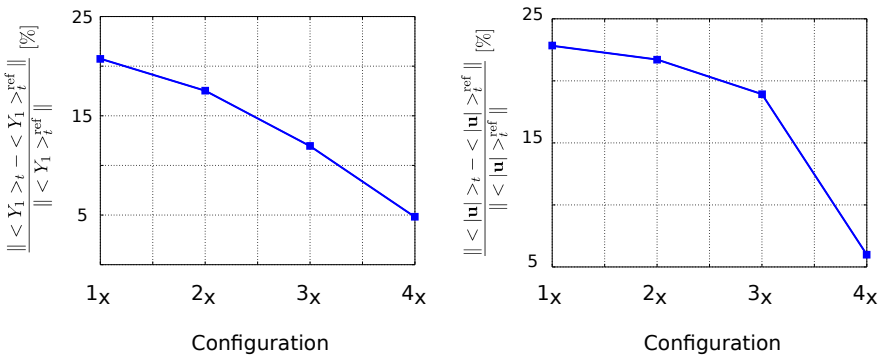

Figure 6.27: Evolution of the L2 norm mean relative error as a function of configurations 1_x to 4_x. Left: helium mass fraction Y_1, right: velocity magnitude $|\mathbf{u}|$.

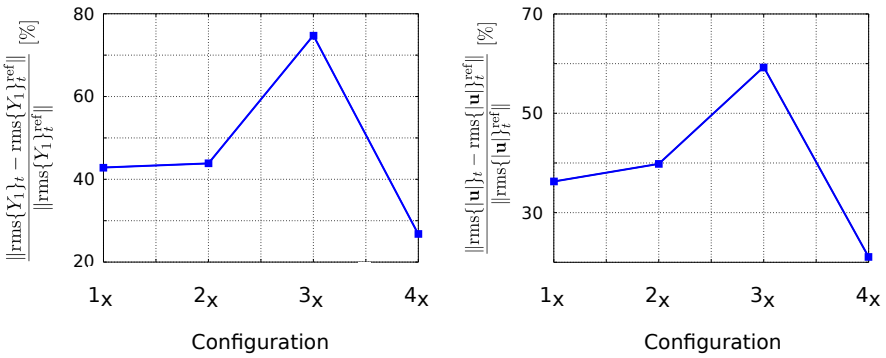

Figure 6.28: Evolution of the L2 norm rms relative error as a function of configurations 1_x to 4_x. Left: helium mass fraction Y_1, right: velocity magnitude $|\mathbf{u}|$

It can be stated that the results are satisfactory and we assume that a convergence is attained. Regarding the mean relative error, it is clear that a significant decrease takes place where the mean mass fraction error decays from 21% to 4.8% and that of $|\mathbf{u}|$ from 23% to 6%. We recall that with such an employed mesh size, the error on evaluating the mean of Y_1 and $|\mathbf{u}|$ is respectively 8% and 12% (subsubsection 6.1.2.3).

It has been figured out again that the convergence of the rms is rather slower. However, the sharp relative error decay from configuration 3_x to 4_x is clearly noted, both on Y_1 and $|\mathbf{u}|$, and it is rather related to the rms field predicted with configuration 3_x (review figures 6.17 and 6.18). We emphasize again that neither physical nor numerical interpretations are provided to explain why such a distribution is recorded. All what we say is that it is a result of a significant influence due the particularly considered exterior domain extensions.

In conclusion, we can say that for a horizontal extension $L_x \geq 6.75$ cm (configuration 4_x), the interior cavity flow becomes almost independent on the exterior region and no further influence will be recorded. Thus, unless stated otherwise, the results presented in the sequel for a simulation with an exterior domain corresponds to those obtained by configuration 4_x.

6.3 Computational cost report

6.3.1 Physical time integration for statistical convergence

To illustrate on the convergence of the performed statistics and on the quasi-stationarity of the solution, we perform a global error convergence study. We recall that the recorded statistics has been carried out over 40 seconds of accumulation, starting from a physical time of 70 s to the end of the simulation at 110 s. Defining the height of the cavity as a reference ($H_r = 14.9$ cm) and the maximum injection velocity as a reference velocity ($\mathbf{u}_r = 2.33$ m.s^{-1}), the 40 s of statistical accumulation corresponds to 625 of non-dimensional time.

In each simulation, the evolution of Y_1 and $|\mathbf{u}|$ at 14,161 fixed probes (17 x 17 x 49) inside the

cavity is recorded again with a frequency of 10^3 Hz. The mean and rms values are evaluated over 5 time windows; respectively as [5:40], [40:80], [50:90], [60:100] and [70:110] seconds. A **reference solution** is considered for a single window average over [70:110] seconds, the interval employed in all the previous post-treatment results.

The L2 norm of the relative error shows satisfactory convergent results in all cases. For example, in configuration 4_x, the relative error on the helium mass fraction Y_1 mean decreases from 2.2% to 0.6% while that of $|\mathbf{u}|$ drastically drop down from 3.7% to 0.95%.

As expected, the convergence of the rms values is rather slower compared to the mean quantities. It has been noticed for example in configuration 4_x, that the error norm of the Y_1 rms decrease from 9.8 % to 3.8% and from 8.8% to 3% for $|\mathbf{u}|$.

6.3.2 Total computational wall-time

The six simulations have been carried out on the CEA–Saclay local cluster. The cluster is organized with different CPU's that do not have the same performance and communication. The total computational cost is summarized in table 6.4.

Configuration	**MPI procs**	**Time [hours]**	**Time [days]**
0_x	20	353.2	14.7
1_x	40	350	14.6
2_x	40	476.2	19.85
3_x	60	505.3	21.1
4_x	80	415.8	17.32
5_x	100	485.14	20.2

Table 6.4: Computational cost: simulations LES with a physical time $t = 110$ seconds, CEA–Saclay CALLISTO cluster.

6.4 Concluding remarks

3D LES results has been presented in this chapter by employing the classical Smagorinsky's SGS model and the CEA TRUST-TrioCFD. At a first stage, the LES configuration has been identified. Different numerical schemes have been tested and the choice was made to well reproduce the physical phenomenon of the problem (mainly a transitional non-laminar regime at the top of the cavity). A grid convergence study has been carried out and a mesh size has been identified to reproduce LES convergent results.

In a next step, numerical simulations have been carried out to study the influence of modelling an exterior region in the computational domain. Analyses performed on time averaged quantities show a lot of similarities in the flow pattern in all cases; basically the kinetic energy distribution and the deformation of the jet axis. However, significant discrepancies have been identified on the helium distribution in the cavity and on the global averaged quantities like volumetric and mass flow-rates. It has been shown that the configuration without an exterior domain, when compared with other configurations, underestimates the volumetric flow rate of fresh air entering the cavity and thus overestimates the total mass of helium inside the cavity. The minimum extension value required so that the flow inside the cavity becomes independent from increasing the size of the exterior domain is identified by performing a convergence study on the exterior domain size. Thus, all the results presented in the sequel of this thesis for a configuration with an exterior domain are devoted to configuration 4_x only.

We have shown that the size of the exterior domain, when taken into account in the LES calculations, can introduce non-symmetrical velocity distributions inside the cavity. In a more general manner, the non-symmetry of the velocity distribution has also been observed in the experiments which can be illustrated by the 2D time averaged velocity magnitude $< |\mathbf{u}|_{YZ} >_t$ in the vertical planes $YZ_{4'}$ and $YZ_{3'}$ (figure 6.29).

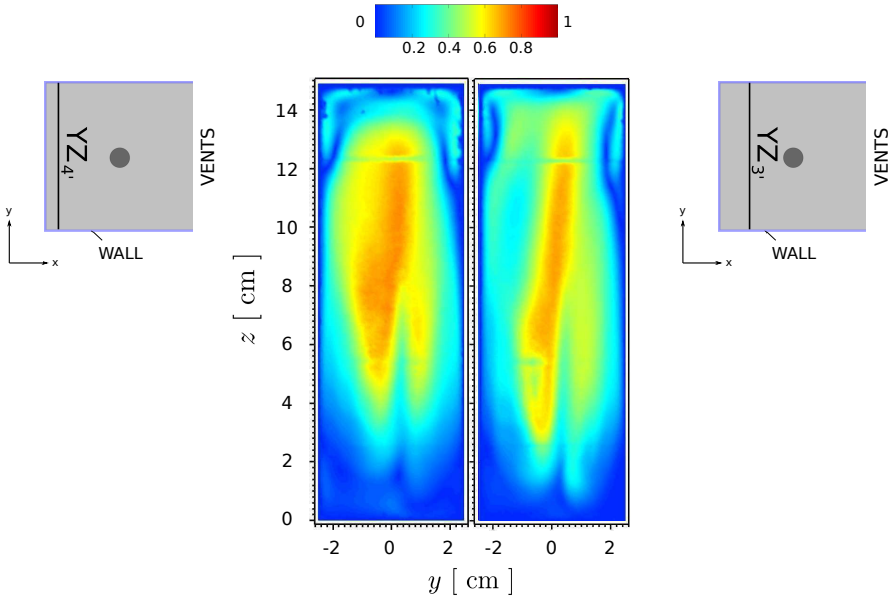

Figure 6.29: PIV measured time averaged flow pattern illustrated by the 2D velocity magnitude $< |\mathbf{u}|_{YZ} >_t$ [m.s^{-1}] iso-contour plot. Left: vertical $YZ_{4'}$-plane, right: vertical $YZ_{3'}$-plane.

Those non-symmetries appear when there is a very slight non-verticality of the experimental set-up (less than 1°) or also when PIV recordings are performed without waiting a time long enough for reaching a steady environment in the experimental garage (after human operations in the garage). Therefore, we want to emphasize the very strong sensitivity of the physical fluctuations on the surroundings. The chosen test-case presented in the present dissertation is a lot more complex than we have foreseen and requires to be very cautious, both numerically

and experimentally.

In the framework of this study, LES preliminary results have been presented in the 23ème Congrès Français de Mécanique (CFM-2017) [SSBMT17] and the International Conference on Hydrogen Safety (ICHS-2017) [SBMS$^+$17] (appendix E).

Chapter 7

LES validation against PIV

Contents

This chapter is devoted to the validations of the performed LES calculations. The accuracy of the statistical fields and a qualification analysis of the LES calculation are firstly presented. In a next step, LES–PIV comparisons in several 2D sections of the cavity are discussed. Finally, CFD predictions are used to characterize the 3D helium concentration distribution as far as no experimental data are currently available on the concentration field due to the limited size of the domain which makes it difficult to employ internal sensors.

The variables employed in the post-treatment throughout the chapter are all defined in appendix C. A description of the carried out PIV technique can be reviewed from section 2.3, and more detailed in the technical report of Jiaying Bi in [Bi17].

7.1 Statistical accuracy

We present the accuracy of the statistical data and the bounds of the numerical–statistical error. Almost all post-treated fields are presented as time averaged quantities in the quasi-steady state solution.

We define the numerical–statistical error (standard error of the mean), recalled from equation (C.5)

$$\mathrm{Err}(\varphi) = \frac{\mathrm{rms}\{\varphi(t)\}_t}{\sqrt{\mathcal{N}}}, \tag{7.1}$$

where $\mathcal{N}$ denotes the number of independent samples and $\varphi(t) = \{Y_1, |\mathbf{u}|\}$.

To identify the number of independent samples in the performed statistics, we estimate the auto-correlation function (ACF) presented in equation (C.4)

$$r(\tau)_{\varphi(t)} = \frac{< \varphi'(t).\varphi'(t+\tau) >_t}{< \varphi'(t)^2 >_t}, \tag{7.2}$$

for a time lag τ.

The sample frequency $f = 10^3$ Hz. The analysis is carried out from the evolution of φ at two fixed probes. First at point $M(x = 0, y = 0, z = 5)$ cm which is situated above the injection by about 1/3 of the cavity's height, while the second is in the fluctuating regime at the top vent $N(x = 2.45, y = 0, z = 13.5)$ cm (see sketch in figure 7.1).

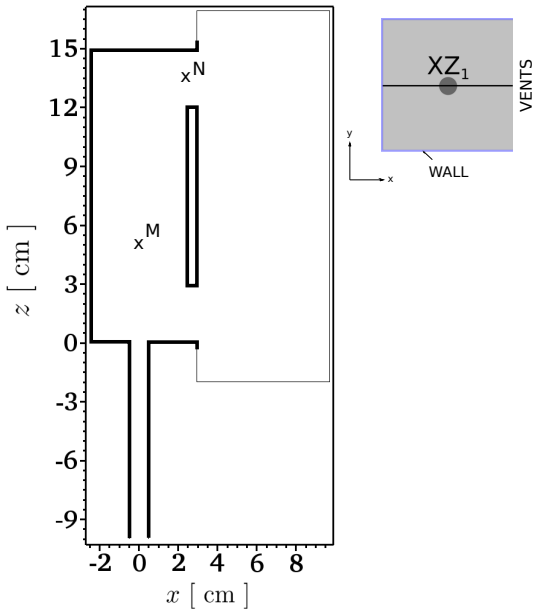

Figure 7.1: Schematic representation of the cavity in the mid-vertical XZ_1-plane showing both spatial positions of the probes $M(x = 0, y = 0, z = 5)$ cm and $N(x = 2.45, y = 0, z = 13.5)$ cm.

It has been figured out that the variation of the ACF is sensitive to both, the quantity φ and the considered point. This means that the statistical accuracy is not uniform and identical in the entire computational domain.

At point M, the ACF evolution of Y_1 and $|\mathbf{u}|$ are plotted respectively in figures 7.2 and 7.3. From the graphs, we note that the correlation rapidly decreases with the time delay τ for both variables. A good quadratic polynomial is fitted around the origin and thus plotted on the same graphs (red line). According to the definition of the Taylor micro-scale λ_f in the book of Pope [Pop00], $\lambda^M_{f_{Y_1}} \approx 0.2$ s and $\lambda^M_{f_{|\mathbf{u}|}} \approx 0.18$ s (intersection of the inscribed fitted parabola with the time delay axis). Thus, from the values of λ_f, we deduce that at the point M, each consecutive 200 samples in the evolution of Y_1 are correlated while the same holds

with 180 samples for $|\mathbf{u}|$.

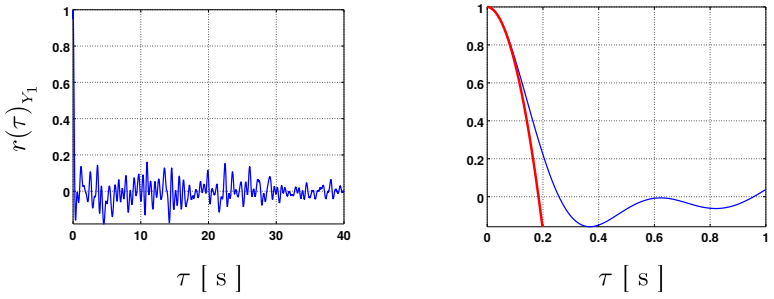

Figure 7.2: ACF(Y_1) at a point $M(x = 0, y = 0, z = 5)$ cm. Left: evolution over the complete statistical time integration $\tau = 40$ s, right: evolution in a zoomed region with $\tau = 1$ s. Red line correspond to the inscribed fitted parabola, used to determine the Taylor micro-scale λ_f.

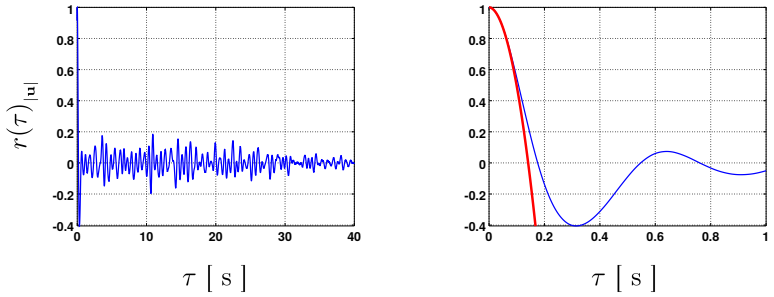

Figure 7.3: ACF($|\mathbf{u}|$) at a point $M(x = 0, y = 0, z = 5)$ cm. Left: evolution over the complete statistical time integration $\tau = 40$ s, right: evolution in a zoomed region with $\tau = 1$ s. Red line correspond to the inscribed fitted parabola, used to determine the Taylor micro-scale λ_f.

At point N, the behavior is quiet different. We consider in figure 7.4 the evolution of ACF(Y_1). Again, the curve decays and the parabola indicates a time scale $\lambda^N_{f_{Y_1}} \approx 0.05$ s. Hence at point N, each consecutive 50 points on the profile of Y_1 are dependent.

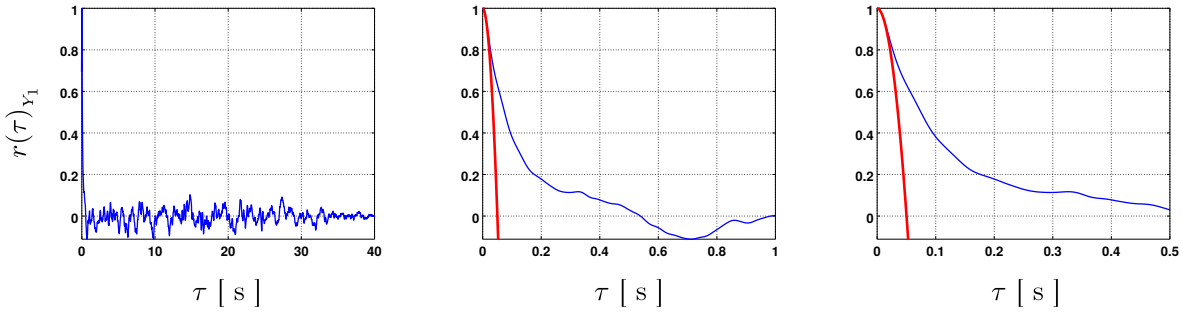

Figure 7.4: ACF(Y_1) at a point $N(x = 2.45, y = 0, z = 13.5)$ cm. Left: evolution over the complete statistical time integration $\tau = 40$ s, middle and right: evolution in a zoomed region with $\tau = 1$ and 0.5 s respectively. Red line correspond to the inscribed fitted parabola, used to determine the Taylor micro-scale λ_f.

We draw attention to the ACF($|\mathbf{u}|$) at a point $N(x = 2.45, y = 0, z = 13.5)$ cm, which is

illustrated in figure 7.5. The curve indicates that the velocity field follows a periodic behavior each 0.7 seconds. Moreover, the inscribed fitted parabola record $\lambda_{f_{|\mathbf{u}|}}^{N} \approx 0.025$ s, showing that the number of correlated samples is 25.

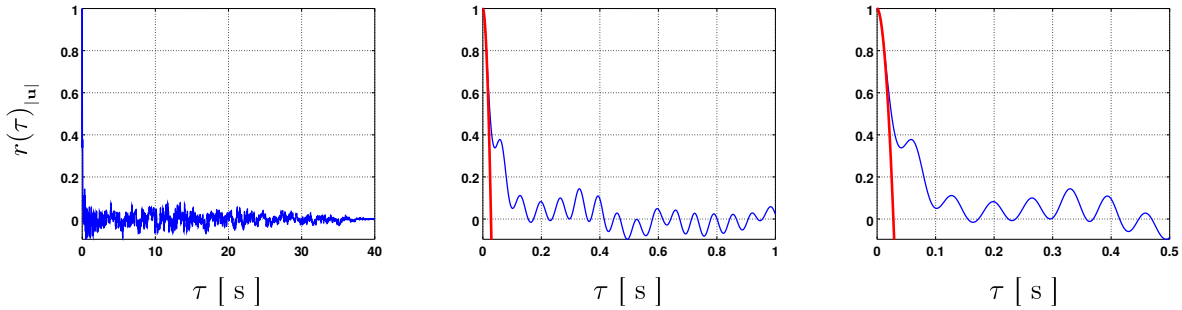

Figure 7.5: ACF($|\mathbf{u}|$) at a point $N(x = 2.45, y = 0, z = 13.5)$ cm. Left: evolution over the complete statistical time integration $\tau = 40$ s, middle and right: evolution in a zoomed region with $\tau = 1$ and 0.5 s respectively. Red line correspond to the inscribed fitted parabola, used to determine the Taylor micro-scale λ_f.

In all cases, we note that the convergence of $r(\tau)$ towards zero is rather long since it has been reached for a time delay of about 40 s, the total time of the statistical recordings in our simulation. This high delay is justified by a low frequency flapping motion that occurs in the studied configuration.

Under the defined frequency f, 40 seconds of statistical recordings correspond to 40×10^3 samples in total, which contain correlated and uncorrelated data. We have illustrated, from the previous figures, that the smallest time scales of the autocorrelation λ_f is not unique and depend on both the spatial location and the fluid variable. Hence, the independent number of samples contained in a time evolution series at different probes positioned inside the cavity are not the same.

As a consequence, the numerical standard error (Err) at the considered points is summarized in table 7.1. We note that the statistical error in the upper part of the cavity near the top vent (point N) is obviously greater than that in the lower part of the cavity near the jet axis. This can be justified by the fact that the fluid variables at point M are not subjected to high fluctuations as those in the top vent vicinity (point N, recall the rms field in figure 6.17).

7.2 Qualification of the performed LES calculation

In chapter 6, we have shown that according to a carried grid convergence study, we could identify the cell size δ necessary for a good prediction. In this section, we look towards investigating wherther the performed LES calculation is well solved or not. To illustrate, we consider the two vertical XZ_1 and $YZ_{4'}$ planes. An LES qualification similar to that carried out by Maragkos et al. while simulating a large helium buoyant plume in [MRWM13] is performed and the analysis is presented in what follows.

Point	Variable $\varphi(t)$	Independent samples $\mathcal{N}$	Error $\mathrm{Err}(\varphi)$
M	Y_1	200	$7 \times 10^{-3}\%$
	$\|\mathbf{u}\|$	222	1.2×10^{-3} m.s^{-1}
N	Y_1	800	$2 \times 10^{-2}\%$
	$\|\mathbf{u}\|$	1600	4.2×10^{-3} m.s^{-1}

Table 7.1: Standard statistical error defined from the ACF at two points situated in different flow regimes.

7.2.1 Modeled to laminar viscosity ratio

The ratio of the modeled SGS to the laminar mixture kinematic viscosity is calculated inside the cavity only (the modeled viscosity in the exterior domain is not taken into account). As presented in [SGMS10], this ratio serves to be a good indicator on the quality of the performed LES. Globally, we observe from figure 7.6 that ν_{SGS}/ν takes a maximum of 0.34 at the quasi-steady state solution, which confirms that a fine LES has been carried out.

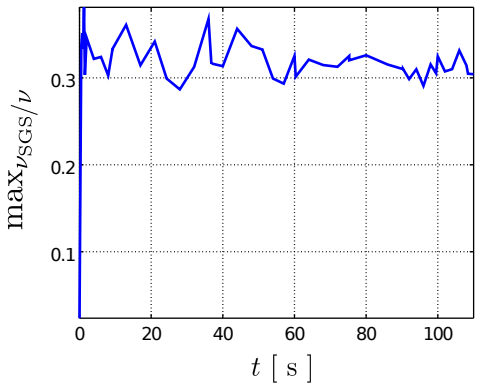

Figure 7.6: LES qualification: instantaneous evolution of the maximum SGS to the mixture laminar viscosity's ratio (ν_{SGS}/ν) inside the cavity.

In what follows, otherwise stated, all the instantaneous fields and profiles are presented at the time $t = 106$ seconds. First, we consider the mid vertical XZ_1-plane where the modeled SGS viscosity ν_{SGS}, the laminar viscosity of the mixture ν and their corresponding ratio ν_{SGS}/ν are considered respectively (figure 7.7).

The iso-contours show that the highest values of ν_{SGS} are recorded at the jet axis and in the recirculating zones located mainly in the top left corner and in the region between the jet-left wall (figure 7.7, left). This is confirmed as far as, by construction, the Smagorinsky's model is linearly dependent of the velocity gradients. The importance of the modeled ν_{SGS} is reflected

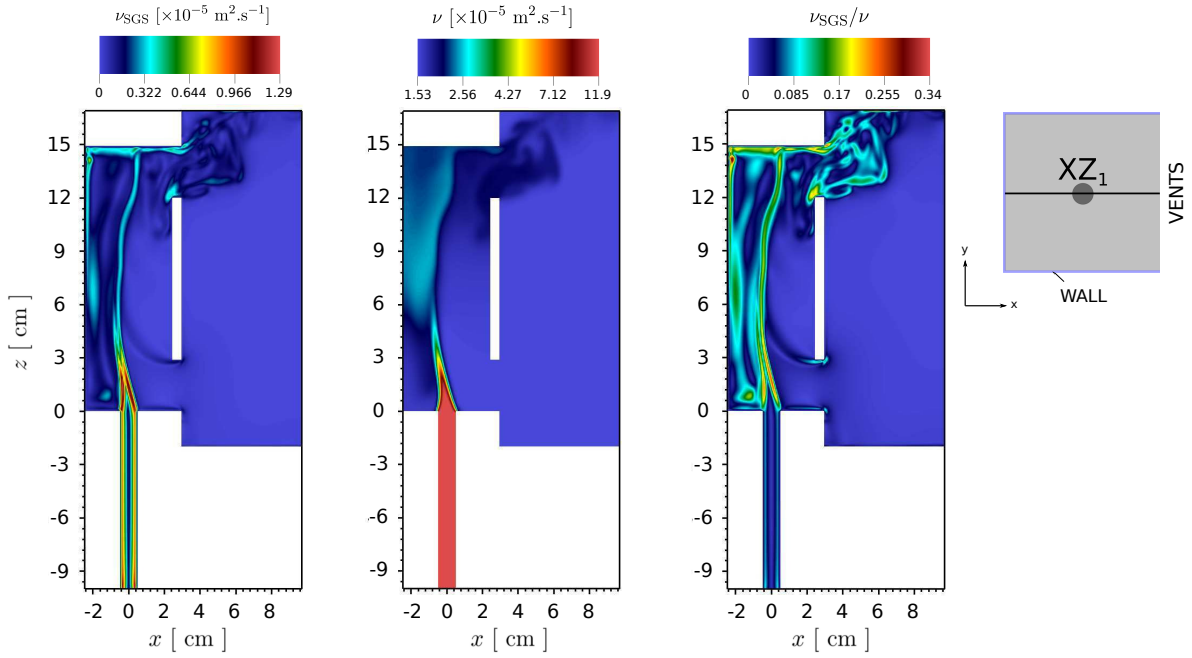

Figure 7.7: Instantaneous iso-contour plots at $t = 106$ seconds in the vertical mid XZ_1-plane. Left: SGS kinematic modeled viscosity ν_{SGS}, middle: mixture kinematic laminar viscosity ν (levels in a log scale), right: viscosity ratio ν_{SGS}/ν.

on the viscosity ratio (figure 7.7 right). It points on the high kinetic energy-dissipative regions.

Similar fields are considered in the vertical $YZ_{4'}$ plane, which contains an main part of the buoyant jet resulting from the inclination towards the left wall (figure 7.8).

We can note that the SGS viscosity and its corresponding ratio are concentrated at the jet axis and in the two recirculating regions situated in the right and left top corners, which is coherent with the definition of the Smagorinsky's SGS viscosity that is related to the macroscopic velocity gradients that are significant in these regions. Moreover, two interesting observations are recorded in this plane. First, the distributions of ν_{SGS} and ν are somehow symmetrical at this particular time instant (a low frequency flapping phenomenon exists in this plane). Next, the effect of the axis deformation in the lower part of the cavity is reflected on the distribution of the viscosities.

Instantaneous horizontal and span-wise profiles of the viscosity ratio are plotted at three different heights ($z = 1.2$, 7.8 and 14.2 cm) in the vertical planes and sketched in figure 7.9.

In the plane XZ_1, we can clearly identify peaks that indicate the position of the jet edges at $z = 1.2$ and 7.8 cm, and the recirculating zones at $z = 14.2$ cm. However in the plane $YZ_{4'}$, the symmetrical distribution is justified at the first to heights, in contrast to the profile of $z = 14.2$ cm that is situated in the fluctuating regime that takes place at the top of the cavity (velocity rms distribution similar to that depicted in the neighbour plane of figure 6.18).

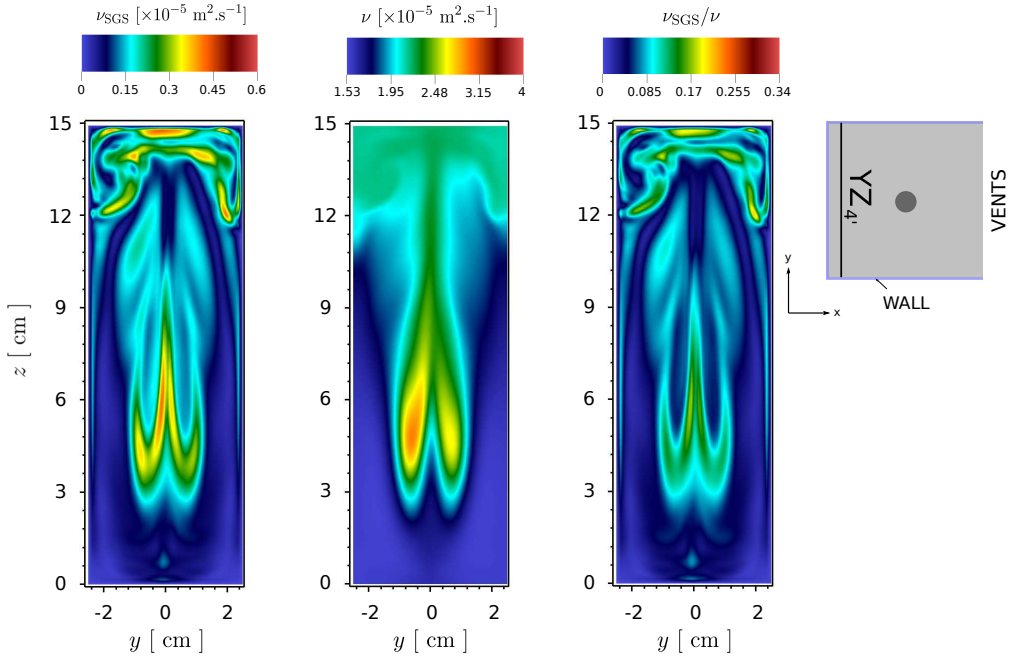

Figure 7.8: Instantaneous iso-contour plots at $t = 106$ seconds in the vertical $YZ_{4'}$-plane. Left: SGS kinematic modeled viscosity ν_{SGS}, middle: mixture kinematic laminar viscosity ν (levels in a log scale), right: viscosity ratio ν_{SGS}/ν.

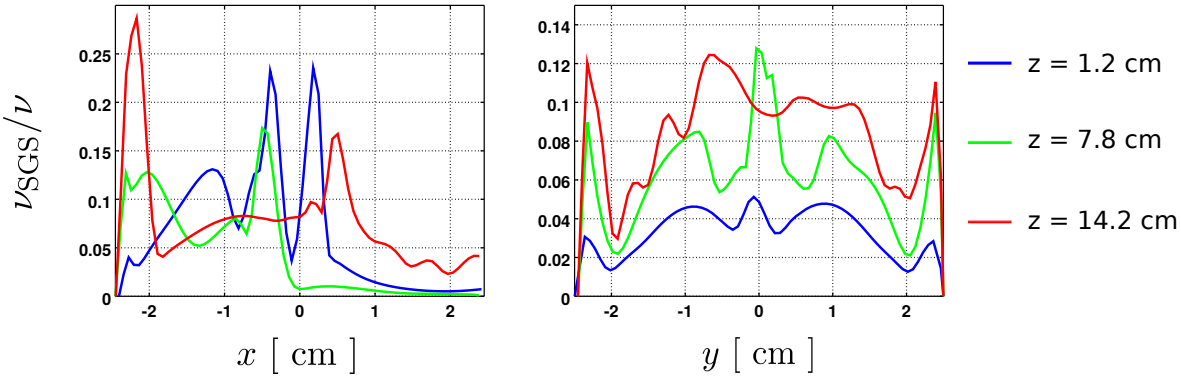

Figure 7.9: Horizontal and span-wise instantaneous profiles ($t = 106$ s) of the viscosity ratio ν_{SGS}/ν. Left: vertical mid XZ_1-plane, right: vertical $YZ_{4'}$-plane.

7.2.2 Kolmogorov length scale

A Kolmogorov length scale η_{LES} is estimated from the obtained LES results using the definition

$$\eta_{LES} = (\nu^3/\epsilon_{LES})^{0.25}, \tag{7.3}$$

where the instantaneous total dissipation rate is evaluated as

$$\epsilon_{LES} = 2(\nu_{SGS} + \nu)(S_{ij}S_{ji}). \tag{7.4}$$

The instantaneous distribution of the Kolmogorov length scale η_{LES} and the ratio of the grid spacing δ to η_{LES} have been estimated in the vertical XZ_1 and $YZ_{4'}$ planes and the iso-contour fields are sketched respectively in figures 7.10 and 7.11.

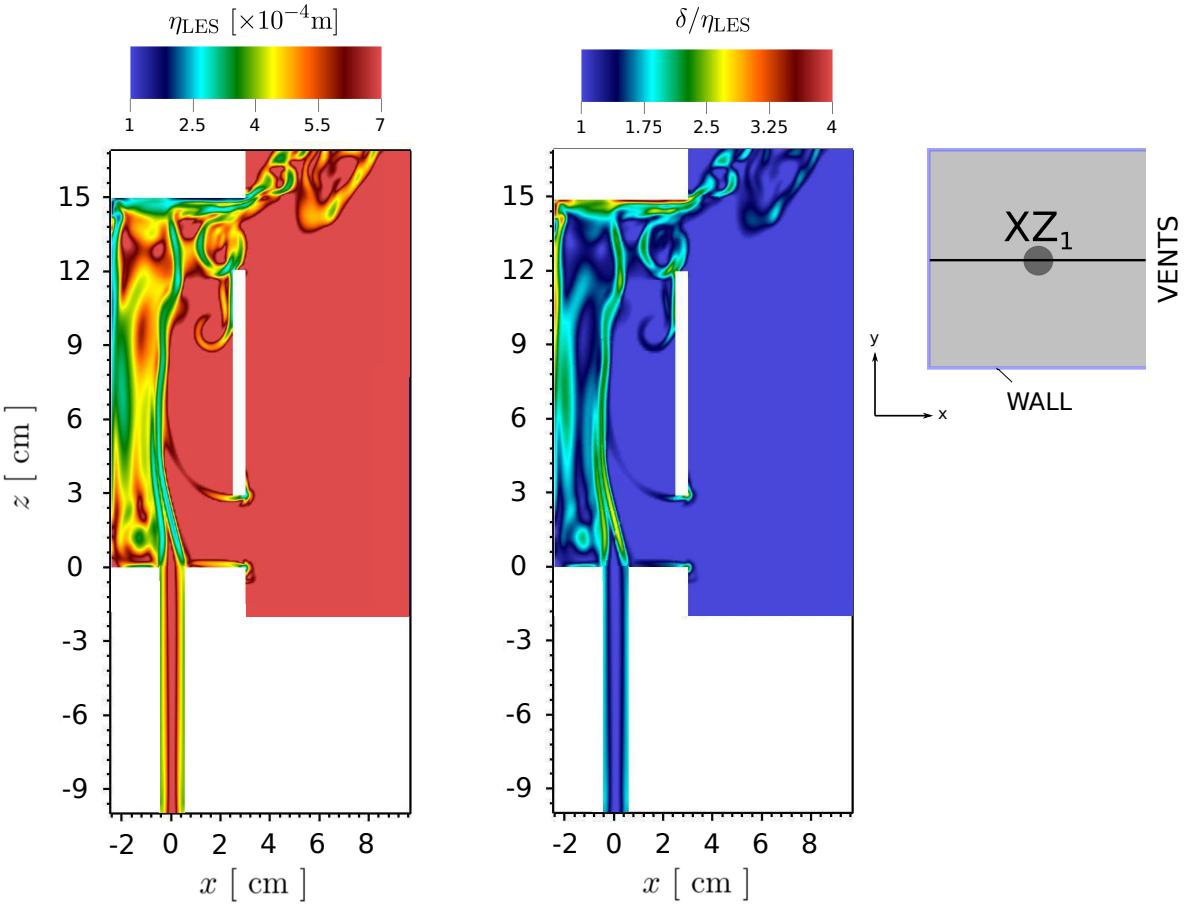

Figure 7.10: Instantaneous iso-contour plots at $t = 106$ seconds in the mid vertical XZ_1-plane. Left: estimated Kolmogorov length scale η_{LES}, right: ratio of the grid spacing δ to Kolmogorov length scale η_{LES}.

It is noted from the two vertical planes that η_{LES} is dependent on the location and thus on the flow pattern, although the maximum ratio δ/η_{LES} is figured out to be 4 at the top ceiling and at most 3 elsewhere, which is relatively small in the practice of LES [MRWM13]. Assuming that the Smagorinsky model is correctly representing the unresolved scales, we can say that the LES is correctly representing the flow.

Instantaneous horizontal and span-wise profiles of δ/η_{LES} along the three considered heights are depicted in figure 7.12. In the mid-vertical XZ_1-plane (figure 7.12, left), the horizontal profiles show that the largest ratios (relatively smallest Kolmogorov length scales) are situated at the jet edges (peaks on the horizontal profiles) and in the recirculation regions near the left wall facing the vents. On contrary, in the region near the bottom vent where the flow is almost uniform, the ratio is smaller than unity which means that the mesh is sufficiently enough to capture the small scales without requiring an eddy-viscosity model.

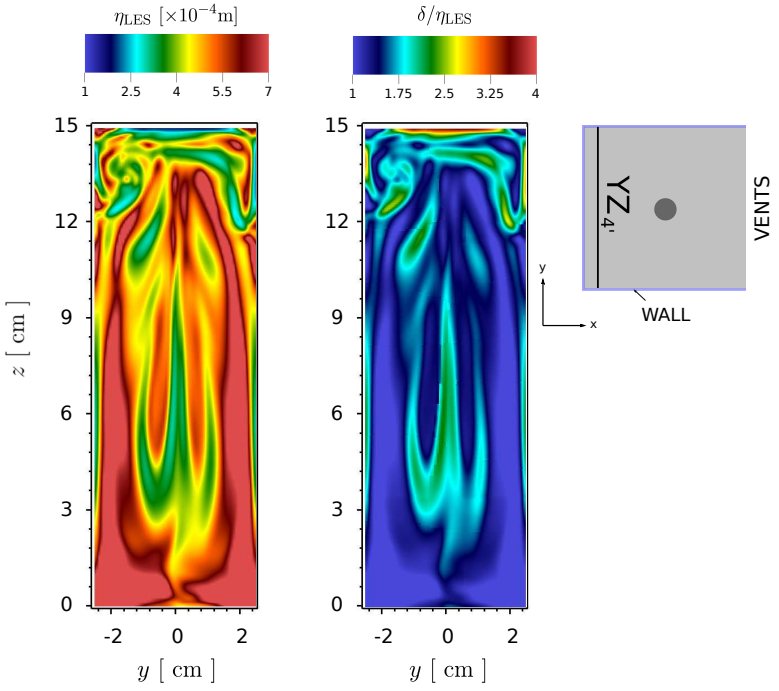

Figure 7.11: Instantaneous iso-contour plots at $t = 106$ seconds in the vertical $YZ_{4'}$-plane. Left: estimated Kolmogorov length scale η_{LES}, right: ratio of the grid spacing δ to Kolmogorov length scale η_{LES}.

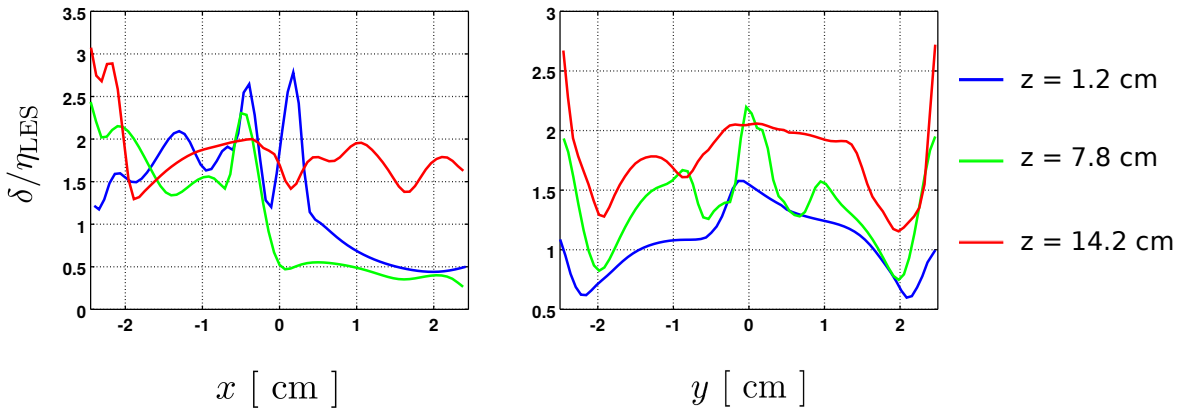

Figure 7.12: Horizontal and span-wise instantaneous profiles ($t = 106$ s) of the grid spacing δ to Kolmogorov length scale η_{LES} ratio. Left: vertical mid XZ_1-plane, right: vertical $YZ_{4'}$-plane.

In the plane $YZ_{4'}$, we note that the largest ratios (smallest length scales) are situated in the vicinity of the solid walls (basically note at the two higher profiles). Globally speaking, the distribution of δ/η_{LES} in this plane shows that the employed mesh size is in average two times larger than the Kolmogorov length scale. Hence, it can be stated that the LES prediction is not far from the DNS solution.

7.3 Comparisons with the PIV measurements

We present here an LES–PIV comparison regarding the velocity fields. As far as the currently available PIV measurements access only the velocity fields in vertical 2D slices, comparisons are presented by considering the instantaneous or time-averaged velocity iso-contours and/or profiles in distinct vertical planes. Thus, no comparisons concerning the concentration distribution and total mass quantities are offered.

7.3.1 Flow pattern: cavity

In figure 7.13, the flow pattern CFD–PIV comparison is illustrated by the iso-contour plot of the $< |\mathbf{u}|_{XZ} >_t$ velocity magnitude in the mid vertical XZ_1-plane.

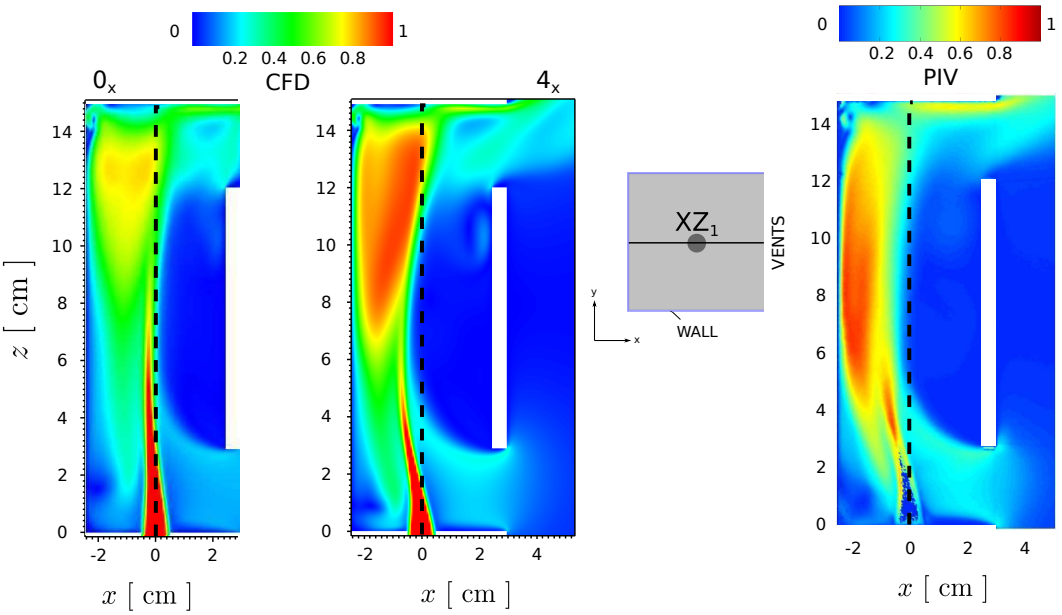

Figure 7.13: CFD-PIV comparison of the time averaged flow pattern illustrated by the 2D velocity magnitude $< |\mathbf{u}|_{XZ} >_t$ [m.s^{-1}] iso-contour plot in the vertical XZ_1-plane. Left: configuration 0_x CFD–LES, middle: configuration 4_x CFD–LES, right: PIV. Thick dashed black line denotes the vertical axis passing through the origin $\mathcal{O}$.

It has been figured out that the global flow pattern obtained from a simulation without an exterior domain (configuration 0_x) is too far from what has been measured by the PIV. In practice, configuration 0_x do not reproduce the inclination of the jet axis due to the air cross-flow effect as that measured by the PIV and predicted by configuration 4_x. Thus, configuration 0_x will not be used in the CFD–PIV validations.

Although the CFD $< |\mathbf{u}|_{XZ} >_t$ iso-contours are in good agreement at the lower part of the cavity with those of the PIV, noticeable discrepancies take place at the top of the cavity. It has been figured out that the plume region in the CFD computation is wider than the experimental

measurements on the one hand, where we see higher velocity magnitudes in a wider region at the top of the CFD visualization. On the other hand, CFD results underestimates the PIV velocity in the recirculating region near the left wall. To illustrate quantitatively, we consider six horizontal profiles in the same plane situated at different heights z = 2, 3.5, 4.5, 5.5, 7 and 14 cm (figure 7.14)).

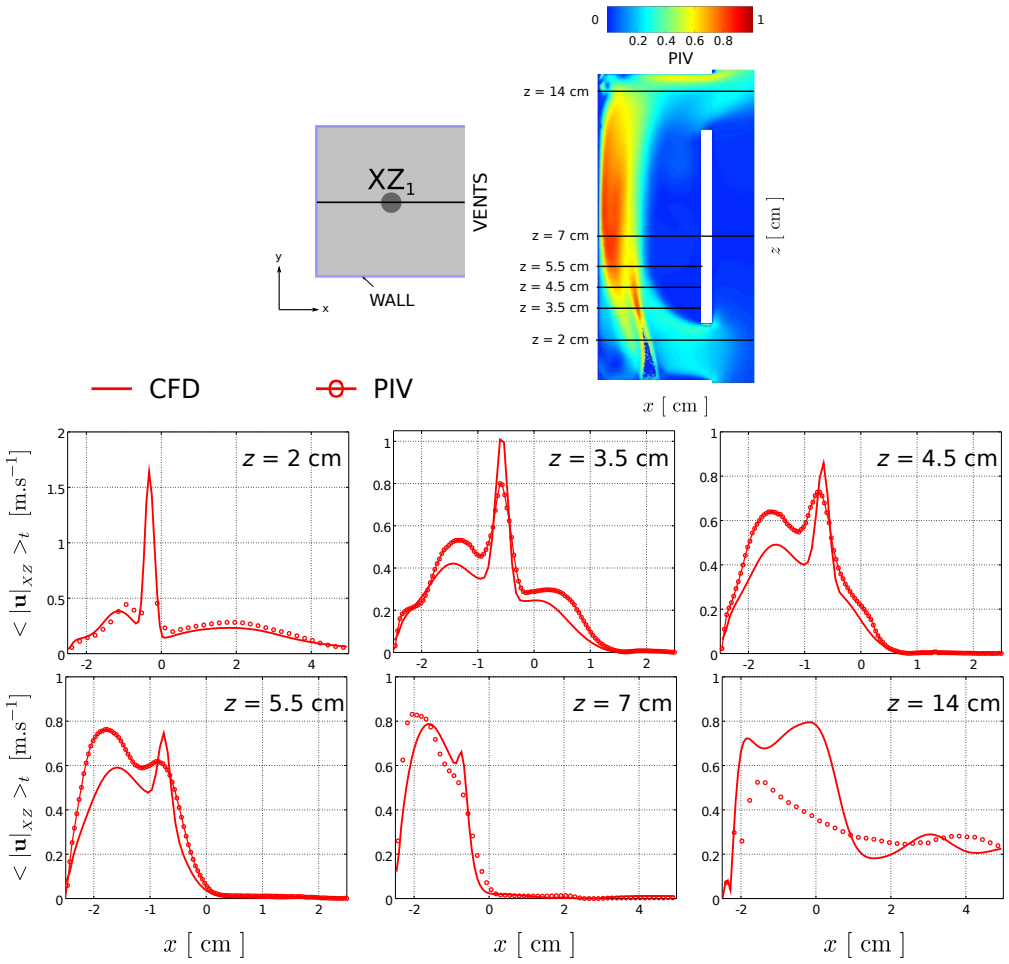

Figure 7.14: CFD-PIV comparison of the time averaged velocity magnitude $< |\mathbf{u}|_{XZ} >_t$ horizontal profiles in the vertical XZ_1-plane. Left to right, top to bottom: z = 2, 3.5, 4.5, 5.5, 7 and 14 cm .

At z = 2 cm, the CFD–PIV $< |\mathbf{u}|_{XZ} >_t$ profiles are in good agreement outside the jet axis. We recall that the PIV measurements inside the jet axis are questionable at this height as far as no additional particles are injected with helium. Quantitative discrepancies starts to be notable as we move in the upward direction (z = 3.5 to 5.5 cm). The CFD calculation always underestimates the PIV velocity in the zone near the left wall, and overestimates the PIV jet axial velocity (underestimation and overestimation can reach about 25%). From a qualitative point of view, we note that the profiles are rather similar and takes almost the same trend. In addition, the agreement between CFD and PIV regarding the position of the jet axis (local maximum) is good. However, the prediction of the horizontal position of the

local maxima near the left wall shows discrepancies while moving in the upward direction (better agreement at $z = 3.5$ compared to 5.5 cm).

The velocity distribution obtained from both approaches (LES and PIV) at $z = 7$ cm indicate that the buoyant jet is almost localized at the same position and with almost the same width. However, the horizontal position of the local maxima near the left wall slightly varies between LES and the PIV. In addition, the PIV measurements do not record the velocity pick predicted by the LES along the jet axis which can probably state that the PIV is more diffusive at this position.

Significant discrepancies are recorded, as expected, at the top of the cavity (profile $z = 14$ cm). In particular, the $< |\mathbf{u}|_{XZ} >_t$ velocity profile shows that the CFD overestimates the measured PIV velocity approximately along the whole width of the cavity (can reach 40%). That contradicts what has been measured from the experiment where it has been figured out that the plume remains mainly concentrated near the left wall. Two points can be stated to explain such discrepancies. Assuming that the PIV is somehow reproducing better the flow pattern, it can be stated at first that the LES is not well capturing the turbulence at the top of the cavity and thus not modelling correctly SGS diffusion to reduce the convective contribution (reduce velocities). A second reason can be probably due to the influence of the helium concentration on the velocity at the top of the cavity (at top–ceiling impact) and near the top vent that can be more concentrated in the PIV at these regions.

Next, we consider the CFD–PIV comparison in the yz-vertical plane series. The CFD–PIV flow pattern in the region near the injection is illustrated by the velocity magnitude $< |\mathbf{u}|_{YZ} >_t$ iso-contours in the vertical $YZ_{2'}$, YZ_1 and YZ_2 planes (figure 7.15).

In the three span-wise vertical planes, it can be stated that the predicted LES flow pattern is not so far from that measured by the PIV. Almost a symmetrical velocity distribution is recorded in both cases, in addition to an almost similar two-vortex structure formed at the top of the cavity. Moreover, the flow pattern outside the buoyant jet is similarly reproduced with both results in the lower part of the cavity. However, in the plane $YZ_{2'}$ (left pair iso-contours) and in accordance with the flow pattern already presented in the mid-vertical XZ_1-plane (figure 7.13), we note clearly from the velocity iso-contours at a height approximately $z = 6$ cm that the CFD slightly underestimates the inclination angle of the jet axis measured by the PIV.

Quantitative comparisons in these planes are presented by employing three span-wise $< |\mathbf{u}|_{YZ} >_t$ profiles situated at the vertical positions $z = 2$, 7 and 14 cm (figure 7.16). In the plane $YZ_{2'}$ (figure 7.16, left), very good agreement is noted outside the jet axis for the lowest profile $z = 2$ cm. At $z = 7$ cm and due to the underestimation of the jet inclination, the CFD overestimates the velocity along and near the jet axis (maximum can reach about 40%), although the span-wise positions of the local minima and maxima are in good agreement. Significant discrepancies are noted at the highest profile ($z = 14$ cm) where the LES overestimated the PIV velocity along the plume's axis and near the solid boundaries (walls). Moreover, the span-wise positions of the local minima predicted by the LES do not agree with the positions measured by the PIV, unlike the position of the local maximum that is in

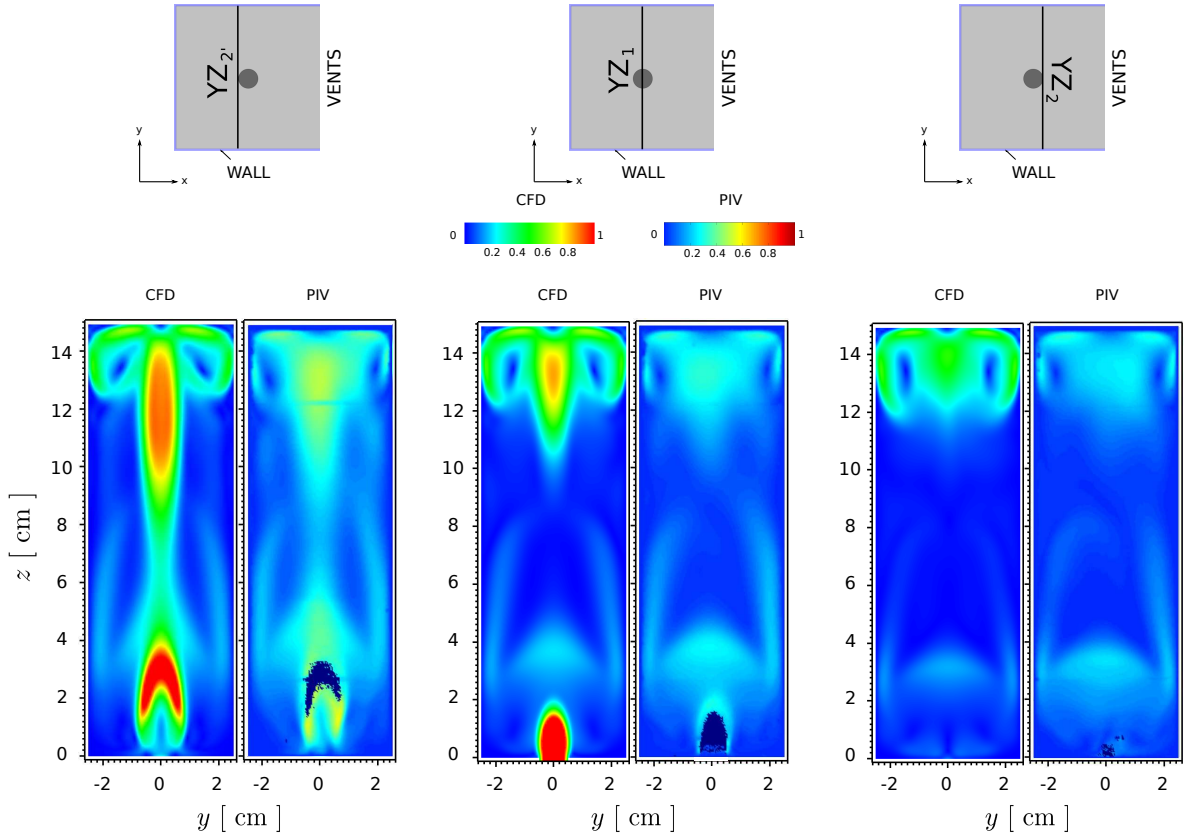

Figure 7.15: CFD-PIV comparison of the time averaged flow pattern illustrated by the 2D velocity magnitude $< |\mathbf{u}|_{YZ} >_t$ [m.s^{-1}] iso-contour plot. Left pair: vertical $YZ_{2'}$-plane, middle pair: vertical mid YZ_1-plane, right pair: vertical YZ_2-plane.

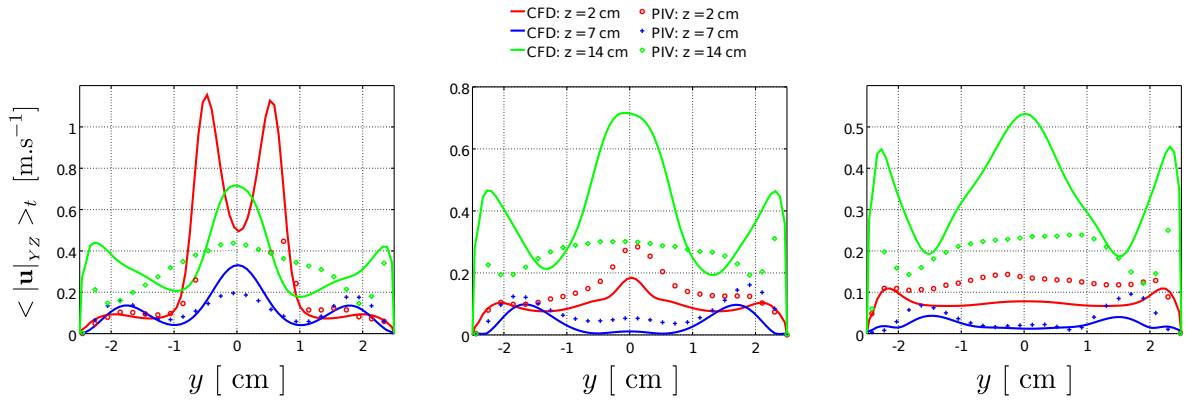

Figure 7.16: CFD-PIV comparison of the time averaged velocity magnitude $< |\mathbf{u}|_{YZ} >_t$ span-wise profiles at $z = 2$, 7 and 14 cm. Left: vertical $YZ_{2'}$-plane, middle: vertical mid YZ_1-plane, right: vertical YZ_2-plane.

good agreement. Again, it can be stated that these discrepancies are probably related to the CFD turbulence model that may not be sufficiently diffusing or due to the different helium

distribution in the upper region that can influence significantly the velocities.

Similarly in the two remaining YZ_1 and YZ_2 planes (respectively figure 7.16 middle and right), we note that the velocity profiles takes almost the same shape in the two lowest positions ($z = 2$ and 7 cm) although PIV overestimates the maximum LES velocity by about 33% in maximum. At the highest profile ($z = 14$ cm), the PIV underestimates the LES velocity probably for the same reasons (CFD turbulence model, different helium distribution).

Finally, we look to the right of the cavity in the vicinity of the vents plane. The flow pattern is illustrated in figure 7.17 by the $< |\mathbf{u}|_{YZ} >_t$ iso-contours in the vertical YZ_3 and YZ_4-planes.

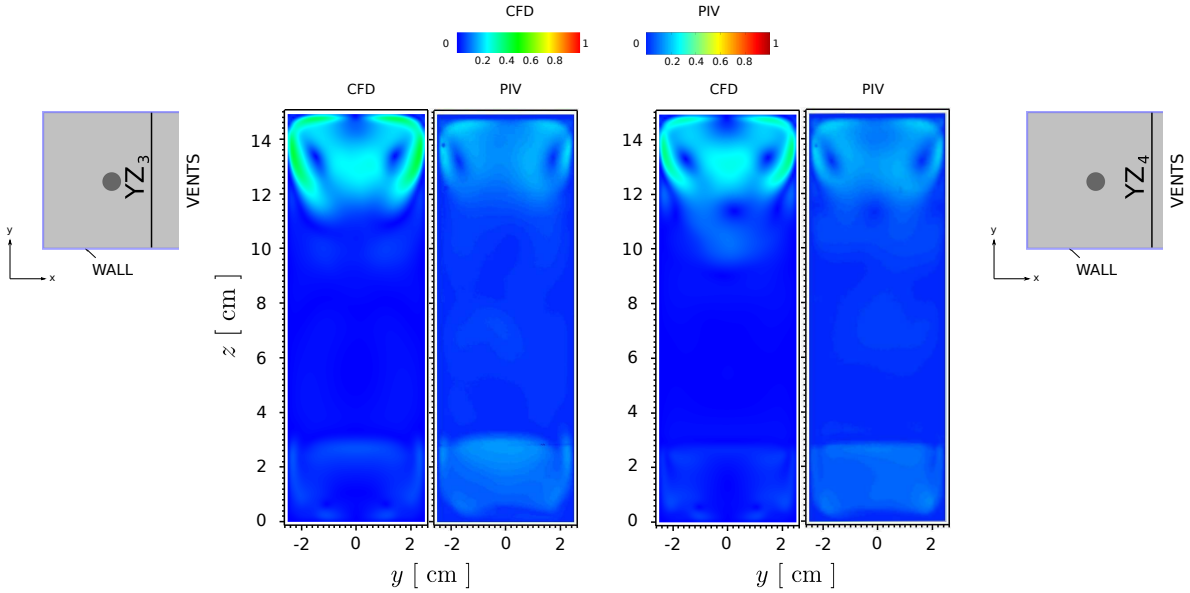

Figure 7.17: CFD-PIV comparison of the time averaged flow pattern illustrated by the 2D velocity magnitude $< |\mathbf{u}|_{YZ} >_t$ [m.s^{-1}] iso-contour plot. Left pair: vertical YZ_3-plane, right pair: vertical YZ_4-plane.

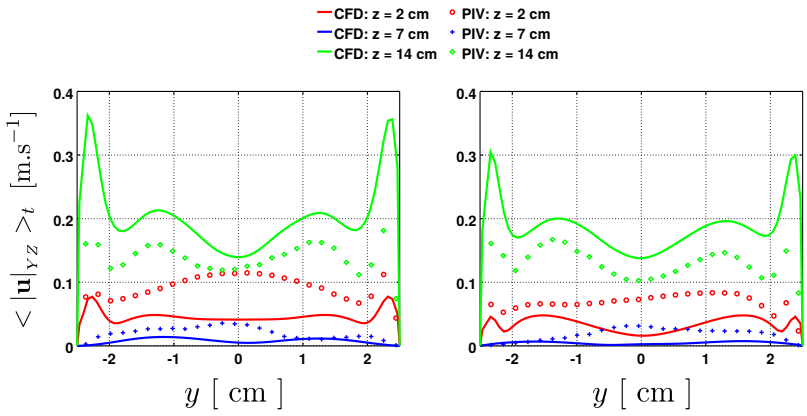

Figure 7.18: CFD-PIV comparison of the time averaged velocity magnitude $< |\mathbf{u}|_{YZ} >_t$ span-wise profiles at $z = 2$, 7 and 14 cm. Left: vertical YZ_3-plane, right: vertical YZ_4-plane.

The iso-contour plots show that the LES–PIV flow pattern is almost the same. In these planes, the velocities are significant in the lower part (because of the air inflow) and at the top (because of the mixture outflow). Almost a quiet region is noted in the middle part. In addition, the similar counter-rotating two-vortex structure is recorded in all cases. We can clearly note that the CFD underestimates the velocity in the vicinity of the bottom vent on the one hand, and overestimates the mixture outflow near the top vent on the second hand. This issue is better illustrated by the three span-wise profiles in figure 7.18.

As expected, we note from figure 7.18 that small velocities are recorded in the middle of both planes ($z = 7$ cm). The LES air inflow velocities (near bottom vent, $z = 2$ cm) underestimate the PIV velocities in both planes (can reach a maximum of 40% at the maximum), although the span-wise positions of the local maxima near the vent's extremities is in a rather good agreement. This issue is inverted at the highest profile (near top vent, $z = 14$ cm) where the predicted LES velocities overestimate the values measured by the PIV (can reach about 45%), although the shape of the profiles are almost similar and the positions of the local minima and maxima are coherent. The issue of the non-correct SGS diffusion and the influence of the helium concentration remain as a first reason for the overestimation issue in the upper part of the cavity. Moreover, the problematic may be due to the outlet boundary condition, basically the limited size of the Ly and Lz extensions in the LES computational domain as far as the convergence study of the exterior domain's size has only been carried along the extension Lx.

7.3.2 Flow pattern: In/out flows

For a global comparison, the time averaged vertical profiles of the velocity component normal to the vents surfaces $< u_1 >_t$ are considered for both vents at three horizontal positions: $x = 2.45$ cm denoting the inner-vent surface, $x = 2.7$ cm denoting the mid surface of the vent and at $x = 2.95$ cm where the outer surface is situated.

At the bottom vent, the vertical profiles of the $< u_1 >_t$ obtained from LES and measured by PIV are superposed for all horizontal positions in figure 7.19 ($y = 0$ cm). In all cases (except the PIV profile at $x = 2.95$ cm), the profiles take a similar inverted parabolic-like distribution shape where the absolute velocity values are strengthened at the edges of the vent. Note that the PIV profile at $x = 2.95$ cm show spurious values that are probably due to intense optical reflection at this location.

In addition, both results show that the absolute values of the horizontal velocity component and the width of the boundary layer which is formed at the edges of the vent increase as we move from the outer towards the inner surface of the vent ($x = 2.95$ to 2.45 cm). However, LES inflow absolute velocity values underestimate the PIV velocities uniformly all along the vent by about 15% which is probably due to the limited size of the span-wise and vertical extensions Ly and Lz.

Next, we consider the out-flow pattern that takes place at the top vent (figure 7.20). We note that the CFD–PIV $< u_1 >_t$ profiles are different in the lower part of the top vent (let us say

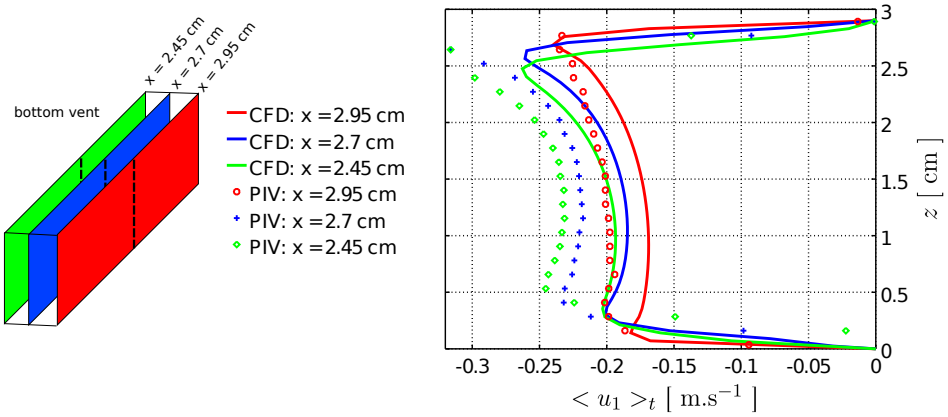

Figure 7.19: CFD–PIV comparison of the time averaged bottom vent in-flow pattern $< u_1 >_t$ in the vertical XZ_1-plane ($y = 0$ cm): $x = 2.45$, 2.7 and 2.95 cm.

$12 \leq z < 14.5$ cm). The numerical simulations (LES) predict in the lower part of the vent a sharp increase of the velocity followed by an almost slight linear increase till about $z = 14.5$ cm where the profiles increase sharply to the maximum. As expected, the LES velocities near the bottom edge of the vent show that the thickness of the formed boundary layer increase as we move from the inner to the outer surface. This is in contrast to the PIV profiles that record in the mid-lower part of the vent almost a linear evolution (except the profile at $x = 2.95$ cm) till about $z = 13.75$ cm followed by a drastic increase to take the maximum. However, the two studies are in good agreement regarding the position and the maximal value of $< u_1 >_t$ in the top layer (although slightly shifted upward in the LES calculation).

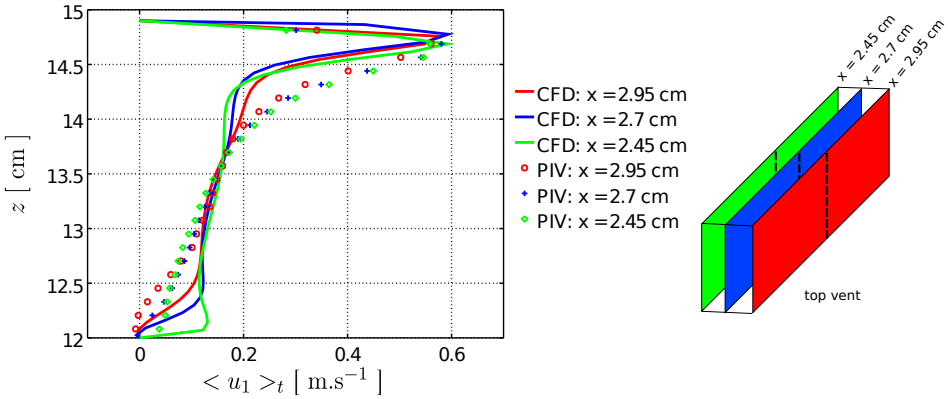

Figure 7.20: CFD–PIV comparison of the time averaged top vent out-flow pattern $< u_1 >_t$ in the vertical XZ_1-plane ($y = 0$ cm): $x = 2.45$, 2.7 and 2.95 cm.

For a global comparison, we calculate the 1D volumetric flow-rate crossing the bottom and top vent respectively in the XZ_1-plane section (integration of the $< u_1 >_t$ vertical profiles at $y = 0$ cm). At the three different horizontal positions, the calculated values are summarized in table 7.2.

The global quantities confirm the previous observation where we note that the LES underes-

		$x = 2.45$ cm	$x = 2.7$ cm	$x = 2.95$ cm
$< Q_v^{bot} >_t$ [$\times 10^{-3}$ m^2.s^{-1}]	**PIV**	6.351551	6.114468	5.730190
	CFD	5.581599	5.500916	5.207046
$< Q_v^{top} >_t$ [$\times 10^{-3}$ m^2.s^{-1}]	**PIV**	5.596905	5.652736	5.430840
	CFD	5.325345	5.231444	5.030402

Table 7.2: CFD–PIV 1D volumetric flow-rate comparisons respectively at the bottom and top vents: mid-vertical XZ_1-plane section ($y = 0$ cm).

timates in the plane XZ_1 the measured PIV air-inflow and mixture's out-flow (about 15%). Moreover, we can clearly see that the volumetric flow-rate in all cases (LES and PIV) decrease while moving from the inner to the outer surface of the vent, which is justified by the absolute velocity values that decrease while moving from $x = 2.45$ to 2.95 cm, both at the bottom vent (all along the vent's height, figure 7.19) and at the top vent (mainly in the lower position for $12 \leq z < 12.5$ cm, figure 7.20).

To compare the effect of the in/out flows in the vents vicinity, we vary the x-horizontal position (also in the XZ_1-plane) where we employ two points inside the cavity (respectively $x = 2$ and 2.2 cm) close to the vents wall and a third one in the exterior domain ($x = 3.2$ cm). Along the height of the cavity, the three vertical profiles are presented in figure 7.21 (z axis is cutted for null velocities).

In the lower part of the domain, we record the similar behavior although the CFD solution underestimates the PIV by approximately 15%. We note that the velocities (in absolute values) are more significant along the profiles situated inside the cavity which is due to the converging flow orientation from the exterior to the limited size of the vent, followed by a diverging orientation inside the cavity.

In the upper part, the PIV velocity profile measured in the exterior of the cavity ($x = 3.2$ cm) matches well with the LES solution. Discrepancies are noted on the two remaining profiles situated inside the cavity($x = 2$ and 2.2 cm). Although both LES and PIV report negative velocity values in the vicinity of the top vent (bottom surface) due to the recirculating flow in this region, the corresponding spatial location of this flow pattern is not uniquely determined (shifted with respect to height). In particular, LES predict the formation of this vortex between about $z = 9 - 10$ cm while PIV measure between a higher position between about $z = 10 - 12$ cm. However, the maximum negative value in the vortex agrees between both the LES and PIV.

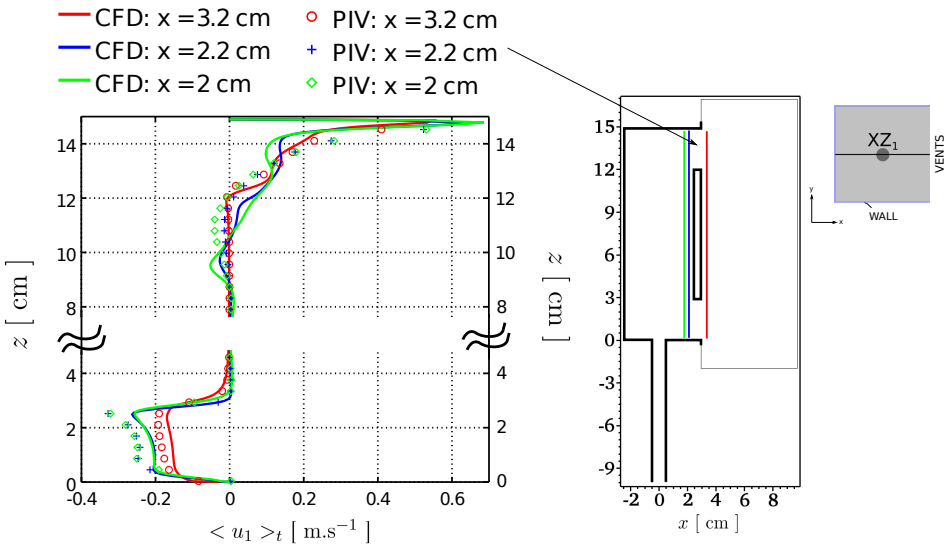

Figure 7.21: CFD-PIV comparison of the time averaged $< u_1 >_t$ horizontal velocity component in the vertical XZ_1-plane ($y = 0$ cm): vertical profiles along $x = 2, 2.2$ and 3.2 cm.

7.3.3 Laminar-to-turbulent transition

In order to identify the approximate height at which the transition from laminar to turbulence occurs firstly, we consider the normalized averaged vertical velocity fluctuations $u_3'^{,N}$, defined as

$$u_3'^{,N} = \frac{\text{rms}\{u_3\}_t}{< u_3 >_t}. \tag{7.5}$$

Both $u_3'^{,N}$ profiles predicted by the LES and measured by PIV along the inclined buoyant jet axis in the lower part of the cavity are depicted in figure 7.22. It is clear that the PIV fluctuations are about four times greater than those predicted by the LES (figure 7.22, left). Having such a significant discrepancies on the vertical velocity oscillations, although in the vicinity of the injection, make the fact of the laminar helium flow assumption inside the pipe questionable. More precisely, it can be stated that the injected fluid during the experiment probably admits more perturbations than the laminar flow initialized in the CFD which justifies the recorded four times larger oscillations. This issue can be due to the fact that the pipe in the numerical simulations is only 10 cm height which is not the case in the experiment where helium is injected to a 10 m flexible pipe connected to a 0.25 m metallic one connected to the bottom of the cavity. Therefore, discrepancies in the velocity oscillations in the lower part of the cavity could probably justify the LES–PIV discrepancies reported on the velocity distribution in the upper part of the cavity (subsection 7.3.1).

The PIV profile reduced by a factor of 4 is sketched with the LES profile in figure 7.22, right. We can clearly note that both profiles take almost a similar shape: both increase to reach a first maximum almost situated at a similar altitude $z \approx 3.8$ cm, followed by an oscillatory behavior around a constant $u_3'^{,N}$ in average (about 6.5% for LES and about 27% for PIV)

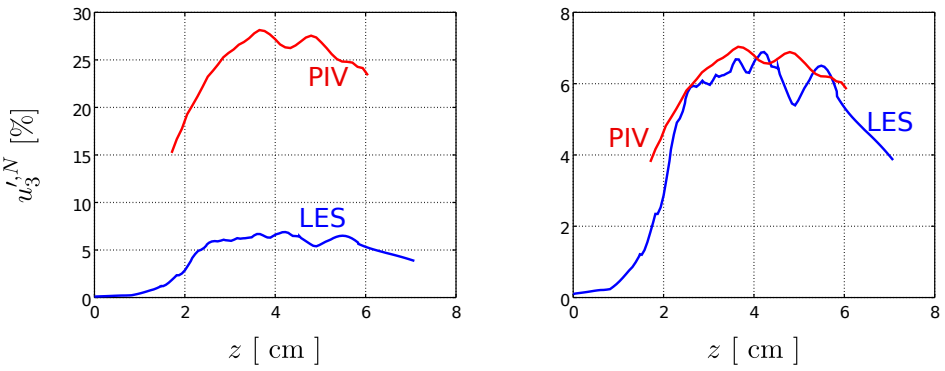

Figure 7.22: Normalized averaged vertical velocity fluctuations $u_3^{\prime,N}$ along the inclined jet axis. Left: initial scale, right: PIV fluctuations reduced by a factor of 4.

to decrease afterwards. According to the work of Plourde et al. carried out on a turbulent thermal plume in [PPKB08], we assume that the transition from laminar to turbulence is located more or less at the altitude of the maxima; in the range of $z \approx 3.8 - 4.5$ cm.

7.4 3D flow description and helium distribution

In this section, we describe the helium distribution inside the cavity. As far as no experimental measurements are currently available for the concentration field, the distribution is illustrated by the helium volume fraction X_1 field predicted from the LES.

At the initial state ($t = 0$ s), the cavity is filled with air at rest. From the first time iteration, helium is convected inside the cavity and a stable, symmetrical-laminar round jet rises inside the cavity pushing the air in all directions at what is called the jet's head. The jet impacts the top ceiling approximately after passing 0.2 seconds of constant injection helium (see figure 7.23).

From the velocity streamlines employed in figure 7.23, we note that the bottom vent is the only source of fresh air entering the cavity. This entering secondary flow impacts the jet axis approximately from the bottom of the cavity till about $z = 5$ cm height. Due to the upward convective motion, the mixture rises and an out-flow takes place at the top vent. This is not a new information and has been discussed thoroughly in the previous chapter and the previous section.

Afterwards, and due to the continuous injection, the flow spreads all over the ceiling, impacting the lateral walls from three surrounding sides and descend in a rotational form (figure 7.24). This rotational flow structure allows the dilution of helium in air. The forth direction corresponds to the top vent where a part of the mixture leaves the cavity.

As time advances, the intensity of the air inflow at the bottom vent is strengthened (compare bottom vent inlet velocity $u_1 \approx -0.05$ m.s^{-1} at time $t = 0.2$ s from figure 7.23 and that

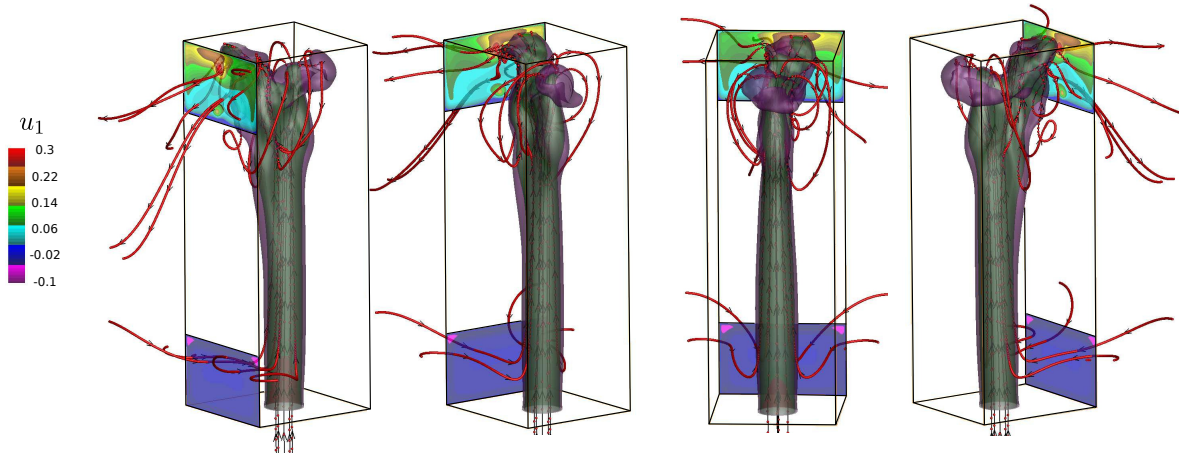

Figure 7.23: 3D instantaneous cavity flow pattern viewed from different positions during the jet-ceiling impact ($t = 0.2$ s): velocity streamlines and X_1 iso-surfaces (levels: 0.15 and 0.25). The iso-contours at the vent surfaces correspond to the magnitude of the horizontal velocity component u_1.

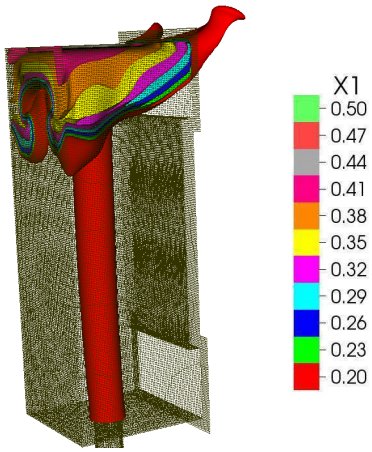

Figure 7.24: 3D instantaneous helium volume fraction X_1 iso-surface contours time evolution ($t = 0.5$ s).

predicted to take place in the quasi-steady state $< u_1 >_t \approx -0.23$ m.s^{-1} from figure 7.19). As a result, pressure gradients build up and cause the jet to deviate towards the left wall facing the vents. From a classical behavior in a normal jet interacting with a tangential flow, the initial jet round axis structure is deformed and thus the jet axis takes the shape depicted in figure 7.25.

It has been noted that the buoyant jet and its axis remain both, oriented to the left of the cavity and deformed till the end of the simulation. Therefore, we consider in what follows the flow pattern in the quasi-steady state solution.

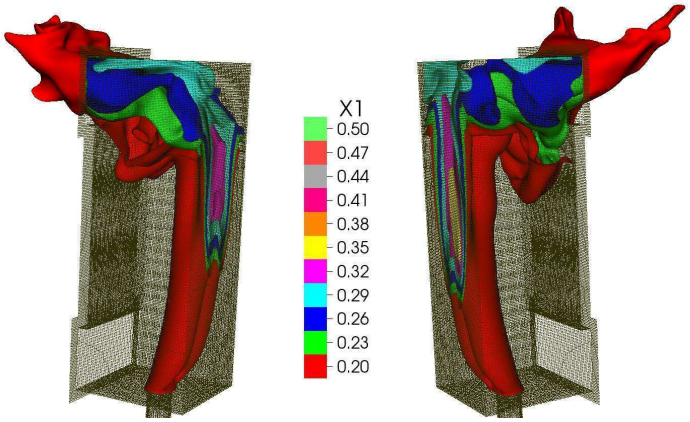

Figure 7.25: 3D instantaneous helium volume fraction X_1 iso-surface contours time evolution: effect of the heavy air cross-flow. Left: $t = 1.75$ s, right: $t = 20.5$ s.

The effect of the buoyant jet axis deformation, known as cross flow effect (see the book of Lee and Chu [LC03]), is illustrated in figure 7.26 by the time-averaged flow pattern in a horizontal xy-plane crossing the bottom vent ($z = 2$ cm). $< X_1 >_t$ iso-contours (grey scale) are superposed by the time averaged velocity $< |\mathbf{u}| >_t$ vector field in a zoomed region of the horizontal plane.

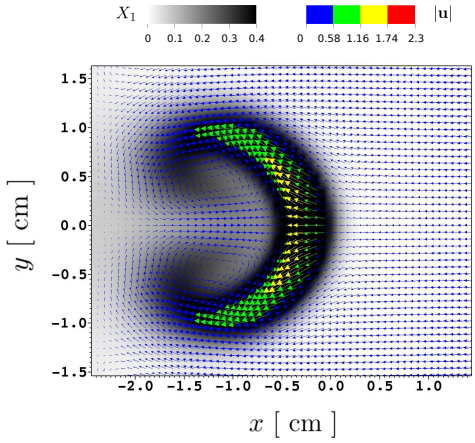

Figure 7.26: Cross-flow effect: flow pattern in the horizontal xy-plane ($z = 2$ cm) illustrated by time-averaged velocity vector field superposed over the time-averaged iso-contours of the helium volume fraction.

It is clear from figure 7.26 that the flow remains symmetrical with respect to the x-horizontal axis, along which the inclination takes place. We can clearly note the two counter-rotating vortices that enter a heavy mixture inside a lighter injected one which induce high density gradients at this position and thus play an important role in building a fluctuating regime at the top of the cavity (refer to subsection 6.1.2.1 for further description of the cross-flow effect and dynamics).

To characterize what takes place in the upper part of the cavity, we consider figure 7.27 where the flow patterns illustrated by the time averaged helium volume fraction $< X_1 >_t$ iso-surfaces.

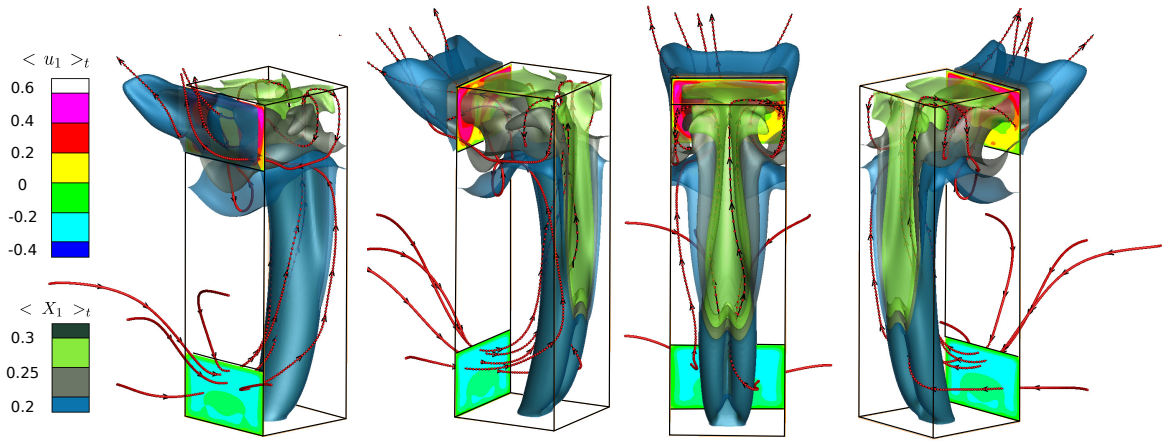

Figure 7.27: 3D flow pattern inside the cavity at the quasi-steady state solution: $< X_1 >_t$ iso-surfaces $[0.2 : 0.05 : 0.3]$ and $< u_1 >_t$ iso-contours at the vents $[-0.4 : 0.2 : 0.6]$. The orientation of the flow is illustrated by the time averaged velocity streamlines.

We note first that there is a significant interaction between the buoyant jet and the cavity's left boundary (wall facing the vents) where the highest helium concentrations are localized in this region.

Secondly, we can clearly note that stratification layers are developed outside the plume with levels basically constituting of 20–30% of pure helium. In the vicinity of the top vent, we note that the 20% layer is situated below the bottom surface of the top vent by about 1–2 cm. This is probably justified by the interaction between the recirculation flow and the stratified layer that has been predicted to develop in this region (recall the recirculation flow predicted between $z = 9-10$ cm and illustrated by the negative velocity values in figure 7.21). However, in the vicinity of the span-wise solid walls, the 20% helium volume fraction level is situated approximately at the same vertical position of the top vent's bottom surface ($z \approx 12$ cm).

7.5 Concluding remarks

In this chapter, validations of the performed LES calculations have been presented. Following an LES qualification study, it has been figured out that a fine LES has been performed and that a small role is played by the SGS model.

In a next step, the necessity of considering an exterior region in the numerical simulations has been justified by performing CFD–PIV comparisons in 2D plane sections covering almost all the cavity. Qualitative comparisons show that the global LES–PIV flow pattern is almost similar. Quantitatively speaking, the LES–PIV velocity profiles in the middle-lower part of the cavity take similar forms and completely agree on the positions of the local minima

and maxima, although a local error relative to the PIV can range between 15–30%. However, significant discrepancies are reported in the upper part of the cavity where we note always the PIV underestimating the LES velocities. Four main reasons can justify these discrepancies: (i) the differences between the CFD–experimental helium distribution that influences the velocities basically at the top of the cavity and in the vicinity of the top vent, (ii) the issue of the outlet boundary condition basically due to the limited span-wise and vertical extension sizes of the exterior domain Ly and Lz, (iii) differences in the fluctuating level of the injected fluid where the flow can be about four times more oscillatory in the injection vicinity of the experiment compared to the numerical simulation, (iv) the LES SGS turbulence model that is probably not modelling correctly the diffusion in the upper part of the cavity.

LES results are employed finally to depict a complete 3D helium flow description. Using time averaged quantities, direct interactions between the buoyant jet on the one hand and either the solid boundaries or the exterior environment on the second hand have been noted. These interactions are probably the reason behind the formation of the helium stratification layers in the upper part of the cavity which contradicts the two layer stratification predicted in such configurations by the theoretical model of Linden et al. [LLSS90]. Further quantitative analysis regarding the simulated configuration and the two stratified theoretical prediction will be carried out in the next chapter.

As far as local discrepancies are recorded between the LES–PIV velocities and since we look towards providing reference numerical solutions in the present work, we perform in a final step a coarse DNS calculation. Carrying out this type of simulation without using any turbulence model is justified with a mesh which has been figured out to be at most 3–4 times bigger than an estimated Kolmogorov length scale. Therefore, a coarse DNS is considered in the next chapter by resuming the final LES solution from $t = 110$ s.

Chapter 8

Coarse DNS calculation: flow analysis

Contents

The present chapter is organized as follows. First, the coarse DNS configuration and the employed statistical time intervals are presented. Second, we carry out LES–DNS–PIV comparisons regarding the 2D velocity fields. Numerical predictions are used afterwards to depict the 3D helium volume fraction distribution and the stratification phenomenon that takes place inside the cavity.

Finally, the turbulent kinetic energy (TKE) equation is considered. In this part, the quality of the resolved coarse DNS is identified mainly from a TKE budget analysis carried out in 2D vertical slices of the computational domain. The limits of the three buoyant jet regions (jet, transitional and plume regions) are identified by analyzing the effect of the turbulent buoyancy production in the cavity. This identification is important as far as the notion of self-similarity is limited in this study, due to both the reduced size of the configuration and the inclination of the buoyant jet axis.

The variables employed in the post-treatment throughout the chapter are all defined in appendix C.

8.1 Coarse DNS configuration

8.1.1 Numerical setup

The previous LES calculation performed on configuration 4_x (cell step-size $\delta = 7 \times 10^{-4}$ m and total cell numbers $= 4,427,588$) has been resumed from $t = 110$ s for a coarse DNS study. Thus, no turbulence model is employed in the present calculation. The solution preserves the quasi-steadiness behavior as shown in figure 8.1 where the time evolution of ρ at a fixed probe in the top of the cavity ($x = 0$, $y = 0$, $z = 13.5$ cm) is depicted. However, the magnitude of the fluctuations increases in average from the LES to the coarse DNS calculation, which is coherent with the approach and enhance the role played by the SGS model.

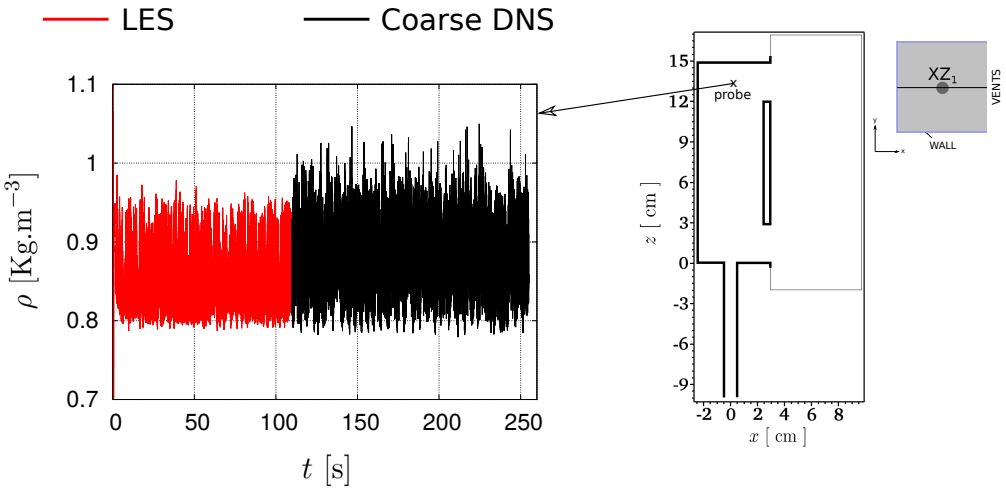

Figure 8.1: Time evolution of the mixture density ρ at a fixed probe in the top of the cavity ($x = 0$, $y = 0$, $z = 13.5$ cm) showing the quasi-steady state.

8.1.2 Statistical recordings

Statistical recordings has been carried out, with a frequency of $1/\delta t$ Hz, on two separate time intervals (windows) $W_1 = [195, 234.6]$ and $W_2 = [234.6, 254.6]$ physical seconds; respectively 39.6 and 20 seconds of data accumulation (non-dimensional time equivalent to 618.75 and 312.5 respectively for a reference height $H_r = 14.9$ cm and a reference velocity $\mathbf{u}_r = 2.33$ m.s^{-1} equals to the maximum injection velocity). We recall that the time average is integrated using the equation

$$< \varphi(\mathbf{x}, t) >_t = \frac{1}{t_{\text{end}} - t_{\text{start}}} \int_{t_{\text{start}}}^{t_{\text{end}}} \varphi(\mathbf{x}, t) dt, \tag{8.1}$$

where t_{start} and t_{end} denote the endpoints of the employed time window .

In figure 8.2, the difference between the two time averaged velocity magnitude fields integrated respectively within W_1 and W_2 ($< |\mathbf{u}|^{W_2} >_t - < |\mathbf{u}|^{W_1} >_t$) is illustrated by the iso-surface plot. The minimal and maximal recorded values takes in absolute value 10^{-6} m.s^{-1} which is rather small compared to the velocity values in the domain. This ensures that the statistics has been carried out on a quasi-steady solution and are rather independent of the employed window, at least for the time-averaged values.

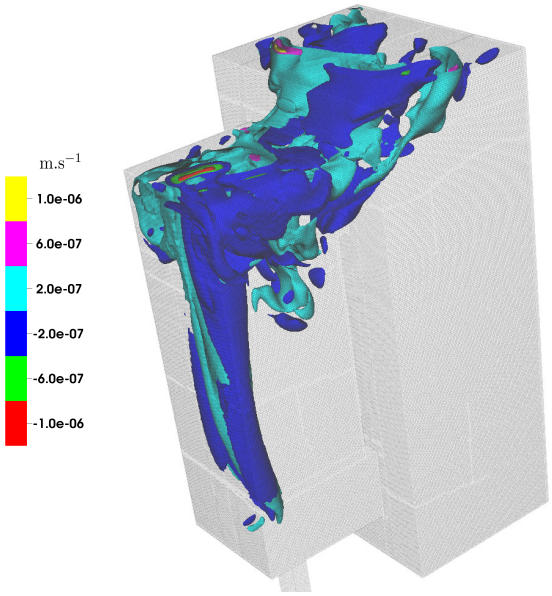

Figure 8.2: Difference between the two time averaged velocity magnitude fields $< |\mathbf{u}|^{W_2} >_t - < |\mathbf{u}|^{W_1} >_t$ illustrated by the iso-surface plot.

The values depicted in figure 8.2 are coherent with the physical phenomenon that takes place in the domain. All the laminar regions situated basically in the injection pipe and at the bottom of the cavity (near the bottom vent) take a zero difference between the average obtained over W_1 and that over W_2. Discrepancies are recorded all along the jet axis, starting from the air-jet impact location, and in the upper part of the cavity which is justified due to the high velocity fluctuations (velocity fluctuations for example can reach 40% of the mean value, figure 8.1).

8.1.3 Kolmogorov and Batchelor length scales

In order to further qualify the coarse DNS resolution, we estimate the Kolmogorov length scale η_{DNS} using the accumulated recorded statistical fields over the window W_2 (dissipation term accumulated only on this interval). From a dimensional analysis, we define an estimate

of the Kolmogorov length scale as [1]

$$\eta_{\mathrm{DNS}} = \left(\frac{< \rho >_t < \nu >_t^3}{|\epsilon_{\mathrm{DNS}}|} \right)^{0.25}, \tag{8.2}$$

where ϵ_{DNS} [Kg.m^{-1}.s^{-3}] is the turbulent dissipation term already defined as

$$\epsilon_{\mathrm{DNS}} = -\left\langle \tau'_{ik} \frac{\partial u'_i}{\partial x_k} \right\rangle_t . \tag{8.3}$$

The superscript " $'$ " is used to refer to the fluctuating component of a field, and thus defined for an arbitrary fluid variable $\varphi(\mathbf{x}, t)$ as

$$\varphi'(\mathbf{x}, t) = \varphi(\mathbf{x}, t) - < \varphi(\mathbf{x}, t) >_t . \tag{8.4}$$

The calculated values of η_{DNS} are illustrated by the iso-contour plots in the vertical planes XZ_1 and $YZ_{4'}$ (figure 8.3).

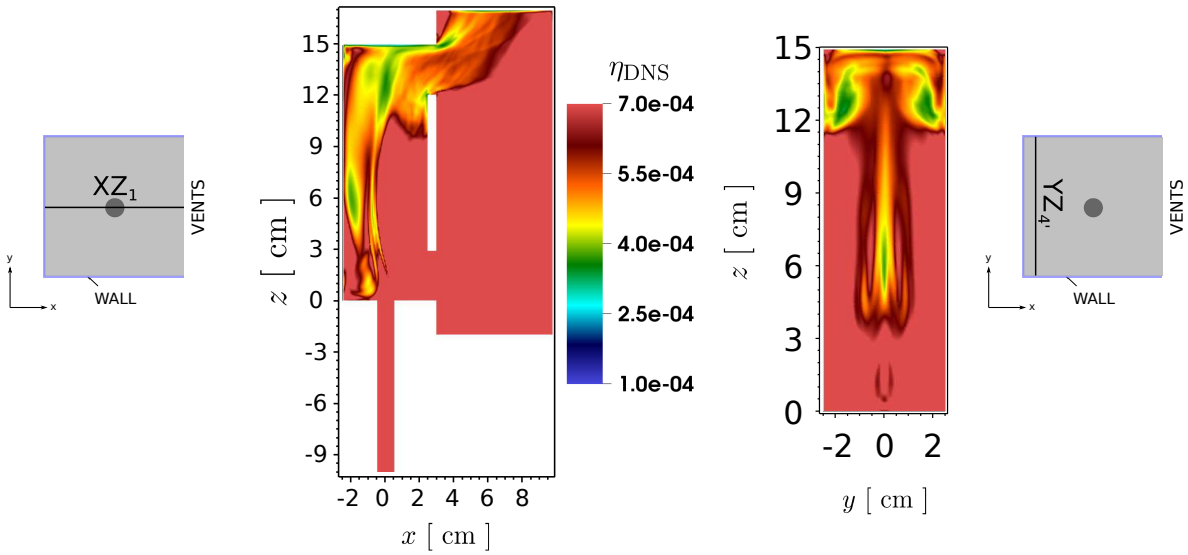

Figure 8.3: The estimated Kolmogorov length scale η_{DNS} illustrated by the iso-contour plots. Left: vertical XZ_1-plane, right: vertical $YZ_{4'}$-plane.

The distribution of η_{DNS} in both planes is rather coherent with the physical phenomena that take place in these planes. For example, we note in the mid-vertical XZ_1-plane (figure 8.3, left) that the mesh size $\delta = 7 \times 10^{-4}$ m is with the same order of η_{DNS} in all laminar zones: the injection pipe, near the lower part of the vents wall and in a big portion of the exterior domain. However, we see that a finer mesh is required in the remaining part of the plane to capture correctly the small scales flowing within the vortices and in the transitional–fluctuating regime.

[1] We emphasize that it is just an estimation as far as the correct definition is $(< \rho\nu^3/|\epsilon_{\mathrm{DNS}}| >_t^R)^{0.25}$ which is unfortunately not recorded in our simulation.

Similarly, we note that a finer mesh is required in the plane $YZ_{4'}$ to capture the small motion scales situated in the top vortices and in the jet axis starting from the spatial position of the laminar to turbulent transition (predicted previously from the LES calculation around $z = 3.8 - 4.5$ cm).

In figure 8.4, we depict the ratio of the mesh size δ to the estimated η_{DNS} in the same vertical planes. From the values recorded in both planes, we note that the biggest ratios are situated at the top of the cavity (position of the plume–ceiling impact) where the employed cell size can be 3 times bigger than η_{DNS}. Elsewhere, the ratio can reach approximately a maximum of 2.5 which is situated in the rotating vortices formed in the upper part of the cavity.

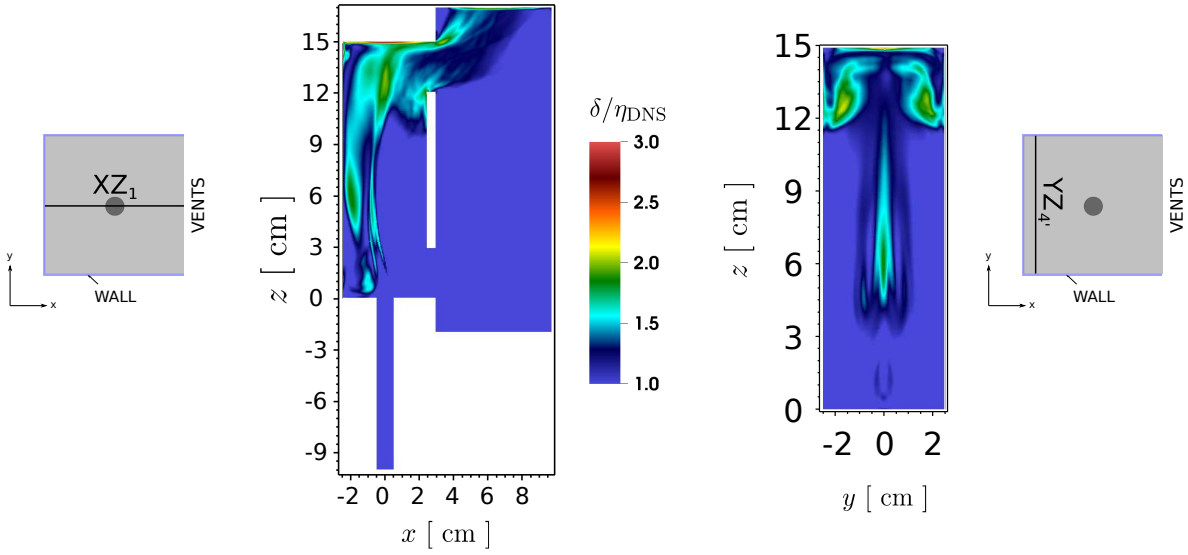

Figure 8.4: Ratio of the grid spacing δ to η_{DNS} illustrated by the iso-contour plots. Left: vertical XZ_1-plane, right: vertical $YZ_{4'}$-plane.

In order to test if the employed mesh size is sufficient for the species mixing dissipation, we calculate the Batchelor length scale $\lambda_{B_{\text{DNS}}}$ defined as

$$\lambda_{B_{\text{DNS}}} = \eta_{\text{DNS}} \times \text{Sc}^{-1/2}, \tag{8.5}$$

where Sc is the dimensionless Schmidt number defined in equation (1.11). In figure 8.5, the evolution of Sc versus the helium volume fraction X_1 is depicted.

From figure 8.5 we note that $\text{Sc} > 1$ inside the injection pipe and its vicinity where X_1 approaches unity (pure helium). In accordance with equation (8.5), the Batchelor length scales $\lambda_{B_{\text{DNS}}}$ are smaller than the Kolmogorov length scales η_{DNS} which are already greater than the employed mesh size δ as far as the flow inside the tube and its vicinity is laminar. Elsewhere in the domain and recalling the helium distribution inside the cavity from section 8.2.3, $\text{Sc} < 1$ and thus the smallest length scales are of size η_{DNS}.

In the two vertical XZ_1 and $YZ_{4'}$ planes, the iso-contours of $\lambda_{B_{\text{DNS}}}$ are presented in figure 8.6. Comparing to the grid spacing δ, we note that the employed mesh is at most 1.4 times

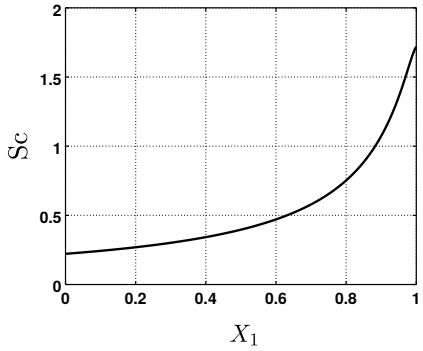

Figure 8.5: Evolution of the Schmidt number (Sc) versus the helium volume fraction X_1.

smaller than $\lambda_{B_{\mathrm{DNS}}}$ in a local spatial positions situated along the jet axis in the pipe vicinity due to the heavy–light fluid impact (thus mixing, both planes) and near the left wall (figure 8.6, left).

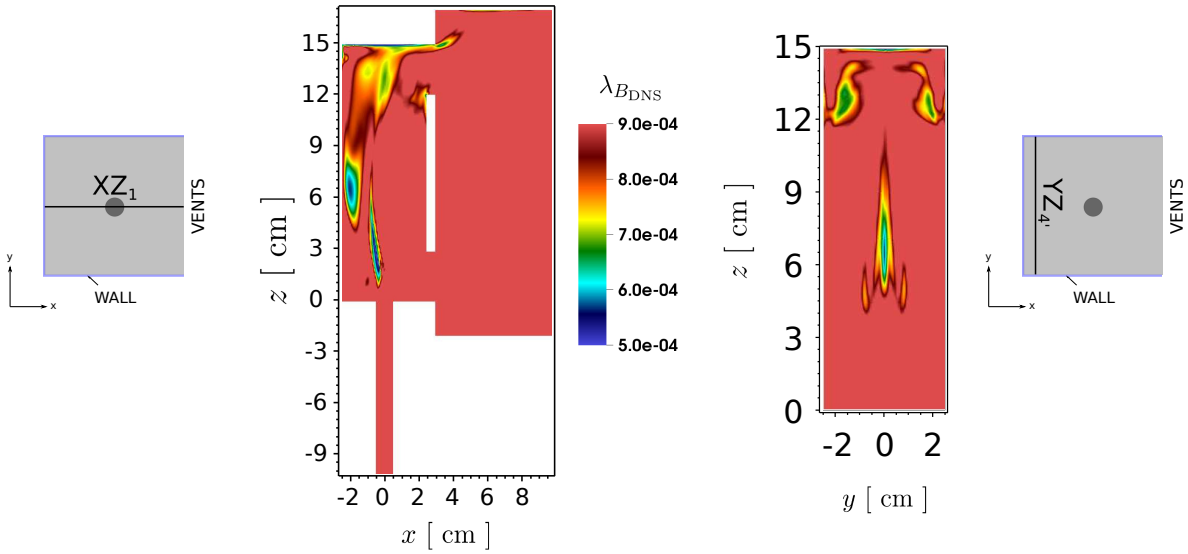

Figure 8.6: The estimated Batchelor length scale $\lambda_{B_{\mathrm{DNS}}}$ illustrated by the iso-contour plots. Left: vertical XZ_1-plane, right: vertical $YZ_{4'}$-plane.

Comparing globally with the Kolmogorov length scale in our configuration, we note that the Batchelor length scales are larger than η_{DNS} in almost all the domain and thus the smallest length scales required to capture all the physical phenomena of the problem, in our case, are the Kolmogorov length scales.

8.1.4 Validity of the Boussinesq eddy-viscosity assumption

Besides the Reynolds Stress Model (RSM) and the non-linear models (refer to the turbulence book of Chassaing et al. [CAA+13]), most popular models employ a Boussinesq hypothesis

[Bou03] based on a turbulent eddy–viscosity evaluation.

Thus, the turbulent viscosity μ_t in the Boussinesq hypothesis is expressed in the linear constitutive equation as

$$- R_{ij} + \frac{2}{3} < \mathcal{K}_t >_t \delta_{ij} = 2\mu_t \Big(< S_{ij} >_t - \frac{1}{3} < S_{kk} >_t \delta_{ij} \Big), \tag{8.6}$$

where $R_{ij} =< \rho u_i' u_j' >_t$ is the Reynolds stress tensor and $\mathcal{K}_t$ is the turbulent kinetic energy (TKE) defined as (see appendix D)

$$\mathcal{K}_t = \frac{1}{2} \rho u_i' u_i'. \tag{8.7}$$

Again, the fields accumulated over the interval W_2 are used. We define the traceless tensors $\mathbb{R}$ and $\mathbb{S}$ respectively as

$$\mathbb{R} = -R_{ij} + \frac{2}{3} < \mathcal{K}_t >_t \delta_{ij}, \tag{8.8}$$

$$\mathbb{S} =< S_{ij} >_t - \frac{1}{3} < S_{kk} >_t \delta_{ij}. \tag{8.9}$$

As presented by Schmitt in [Sch07], equation (8.6) is only valid when the tensors $\mathbb{R}$ and $\mathbb{S}$ are aligned. To test the alignment of the tensors, an indicator ρ_{RS} defined through the inner product as

$$\rho_{RS} = \frac{|\mathbb{R} : \mathbb{S}|}{\|\mathbb{R}\| \|\mathbb{S}\|}, \tag{8.10}$$

can be used. The norm $\| \cdot \|$ is defined for any tensor $\mathbb{A}$ as

$$\|\mathbb{A}\|^2 = \mathbb{A} : \mathbb{A}, \tag{8.11}$$

and " : " is the tensorial contraction operator.

ρ_{RS} is in fact similar to the cosine of the angle between two vectors and thus is between 0 and 1. When $\rho_{RS} = 1$, the tensors $\mathbb{R}$ and $\mathbb{S}$ are aligned and the Boussinesq hypothesis described in equation (8.6) should be valid. The more the indicator approaches 0, the more the assumption is invalid. It could be rather considered that the alignment approximately holds true for angles smaller than $\pi/6$ ($\rho_{RS} > 0.86$) [Sch07].

In our case, the values of ρ_{RS} have been calculated and are thus illustrated by the iso-contour plots in the vertical planes XZ_1 and $YZ_{4'}$ (figure 8.7).

Focusing on the distribution inside the cavity at first and mainly in the regions where significant velocity gradients occur, we can clearly note that the tensors $\mathbb{R}$ and $\mathbb{S}$ can be assumed aligned outside the buoyant jet near the right wall, in a small region of the plume and near the bottom-left corner (figure 8.7, left), and in small regions situated in the lower part of the cavity outside the buoyant jet and in small part of the top vortices in the plane $YZ_{4'}$ (figure 8.7, right). Outside the cavity and far away from the area of interest, we note some regions

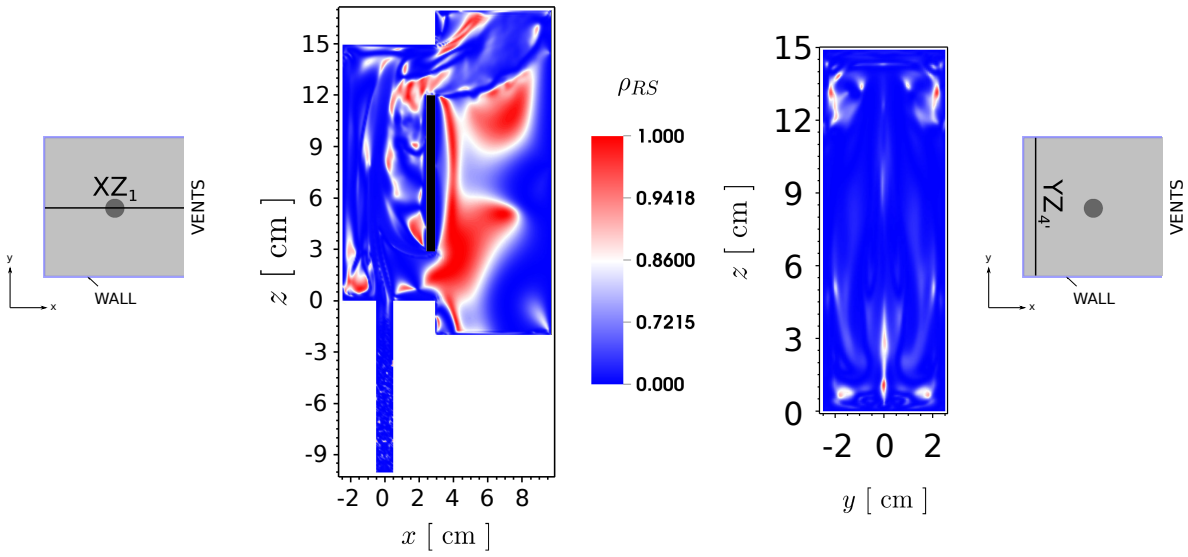

Figure 8.7: Values of the indicator ρ_{RS} illustrated by the iso-contour plots. Left: vertical XZ_1-plane, right: vertical $YZ_{4'}$-plane

having surprisingly a low ρ_{RS} indicator (figure 8.7, left). In particular, these regions have a very low or even zero velocity gradients ($\|\mathbb{S}\| \approx 0$) which explain the arbitrary distribution of ρ_{RS}.

In the area of interest, the tensors are assumed to be not aligned as far as the indicator is mainly between [0,0.86]. Hence in our situation, a model based on the Boussinesq relationship must lead to inaccurate results.

8.2 Time averaged fields

8.2.1 Flow pattern inside the cavity: CFD–PIV velocity comparisons

Here, the coarse DNS time averaged velocity fields and profiles are compared with those predicted by the LES and measured with the PIV technique. More precisely, we present comparisons of the velocity fields which are calculated similarly to those in the PIV (in 2D vertical xz or yz planes) to depict on the influence of the turbulence model on the prediction of the velocity fields.

We consider at first the time averaged flow pattern in the mid-vertical XZ_1-plane ($y = 0$). In figure 8.8 (top-left), the LES and coarse DNS 2D time averaged (window W_1) velocity magnitude $< |\mathbf{u}|_{XZ} >_t$ iso-contours are depicted where we note that the global flow pattern is almost similar. In particular, the recirculating zones and the jet axis inclination (due to the heavy air inflow), in addition to the air–helium mixture leaving from the top thin layer are all similarly predicted by both CFD approaches.

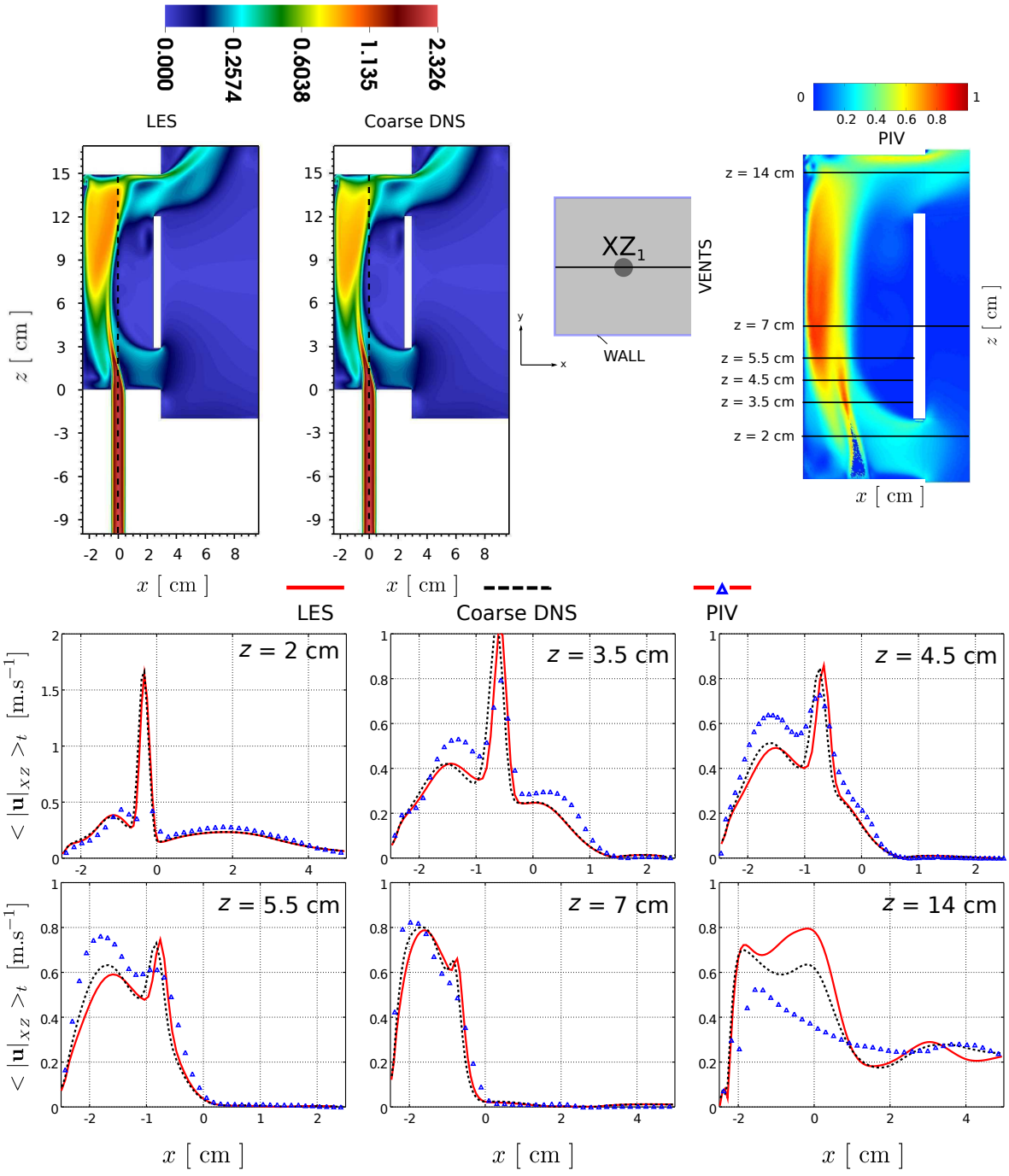

Figure 8.8: CFD–PIV comparison of the time averaged flow pattern illustrated by the 2D velocity magnitude $< |\mathbf{u}|_{XZ} >_t$ [m.s^{-1}] in the vertical XZ_1-plane. Top: iso-contour plot, bottom: horizontal profiles respectively at z = 2, 3.5, 4.5, 5.5, 7 and 14 cm (window W_1). Thick dashed black line denotes the vertical axis passing through the origin $\mathcal{O}$.

Qualitative discrepancies are mainly reported in the upper-left part of the cavity; basically in the structure of the plume region. From the colorbar legend, we can note that the velocity

magnitudes near the left wall facing the upper vent are slightly reduced in the coarse DNS prediction. In addition, compared to the vertical axis (black dashed line), we note that the plume's upper part (approaching the ceiling) is slightly wider in the LES field. This might be due to a small diffusion induced by the Smagorinsky SGS model in the regions where velocity gradients dominate.

To quantify these discrepancies, we consider the time averaged 2D velocity magnitude $< |\mathbf{u}|_{XZ} >_t$ horizontal profiles at six distinct heights $z = 2$, 3.5, 4.5, 5.5, 7 and 14 cm in the mid vertical plane ($y = 0$, figure 8.8, bottom). The horizontal profiles measured from the PIV at the same vertical positions are superposed over the same plots.

The general shape of the horizontal profiles predicted from the LES and the coarse DNS calculations show great similarities at all heights. We note that the profiles are more slightly shifted towards the left in the coarse DNS calculation than those in the LES (mainly the profiles devoted to $z = 3.5$, 4.5, 5.5 and 7 cm) which means that the jet inclination towards the left wall is slightly strengthened with the DNS prediction.

At the top ($z = 14$ cm), the profile show greater discrepancies where the maximum velocity predicted by the LES in the plume region is reduced in the coarse DNS calculation by about 0.18 m.s^{-1} (about 30% relative to coarse DNS), at the same position, to take a maximum value near the left wall. This is in accordance with the velocity iso-contours depicted in figure 8.8 (top-left).

Comparing with the PIV measurements, we can note discrepancies between the CFD predictions and the measured velocities. Basically, the velocity magnitude predicted by CFD underestimates the measured one at all heights (maximum about 20%), except at the top where the values are overestimated (maximum can reach 100% for LES and 65% for coarse DNS relative to the PIV). However, the horizontal position of the maximum measured velocity along the jet axis and near the left wall, in addition to the positions of the sharp velocity gradients, are better predicted by the DNS at several vertical positions of the plane XZ_1. Therefore, it can be stated that the coarse DNS agrees with the PIV in the mid-vertical XZ_1-plane better than the LES.

We draw attention to the CFD–PIV discrepancies reported at the top of the cavity ($z = 14$ cm, figure 8.8, bottom–right). By just looking to the CFD velocity prediction as a first insight (coarse DNS velocity reduced by about 30% compared to LES), it can be stated then that this is the effect of the SGS model that is not modelling correctly the diffusion in the top of the cavity. However, this justification can not explain the discrepancies between the coarse DNS and the PIV profile. Therefore, two additional issues are probably inducing the discrepancies: the difference in the helium distribution at the top and near the top vent which influences significantly the velocity distribution at first and the fact of the laminar-injected flow at second where oscillations measured with PIV are four time greater than those in the CFD.

Next, we consider the CFD time averaged flow pattern (window W_1 for coarse DNS) illustrated by the 2D velocity magnitude $< |\mathbf{u}|_{YZ} >_t$ iso-contours in the vertical $YZ_{2'}$-plane (figure 8.9,

top-left). Qualitatively speaking, the flow pattern predicted by both CFD calculations is very similar. However, in the middle part of the plane (about $z = 4.5$ to 8 cm), the reduced velocity iso-contours show clearly that the jet axis is inclined more towards the left wall facing the vents plane in the DNS calculation. Moreover, we can see that the LES prediction overestimates the DNS velocity in the plumes region. This is in accordance with the observation noted on the horizontal profiles situated at similar heights in the mid-vertical XZ_1-plane (recall figure 8.8, bottom).

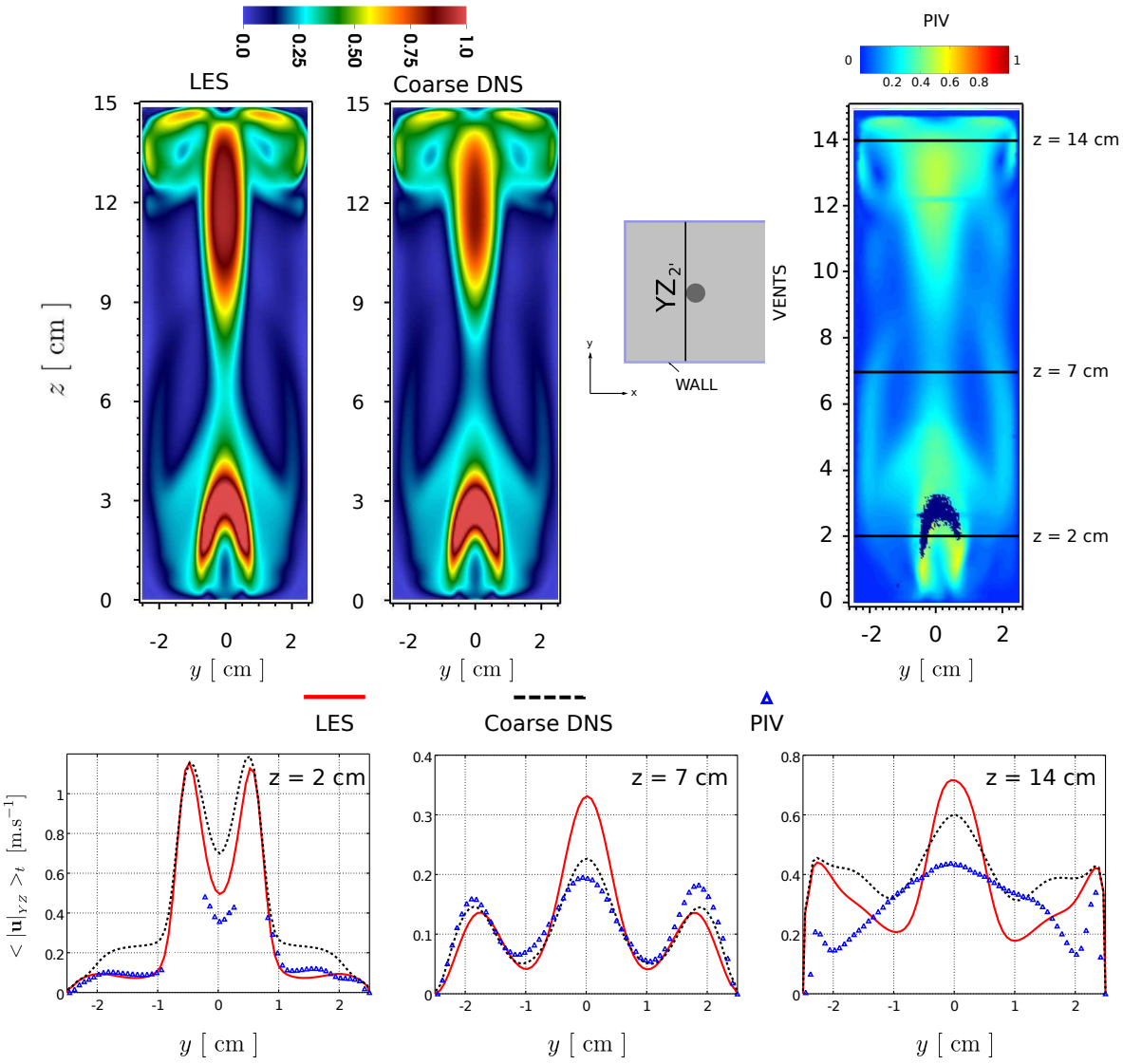

Figure 8.9: CFD–PIV comparison of the time averaged flow pattern illustrated by the 2D velocity magnitude $< |\mathbf{u}|_{YZ} >_t$ [m.s^{-1}] in the vertical $YZ_{2'}$-plane. Top: iso-contour plot, bottom: span-wise profiles respectively at $z = 2$, 7 and 14 cm (window W_1).

Quantitatively, we depict in figure 8.9 (bottom) three span-wise profiles situated in the same vertical plane at heights $z = 2$, 7 and 14 cm. At the lowest position ($z = 2$ cm, figure 8.9 bottom-left), the velocity magnitude obtained by the DNS overestimates both the LES pre-

diction (maximum about 28%) and the PIV measurement (maximum about 80%). However, the span-wise location of the minimum velocity inside the jet is well predicted by both CFD approaches. We recall that the discrepancies near the injection are probably due to the PIV uncertainty in the injection vicinity.

In the same plane and at the same height ($z = 2$ cm), we note that the LES prediction matches more the experimental measurements outside the jet axis. Assuming the PIV measurements are certain in these regions, it can be stated that the Smagorinsky LES SGS model prediction is better than the coarse DNS at this position.

In the middle of the cavity ($z = 7$ cm, figure 8.9 bottom-middle), the DNS prediction better agrees with the PIV measurement than the LES (minimum and maximum locations, profile shape). Basically, the velocity overestimation reduced from 65% (by LES) to 15% (by the coarse DNS). This ensures again that the DNS predicts better the correct jet inclination at this height.

As expected, significant discrepancies are recorded at the top of the cavity ($z = 14$ cm, figure 8.9 bottom-right). The span-wise location of the local velocity maxima is well predicted by both CFD approaches, unlike the position of the local minima where both LES and the coarse DNS predict the positions to be closer to the plume axis. Moreover, we note that the maximum velocity along the plume axis decreases by 16% from the LES to DNS calculation and thus approaches the measured PIV value. However, still the velocity is overestimated by about 40% from the measured value.

The agreement of both CFD approaches with the PIV regarding the position of the local maxima only can highlight over two main points: either there is uncertainty in the PIV measurements at this position or that the CFD is not correctly predicting the structure of the two vortices created in the upper part of the cavity. Besides, the difference of the maximum velocity value can justify again the problematic of the LES SGS model in representing the diffusion at the top of the cavity, coupled with the probable issue of the different helium distribution and/or the issue of the different velocity oscillations in the vicinity of the injection.

8.2.2 Flow across top and bottom vents

We present in this subsection the LES-DNS-PIV comparisons regarding the air inflow and the mixture outflow respectively at the bottom and top vents. To illustrate, we consider in figure 8.10 the vertical profiles of the time averaged horizontal velocity component normal to the vents surfaces $< u_1 >_t$ (window W_1 for coarse DNS) in the mid-vertical XZ_1-plane ($y = 0$) traversing both the bottom and top vents at the horizontal position $x = 2.7$ cm (mid-vent surface).

At the bottom vent (figure 8.10, left), both CFD profiles are almost superposed and still the CFD predicted velocity inflow underestimates the PIV by about 15%, uniformly all along the vent's height. We justify this underestimation again to be related to the reduced size of the exterior domain, or maybe uncertainty in the PIV measurements.

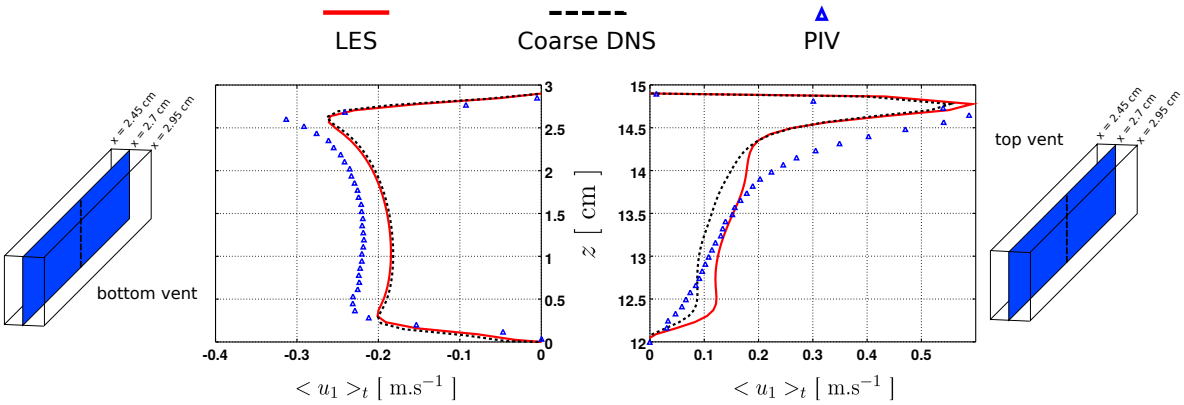

Figure 8.10: LES-DNS-PIV comparisons of the time averaged $< u_1 >_t$ vertical profiles in the vertical XZ_1-plane at the horizontal position $x = 2.7$ cm. Left: bottom vent inflow, right: top vent outflow.

CFD discrepancies are recorded in the lower part of the top vent where the coarse DNS prediction underestimates the LES velocity by about 35% (figure 8.10, right). However, both CFD predicted profiles take almost the same shape along the height of the vent. A sharp increase is noted on the CFD profiles in the lower part of the vent followed by a slight linear increase to reach the top layer where the velocity increase sharply to the maximal $< u_1 >_t$ value, unlike the PIV profile that increases almost linearly from the lowest position of the vent followed by a final slight increase to take the maximum value. Comparing with the PIV profile at the top, we note that the value of the maximum outflow velocity is better predicted by the LES rather than the coarse DNS approach.

Due to the conservation principle, the variation on the coarse DNS–LES $< u_1 >_t$ vertical profiles only along the top vent and not along the bottom vent must be justified by a complete redistribution of the outflow over the entire top vent surface. This is justified at first by visualizing the time averaged $< u_1 >_t$ iso-contour plot at the inner surface of the top vent ($x = 2.7$ cm, figure 8.11).

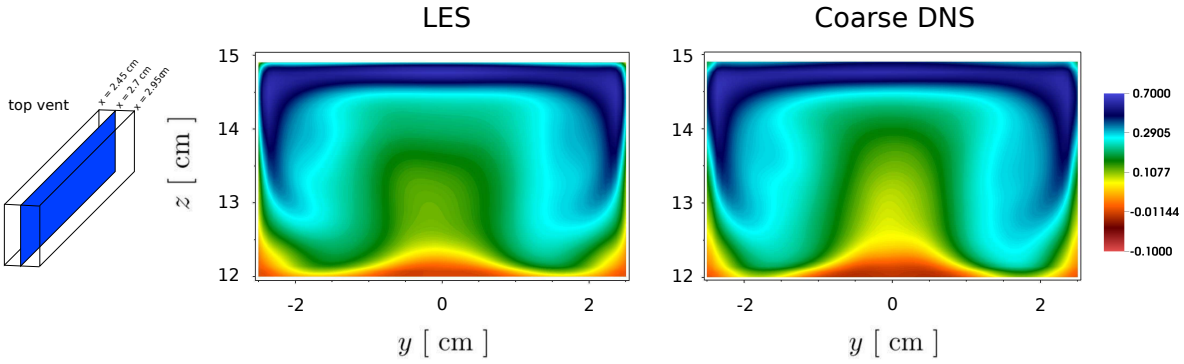

Figure 8.11: CFD comparison of the time averaged flow pattern illustrated by the x-horizontal velocity component $< u_1 >_t$ [m.s^{-1}] iso-contour plot at the inner surface of the top vent ($x = 2.7$ cm). Left: LES, right: Coarse DNS.

All along the lower-middle region of the top vent, the $< u_1 >_t$ iso-contours show that the velocities predicted by the coarse DNS calculation underestimates those of the LES. This underestimation is inverted to an overestimation in the lower extremities regions of the top vent. However, coarse DNS predict a better symmetrical distribution than the LES calculation.

For a global CFD comparison, the time averaged volumetric flow-rate of the inflow and outflow (respectively $< Q_v^{bot} >_t$ and $< Q_v^{top} >_t$) are calculated and summarized in table 8.1.

Configuration	$< Q_v^{bot} >_t$ [$\times 10^{-4}$ m^3.s^{-1}]	$< Q_v^{top} >_t$ [$\times 10^{-4}$ m^3.s^{-1}]	$< \mathcal{M}_{He} >_t$ [$\times 10^{-6}$ kg]	$< q_{He}^{top} >_t$ [$\times 10^{-5}$ kg.s^{-1}]
LES	-2.60348	3.49892	8.47855	1.39376
Coarse DNS	-2.61391	3.51290	8.29632	1.39840

Table 8.1: Global time averaged quantities employed for the LES–DNS comparisons: helium total mass, mass and volumetric flow-rates.

The flow-rates traversing the bottom and top vents predicted by both CFD approaches are almost similar (0.04% error relative to coarse DNS solution). This confirms the redistribution of $< u_1 >_t$, mainly along the surface of the top vent as seen in figure 8.11, where DNS underestimate the LES velocity at the middle of the vent and overestimates at the extremities to ensure the volume conservation principle.

In conclusion, local discrepancies on the velocity field distribution have been mainly reported in the upper part of the cavity (plumes region) where it has been figured out that the LES overestimates both, the coarse DNS and PIV velocities. Globally, it can be stated that the results predicted by the coarse DNS agree better with the PIV measurements. However, as far as no influence of the air inflow has been reported with different CFD approaches and due to the volume conservation principle, the time averaged volumetric flow-rate across the top vent is independent on the employed CFD approach.

8.2.3 Air–helium distribution: CFD compariosons

Now, we serve both CFD predictions to analyze the effect of the turbulence model on the 3D helium distribution inside the cavity. We first consider in figure 8.12 the time averaged helium volume fraction $< X_1 >_t$ iso-contours in the vertical XZ_1-plane (window W_1 for coarse DNS).

Qualitatively, the helium distribution inside the cavity is almost similarly predicted by the LES and coarse DNS calculations. However, two slight discrepancies are reported: first in a small circular structure created near the jet axis in the bottom left of the cavity where we note that the LES calculation predict less helium levels compared to the coarse DNS, and second in the region of the top vent where the LES predicts a slightly less-diluted mixture

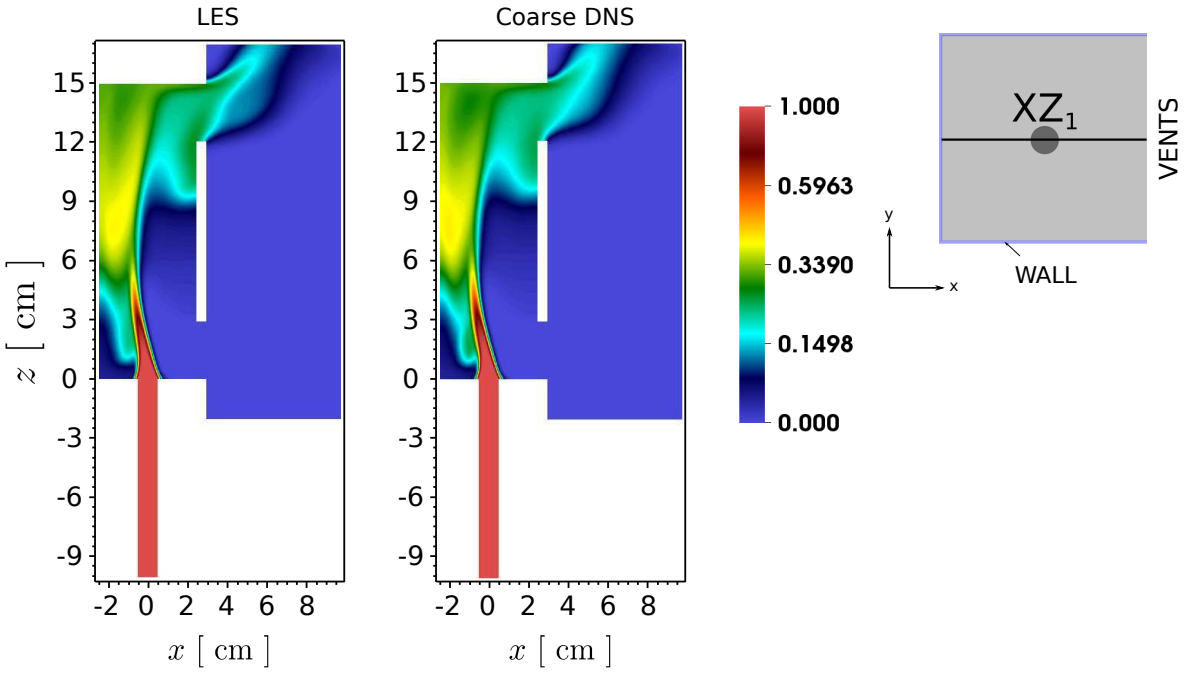

Figure 8.12: CFD comparison of the time averaged flow pattern illustrated by the helium volume fraction $< X_1 >_t$ iso-contour plot in the vertical XZ_1-plane. Left: LES, right: Coarse DNS (window W_1).

(more helium) compared to the coarse DNS.

Next, we consider the $< X_1 >_t$ iso-contours in the mid-vertical YZ_1-plane (figure 8.13). The effect of the reduced velocities already noted from the coarse DNS results in the top plume region is clearly reflected on the the helium volume fraction, where slightly more concentration levels are recorded by the LES calculation. Moreover, we can clearly note that similar helium stratification layers are predicted by the two CFD approaches and thus situated almost in the same vertical position.

The time averaged helium volume fraction $< X_1 >_t$ flow pattern in the vertical $YZ_{4'}$ and YZ_4 planes is depicted in figure 8.14. Almost no discrepancies are noted in the left $YZ_{4'}$-plane (figure 8.14, left) where both calculations predict almost a similar structure of the deviated jet and helium levels in the descending rotational flow.

Slight variations between the LES-DNS predictions are reported in the vertical YZ_4-plane close to the vents where we note that the helium concentration levels are slightly reduced in the coarse DNS calculation. This observation is in accordance with the distribution in the mid-vertical XZ_1-plane (recall figure 8.12) where we noted that the LES predict slight higher helium concentration levels in the recirculating flow near the top vent. However, due to the interaction between the plume ant the exterior environment throughout the top vent, we note that the stratified layer (considering the level 20% of helium) predicted by both approaches is placed approximately at the same height below the lower surface of the top vent (z approximately between 9 to 10 cm).

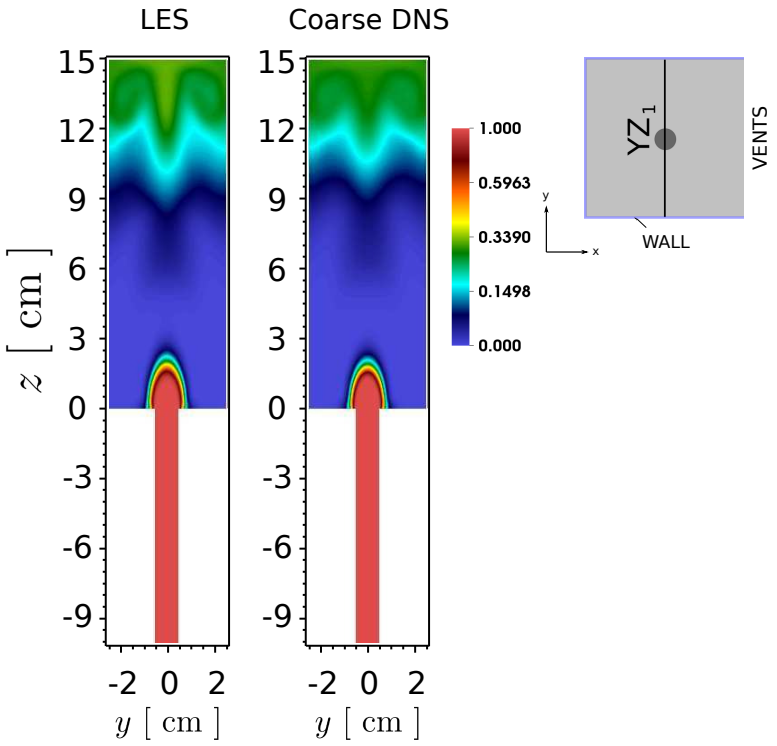

Figure 8.13: CFD comparison of the time averaged flow pattern illustrated by the helium volume fraction $< X_1 >_t$ iso-contour plot in the vertical YZ_1-plane. Left: LES, right: Coarse DNS (window W_1).

Globally, the predicted total mass of helium $< \mathcal{M}_{He} >_t$ inside the cavity for both CFD calculations has been calculated and thus stated in table 8.1. It can be stated that the mass predicted by the LES is not so different from that of the coarse DNS (2.2% error relative to coarse DNS, LES slightly larger). The agreement between both CFD approaches regarding the helium mass values inside the cavity is furthermore confirmed by the top vent helium mass flow-rates $< q_{He}^{top} >_t$, which are almost similarly predicted (0.3% error relative to coarse DNS), in addition to the CFD agreement of the air inflow volumetric flow-rates at the bottom vent.

8.2.4 Helium stratification

To characterize the vertical concentration levels, eight points (uniformly distributed in the horizontal xy-planes) labelled from A to H are employed outside the buoyant jet. The points are fixed in the xy-horizontal plane and thus the time averaged vertical helium volume fraction $< X_1 >_t$ profiles are considered along them (window W_1 for coarse DNS). A top-view of the cavity showing the position of the employed points is illustrated at the top of figure 8.15. The thick red point denotes the projection onto the origin $\mathcal{O}$ of the cartesian system, exhibiting the tube dimension.

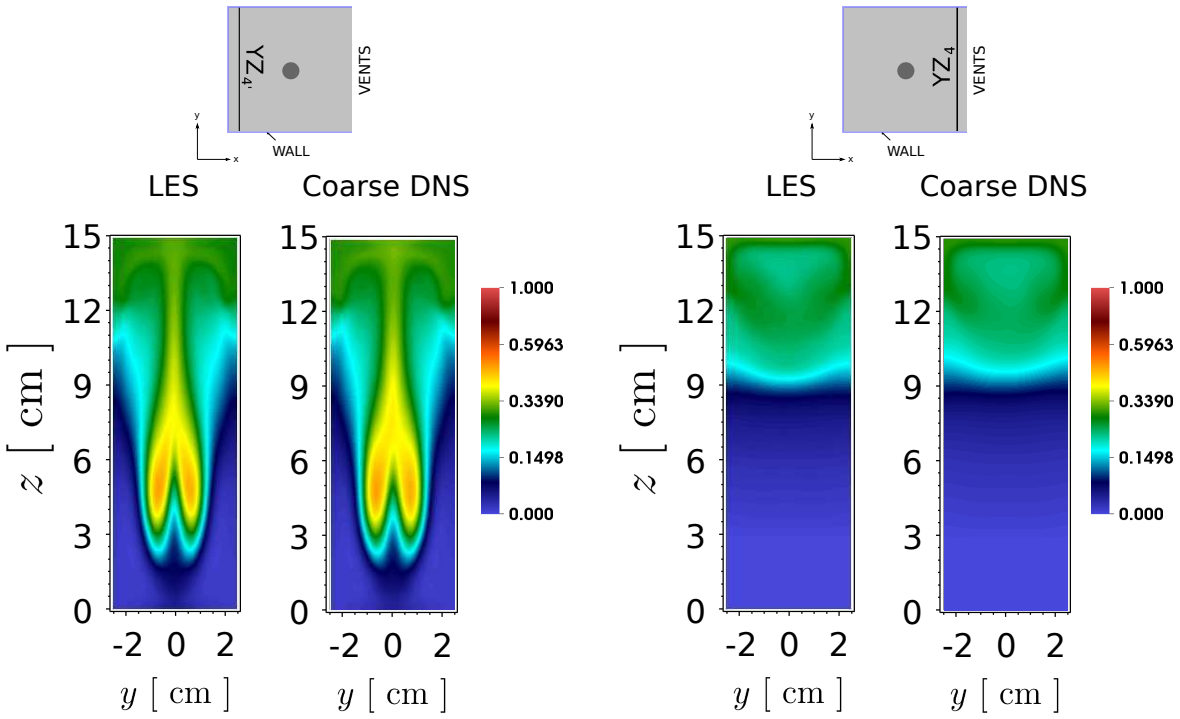

Figure 8.14: LES–DNS comparisons of the time averaged flow pattern illustrated by the helium volume fraction $< X_1 >_t$ iso-contour plot. Left pair: vertical $YZ_{4'}$-plane , right pair: vertical YZ_4-plane.

The vertical profiles of $< X_1 >_t$ at the eight points (points A to H) and along the inclined buoyant jet axis are plotted for both CFD approaches in figure 8.15. We emphasize that the profile along the buoyant jet axis is not identical to the profile along the vertical axis (along the origin $\mathcal{O}$) and is rather defined as the maximum $< X_1 >_t$ value of the horizontal profile in the spreading region (Gaussian profile) with respect to the inclination of the buoyant jet, as described by Lee et al in [LC03].

The shape of the vertical profiles predicted by both calculations at all positions are very similar. Therefore, we describe firstly the behavior independent of the CFD approach.

Four main types of profiles are observed. One is the profile along the jet axis (figure 8.15, center) with a $< X_1 >_t$ starting from 1 (pure helium) at the base of the cavity followed by a decay up to around $z = 7$ cm. Afterwards, a slight increase is noted till about a height $z \approx 9$ cm followed a slight stratified layer with reduced helium levels until reaching the top of the cavity.

The second type is along point E (near the center of the left wall, figure 8.15, middle–left) where the helium volume fraction increases from the bottom of the cavity to $z \approx 7$ cm followed by approximately by the same kind of reduced levels stratified layer followed along the jet axis. This could be expected as the jet is located near the left wall above $z = 7$ cm and therefore the profiles along E and the jet starting from this vertical position are more or less

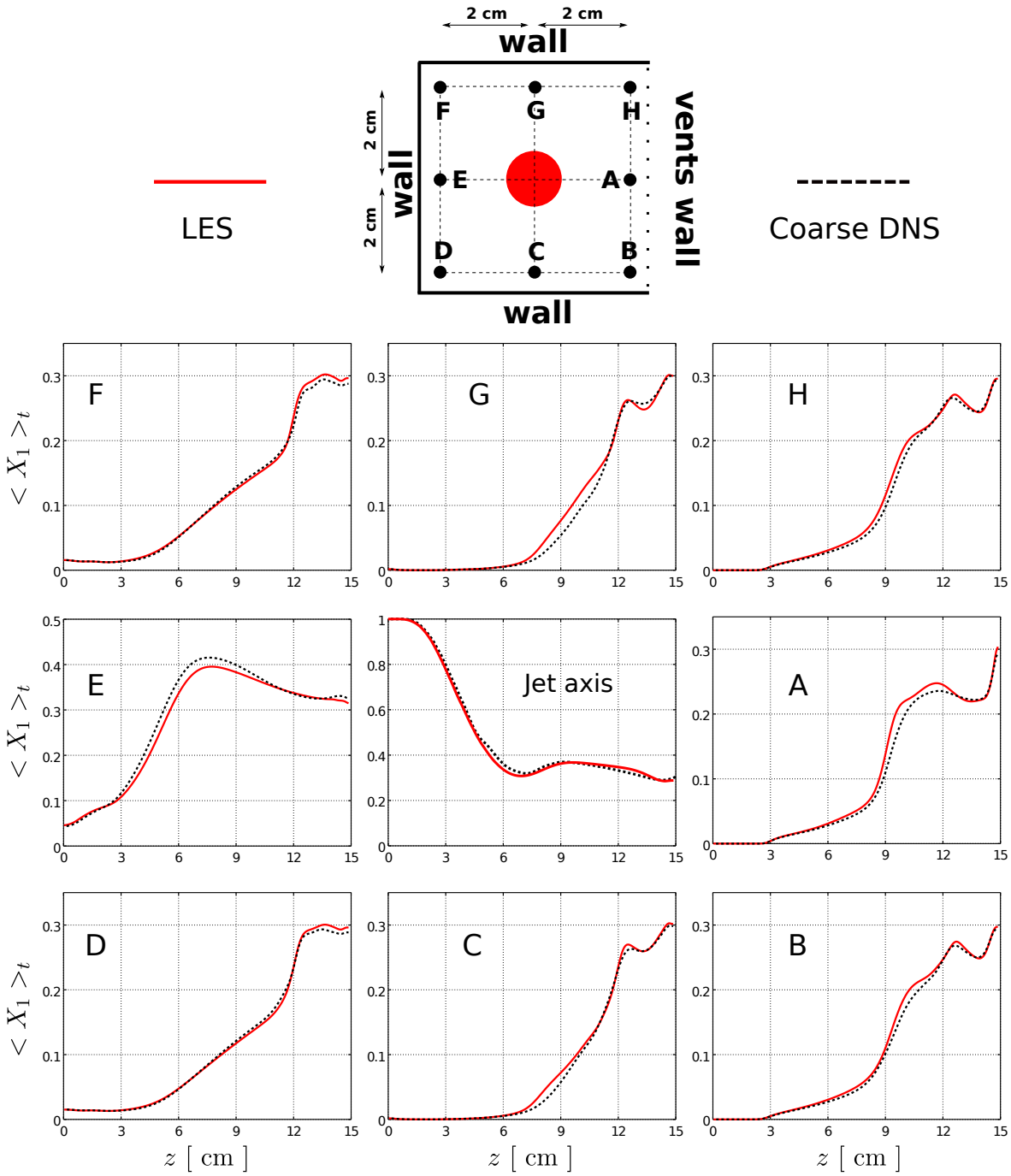

Figure 8.15: Coarse DNS-LES comparisons of the time averaged $< X_1 >_t$ vertical profiles along the eight points A to H (uniformly distributed in the horizontal xy-sections) and along the inclined jet axis.

the same. The stratification behavior is more complex to explain and is certainly due to the strong interaction between the jet and the wall. No simple analysis of the flow structure can predict such a stratification with reduced helium volume fraction levels.

The third type is observed along points D and F situated near the corners facing the vents wall (figure 8.15, top–left and bottom–left). We note that two homogeneous layers are formed in the left of the cavity: first constituting approximately of 0.2% of helium and situated from the bottom of the cavity till about $z = 3$ cm and a second constituting approximately of 30% of helium and situated from about $z = 12.5$ cm till the top of the cavity. These two homogeneous layers are separated by a stratified layer.

The remaining curves (along points A to C and G to H) exhibit a similar forth type of profile (figure 8.15, right, top–middle and bottom–middle). We note that a homogeneous layer constituting of pure air is formed from the bottom of the cavity till about $z = 3$ cm, which is approximately equivalent to the hight of the bottom vent. A stratified layer is formed afterwards till about $z = 12$ cm, followed by a slight decrease for about 0.5 cm to take a stratified behavior afterwards till the top of the cavity. The slight decrease at the top is probably due to the recirculating flow induced by the top vortices that entrains denser mixture inside them, while the stratified layer at the top is due to the boundary layer formed at the ceiling from which the mixture spreads and exits through the top vent.

We consider now the influence of the turbulence model on the $< X_1 >_t$ distribution. Almost no influence is reported on the profile devoted for the jet axis. Along points A to D and F to H (far from the buoyant jet), the maximum helium concentration (29–30%) situated at the top of the cavity is almost similarly predicted by both CFD calculations (maximum error of 1.5% at points F and D relative to coarse DNS).

Slight discrepancies are recorded depending on the profile's location and the employed CFD approach. Starting from about the mid-height of the cavity to the lower height of the top vent (let us say $6 \leq z < 12$ cm), the LES volume fraction prediction slightly overestimates the coarse DNS along points A, B, C, G and H (maximum can be as 35% of overestimation). Moreover, if we consider the profiles along points D and F (in the vicinity of the corners near the left wall), we note that the LES slightly overestimates the helium concentration in the top homogeneous layer by about 1.5% relative to the coarse DNS calculation. The concentration overestimation can be probably justified by additional diffusion induced by the LES Smagorinsky SGS model in the vicinity of the walls where high velocity gradients take place.

Oppositely is the case of the profile along point E which contains a big part of the inclined buoyant jet. In particular, the coarse DNS $< X_1 >_t$ profile shows that the predicted concentration overestimates the LES values, let us say between $3 \leq z < 11$ cm, by about a maximum of 4% (relative to the coarse DNS). It can be stated that this issue is related to the jet inclination which has been noted to be more strengthened in the coarse DNS compared to the LES prediction (recall the velocity distribution in the mid-vertical plane XZ_1).

To describe globally the helium distribution inside the cavity, we consider the mean profiles of the similar third and fourth types; mean of the profiles along points A to C and G to H on the one hand and mean of the profiles along D and F on the second hand. In figure 8.16, both mean profiles in addition to the profiles along point E and the jet axis are sketched.

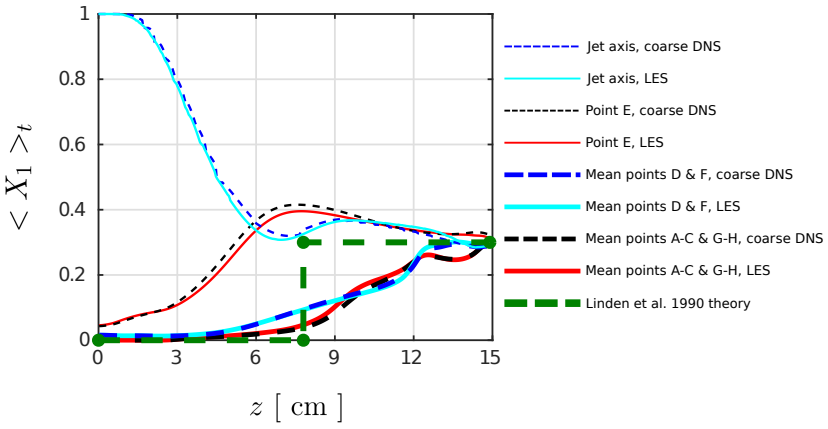

Figure 8.16: Coarse DNS-LES comparisons of the time averaged $< X_1 >_t$ average vertical profile for points A to C and G to H, average vertical profile for points D and F, vertical profiles along point E and the jet axis. Thick green dashed line corresponds to the estimated neutral plan position according to the theory of Linden et al. [LLSS90].

The stratification layer situated from about $z = 3$ cm till 12 cm is noted on all the mean profiles. The plateau seen above this height on the mean profiles of points D and F corresponds to the homogeneous layer formed in the left of the cavity whose height is almost identical to the height of the top vent (≈ 2.9 cm). According to Bernard-Michel et al. in [BMSH17], the height of the homogeneous layer is directly dependent on the internal structure of the counter-rotating vortices. These vortices result from the impact of the buoyant jet with the top-ceiling (see figure 8.9) and dilute the mixture at the top of the cavity. This phenomenon is independent of the top vents' size although it influences significantly the flow pattern across the top vent. Hence, no physical interpretations are currently available to comment in our configuration on the relation between the thickness of the homogeneous layer and the height of the vent.

In such configurations, the theory of Linden et al. [LLSS90] predicts that a helium homogeneous layer will be formed at the top of the cavity separated by an air homogeneous layer from below. In figure 8.16, we depict by the thick green dashed line an estimation performed by Bernard-Michel et al. in [BMSH17] regarding the position and the concentration of the homogeneous layer. We see that the simulated configuration is not situated in the framework of the Linden's theory which predicts a homogeneous layer of height approximately 7 cm in the upper part. However, the maximum concentration of helium at the top (29–30%) and in the predicted homogeneous 2.9 cm layer is in good agreement with the theory.

Being far from the Linden's prediction can be justified by that the helium concentration distribution in our configuration is not 1D as in the theory as far as direct interactions between the buoyant jet and both, the walls and exterior environment take place. However, the fact that maximum concentration is in good agreement with the theoretical prediction is due to the fact of the rather good agreement between the air inflow volumetric flow-rate (bottom vent) predicted by both CFD approaches and the one measured by PIV. Assuming

that the theory agrees with the experiment on the volumetric flow-rate air inflow and since the ratio between that inflow flux and the injected flux is directly connected to that maximum concentration, the agreement of the maximum concentration is justified.

8.3 Turbulent analysis

In this section, we present a turbulence statistical study performed on the coarse DNS solution to qualify the dominant terms presenting in the TKE equation. The statistical fields used in the post-processing correspond to the accumulation carried out over the window W_2 since the correlation terms are recorded over this window only (20 seconds of accumulation ≈ 312.5 as a dimensionless time).

8.3.1 TKE budget

The TKE equation can be written in two forms depending on whether the density weighted averaging operator (Favre) is employed or not (Reynolds averaging is only used otherwise). In what follows, we consider the equation expressed only in the Reynolds sense [2] (average operator $< \cdot >_t^R$) in order to analyze the contribution of the turbulent buoyancy production in the TKE production (refer to appendix D and the turbulence book of Chassaing et al. [CAA+13] for further information).

The Reynolds TKE equation is expressed as

$$\underbrace{\cancelto{0}{\frac{\partial}{\partial t}\Big(< \mathcal{K}_t >_t^R \Big)}}_{\text{transient}} + \underbrace{\frac{\partial}{\partial x_k}\Big(< \mathcal{K}_t >_t^R < u_k >_t^R \Big)}_{\text{convective (1)}} = \underbrace{- < \rho u_i' u_k' >_t^R \frac{\partial < u_i >_t^R}{\partial x_k}}_{\text{shear production (2)}}$$

$$\underbrace{-\frac{\partial}{\partial x_k}\Big\{ \frac{1}{2} < \rho u_i' u_i' u_k' >_t^R \Big\}}_{\text{turbulent diffusion (3)}} + \underbrace{\frac{\partial}{\partial x_k}\Big\{ < \tau_{ik}' u_i' >_t^R \Big\}}_{\text{external power of viscous fluctuations (4)}}$$

$$\underbrace{-\frac{\partial}{\partial x_i}\Big(< P' u_i' >_t^R \Big)}_{\text{external power of pressure fluctuations (5)}} + \underbrace{\Big\langle P' \frac{\partial u_i'}{\partial x_i} \Big\rangle_t^R}_{\text{pressure fluctuation dilatation correlation (6)}}$$

$$\underbrace{-\Big\langle \tau_{ik}' \frac{\partial u_i'}{\partial x_k} \Big\rangle_t^R}_{\text{turbulent dissipation (7)}} + \underbrace{< \rho u_i' >_t^R g_i}_{\text{turbulent buoyancy production term (8)}} \underbrace{-G}_{\text{extra term (9)}} , \tag{8.12}$$

where

$$G = < \rho u_i' >_t^R \frac{\mathrm{D}}{\mathrm{Dt}}\Big(< u_i >_t^R \Big). \tag{8.13}$$

[2] We emphasize that the contribution of buoyancy do not appear in the TKE equation expressed in the Favre sense.

Normally, the transient term vanishes if converging statistical fields are used. This fact has been verified in our case and the transient term is 3 to 5 times in order of magnitude smaller than the other terms.

In order to analyze the contribution of each of the ten distinct terms appearing in the TKE equation (8.12), we consider the iso-contour plot of each term in the mid-vertical XZ_1-plane, graphed to the same color-bar scale $[-6:6]$ with a step of 3 Kg.m^{-1}.s^{-3} (figure 8.17).

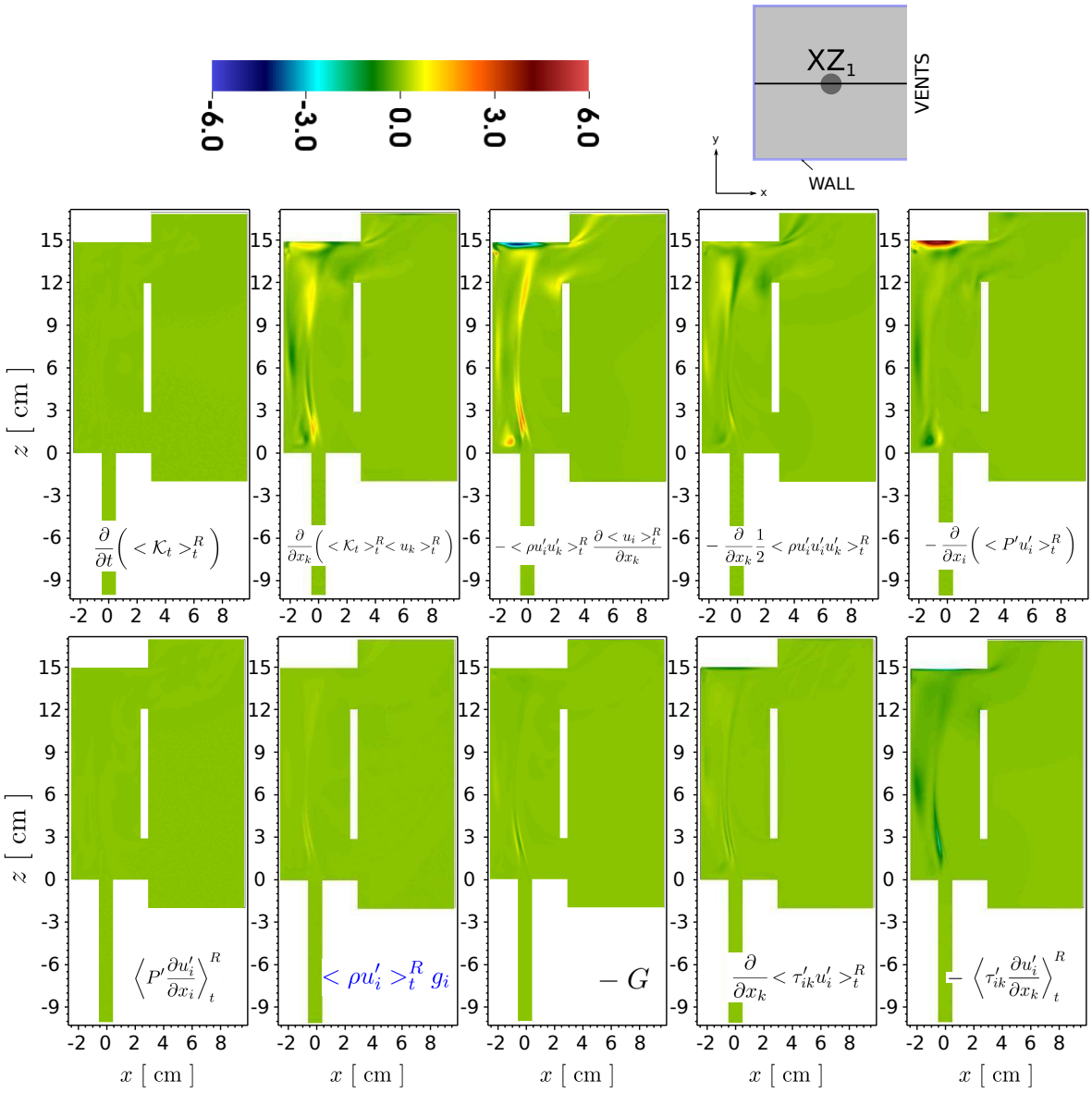

Figure 8.17: The contribution of the ten different terms appearing in the TKE equation: iso-contour plot in the mid-vertical XZ_1-plane, unique scale [Kg.m^{-1}.s^{-3}].

The significant contributions in this plane are predicted by the convective, shear production, turbulent diffusion, external power of pressure fluctuations and the turbulent dissipation terms. Smaller effects are recorded with the extra term G, turbulent buoyancy production

and viscous fluctuations terms. Very low contribution is owed for the pressure fluctuation dilatation correlation term in the TKE equation.

In all cases, the greatest absolute values are situated along the jet axis, the recirculating zones (top left corner, top-vent vicinity and bottom left corner) and in the transitional–plume regimes situated at the mid–top of the cavity. Null values are obviously recorded in the laminar regions situated in the lower vent vicinity, injection pipe and near the right vents wall.

To illustrate the TKE budget, we consider the vertical profiles of each term in the TKE equation and situated in two vertical planes; along $x = -2$ and $x = 0$ cm in the mid-vertical XZ_1-plane and along $y = -2$ cm in the vertical $YZ_{4'}$-plane (figure 8.18).

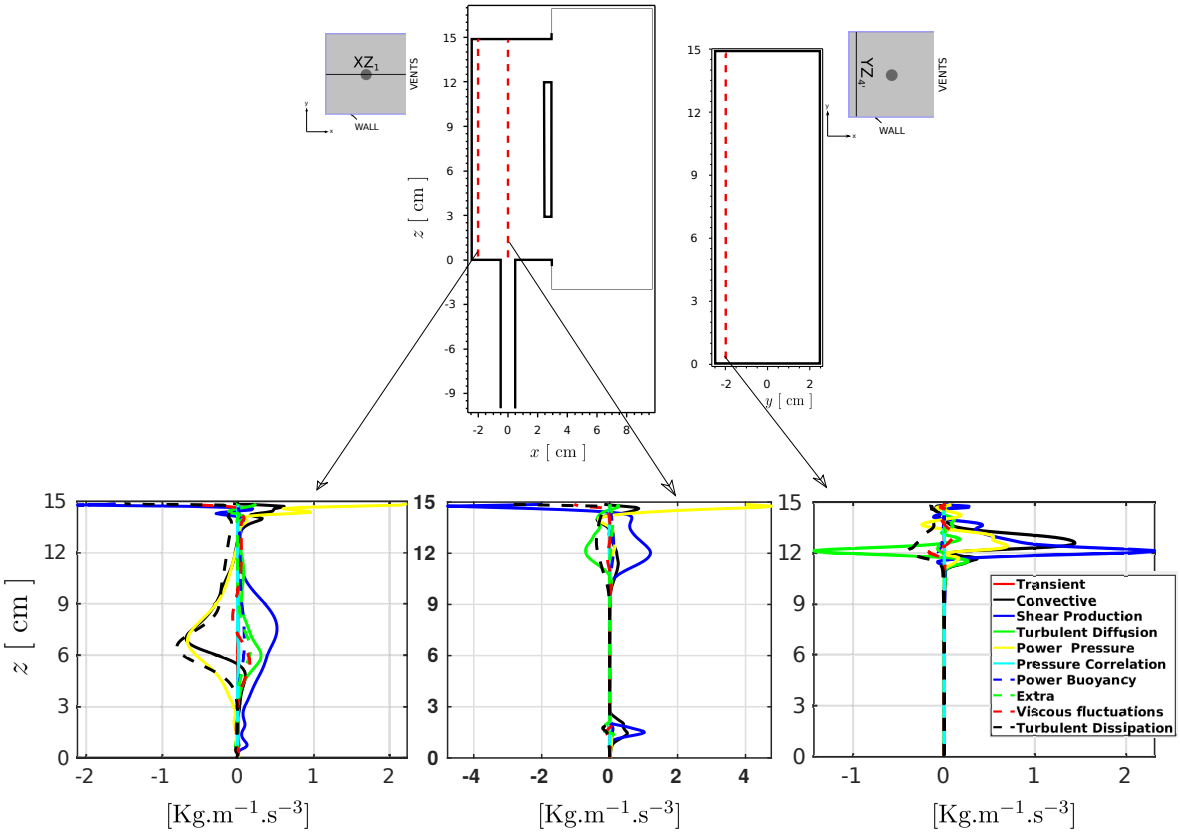

Figure 8.18: TKE budget in illustrated by vertical profiles for each term contribution. Left and middle: respectively along $x = -2$ and $x = 0$ cm in the mid-vertical XZ_1-plane, right: along $y = -2$ cm in the vertical $YZ_{4'}$-plane.

In the vicinity of the left wall of the plane XZ_1 (figure 8.18, left), the highest absolute values are predicted at the top of the cavity (due to the top-ceiling impact and the recirculating flow in the vicinity of the left corner) and along a big portion near the left wall where the flapping motion of the jet axis takes place ($z \approx 5$ to 10 cm). Along the vertical $(\mathcal{O}z)$-axis (figure 8.18, middle), the values are dominant at the top of the cavity in the region of the plume and near the top wall due to the plume-ceiling impact, and at the bottom of the cavity

due to the air-helium impact at this position. Similar is the case in the span-wise vertical $YZ_{4'}$-plane figure 8.18, right) where the highest absolute values are predicted to take place in the rotating vortex that is formed at the top of the cavity.

In both planes, we note again that the five dominant terms are globally the external power of pressure fluctuations, the turbulent dissipation, the shear production, the turbulent diffusion and the convective terms. In figure 8.19, the iso-contour plots of these five terms are depicted in both planes with a convenient scale (independently for each contribution).

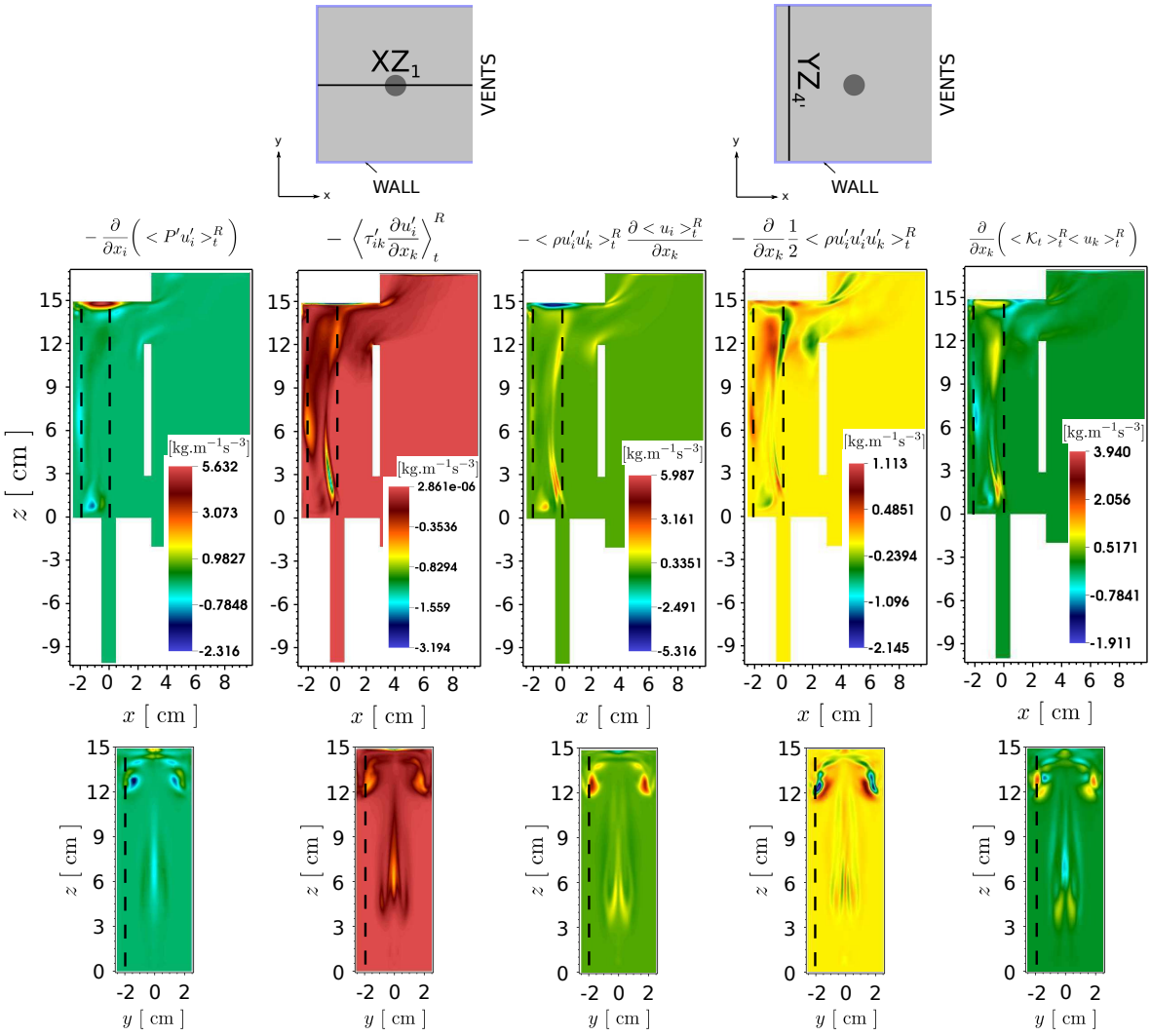

Figure 8.19: The contribution of the five main dominant terms appearing in the TKE budget illustrated by iso-contour plots [Kg.m^{-1}.s^{-3}]. Top: mid-vertical XZ_1-plane, bottom: vertical $YZ_{4'}$-plane.

We can clearly note the location of the maximum absolute values in the plane XZ_1 (dashed black line in figure 8.19, top) and in the span-wise vertical $YZ_{4'}$-plane (dashed black line in figure 8.19, bottom). This is in accordance with the physical phenomena that take place at the top and the left of the cavity (plume region, plume-ceiling impact, air-helium impact and

recirculating flows).

Finally, in order to depict the accuracy of the TKE balance, we compare in figure8.20 the contribution of the convective term (1) with the sum of the remaining terms appearing to the right hand side of equation (8.12) (terms $(2)+(3)+\cdots+(9)$) along the same vertical profiles employed previously. We note a difficulty of convergence in specific flow regions: air-jet cross flow impacting the jet axis, interaction plume-wall (left) and the rotating vortices at the top corners. Generally speaking, the un-balance can vary from several error percentages to 25% (relative to the largest contribution along the considered profile).

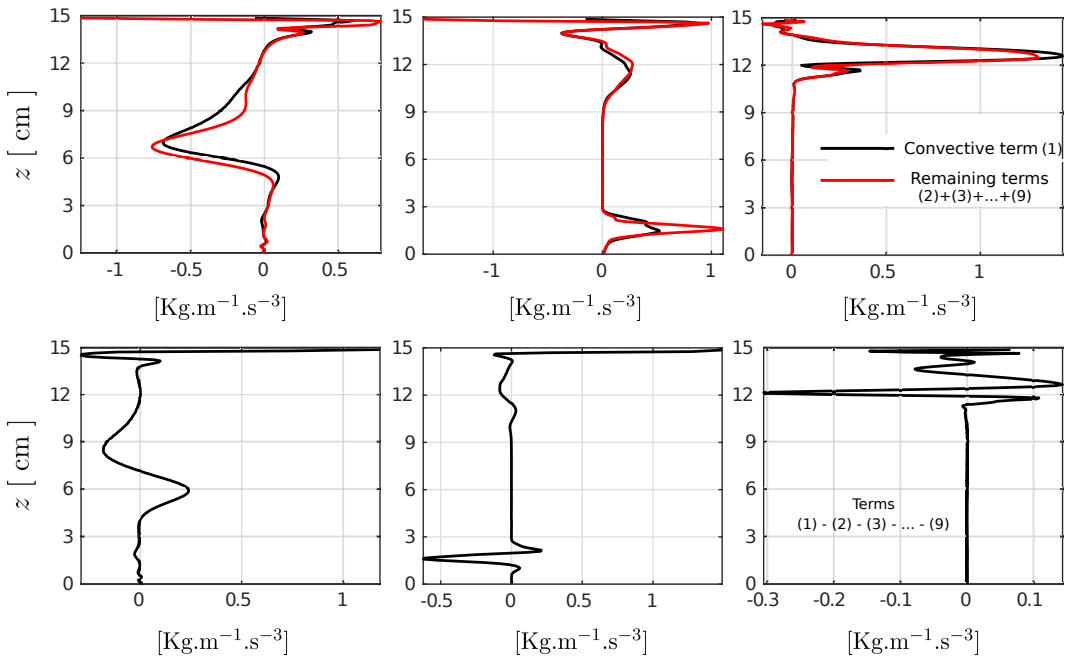

Figure 8.20: Illustration of the TKE budget balance in [Kg.m^{-1}.s^{-3}] along both lines $x = -2$ cm in the mid-vertical XZ_1-plane and $y = -2$ cm in the vertical $YZ_{4'}$-plane. Top: comparison of the convective term contribution to the remaining terms, bottom: the TKE balance.

The non-balance of the TKE budget can be probably due to the statistical post-treatment methodology of the coarse DNS: time convergence of the second and third order correlations, numerical interpolation of the DNS data and the flow in-homogeneity.

8.3.2 Defining the buoyant jet regions: effect of the turbulent buoyancy production term

We recall that the TKE equation (8.12) has been derived in the sense of Reynolds averaging in order to analyze the effect of the external production of the buoyancy term $< \rho u_i' >_t^R g_i$, which does not appear if the averaging operator is a density weighted average (Favre sense). In this subsection, we qualify the effect of the buoyancy for producing the TKE inside the domain although that it has been figured out that its contribution is much smaller compared

to the other five main terms. In particular, we focus on this term to identify the size of the plume region with respect to the buoyant jet and its influence due to the limited height of the cavity.

The term $< \rho u_i' >_t^R$ denotes the turbulent mass flux and is identical to $< \rho' u_i' >_t^R$ as far as $< u_i' >_t^R = 0$ (refer to appendix D). It is clear that the density fluctuations ρ' play an important role in the turbulent mass flux field. In the mid-vertical XZ_1-plane, the helium mass fraction and the density fluctuations are illustrated by the rms field iso-contours (figure 8.21). Highest oscillations are observed on the edges of the jet in the mid-lower part of the cavity due to the heavy air cross-flow impacting the injected (helium) light fluid. Smaller oscillations (by about 60% compared to maximal value) are predicted around the axis of the plume in the upper part of the cavity, near the left flow and in the upper exterior region where there is a direct interaction between the mixture leaving from the top vent and the heavy ambient exterior fluid. As expected, zero fluctuations are recorded in the laminar zones (inside the pipe and in the vicinity of the bottom vent).

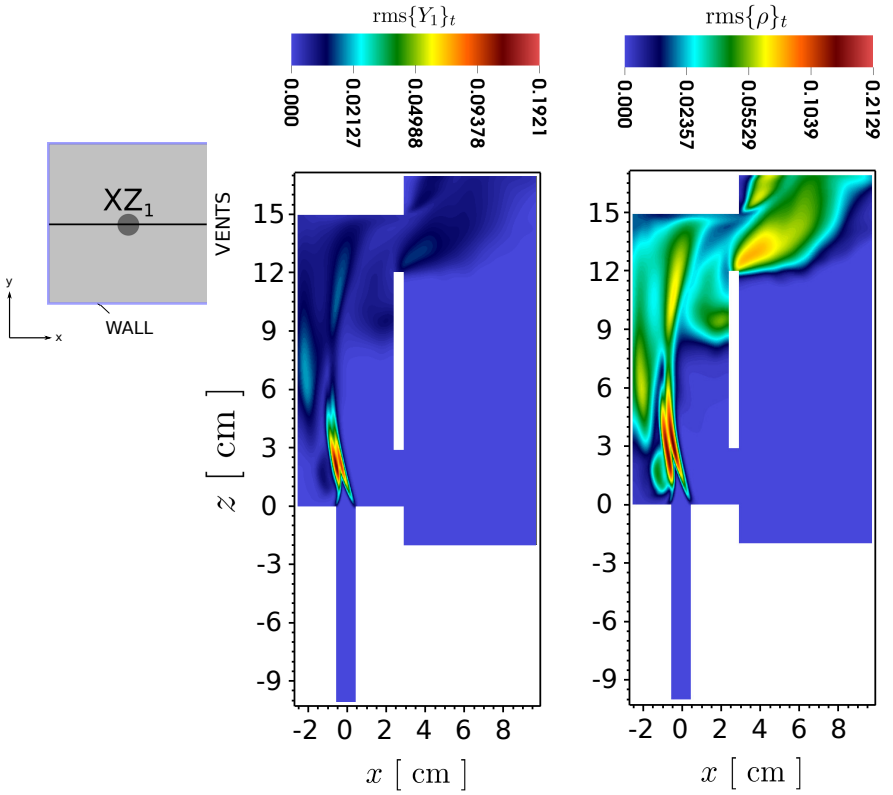

Figure 8.21: RMS iso-contours in the mid-vertical XZ_1-plane. Left: helium mass fraction (rms$\{Y_1\}_t$), right: mixture's density (rms$\{\rho\}_t$).

The distribution of the $< \rho u_i' >_t^R g_i$ in the mid-vertical XZ_1-plane is illustrated by the iso-contour plot in figure 8.22. From the color-bar legend, we can clearly note that the highest values are situated mainly along the buoyant jet axis and edges, in addition to the region near the left wall and the top vent, which is in accordance with the distribution of the density oscillations illustrated previously by the rms$\{\rho\}_t$ field in figure 8.21 (right).

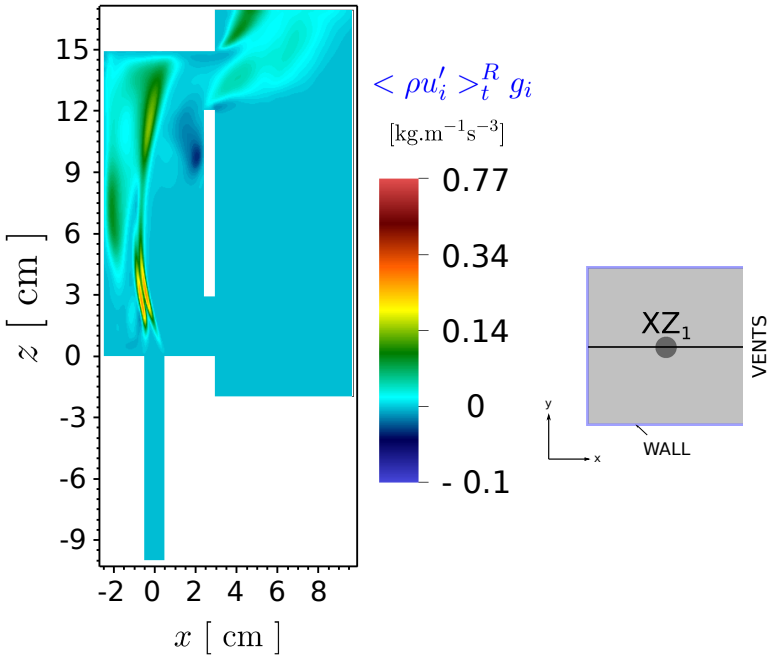

Figure 8.22: The contribution of the external buoyancy production term $< \rho u_i' >_t^R g_i$ appearing in the TKE equation illustrated by iso-contour plots [Kg.m^{-1}.s^{-3}] in the mid-vertical XZ_1-plane.

To describe quantitatively the contribution of the turbulent buoyancy production term, we consider at first the values along the edge of the inclined buoyant jet defined at the positions of the highest fluctuations near the inclined buoyant jet axis (figure 8.23). We note a sharp increase while moving from the bottom of the cavity to reach a maximal value at about 3.2 cm, followed by a decrease till about $z \approx 8$ cm. Afterwards, the values increase to take a local maximum (value about 55% smaller than the maximal value situated at $z \approx 3.2$ cm) at about a height 11.4 cm to decrease finally to reach the top of the cavity.

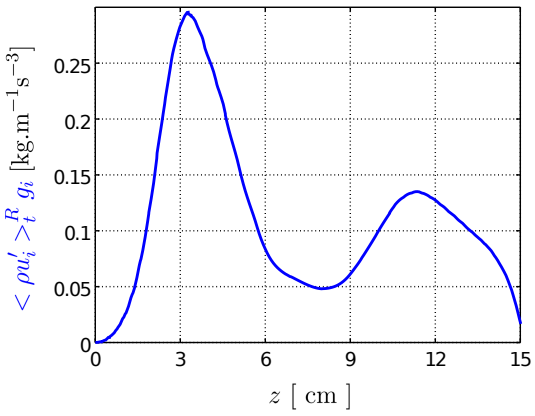

Figure 8.23: The variation of the external buoyancy production term $< \rho u_i' >_t^R g_i$ along the edge of the inclined buoyant jet in the mid vertical XZ_1-plane.

For a complete description in the plane XZ_1, the height of the cavity is divided into three parts: first part situated from the bottom of the cavity ($z = 0$) to $z = 6$ cm, second from $z = 6$ to $z = 9$ cm and the third from $z = 9$ cm till the top of the cavity. The effect of the buoyancy production is analyzed for each part in what follows:

- First part ($z = 0$ to 6 cm):

We note that the largest values of the buoyancy production are situated on the jet axis between $z = 1.5$ to 5 cm due to the heavy–light fluid impact (figures 8.22 and 8.23). In particular, the significant density fluctuations localized at the impact position (figure8.21) induces a big turbulent mass flux $< \rho u_i' >_t^R$ and thus leads to an important buoyancy production. It can be stated that this part is constituted mainly of a jet region (recall laminar-to-turbulent transition has been predicted by LES to occur at $z = 3.8 - 4.5$ cm). From $z = 5$ to 6 cm, the effect of the heavy–light impact is reduced and thus reflected on the values of $< \rho u_i' >_t^R g_i$.

Quantitatively speaking, we consider four horizontal profiles situated respectively at heights $z = 1.5$, 3, 4.5 and 6 cm (figure 8.24, left). Moving from the lower part of the cavity (black profile) till $z = 3$ cm (red profile), we note that the buoyancy production increases in about 90% due to the significant turbulent mass flux at this location (approximately at the same height with the bottom vent top-surface).

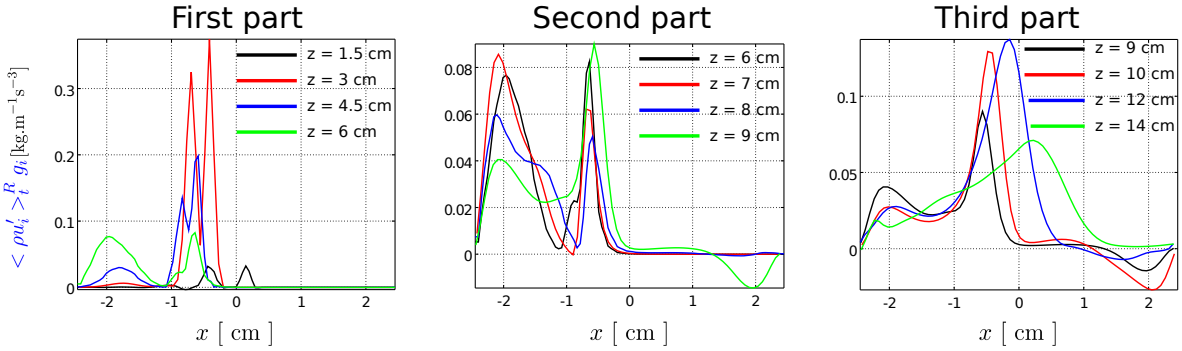

Figure 8.24: The contribution of the external production of the buoyancy term $< \rho u_i' >_t^R g_i$ appearing in the TKE equation illustrated by seven horizontal profiles in the mid-vertical XZ_1-plane. Left: first part from $z = 0$ to 6 cm, middle: second part from $z = 6$ to 9 cm, right: third part from $z = 9$ to 14.9 cm.

As we move toward the upward profiles (to $z = 4.5$ and 6 cm), we note that the buoyancy production contribution is reduced successively due to the reduced effect of the turbulent mass flux above the air–helium impact position. However, the shape of the profiles near the left wall at the two higher altitudes are different compared to the two lower profiles (those at $z = 1.5$ and 3 cm) where we note additional buoyancy production taking place in the left part of the cavity due to the interaction of the jet with the recirculating flow at these locations.

- Second part ($z = 6$ to 9 cm):

Along the buoyant jet axis and edges, the buoyancy contribution is reduced in this zone as we move towards greater altitude until reaching approximately $z = 8.5$ cm where we note that

the values of $< \rho u_i' >_t^R g_i$ start increasing. We predict here the end of the transitional regime and thus the starting of the buoyant dominant zone (plume).

This can be illustrated also by the horizontal profiles at $z = 7$, 8 and 9 cm (figure 8.24, middle). The reduced values along the buoyant jet axis (compared to the first part) can be noted by comparing the black, red and blue solid lines (decrease of the values at $z = 6$ cm from the first part to $z = 7$ and 8 cm respectively in the second part by about a maximum of 25%). An increase is noted afterwards (about 40%) for the highest profile at $z = 9$ cm (green profile).

Moreover, two interesting phenomena are predicted in the second part of the cavity situated in the middle of the vertical XZ_1-plane. First, at $z = 7$ and 8 cm (in the jet–plume transitional regime), the maximum turbulent buoyancy production is predicted near the left wall probably due to the direct interaction between the inclined buoyant jet ant the solid boundary. Second, we note in the starting position of the plume ($z = 9$ cm, green profile in figure 8.24, middle) that there is further a destruction near the right wall (in absolute value 50% smaller than the production near the left wall) basically due to the descending rotating motion recorded near the top vent. However in average, the main turbulent buoyancy production in the plume is situated at the plume's axis.

- Third part ($z = 9$ to 14.9 cm):

Finally, we are situated in the pure plume regime. The turbulent buoyancy production increases along the plume's axis as we move in the upward direction. This is illustrated in the horizontal profiles at $z = 10$ and 12 cm (respectively red and blue solid lines compared to the black profile, figure 8.24, right). We can also note that the maximum buoyancy production in the plume is about 60% smaller than that produced at the bottom ($z = 3$ cm). Afterwards, as we approach the top ceiling ($z = 14$ cm, green profile), the buoyancy production contribution is reduced significantly (about 50%) due to the presence of the solid boundary, and thus the end of the plume regime is reached. This variation which is recorded in the upper part of the cavity, is in accordance with the density oscillations already illustrated by the rms$\{\rho\}_t$ field (recall figure 8.21, right).

8.4 Concluding remarks

In this chapter, a coarse DNS calculation carried out by resuming the previous LES configuration is considered. It has been figured out at first that the turbulent Reynolds stress tensor is almost not aligned with the viscous one (at least in the region of interest: buoyant jet edges, recirculating zones and vortices) which is questionable regarding the validity of the linear eddy viscosity models. Hence, non-linear or RSM models might be required to simulate such flows.

The influence of employing a Smagorinsky SGS model in the numerical simulations is analyzed at second. First, the LES velocity distribution is compared to those predicted by the

coarse DNS and those measured by PIV in 2D plane sections. Next, as far as no experimental measurements regarding the helium distribution are currently available, comparisons regarding the CFD 3D helium distribution are presented.

Discrepancies regarding the CFD predictions of the velocity values are mainly reported at the top of the cavity where the LES tend to overestimate the coarse DNS velocities. As far as the velocity distribution predicted by the coarse DNS approaches better the PIV measurement in the entire domain, it can be stated that the employed LES Smagorinsky SGS model is probably not capturing correctly the turbulence at the top of the cavity. Moreover, discrepancies between the coarse DNS and the PIV velocities can be justified furthermore either due to the differences between the numerical–experimental helium distribution in the upper part of the cavity and mainly near the top vent, and/or the differences between the the numerical–experimental fluctuation level of the injected fluid that has been noted to be about four times more significant in the experiment compared to the numerical simulation. Moreover, the fact that the sensitivity study, which has been carried out previously along the influence of the horizontal exterior domain's dimension only, may explain the recorded discrepancies. In particular, further investigations regarding the influence of the remaining span-wise and vertical exterior dimensions on the flow fields is probably necessary to be carried out in a future work.

When considering the 3D helium volume fraction fields, we note that slight local discrepancies take place when comparing vertical profiles predicted in by both CFD approaches, although global quantities (helium total mass in the cavity and the maximum concentration) are almost similarly predicted. In addition, both calculations predict a stratified concentration regime inside the cavity which make the simulated configuration not situated in the framework of the theoretical predictions; theory of Linden et al. [LLSS90] that predict the formation a bi-layer simple stratification.

Finally, we present some statistical post-treatment carried out on the turbulent kinetic energy (TKE) equation which has been derived by considering only the Reynolds averages. Using this formulation, the external turbulent buoyancy production term is served to identify the three regions of the buoyant jet: pure jet, jet-to-plume transition and pure plume regions. From the literature, these regions could be identified from the auto-similar behavior of the profiles that take place only in the jet and plume regions. However, we rather use the methodology of analyzing the turbulent buoyancy production term as far as we are situated in a configuration where the buoyant jet axis is inclined and the lateral cavity's wall boundaries influences significantly the flow to limit the case of having self-similar solutions.

Conclusions and perspectives

The theme of this study is situated in the framework of security assessment of systems using hydrogen as an energy carrier. The physical problem considered in this dissertation describes an indoor hydrogen release scenario that takes place in a semi-confined vented environment subjected to a natural ventilation system. This scenario, which originates either from a human or a technical error, leads to hazardous consequences due to the concentration accumulation. We mimic the CEA Saclay experimental facility and thus present numerical simulations of an air–helium buoyant jet rising in a two vented cavity. Two CFD codes have been used in the numerical study: LIMSI–CNRS SUNFLUIDH (axi-symmetrical geometries) and CEA TRUST–TrioCFD (3D configurations). Both LES and DNS CFD approaches have been used to simulate the industrial problem. As far as we consider a mass variation problem with small bulk velocities, the low Mach number (LMN) approximation is justified in the work.

Starting from the available experimental PIV measurements, we explore a numerical model that can satisfactory approach the recorded flow pattern. This numerical model has been achieved by following a successive organization of the work where axi-symmetrical simulations have been considered at first. From the first results, different LES calculations are considered where the configuration that approaches the experimental data is identified. Finally, reference numerical solutions are provided by the means of a coarse DNS.

Investigations regarding the influence of imposing inlet/outlet boundary conditions, respectively at the tube and the vent surfaces, have been tested firstly on 2D axi-symmetrical configurations in order to propose a better methodology to approach the natural boundary conditions. Two main conclusions have been figured out at this stage. First, it has been noted that modelling the injection pipe in the computational domain is required in order to take into account both the convective and diffusive injection contributions. Second, it has been figured out that modelling an exterior region in the computational domain influences significantly the flow inside the cavity and thus leads to different concentration distributions. In such situations, one must take care of the size of the exterior domain since non-physical concentration stratification can develop if a reduced exterior dimension is modelled. Therefore, the size of the exterior domain is an important parameter and thus requires a sensitive analysis study to reproduce convergent solutions.

In a next step, we pass to consider 3D cartesian computations modelling the experimental set-up. The LES configuration has been identified at first after performing a sensitivity analysis and an adaptation of the numerical parameters. A small role of the SGS model has been observed in our simulations where small SGS to molecular viscosity ratios are recorded in the computational domain for a used mesh predicted to be, in local spatial locations, at most 3–4 times greater than the Kolmogorov length scale.

The problematic of approaching the 3D natural boundary conditions has been analyzed secondly by considering different horizontal extensions of open exterior domains. A sensitivity analysis has been carried out by performing a convergence study on the size of the exterior

domain. At the end of this study, it has been figured out that an exterior domain with a corresponding volume greater than that of the studied cavity, is required so that the interior cavity flow is not influenced any more by the exterior environment. Sufficiently satisfactory converged time-averaged fields are thus obtained.

Qualitative comparisons show that the global LES–PIV flow pattern is almost similar. This comparisons enforced the necessity of considering an exterior region in the numerical simulations. Quantitatively speaking, discrepancies are mainly recorded in the upper part of the cavity where the LES tends to overestimate the PIV velocities. However globally, a good agreement is noted regarding the volumetric flow-rate of air inflow from the bottom vent and consequently, the volumetric flow-rate of mixture leaving from the top vent. As far as we look towards providing reference numerical solutions in the present work and since local discrepancies are recorded between the LES and PIV velocities, a coarse DNS calculation is carried out in a final step by resuming a calculation without a turbulence model starting from the final LES solution. This is justified by the fact that a sufficiently fine mesh has been used in the simulations (maximum about 3–4 times greater than the Kolmogorov length scale).

Almost no discrepancies are recorded in the lower part of the cavity between both the LES and the coarse DNS solutions, which are in good agreement with the PIV measurements. Discrepancies are however noted in the upper part of the cavity where the coarse DNS prediction agrees better than the LES with the PIV measurements, although local discrepancies up to 45% can take place. Noting discrepancies between the coarse DNS velocities and those measured with the PIV are perhaps due to the differences between the numerical–experimental helium distribution in the upper part of the cavity and mainly near the top vent. In addition, the discrepancies could probably be due to the differences between the numerical–experimental fluctuating level, mainly near the injection surface, which have been noted to be about four times larger in the experiment compared to the simulation. Finally, the issue of the outlet boundary condition might stand behind the recorded discrepancies as far as the sensitivity analysis regarding the size of the exterior domain has been carried out in the present work only along the horizontal direction. Therefore, the sensitivity of the velocity profiles regarding the span-wise and vertical dimensions of the exterior domain require further investigations.

Since no concentration measurements are currently available, we rely on the coarse DNS prediction to analyze the 3D helium volume fraction field. Regarding the global stratified distribution, numerical predictions show that the simulated configuration is not situated in the framework of the theoretical Linden et al. model [LLSS90] which predict the formation of a simple bi-stratified layer. The difference between the stratified regime reproduced by the coarse DNS approach and the theoretical bi-layer predicted regime might be due to the reduced size of the studied configuration where significant direct interactions are noted between the buoyant jet from one side, and both the lateral walls of the cavity and the exterior environment through the top vent from other side. Moreover, the entrainment coefficient modelled in the theory can also explain the recorded discrepancies since it can be not pertinent in such a semi–confined configuration. A good agreement on the same maximum concentration at the top of the cavity is however noted between the presented numerical results and the theory's prediction.

Turbulent analysis are finally presented by carrying out a statistical post-treatment on the turbulent kinetic energy (TKE) equation which has been derived by considering only the Reynolds averages. Using this formulation, the external turbulent buoyancy production term is served to identify the three regions of the buoyant jet: pure jet, jet-to-plume transition and pure plume regions.

The main numerical difficulties and challenges faced by considering the numerical study of the low release flow problem in a two vented cavity are treated. Therefore, it can be stated that we have provided in this study a numerical tool that can be reliable for future studies. This point is extremely interesting and forms a basis to carry out future investigations and treat furthermore the perspectives of this work. We summarize in what follows interesting topics that could been studied in a future work and that will be probably undertaken in the next PhD research. Perspectives of this work can be described in two blocks: physical and numerical interests.

As justified previously, the recorded CFD–PIV velocities discrepancies can perhaps originate from different concentration distribution in the cavity, mainly at the top of the cavity and in the vicinity of the top vent. Therefore, it would be interesting to get experimental concentration measurements in the future so that further complete investigations can be provided regarding the physics of the problem.

The simulated configuration has been noted to be not situated in the framework of the theoretical Linden at al. model [LLSS90] due to the reduced size of the cavity, coupled with the release conditions, which induce direct interaction between the solid boundaries and the exterior environment and thus limit the theoretical prediction. Identifying numerical–physical parameters that can reproduce the Linden configuration is a necessary step to test the validity and/or the limitation of the theoretical predictions. Increasing the dimensions of the cavity and/or the release volumetric flow-rate are mainly the first parameters to check.

Modelling and estimating the entrainment coefficient in limited configurations is an important topic in this subject although not treated in the present work. The work undertaken here will allow in providing information regarding this parameter and therefore helps in the improvement of the theoretical models. Achieving such a work mainly requires the treatment of a bigger geometrical configuration so that the interactions between the buoyant jet and the solid boundaries are reduced. In such a case, we expect to record self-similar solutions from which we employ to define the buoyant jet spreading rate and thus the entrainment coefficient.

As demonstrated in the numerical simulations presented in different cases, modelling the pipe and an exterior region in the computational domain help in approaching better the natural boundary conditions. Adapting new inlet/outlet boundary conditions that can be prescribed directly at the pipe and vent surfaces which mimic the presence of additional regions in the computational domain is an important perspective of this work. Such an approach helps in reducing the computational cost of the simulations from which one can benefit to carry out a complete DNS at the size of the Kolmogorov length scale.

Appendix A

Low Mach Number asymptotic analysis

Dimensionless equations

The reference length L_r is chosen to be the height of the cavity H. We denote by T_r and $P_{\text{thm}r}$ respectively the reference temperature and pressure and chosen to be the actual values of the studied problem. However, the choice of defining the reference velocity $\mathbf{u}_r$ is not unique and it depends on the type of the problem.

We define the dimensionless differential operators and quantities (denoted with the * superscript) as follows

$$x_i^* = \frac{x_i}{L_r}, \quad \frac{\partial}{\partial x_i^*} = L_r \frac{\partial}{\partial x_i}, \quad t^* = \frac{\mathbf{u}_r t}{L_r}, \quad \frac{\partial}{\partial t^*} = \frac{L_r}{\mathbf{u}_r}\frac{\partial}{\partial t},$$

$$\rho^* = \frac{\rho}{\rho_r}, \quad \nu^* = \frac{\nu}{\nu_r}, \quad P_{\text{thm}}^* = \frac{P_{\text{thm}}}{P_{\text{thm}r}},$$

$$T^* = \frac{T}{T_r} = 1, \quad D^* = \frac{D}{D_r}, \quad \mu^* = \frac{\mu}{\mu_r}, \quad \mathbf{u}^* = \frac{\mathbf{u}}{\mathbf{u}_r}.$$

Substituting into equations (3.11), (3.12), (3.15) and (3.21), the non dimensional governing equations read

$$\frac{\partial \rho^* Y_1^*}{\partial t^*} + \frac{\partial}{\partial x_i^*}(\rho^* Y_1^* u_i^*) = \frac{1}{\text{Re}_r.\text{Sc}_r}\frac{\partial}{\partial x_i^*}\left(D^*\rho^*\frac{\partial Y_1^*}{\partial x_i^*}\right), \tag{A.1}$$

$$\frac{\partial \rho^*}{\partial t^*} + \frac{\partial}{\partial x_i^*}(\rho^* u_i^*) = 0, \tag{A.2}$$

$$\frac{\partial (\rho^* u_j^*)}{\partial t^*} + \frac{\partial}{\partial x_i^*}(\rho^* u_j^* u_i^*) = -\frac{1}{\widetilde{\text{Ma}}^2}\frac{\partial P_{\text{thm}}^*}{\partial x_j^*} + \frac{1}{\text{Re}_r}\frac{\partial}{\partial x_i^*}\tau_{ij}^* + \frac{1}{\text{Fr}_r}\rho^*\hat{z}_j, \tag{A.3}$$

$$\rho^* = P_{\text{thm}}^* M_{\text{mix}}^*, \tag{A.4}$$

where Re_r and Sc_r are respectively the reference Reynold and Schmidt numbers similarly defined in section 2.2.3, $\text{Fr}_r = \mathbf{u}_r^2/\mathbf{g}L_r$ is the reference Froude number which represents the ratio of the inertial force to the weight of a fluid element and $\hat{\mathbf{z}} = (0, 0, -1)$ is a negative

unit normal in the direction of the gravitational acceleration. $\widetilde{\mathrm{Ma}} = \sqrt{\frac{\rho_r}{P_{\mathrm{thm}r}}}\mathbf{u}_r$ is a modified reference Mach number [Mül99].

Numerical resolution for LMN are well known to be challenging [TCC00]. For instance, the term $1/\widetilde{\mathrm{Ma}}^2$ in equation (A.3) leads to significant computational errors for $\widetilde{\mathrm{Ma}} \to 0$.

LMN asymptotics

LMN asymptotics were initially used to prove that under certain conditions, the solution of a compressible system can converge to the incompressible solution as $\mathrm{Ma} \to 0$ [KM82, KLN91]. We follow in subsection a similar approach as the one presented by Majda [Maj84, MS85] to derive the set of equations that govern the flow under the LMN hypothesis.

The asymptotic analysis is seen as a regular perturbation problem. Thus, all the flow variables are expressed as a power of $\widetilde{\mathrm{Ma}}$ [Mül99] as follows

$$\rho^* = \rho^*_0 + \rho^*_1\widetilde{\mathrm{Ma}} + \rho^*_2\widetilde{\mathrm{Ma}}^2 + \cdots = \rho^*_0 + \rho^*_1\widetilde{\mathrm{Ma}} + \rho^*_2\widetilde{\mathrm{Ma}}^2 + \mathcal{O}(\widetilde{\mathrm{Ma}}^2),$$
$$u^*_i = u^*_{i\,0} + u^*_{i\,1}\widetilde{\mathrm{Ma}} + u^*_{i\,2}\widetilde{\mathrm{Ma}}^2 + \cdots = u^*_{i\,0} + u^*_{i\,1}\widetilde{\mathrm{Ma}} + u^*_{i\,2}\widetilde{\mathrm{Ma}}^2 + \mathcal{O}(\widetilde{\mathrm{Ma}}^2),$$
$$Y^*_1 = Y^*_{1\,0} + Y^*_{1\,1}\widetilde{\mathrm{Ma}} + Y^*_{1\,2}\widetilde{\mathrm{Ma}}^2 + \cdots = Y^*_{1\,0} + Y^*_{1\,1}\widetilde{\mathrm{Ma}} + Y^*_{1\,2}\widetilde{\mathrm{Ma}}^2 + \mathcal{O}(\widetilde{\mathrm{Ma}}^2),$$
$$P^*_{\mathrm{thm}} = P^*_{\mathrm{thm}0} + P^*_{\mathrm{thm}1}\widetilde{\mathrm{Ma}} + P^*_{\mathrm{thm}2}\widetilde{\mathrm{Ma}}^2 + \cdots = P^*_{\mathrm{thm}0} + P^*_{\mathrm{thm}1}\widetilde{\mathrm{Ma}} + P^*_{\mathrm{thm}2}\widetilde{\mathrm{Ma}}^2 + \mathcal{O}(\widetilde{\mathrm{Ma}}^2),$$

We assume that Re_r, Sc_r and Fr_r remain constant as we vary $\widetilde{\mathrm{Ma}}$. After substituting in equations (A.1), (A.2), (A.3) and (A.4), we obtain

- **Species conservation equation:**

$$\frac{\partial}{\partial t^*}\Big\{\rho^*_0 Y^*_{1\,0} + \widetilde{\mathrm{Ma}}(\rho^*_0 Y^*_{1\,1} + \rho^*_1 Y^*_{1\,0}) + \widetilde{\mathrm{Ma}}^2(\rho^*_0 Y^*_{1\,2} + \rho^*_1 Y^*_{1\,1} + \rho^*_2 Y^*_{1\,0}) + \cdots\Big\} + \frac{\partial}{\partial x^*_i}\Big\{\rho^*_0 Y^*_{1\,0} u^*_{i\,0} + \widetilde{\mathrm{Ma}}(\rho^*_0 Y^*_{1\,0} u^*_{i\,1} + \rho^*_0 Y^*_{1\,1} u^*_{i\,0} + \rho^*_1 Y^*_{1\,0} u^*_{i\,0}) + \widetilde{\mathrm{Ma}}^2(\rho^*_2 Y^*_{1\,0} u^*_{i\,0} + \rho^*_0 Y^*_{1\,2} u^*_{i\,0} + \rho^*_0 Y^*_{1\,0} u^*_{i\,2} + \rho^*_0 Y^*_{1\,1} u^*_{i\,1} + \rho^*_1 Y^*_{1\,0} u^*_{i\,1} + \rho^*_1 Y^*_{1\,1} u^*_{i\,0}) + \cdots\Big\} = \frac{1}{\mathrm{Re}_r.\mathrm{Sc}_r}\frac{\partial}{\partial x^*_i}\Big\{D^*\rho^*_0\frac{\partial Y^*_{1\,0}}{\partial x^*_i} + \widetilde{\mathrm{Ma}}\Big(D^*\rho^*_1\frac{\partial Y^*_{1\,0}}{\partial x^*_i} + D^*\rho^*_0\frac{\partial Y^*_{1\,1}}{\partial x^*_i}\Big) + \widetilde{\mathrm{Ma}}^2\Big(D^*\rho^*_0\frac{\partial Y^*_{1\,2}}{\partial x^*_i} + D^*\rho^*_1\frac{\partial Y^*_{1\,1}}{\partial x^*_i} + D^*\rho^*_2\frac{\partial Y^*_{1\,0}}{\partial x^*_i}\Big) + \cdots\Big\}, \quad \text{(A.5)}$$

which can be arranged as

$$\left\{\frac{\partial}{\partial t^*}(\rho_0^*Y_{1\,0}^*)+\frac{\partial}{\partial x_i^*}(\rho_0^*Y_{1\,0}^*u_{i\,0}^*)-\frac{1}{\mathrm{Re}_r.\mathrm{Sc}_r}\frac{\partial}{\partial x_i^*}\left(D^*\rho_0^*\frac{\partial Y_{1\,0}^*}{\partial x_i^*}\right)\right\}+\widetilde{\mathrm{Ma}}\left\{\frac{\partial}{\partial t^*}(\rho_0^*Y_{1\,1}^*+\rho_1^*Y_{1\,0}^*)+\right.$$
$$\frac{\partial}{\partial x_i^*}(\rho_0^*Y_{1\,0}^*u_{i\,1}^*+\rho_0^*Y_{1\,1}^*u_{i\,0}^*+\rho_1^*Y_{1\,0}^*u_{i\,0}^*)-\frac{1}{\mathrm{Re}_r.\mathrm{Sc}_r}\frac{\partial}{\partial x_i^*}\left(D^*\rho_1^*\frac{\partial Y_{1\,0}^*}{\partial x_i^*}+D^*\rho_0^*\frac{\partial Y_{1\,1}^*}{\partial x_i^*}\right)\Bigg\}+\widetilde{\mathrm{Ma}}^2\Bigg\{$$
$$\frac{\partial}{\partial t^*}(\rho_0^*Y_{1\,2}^*+\rho_1^*Y_{1\,1}^*+\rho_2^*Y_{1\,0}^*)+\frac{\partial}{\partial x_i^*}(\rho_2^*Y_{1\,0}^*u_{i\,0}^*+\rho_0^*Y_{1\,2}^*u_{i\,0}^*+\rho_0^*Y_{1\,0}^*u_{i\,2}^*+\rho_0^*Y_{1\,1}^*u_{i\,1}^*+\rho_1^*Y_{1\,0}^*u_{i\,1}^*+$$
$$\rho_1^*Y_{1\,1}^*u_{i\,0}^*)-\frac{1}{\mathrm{Re}_r.\mathrm{Sc}_r}\frac{\partial}{\partial x_i^*}\left(D^*\rho_0^*\frac{\partial Y_{1\,2}^*}{\partial x_i^*}+D^*\rho_1^*\frac{\partial Y_{1\,1}^*}{\partial x_i^*}+D^*\rho_2^*\frac{\partial Y_{1\,0}^*}{\partial x_i^*}\right)\Bigg\}+\mathcal{O}(\widetilde{\mathrm{Ma}}^2)=0. \tag{A.6}$$

Assuming that equation (A.6) holds true, then

$$\frac{\partial(\rho^*Y_1^*)_\alpha}{\partial t^*}+\frac{\partial}{\partial x_i^*}(\rho^*Y_1^*u_i^*)_\alpha=\frac{1}{\mathrm{Re}_r.\mathrm{Sc}_r}\frac{\partial}{\partial x_i^*}\left(D^*\rho^*\frac{\partial Y_1^*}{\partial x_i^*}\right)_\alpha \quad : \quad \alpha=0,1,2. \tag{A.7}$$

- **Mass conservation equation:**

$$\frac{\partial}{\partial t^*}\left\{\rho_0^*+\rho_1^*\widetilde{\mathrm{Ma}}+\rho_2^*\widetilde{\mathrm{Ma}}^2+\cdots\right\}+\frac{\partial}{\partial x_i^*}\left\{\rho_0^*u_{i\,0}^*+\widetilde{\mathrm{Ma}}(\rho_0^*u_{i\,1}^*+\rho_1^*u_{i\,0}^*)+\widetilde{\mathrm{Ma}}^2(\rho_0^*u_{i\,2}^*+\rho_1^*u_{i\,1}^*+\right.$$
$$\left.\rho_2^*u_{i\,0}^*)+\cdots\right\}=0, \tag{A.8}$$

simplified as

$$\left\{\frac{\partial\rho_0^*}{\partial t^*}+\frac{\partial}{\partial x_i^*}(\rho^*u_i^*)_0\right\}+\widetilde{\mathrm{Ma}}\left\{\frac{\partial\rho_1^*}{\partial t^*}+\frac{\partial}{\partial x_i^*}(\rho^*u_i^*)_1\right\}+\widetilde{\mathrm{Ma}}^2\left\{\frac{\partial\rho_2^*}{\partial t^*}+\frac{\partial}{\partial x_i^*}(\rho^*u_i^*)_2\right\}+\mathcal{O}(\widetilde{\mathrm{Ma}}^2)=0. \tag{A.9}$$

Equation (A.9) holds if and only if

$$\frac{\partial\rho_\alpha^*}{\partial t^*}+\frac{\partial}{\partial x_i^*}(\rho^*u_i^*)_\alpha=0 \quad : \quad \alpha=0,1,2. \tag{A.10}$$

- **Momentum conservation equation:**

$$\frac{\partial}{\partial t^*}\left\{\rho_0^*u_{j\,0}^*+\widetilde{\mathrm{Ma}}(\rho_1^*u_{j\,0}^*+\rho_0^*u_{j\,1}^*)+\widetilde{\mathrm{Ma}}^2\rho_1^*u_{j\,1}^*+\cdots\right\}+\frac{\partial}{\partial x_i^*}\left\{\rho_0^*u_{j\,0}^*u_{i\,0}^*+\widetilde{\mathrm{Ma}}(\rho_1^*u_{j\,0}^*u_{i\,0}^*+\right.$$
$$\rho_0^*u_{j\,1}^*u_{i\,0}^*+\rho_0^*u_{j\,0}^*u_{i\,1}^*)+\widetilde{\mathrm{Ma}}^2(\rho_0^*u_{j\,1}^*u_{i\,1}^*+\rho_1^*u_{j\,0}^*u_{i\,1}^*+\rho_1^*u_{j\,1}^*u_{i\,0}^*)+\cdots\Bigg\}=-\frac{1}{\widetilde{\mathrm{Ma}}^2}\frac{\partial}{\partial x_j^*}\Bigg\{P_{\mathrm{thm}0}^*+$$
$$P_{\mathrm{thm}1}^*\widetilde{\mathrm{Ma}}+P_{\mathrm{thm}2}^*\widetilde{\mathrm{Ma}}^2+\cdots\Bigg\}+\frac{1}{\mathrm{Re}_r}\frac{\partial}{\partial x_i^*}\left\{\tau_{ij\,0}^*+\cdots\right\}+\frac{1}{\mathrm{Fr}_r}\left\{\rho_0^*+\rho_1^*\widetilde{\mathrm{Ma}}+\rho_2^*\widetilde{\mathrm{Ma}}^2\cdots\right\}\hat{z}_j, \tag{A.11}$$

where $\tau_{ij\,0}^*=2\mu_0^*e_{ij\,0}^*$.

Thus, equation (A.11) simplifies as

$$\frac{\partial P^*_{\text{thm}0}}{\partial x^*_j}\widetilde{\text{Ma}}^{-2} + \frac{\partial P^*_{\text{thm}1}}{\partial x^*_j}\widetilde{\text{Ma}}^{-1} + \frac{\partial}{\partial t^*}(\rho^*_0 u^*_{j\,0}) + \frac{\partial}{\partial x^*_i}(\rho^*_0 u^*_{j\,0} u^*_{i\,0}) + \frac{\partial P^*_{\text{thm}2}}{\partial x^*_j} - \frac{1}{\text{Re}_r}\frac{\partial \tau^*_{ij_0}}{\partial x^*_i} - \frac{1}{\text{Fr}_r}\rho^*_0 \hat{z}_j + \mathcal{O}(\widetilde{\text{Ma}}^0) = 0. \quad \text{(A.12)}$$

To satisfy equation (A.12), we require the following

$$\frac{\partial P^*_{\text{thm}0}}{\partial x^*_j} = 0 \quad \text{(A.13)}$$

$$\frac{\partial P^*_{\text{thm}1}}{\partial x^*_j} = 0 \quad \text{(A.14)}$$

$$\frac{\partial}{\partial t^*}(\rho^*_0 u^*_{j\,0}) + \frac{\partial}{\partial x^*_i}(\rho^*_0 u^*_{j\,0} u^*_{i\,0}) = -\frac{\partial P^*_{\text{thm}2}}{\partial x^*_j} + \frac{1}{\text{Re}_r}\frac{\partial \tau^*_{ij_0}}{\partial x^*_i} + \frac{1}{\text{Fr}_r}\rho^*_0 \hat{z}_j \quad \text{(A.15)}$$

- **Equation of state:**

$$\rho^*_0 + \rho^*_1\widetilde{\text{Ma}} + \rho^*_2\widetilde{\text{Ma}}^2 + \cdots = P^*_{\text{thm}0}{M_{\text{mix}0}}^* + \widetilde{\text{Ma}}\Big\{P^*_{\text{thm}0}{M_{\text{mix}1}}^* + P^*_{\text{thm}1}{M_{\text{mix}0}}^*\Big\} + \widetilde{\text{Ma}}^2\Big\{P^*_{\text{thm}0}{M_{\text{mix}2}}^* + P^*_{\text{thm}1}{M_{\text{mix}1}}^* + P^*_{\text{thm}2}{M_{\text{mix}0}}^*\Big\} + \cdots . \quad \text{(A.16)}$$

Following a similar procedure as in the conservation equation and truncating to an order of $\mathcal{O}(\widetilde{\text{Ma}}^2)$, we obtain

$$\rho^*_\alpha = P^*_{\text{thm}\alpha}{M_{\text{mix}\alpha}}^* \quad : \quad \alpha = 0, 1, 2. \quad \text{(A.17)}$$

LMN dimensionless equations

From equations (A.13) and (A.14), we prove that the thermodynamic pressure $P^*_{\text{thm}0}$ and the acoustic pressure $P^*_{\text{thm}1}$ are uniform in space; thus functions of the time t only.

Using single scale asymptotic analysis, we consider the zero Mach-order equations; denoted by the LMN equations. In this approximation, all acoustic effects are filtered out and the total pressure is uniform in space up to fluctuations of order $\widetilde{\text{Ma}}^2$,

$$P^*_{\text{thm}}(\mathbf{x}, t) = P^*_0(t) + \widetilde{\text{Ma}}^2 P^*_2(\mathbf{x}, t). \quad \text{(A.18)}$$

The dimensionless system of equations at the zero Mach-order reads

$$\frac{\partial \rho^* Y_1^*}{\partial t^*} + \frac{\partial}{\partial x_i^*}(\rho^* Y_1^* u_i^*) = \frac{1}{\mathrm{Re}_r.\mathrm{Sc}_r}\frac{\partial}{\partial x_i^*}\left(D^*\rho^*\frac{\partial Y_1^*}{\partial x_i^*}\right), \tag{A.19}$$

$$\frac{\partial \rho^*}{\partial t^*} + \frac{\partial}{\partial x_i^*}(\rho^* u_i^*) = 0, \tag{A.20}$$

$$\frac{\partial \rho^* u_j^*}{\partial t^*} + \frac{\partial}{\partial x_i^*}(\rho^* u_j^* u_i^*) = -\frac{\partial P_2^*}{\partial x_j^*} + \frac{1}{\mathrm{Re}_r}\frac{\partial \tau_{ij}^*}{\partial x_i^*} + \frac{1}{\mathrm{Fr}_r}\rho^* \hat{z}_j, \tag{A.21}$$

$$\rho^* = P_0^* M_{\mathrm{mix}}^*. \tag{A.22}$$

Appendix B

LES approach and SGS models

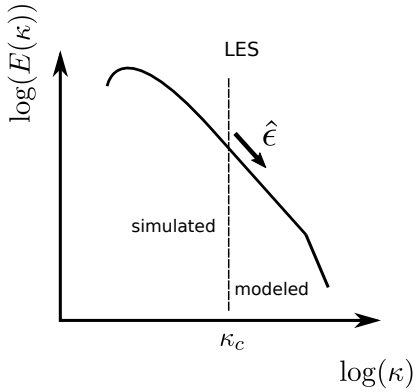

Figure B.1: Energy spectrum in LES approach: modeled against simulated zones.

The LES models are situated between the DNS and RANS-FANS approaches. It takes the advantage of the fact that large length scale are sensitively dependent on the geometry and the initial-boundary conditions on one side, and that smallest scales are isotropically universal on the other side. In practice, the main idea behind LES is to filter out the fine or high frequency scales of motion and solve directly for the large scales. The effect of the sub-grid scales (SGS) is modeled by an appropriate SGS turbulence model.

Smagorinsky in [Sma63], introduced the first notion of scale separation while studying the movements in the atmosphere. Later, Lilly in [Lil62] used the notion of Smagorinsky and had proposed a modification on the model. Deardorff in [Dea70] performed afterwords LES simulations for turbulent flows inside canals and thus proposed some modifications. The formalism of the filter function (spatial filter), the same as we use today, was firstly introduced by Leonard in [Leo75]. The generalization was carried out by Germano in [Ger92], for which the filter takes into consideration the time variable.

Two notions of spatial filtering are required for density variable flows. The first is the classical averaging (sense of Reynold) which we denote by the over-bar symbol ($\overline{\cdot}$). The second notion is used to treat the density dependence. Thus, we introduce the density weighted average (sense of Favre), denoted by the tilde symbol ($\widetilde{\cdot}$). For an arbitrary fluid variable φ transported with ρ, say $\mathbf{u}, Y$ or T, we write

$$\widetilde{\varphi} = \frac{\overline{\rho\varphi}}{\overline{\rho}}. \tag{B.1}$$

The classical LES filter is normally defined, in the physical space, for an arbitrary variable f as

$$\overline{f}(\mathbf{x},t) = \int_{-\infty}^{\infty}\int_{-\infty}^{\infty}\int_{-\infty}^{\infty} f(\mathbf{\Xi},t)\mathcal{G}(\mathbf{\Xi},\mathbf{x})d\mathbf{\Xi}, \tag{B.2}$$

where $\mathcal{G}$ denotes the filter of width Δ [Ald13]. The fluctuations of f from the filtered quantity $\overline{f}$ is defined as

$$f' = f - \overline{f}. \tag{B.3}$$

For spatially and temporally invariant and localized filter functions, the filter is defined as

$$\mathcal{G}(\mathbf{\Xi},\mathbf{x}) = G(\mathbf{\Xi}-\mathbf{x}), \tag{B.4}$$

and satisfying the relations

$$G(\mathbf{x}) = G(-\mathbf{x}) \quad \text{and} \quad \int_{-\infty}^{\infty}\int_{-\infty}^{\infty}\int_{-\infty}^{\infty} G(\mathbf{x})d\mathbf{x} = 1. \tag{B.5}$$

Thus, a filtered quantity can be simply re-defined as

$$\overline{f}(\mathbf{x},t) = G \star f(\mathbf{x},t), \tag{B.6}$$

where $\star$ stands for the convolution operator.

For a weighted density filtered quantity $\widetilde{\varphi}$, we define the fluctuating component as

$$\varphi'' = \varphi - \widetilde{\varphi}. \tag{B.7}$$

It is important to note that the filter operator preserves the linearity property (say for example $\overline{f+g} = \overline{f} + \overline{g}$ and $\overline{\beta f} = \beta\overline{f}$ for any flow variables f,g and a scalar β). However, it does not satisfy in general the Reynold's operator, which means

$$\overline{\overline{f}} = G \star [G \star f] \neq \overline{f}, \tag{B.8}$$

$$\overline{f'} \neq 0. \tag{B.9}$$

The most frequently used filters in the framework of LES are the box filter (top-hat), Gaussian filter and the spectral cut-off. The respective definitions differ by considering a physical or a spectral space, and can be reviewed from [Bri04]. The box filter is mostly used for finite difference or volumes scheme with a filter width Δ usually taken as

$$\Delta = (\delta_x\delta_y\delta_z)^{1/3}, \tag{B.10}$$

where δ_x, δ_y and δ_z are respectively the grid spacing, per direction, of a cartesian mesh. Thus, the filtered quantity would just be the averaged quantity in a considered cell. The Gaussian filter is similarly used with a Gaussian distribution on a width Δ, defined similarly as equation (B.10). Finally, the cut-off filter is based on the cut-off wave number $k_c = \pi/\Delta$ (figure B.1). Most LES models are based on analysis of this filter [Wor03]. The choice of the filter is not

trivial for special simulations and can lead to different results for different filters, as showed by Salvetti and Beaux in [SB98].

The system of LES equations that govern the flow problem is obtained after applying the filtering operation on the conservation equations (mass, momentum, species and energy). Similar to the RANS-FANS derivation, additional terms appear on the right hand side of the conservation equations. They are respectively $-\nabla.\tau^{\mathrm{SGS}}$, $-\nabla.\xi^{\mathrm{SGS}}$ and $-\nabla.\mathcal{H}^{\mathrm{SGS}}$, where τ^{SGS} denotes the SGS stress tensor term (Reynold's), ξ^{SGS} the SGS mass flux and the SGS heat flux $\mathcal{H}^{\mathrm{SGS}}$. They are respectively defined as

$$\tau^{\mathrm{SGS}} = \overline{\rho}\Big(\widetilde{\mathbf{u}\otimes\mathbf{u}} - \widetilde{\mathbf{u}}\otimes\widetilde{\mathbf{u}}\Big), \tag{B.11}$$

$$\xi^{\mathrm{SGS}} = \overline{\rho}\Big(\widetilde{\mathbf{u}Y} - \widetilde{\mathbf{u}}\widetilde{Y}\Big), \tag{B.12}$$

$$\mathcal{H}^{\mathrm{SGS}} = \overline{\rho}\Big(\widetilde{\mathbf{u}T} - \widetilde{\mathbf{u}}\widetilde{T}\Big). \tag{B.13}$$

The heart of the LES models is in the extra tensors that appear as new unknown variables, and thus require modelling. We emphasize that the SGS modelling of LES is based on the fact of the universal properties of small turbulence scales. This is generally verified far from the solid boundaries (wall) as stated in [Sag06].

The starting point is the modelling of the stress tensor term τ^{SGS}. Generally, the idea is based on an eddy-viscosity model (say the Boussinesq's hypothesis, mixing length) [Cha04]. Classical Smagorinsky's model is one of the widely used models [Sma63]. It is based on the hypothesis of the mixing length model, where the SGS viscosity μ^{SGS} is considered to be proportional to Δ and a convenient velocity scale. The model finally reads

$$\tau^{\mathrm{SGS}} - \frac{1}{3}\,\mathrm{diag}(\tau^{\mathrm{SGS}}) = -2\mu^{\mathrm{SGS}}\ \overline{S}, \tag{B.14}$$

where

$$\mu^{\mathrm{SGS}} = \overline{\rho}(C_s\Delta)^2\sqrt{2\ \overline{S} : \overline{S}}, \tag{B.15}$$

where : denotes the tensor contraction operator and S is the symmetrical part of the deformation tensor defined as

$$S = \frac{1}{2}\Big((\nabla\otimes\mathbf{u}) + {}^{T}(\nabla\otimes\mathbf{u})\Big). \tag{B.16}$$

The Smagorinsky's constant is determined from the local balance hypothesis between the production and dissipation of the turbulent kinetic energy k_t. Considering a homogeneous isotropic turbulence, the spectrum of k_t is a spectrum of Kolmogorov, already presented in equation (1.5). Assuming that the cut-off is situated in the inertial range (figure B.1), Smagorinsky figured out that the constant must be defined as

$$C_s = \frac{1}{\pi}\left(\frac{3C}{2}\right)^{-3/4} = 0.18, \tag{B.17}$$

in order to be in agreement with the Kolmogorov's spectrum ($C = 1.4$, the Kolmogorov's constant).

It is clear that the Smagorinsky's model does not take into account the rotational part of the deformation tensor,

$$\Omega = \frac{1}{2}\Big((\nabla \otimes \mathbf{u}) - {}^{T}(\nabla \otimes \mathbf{u})\Big), \tag{B.18}$$

which itself plays an important role in the turbulent dissipation. In addition, this model is known to be of order $\mathcal{O}(1)$ at the walls, meaning that the modelled viscosity is not null near the walls regions [Cha04]. Thus, Nicoud et al in [ND99a] propose a model named as the Wall-Adapting Local Eddy-Viscosity (WALE) which take into account all the components of the deformation tensor and combined to obtain a neighbouring asymptotic behavior at the walls of third order, thus approaching a zero viscosity value.

Regarding the SGS flux terms ξ^{SGS} and $\mathcal{H}^{\mathrm{SGS}}$ (mass or heat tensors), the general models used are the constant Schmidt and Prandtl SGS models, derived from the Fick's hypothesis. The flux tensors are modeled as

$$\xi^{\mathrm{SGS}} = -\overline{\rho} D^{\mathrm{SGS}} \nabla \widetilde{Y}, \tag{B.19}$$

$$\mathcal{H}^{\mathrm{SGS}} = -\overline{\rho} \alpha^{\mathrm{SGS}} \nabla \widetilde{T}, \tag{B.20}$$

where

$$\overline{\rho} D^{\mathrm{SGS}} = \frac{\mu^{\mathrm{SGS}}}{\mathrm{Sc}^{\mathrm{SGS}}}, \tag{B.21}$$

$$\overline{\rho} \alpha^{\mathrm{SGS}} = \frac{\mu^{\mathrm{SGS}}}{\mathrm{Pr}^{\mathrm{SGS}}}, \tag{B.22}$$

with D^{SGS} and α^{SGS} are respectively the modeled SGS molecular and thermal diffusivity. The SGS Schmidt and Prandtl numbers are assumed constants in this model, usually with values between 0.5 and 1.1 [Cha04].

From a physical point of view, the constant Schmidt and Prandtl models assume that the SGS fluxes are perfectly correlated with the concentration and temperature gradients. However, there exists other models that does not employ the Fick hypothesis, say the dynamic scalar and the similarity scale models.

The list of models is too long and much more and more models exist in the literature. Note that much more models exists for closing the momentum equation rather than the scalar equations. A good review can be seen in the book of Sagaut in [Sag06] or in the Ph.D. dissertations of Chatelain in [Cha04], Worthy in [Wor03] and Brillant in [Bri04].

Appendix C

Post-treatment quantities

In this appendix, we define the quantities that are used to post-treat the numerical results. The terms t_{start} and t_{end} denote respectively the starting and ending times at which the statistical fields are recorded. The value of t_{start} is different from one simulation to another and depends on the time at which a quasi-steady state is assumed.

Consider an arbitrary flow variable $\varphi(\mathbf{x}, t)$, we define

- Time averaging operator: $< \cdot >_t$

$$< \varphi(\mathbf{x}, t) >_t = \frac{1}{t_{\text{end}} - t_{\text{start}}} \int_{t_{\text{start}}}^{t_{\text{end}}} \varphi(\mathbf{x}, t) dt, \tag{C.1}$$

- Fluctuating part of a field field: $(\cdot)'$

$$\varphi'(\mathbf{x}, t) = \varphi(\mathbf{x}, t) - < \varphi(\mathbf{x}, t) >_t, \tag{C.2}$$

- Root mean square: $\text{rms}\{\cdot\}_t$

$$\text{rms}\{\varphi(\mathbf{x}, t)\}_t = \left(\frac{1}{t_{\text{end}} - t_{\text{start}}} \int_{t_{\text{start}}}^{t_{\text{end}}} (\varphi'(\mathbf{x}, t))^2 dt \right)^{1/2}, \tag{C.3}$$

- Auto-correlation over a time lag τ:

$$r(\tau)_{\varphi(\mathbf{x},t)} = \frac{< \varphi'(\mathbf{x}, t).\varphi'(\mathbf{x}, t + \tau) >_t}{< \varphi'(\mathbf{x}, t)^2 >_t}, \tag{C.4}$$

- Numerical statistical error:

$$\text{Err}(\varphi) = \frac{\text{rms}\{\varphi(\mathbf{x}, t)\}_t}{\sqrt{\mathcal{N}}}, \tag{C.5}$$

  where $\mathcal{N}$ denotes the number of uncorrelated samples,

- Normalized average fluctuations at a fixed point in space:

$$\varphi'^{,N} = \frac{\text{rms}\{\varphi(\mathbf{x}, t)\}_t}{< \varphi(\mathbf{x}, t) >_t}, \tag{C.6}$$

- Helium volume fraction: X_1

$$X_1 = \frac{\rho - \rho_{\text{amb}}}{\rho_{\text{inj}} - \rho_{\text{amb}}}, \tag{C.7}$$

- Volumetric flow-rates crossing the vents:

$$Q_v^{\Lambda} = \int_{\partial\Omega_{\text{out}}^{\Lambda}} u_1 d\sigma, \tag{C.8}$$

where $\Lambda = \{\text{bot, top}\}$ and $\partial\Omega_{\text{out}}^{\text{bot}}$, $\partial\Omega_{\text{out}}^{\text{top}}$ denote the surface area of the bottom and top vent respectively,

- Helium mass flow-rates crossing the vents:

$$q_{\text{He}}^{\Lambda} = \int_{\partial\Omega_{\text{out}}^{\Lambda}} \rho_{\text{inj}} X_1 u_1 d\sigma, \tag{C.9}$$

- Helium total mass inside the cavity: $\mathcal{M}_{\text{He}}$

$$\mathcal{M}_{\text{He}} = \int_{\mathcal{V}} \rho_{\text{inj}} X_1 d\mathcal{V}, \tag{C.10}$$

- Velocity magnitude: $|\mathbf{u}|$

$$|\mathbf{u}| = \Big(\sum_i^3 u_i^2 \Big)^{1/2}, \tag{C.11}$$

- Velocity magnitude in the xz-plane: $|\mathbf{u}|_{XZ}$

$$|\mathbf{u}|_{XZ} = \Big(u_1^2 + u_3^2 \Big)^{1/2}, \tag{C.12}$$

- Velocity magnitude in the yz-plane: $|\mathbf{u}|_{YZ}$

$$|\mathbf{u}|_{YZ} = \Big(u_2^2 + u_3^2 \Big)^{1/2}, \tag{C.13}$$

- Kinetic energy: E_k

$$E_k = \frac{1}{2} \sum_i^3 u_i^2, \tag{C.14}$$

- Field norm: $\| \cdot \|$

$$\|\varphi(x,y,z)\| = \Big(\sum_{i,j,k} \varphi_{i,j,k}^2 \Big)^{1/2}. \tag{C.15}$$

Appendix D

Reynolds-Favre averaged Navier-Stokes (RANS-FANS) equations

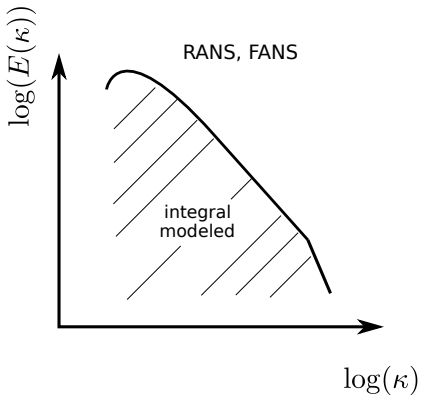

Figure D.1: Energy spectrum in FANS approach: modeled against simulated zones.

In this approach, the time scales of the turbulent flow are assume unique and the integral of the energy spectrum is modelled (figure D.1). The obtained solution is time independent; basically a time averaged solution.

The basic idea was firstly presented by Reynolds in [Rey95] where the fluid variables are splitted into an averaged and a fluctuating component. For incompressible fluids with non-varying density, the Reynolds averaged operator is defined as

$$< (\cdot) >_t^R = \lim_{\mathcal{T}\to\infty} \frac{1}{\mathcal{T}} \int_{t_0}^{t_0+\mathcal{T}} (\cdot)\, dt. \tag{D.1}$$

Thus, for any fluid variable φ, the Reynolds decomposition reads

$$\varphi = < \varphi >_t^R + \varphi', \tag{D.2}$$

where φ' denotes the fluctuating component. The set of RANS equations is obtained as follows. First, the fluid variables appearing in the instantaneous differential equations are decomposed using equation (D.2). Next, the time averaged operator, defined in equation (D.1), is employed.

In cases of variable density flows, the procedure had been generalized with Favre in [Fav65] by defining the density weighted average operator as

$$< (\cdot) >_t^F = \frac{\lim\limits_{\mathcal{T}\to\infty} \frac{1}{\mathcal{T}} \int_{t_0}^{t_0+\mathcal{T}} \rho\ (\cdot)\ dt}{< \rho >_t^R} = \frac{< \rho\ (\cdot) >_t^R}{< \rho >_t^R}. \tag{D.3}$$

In the sense of the density weighted averages, the Favre decomposition is similar to the Reynolds which reads

$$\varphi =< \varphi >_t^F + \varphi'', \tag{D.4}$$

where φ'' denotes the fluctuating part that contains also the fluctuations of ρ. Employing the Favre's decomposition and taking the complete average over the instantaneous density dependent equation, the FANS set of equations is obtained.

The two means are related with each others and the following properties hold

$$\left\langle < \varphi >_t^R \right\rangle_t^R =< \varphi >_t^R, \tag{D.5}$$

$$< \rho\varphi >_t^R =< \varphi >_t^F < \rho >_t^R, \tag{D.6}$$

$$< \varphi' >_t^R =< \varphi'' >_t^F = 0, < \varphi'' >_t^R \neq 0 \text{ and } < \rho\varphi'' >_t^R = 0, \tag{D.7}$$

$$< \varphi >_t^F =< \varphi >_t^R + \frac{< \rho'\varphi' >_t^R}{< \rho >_t^R} \text{ and } < \varphi'' >_t^R = -\frac{< \rho'\varphi' >_t^R}{< \rho >_t^R}. \tag{D.8}$$

The issue with this approach rises from the additional correlated terms (Reynolds stress, mass and heat fluxes) that appear in the RANS-FANS equations [CAA+13]. This is the closure problem and a suitable turbulence model is required to close the equations. We present in what follows some of the classical employed models, known for a one point closure problem. Regarding the spectral closure models, known as two point closure problems, one can refer to [Ber03].

The one point closure turbulence models presented in what follows are either based on a turbulent viscosity hypothesis (the algebraic zero equation model, the one equation model and the two equation models), or based on solving the Reynold's-stress transport equations (extra six equations).

In the algebraic model, say the Boussinesq and mixing length models, we do not require any additional equation to solve the problem and thus are generally used in simple flow geometries [BL78, Ceb12]. The one equation model solves an equation for the turbulent kinetic energy k_t transport. This model has higher accuracy than the zero equation models and thus the modelled turbulent viscosity μ_t is easily deduced by the Prandtl hypothesis [TSGR61].

The list of two equation models is too long and thus commonly used, depending on the problem [Chu07]. For example, the $k-\epsilon$ model solves two additional equations, one for the turbulent kinetic energy k_t and a second for the turbulent dissipation rate ϵ [JL72]. The realizable $k-\epsilon$, the $k-\omega$ and SST $k-\omega$ models form similar types of turbulence models and

can be reviewed from [SLS$^+$95, Wil88, Men92].

If the Reynold's tensor equation is considered, there is no requirement for modelling the turbulent viscosity μ_t. Basically, we require to solve six additional equations for the stress tensor and one for the dissipation ϵ. This model is more complicated to implement and requires higher computational effort, compared with the turbulent viscosity models (the cost can reach two times longer than what is required for the $k-\epsilon$ model [Pop00]). However, the Reynold's stress model offers a great potential for accurate calculations.

FANS equations: Binary grouping

Employing the Favre's decomposition over equations (3.26), (3.24), (3.25) and (3.27), the FANS system of equations reads

$$\frac{\partial}{\partial t}\Big(< \rho >_t^R < Y_1 >_t^F \Big) + \frac{\partial}{\partial x_i}\Big(< \rho >_t^R < Y_1 >_t^F < u_i >_t^F \Big) = \frac{\partial}{\partial x_i}\left(\Big\langle D\rho \frac{\partial Y_1}{\partial x_i} \Big\rangle_t^R \right) - \frac{\partial}{\partial x_i}\left(\Big\langle \rho Y_1'' u_i'' \Big\rangle_t^R \right), \quad \text{(D.9)}$$

$$< \rho >_t^R = \frac{p}{RT} < M_{\text{mix}} >_t^F, \quad \text{(D.10)}$$

$$\frac{\partial}{\partial t}\Big(< \rho >_t^R < u_i >_t^F \Big) + \frac{\partial}{\partial x_k}\Big(< \rho >_t^R < u_i >_t^F < u_k >_t^F \Big) = -\frac{\partial}{\partial x_i}\Big(< P >_t^R \Big) + \frac{\partial}{\partial x_k}\Big(< \tau_{ik} >_t^R \Big) - \frac{\partial}{\partial x_k}\Big(\Big\langle \rho u_i'' u_k'' \Big\rangle_t^R \Big) + < \rho >_t^R g_i, \quad \text{(D.11)}$$

$$\frac{\partial}{\partial t}\Big(< \rho >_t^R \Big) + \frac{\partial}{\partial x_i}\Big(< \rho >_t^R < u_i >_t^F \Big) = 0, \quad \text{(D.12)}$$

where

$$\begin{aligned} < \tau_{ik} >_t^R = & \left\langle \mu \left(\frac{\partial u_i}{\partial x_k} + \frac{\partial u_k}{\partial x_i} \right) \right\rangle_t^R - \frac{2}{3}\Big\langle \mu \delta_{ik} \frac{\partial u_k}{\partial x_k} \Big\rangle_t^R = \left\langle \mu'' \left(\frac{\partial u_i''}{\partial x_k} + \frac{\partial u_k''}{\partial x_i} \right) \right\rangle_t^R + \\ & < \mu'' >_t^R \left(\frac{\partial < u_i >_t^F}{\partial x_k} + \frac{\partial < u_k >_t^F}{\partial x_i} \right) + < \mu >_t^F \left(\Big\langle \frac{\partial u_i''}{\partial x_k} + \frac{\partial u_k''}{\partial x_i} \Big\rangle_t^R \right) + \\ & < \mu >_t^F \left(\frac{\partial < u_i >_t^F}{\partial x_k} + \frac{\partial < u_k >_t^F}{\partial x_i} \right) - \frac{2}{3}\delta_{ik}\Big\{ \Big\langle \mu'' \frac{\partial u_k''}{\partial x_k} \Big\rangle_t^R + \\ & < \mu'' >_t^R \frac{\partial < u_k >_t^F}{\partial x_k} + < \mu >_t^F \frac{\partial < u_k'' >_t^R}{\partial x_k} + < \mu >_t^F \frac{\partial < u_k >_t^F}{\partial x_k} \Big\}. \end{aligned} \quad \text{(D.13)}$$

RANS equations: Ternary grouping

Without using the notion of Favre's averaging, the RANS system of equations reads

$$\frac{\partial}{\partial t}\Big(< \rho >_t^R < Y_1 >_t^R \Big) + \frac{\partial}{\partial x_i}\Big(< \rho >_t^R < Y_1 >_t^R < u_i >_t^R \Big) = \frac{\partial}{\partial x_i}\left(\Big\langle D\rho \frac{\partial Y_1}{\partial x_i} \Big\rangle_t^R \right) - \frac{\partial}{\partial x_i}\left(\Big\langle \rho Y_1' u_i' \Big\rangle_t^R \right) - A, \quad \text{(D.14)}$$

$$< \rho >_t^R = \frac{p}{RT} < M_{\text{mix}} >_t^R, \quad \text{(D.15)}$$

$$\frac{\partial}{\partial t}\Big(< \rho >_t^R < u_i >_t^R \Big) + \frac{\partial}{\partial x_k}\Big(< \rho >_t^R < u_i >_t^R < u_k >_t^R \Big) = -\frac{\partial}{\partial x_i}\Big(< P >_t^R \Big) + \frac{\partial}{\partial x_k}\Big(< \tau_{ik} >_t^R \Big) - \frac{\partial}{\partial x_k}\Big(\Big\langle \rho u_i' u_k' \Big\rangle_t^R \Big) + < \rho >_t^R g_i - B, \quad \text{(D.16)}$$

$$\frac{\partial}{\partial t}\Big(< \rho >_t^R \Big) + \frac{\partial}{\partial x_i}\Big(< \rho >_t^R < u_i >_t^R \Big) = -C, \quad \text{(D.17)}$$

where

$$A = \frac{\partial}{\partial t}\Big(< \rho Y_1' >_t^R \Big) + \frac{\partial}{\partial x_i}\Big(< \rho u_i' >_t^R < Y_1 >_t^R + < \rho Y_1' >_t^R < u_i >_t^R \Big), \quad \text{(D.18)}$$

$$B = \frac{\partial}{\partial t}\Big(< \rho u_i' >_t^R \Big) + \frac{\partial}{\partial x_k}\Big(< \rho u_i' >_t^R < u_k >_t^R + < \rho u_k' >_t^R < u_i >_t^R \Big), \quad \text{(D.19)}$$

$$C = \frac{\partial}{\partial x_i}\Big(< \rho' u_i' >_t^R \Big), \quad \text{(D.20)}$$

$$< \tau_{ik} >_t^R = \Big\langle \mu \left(\frac{\partial u_i}{\partial x_k} + \frac{\partial u_k}{\partial x_i} \right) \Big\rangle_t^R - \frac{2}{3}\Big\langle \mu \delta_{ik} \frac{\partial u_k}{\partial x_k} \Big\rangle_t^R = \Big\langle \mu' \left(\frac{\partial u_i'}{\partial x_k} + \frac{\partial u_k'}{\partial x_i} \right) \Big\rangle_t^R + < \mu >_t^R \left(\frac{\partial < u_i >_t^R}{\partial x_k} + \frac{\partial < u_k >_t^R}{\partial x_i} \right) - \frac{2}{3}\delta_{ik} \left\{ \Big\langle \mu' \frac{\partial u_k'}{\partial x_k} \Big\rangle_t^R + < \mu >_t^R \frac{\partial < u_k >_t^R}{\partial x_k} \right\}. \quad \text{(D.21)}$$

Transport equation of the Reynold's tensor : Binary grouping

The equation is derived from expanding the following

$$\Big\langle u_j''\Big\{\frac{\partial\rho u_i}{\partial t}+\frac{\partial}{\partial x_k}(\rho u_i u_k)=-\frac{\partial P}{\partial x_i}+\frac{\partial\tau_{ik}}{\partial x_k}+\rho g_i\Big\}\Big\rangle_t^R+\Big\langle u_i''\Big\{\frac{\partial\rho u_j}{\partial t}+\frac{\partial}{\partial x_k}(\rho u_j u_k)=$$
$$-\frac{\partial P}{\partial x_j}+\frac{\partial\tau_{jk}}{\partial x_k}+\rho g_j\Big\}\Big\rangle_t^R-\Big\langle(u_i''u_j''+u_i''<u_j>_t^F+u_j''<u_i>_t^F)\Big\{\frac{\partial\rho}{\partial t}+\frac{\partial}{\partial x_k}(\rho u_k)=0\Big\}\Big\rangle_t^R.$$

We obtain

$$\frac{\partial}{\partial t}\Big(<\rho u_i''u_j''>_t^R\Big)+\frac{\partial}{\partial x_k}\Big(<\rho u_i''u_j''>_t^R<u_k>_t^F\Big)=-$$
$$\Big\{<\rho u_i''u_k''>_t^R\frac{\partial<u_j>_t^F}{\partial x_k}+<\rho u_j''u_k''>_t^R\frac{\partial<u_i>_t^F}{\partial x_k}\Big\}-$$
$$\frac{\partial}{\partial x_k}\Big\{<\rho u_i''u_j''u_k''>_t^R-<\tau_{jk}u_i''>_t^R-<\tau_{ik}u_j''>_t^R+<u_i''P'>_t^R\,\delta_{jk}+<u_j''P'>_t^R\,\delta_{ik}\Big\}-$$
$$<u_i''>_t^R\frac{\partial<P>_t^R}{\partial x_j}-<u_j''>_t^R\frac{\partial<P>_t^R}{\partial x_i}+$$
$$\Big\langle P'\Big(\frac{\partial u_j''}{\partial x_i}+\frac{\partial u_i''}{\partial x_j}\Big)\Big\rangle_t^R-$$
$$\Big\{\Big\langle\tau_{ik}\frac{\partial u_j''}{\partial x_k}\Big\rangle_t^R+\Big\langle\tau_{jk}\frac{\partial u_i''}{\partial x_k}\Big\rangle_t^R\Big\},\tag{D.22}$$

where the terms on the right hand side are respectively the production term of the average motion, the diffusion term due to the velocity, pressure and viscous fluctuations, the term of interaction between average pressure and velocity fluctuations, the term of turbulent energy distribution and finally the destruction term by the viscous effect.

Introducing the kinematic turbulent Reynold's stress tensor

$$R_{ij}=<u_i''u_j''>_t^F=\frac{<\rho u_i''u_j''>_t^R}{<\rho>_t^R},\tag{D.23}$$

and employing the decomposition on the viscous term

$$\tau_{ik}=<\tau_{ik}>_t^R+\tau_{ik}',\tag{D.24}$$

the transport equation of the Reynold's tensor following a binary grouping simplifies to

$$\frac{\partial}{\partial t}\Big(< \rho >_t^R R_{ij}\Big)+\frac{\partial}{\partial x_k}\Big(< \rho >_t^R R_{ij} < u_k >_t^F \Big) = - < \rho >_t^R \Big(R_{jk}\frac{\partial < u_i >_t^F}{\partial x_k}+R_{ik}\frac{\partial < u_j >_t^F}{\partial x_k}\Big)$$
$$- \frac{\partial}{\partial x_k}\Big\{ < \rho u_i'' u_j'' u_k'' >_t^R - < \tau_{jk}' u_i'' >_t^R - < \tau_{ik}' u_j'' >_t^R + < u_i'' P' >_t^R \delta_{jk}+ < u_j'' P' >_t^R \delta_{ik}\Big\}$$
$$+ < u_i'' >_t^R \Big(\frac{\partial < \tau_{jk} >_t^R}{\partial x_k} - \frac{\partial < P >_t^R}{\partial x_j}\Big)+ < u_j'' >_t^R \Big(\frac{\partial < \tau_{ik} >_t^R}{\partial x_k} - \frac{\partial < P >_t^R}{\partial x_i}\Big)+$$
$$\Big\langle P'\Big(\frac{\partial u_j''}{\partial x_i}+\frac{\partial u_i''}{\partial x_j}\Big)\Big\rangle_t^R - \Big\langle \tau_{ik}'\frac{\partial u_j''}{\partial x_k}\Big\rangle_t^R - \Big\langle \tau_{jk}'\frac{\partial u_i''}{\partial x_k}\Big\rangle_t^R. \quad \text{(D.25)}$$

Transport equation of the Reynold's tensor : Ternary grouping

The equation is derived from expanding the following

$$\Big\langle u_j'\Big\{\frac{\partial \rho u_i}{\partial t}+\frac{\partial}{\partial x_k}(\rho u_i u_k) = -\frac{\partial P}{\partial x_i}+\frac{\partial \tau_{ik}}{\partial x_k}+\rho g_i\Big\}\Big\rangle_t^R + \Big\langle u_i'\Big\{\frac{\partial \rho u_j}{\partial t}+\frac{\partial}{\partial x_k}(\rho u_j u_k) =$$
$$-\frac{\partial P}{\partial x_j}+\frac{\partial \tau_{jk}}{\partial x_k}+\rho g_j\Big\}\Big\rangle_t^R - \Big\langle (u_i'u_j'+u_i' < u_j >_t^R + u_j' < u_i >_t^R)\Big\{\frac{\partial \rho}{\partial t}+\frac{\partial}{\partial x_k}(\rho u_k)=0\Big\}\Big\rangle_t^R.$$

We obtain

$$\frac{\partial}{\partial t}\Big(R_{ij}\Big)+\frac{\partial}{\partial x_k}\Big(R_{ij} < u_k >_t^R\Big) = -\Big(R_{ik}\frac{\partial < u_j >_t^R}{\partial x_k}+R_{jk}\frac{\partial < u_i >_t^R}{\partial x_k}\Big)-$$
$$\frac{\partial}{\partial x_k}\Big\{ < \rho u_i' u_j' u_k' >_t^R - < \tau_{jk}' u_i' >_t^R - < \tau_{ik}' u_j' >_t^R \Big\}-$$
$$\Big\{\frac{\partial}{\partial x_j}\Big(< P' u_i' >_t^R \Big)+\frac{\partial}{\partial x_i}\Big(< P' u_j' >_t^R \Big)\Big\}+$$
$$\Big\langle P'\Big(\frac{\partial u_j'}{\partial x_i}+\frac{\partial u_i'}{\partial x_j}\Big)\Big\rangle_t^R - \Big\{\Big\langle \tau_{ik}'\frac{\partial u_j'}{\partial x_k}\Big\rangle_t^R + \Big\langle \tau_{jk}'\frac{\partial u_i'}{\partial x_k}\Big\rangle_t^R\Big\}+$$
$$\Big(< \rho u_j' >_t^R g_i+ < \rho u_i' >_t^R g_j\Big) - E, \quad \text{(D.26)}$$

where

$$R_{ij} =< \rho u_i' u_j' >_t^R, \quad \text{(D.27)}$$

$$E = < \rho u_j' >_t^R \frac{\partial < u_i >_t^R}{\partial t} + < \rho u_i' >_t^R \frac{\partial < u_j >_t^R}{\partial t} + \\ < u_k >_t^R < \rho u_j' >_t^R \frac{\partial < u_i >_t^R}{\partial x_k} + < u_k >_t^R < \rho u_i' >_t^R \frac{\partial < u_j >_t^R}{\partial x_k}. \quad \text{(D.28)}$$

By performing a ternary grouping in the Reynold's stress equation, three major differences are noticed from the case where a binary grouping is employed. First is the contribution of the gravitational terms. Second, the contribution of the mean pressure in the diffusion term is removed. Finally, turbulent mass fluxes appear as an additional terms [CAA+13].

Transport equation of the turbulent kinetic energy : Binary grouping

We denote the instantaneous turbulent kinetic energy (TKE)

$$\mathcal{K}_t = \frac{1}{2} u_i'' u_i''. \quad \text{(D.29)}$$

According to definition of the Favre, the averaged TKE reads

$$< \mathcal{K}_t >_t^F = \frac{1}{2} < u_i'' u_i'' >_t^F = \frac{1}{2} \frac{< \rho u_i'' u_i'' >_t^R}{< \rho >_t^R}. \quad \text{(D.30)}$$

Contract $i = j$ and sum the Reynold's tensor equation (D.22) to obtain

$$\frac{\partial}{\partial t}\Big(< \rho >_t^R < \mathcal{K}_t >_t^F \Big) + \frac{\partial}{\partial x_k}\Big(< \rho >_t^R < \mathcal{K}_t >_t^F < u_k >_t^F \Big) = \\ - < \rho >_t^R < u_i'' u_k'' >_t^F \frac{\partial < u_i >_t^F}{\partial x_k} - \frac{\partial}{\partial x_k}\Big\{ < \rho >_t^R < \mathcal{K}_t u_k'' >_t^F - < \tau_{ik} u_i'' >_t^R \Big\} - \\ \frac{\partial}{\partial x_i}\Big(< P >_t^R < u_i'' >_t^R \Big) - \frac{\partial}{\partial x_i}\Big(< P' u_i'' >_t^R \Big) + \Big\langle P \frac{\partial u_i''}{\partial x_i} \Big\rangle_t^R - \Big\langle \tau_{ik} \frac{\partial u_i''}{\partial x_k} \Big\rangle_t^R. \quad \text{(D.31)}$$

As carried out in the Reynolds tensor equation, further simplifications can be performed by splitting

$$\tau_{ik} = < \tau_{ik} >_t^R + \tau_{ik}', \ \ldots$$

Transport equation of the turbulent kinetic energy : Ternary grouping

Define

$$\mathcal{K}_t = \frac{1}{2}\rho u_i' u_i'. \tag{D.32}$$

Contract the indices of equation (D.26) and sum to obtain

$$\begin{aligned}\frac{\partial}{\partial t}\Big(< \mathcal{K}_t >_t^R \Big) + \frac{\partial}{\partial x_k}\Big(< \mathcal{K}_t >_t^R < u_k >_t^R \Big) = - < \rho u_i' u_k' >_t^R \frac{\partial < u_i >_t^R}{\partial x_k} - \\ \frac{\partial}{\partial x_k}\Big\{\frac{1}{2} < \rho u_i' u_i' u_k' >_t^R - < \tau_{ik}' u_i' >_t^R \Big\} - \frac{\partial}{\partial x_i}\Big(< P' u_i' >_t^R \Big) + \Big\langle P' \frac{\partial u_i'}{\partial x_i} \Big\rangle_t^R - \\ \Big\langle \tau_{ik}' \frac{\partial u_i'}{\partial x_k} \Big\rangle_t^R + < \rho u_i' >_t^R g_i - G,\end{aligned} \tag{D.33}$$

where

$$G = < \rho u_i' >_t^R \frac{\partial < u_i >_t^R}{\partial t} + < u_k >_t^R < \rho u_i' >_t^R \frac{\partial < u_i >_t^R}{\partial x_k}. \tag{D.34}$$

Appendix E

Scientific production

Posters

1. **Saikali, E.**, Sergent, A., Bernard-Michel, G. and Tenaud, C. "Numerical simulation of air-helium plumes in a semi-confined cavity with two vents: a DNS approach." Forum d'étudiants et workshop scientifique sur la transition energétique (WTE), Université Paris Saclay, 4 – 5 October 2016, EDF Lab Paris-Saclay Centre, Palaiseau, France.

2. **Saikali, E.**, Sergent, A., Bernard-Michel, G. and Tenaud, C. "Numerical simulation of air-helium plumes in a semi-confined cavity with two vents: a DNS approach." 16es journées scientifiques de la DANS, 25 – 27 Mai 2016, CEA Saclay, Gif-sur-Yvette, France.

Selected talks

1. **Saikali, E.**, Sergent, A., Bernard-Michel, G. and Tenaud, C. "Highly resolved large eddy simulations of a transitional air-helium buoyant jet in a two vented enclosure: validation with experimental PIV measurements." séminaire de mécanique interne, 23 juin 2017, LIMSI-CNRS, Orsay, France.

2. **Saikali, E.**, Bernard-Michel, G. and Studer, E. "Applications of TrioCFD for non-nuclear and nuclear hydrogen safety." Séminaire utilisateurs TrioCFD, 20 juin 2017, CEA Saclay, Gif-sur-Yvette, France.

3. **Saikali, E.**, Sergent, A., Bernard-Michel, G. and Tenaud, C. "Numerical simulation of Air/Helium plumes in a semi-confined cavity with one vent." Journée scientifique ETE (Energie - Transferts - Efficacité), 15 December 2015, Orsay, France.

Conference proceedings

1. **Saikali, E.**, Sergent, A., Bernard-Michel, G. and Tenaud, C. "Large eddy simulations of an air-helium buoyant jet in a two vented enclosure: influence of the outlet boundary condition." Proceedings of the 23ème Congrès Français de Mécanique, 2017.

2. **Saikali, E.**, Bernard-Michel, G., Sergent, A., Tenaud, C. and Salem, R. "Highly resolved large eddy simulations of a transitional air-helium buoyant jet in a two vented

enclosure: validation against PIV measurements." Proceedings of the International Conference on Hydrogen Safety, 2017.

3. Bernard-Michel, G., **Saikali, E.** and Houssin, D. "Experimental measurements, CFD simulations and model for a helium release in a two vents enclosure." Proceedings of the International Conference on Hydrogen Safety, 2017.

Bibliography

[ABD+85] F Angrand, V Billey, A Dervieux, JA Desideri, J Periaux, and B Stoufflet. *On the use of rational Runge-Kutta methods in Euler steady-state computations*, pages 77–81. Springer Berlin Heidelberg, Berlin, Heidelberg, 1985.

[ABF15] PE Angeli, U Bieder, and G Fauchet. Overview of the triocfd code: main features, v&v procedures and typical applications to nuclear engineering. In *Proceedings of 16th International Topical Meeting on Nuclear Reactor Thermal Hydraulics (NURETH-16), Chicago, USA*, 2015.

[Abr65] G Abraham. Entrainment principle and its restrictions to solve problems of jets. *Journal of Hydraulic Research*, 3(2):1–23, 1965.

[Ald13] A Aldama. *Filtering techniques for turbulent flow simulation*, volume 56. Springer Science & Business Media, 2013.

[Ber03] JP Bertoglio. Two-point closures and turbulence modeling. In *TSFP DIGITAL LIBRARY ONLINE*. Begel House Inc., 2003.

[BG75] RG Bill and B Gebhart. The transition of plane plumes. *International Journal of Heat and Mass Transfer*, 18(4):513 – 526, 1975.

[BHT59] GK Batchelor, ID Howells, and AA Townsend. Small-scale variation of convected quantities like temperature in turbulent fluid part 2. the case of large conductivity. *Journal of Fluid Mechanics*, 5(1):134–139, 1959.

[Bi17] J Bi. Expériences piv d'un jet d'hélium dans une cavité de deux évents et comparison des résultats numériques-expérimentaux. CEA technical report, 2017.

[BL78] BS Baldwin and H Lomax. *Thin layer approximation and algebraic model for separated turbulent flows*, volume 257. American Institute of Aeronautics and Astronautics, 1978.

[BMCN+13] G Bernard-Michel, B Cariteau, J Ni, S Jallais, E Vyazmina, D Melideo, D Baraldi, and A Venetsanos. Cfd benchmark based on experiments of helium dispersion in a 1 m3 enclosure–intercomparisons for plumes. In *Proceedings of ICHS 2013*. 2013.

[BMHA17] G Bernard-Michel and D Houssin-Agbomson. Comparison of helium and hydrogen releases in 1 m 3 and 2 m 3 two vents enclosures: Concentration measurements at different flow rates and for two diameters of injection nozzle. *International Journal of Hydrogen Energy*, 42(11):7542–7550, 2017.

[BMSH17] G Bernard-Michel, E Saikali, and D Houssin. Experimental measurements, cfd simulations and model for a helium release in a two vents enclosure. In *Proceeding of the International Conference on Hydrogen Safety, Hamburg, Germany*, 2017.

[BMTVG12] G Bernard-Michel, J Trochon, E Vyazmina, and O Gentilhomme. Resultat du benchmark ventilation sur 3 essais gamelan dans le cadre du projet anr dimitrhy. Technical report, Technical Report DEN/DANS/ DM2S/STMF/LIEFT/RT/12/020/A., CEA Saclay DEN/DANS/DM2S/STMF /LIEFT, 2012.

[Bou03] J Boussinesq. *Théorie analytique de la chaleur: mise en harmonie avec la thermodynamique et avec la théorie mécanique de la lumière*, volume 2. Gauthier-Villars, 1903.

[BP08] G Blanquart and H Pitsch. Large-eddy simulation of a turbulent buoyant helium plume. *Bulletin of the American Physical Society*, 53, 2008.

[Bri04] G Brillant. Simulations des grandes échelles thermiques et expériences dans le cadre d'effusion anisotherme. *These d'Université, Institut National des Sciences Appliquées de Lyon*, 2004.

[BSL07] R Bird, W Stewart, and E Lightfoot. *Transport Phenomena*. John Wiley & Sons, 2007.

[BT69] WD Baines and JS Turner. Turbulent buoyant convection from a source in a confined region. *Journal of Fluid mechanics*, 37(01):51–80, 1969.

[CAA+13] P Chassaing, RA Antonia, F Anselmet, L Joly, and S Sarkar. *Variable density fluid turbulence*, volume 69. Springer Science & Business Media, 2013.

[Ceb12] T Cebeci. *Analysis of turbulent boundary layers*, volume 15. Elsevier, 2012.

[Cha04] A Chatelain. *Simulation des Grandes Echelles d'écoulements turbulents avec transferts de chaleur*. PhD thesis, Institut National Polytechnique de Grenoble-INPG, 2004.

[CHP06] S Chhabra, P Huq, and A Prasad. Characteristics of small vortices in a turbulent axisymmetric jet. *Journal of fluids engineering*, 128(3):439–445, 2006.

[Chu07] W Chung. A cfd investigation of turbulent buoyant helium plumes. Master's thesis, University of Waterloo, 2007.

[CKT08] G Carazzo, E Kaminski, and S Tait. On the rise of turbulent plumes: Quantitative effects of variable entrainment for submarine hydrothermal vents, terrestrial and extra terrestrial explosive volcanism. *Journal of Geophysical Research: Solid Earth*, 113(B9), 2008.

[CML94] R Cleaver, M Marshall, and P Linden. The build-up of concentration within a single enclosed volume following a release of natural gas. *Journal of Hazardous Materials*, 36(20):226, 1994.

[Cor51] S Corrsin. On the spectrum of isotropic temperature fluctuations in an isotropic turbulence. *Journal of Applied Physics*, 22(4):469–473, 1951.

[CR80a] CJ Chen and W Rodi. *Vertical Turbulent Buoyant Jets:*. HMT, the Science and Applications of Heat and Mass Transfer Series. Elsevier Science & Technology, 1980.

[CR80b] CJ Chen and W Rodi. Vertical turbulent buoyant jets: a review of experimental data. *NASA STI/Recon Technical Report A*, 80, 1980.

[CT12] B Cariteau and I Tkatschenko. Experimental study of the concentration build-up regimes in an enclosure without ventilation. *International Journal of Hydrogen Energy*, 37(22):17400 – 17408, 2012. HySafe 1.

[CT13] B Cariteau and I Tkatschenko. Experimental study of the effects of vent geometry on the dispersion of a buoyant gas in a small enclosure. *International Journal of Hydrogen Energy*, 38(19):8030 – 8038, 2013.

[DC] DEN-CEA. TRUST-TrioCFD code version 1.7.4. `http://www-trio-u.cea.fr`.

[DCJ+13] G Desrayaud, E Chénier, A Joulin, A Bastide, B Brangeon, JP Caltagirone, Y Cherif, R Eymard, C Garnier, S Giroux-Julien, Y Harnane, P Joubert, N Laaroussi, S Lassue, P Le Quéré, R Li, D Saury, A Sergent, S Xin, and A Zoubir. Benchmark solutions for natural convection flows in vertical channels submitted to different open boundary conditions. *International Journal of Thermal Sciences*, 72:18–33, 2013.

[Dea70] J Deardorff. A numerical study of three-dimensional turbulent channel flow at large reynolds numbers. *Journal of Fluid Mechanics*, 41(2):453–480, 1970.

[DLT+11] A Davaille, A Limare, F Touitou, I Kumagai, and J Vatteville. Anatomy of a laminar starting thermal plume at high prandtl number. *Experiments in Fluids*, 50(2):285–300, 2011.

[EKDB08] P Edwards, V Kuznetsov, W David, and N Brandon. Hydrogen and fuel cells: Towards a sustainable energy future. *Energy Policy*, 36(12):4356 – 4362, 2008. Foresight Sustainable Energy Management and the Built Environment Project.

[Fav65] AJ Favre. The equations of compressible turbulent gases. Technical report, Aix-Marseille university (France): Inst de mecanique statistique de la turbulence, 1965.

[FHAJ+17] B Fuster, D Houssin-Agbomson, S Jallais, E Vyazmina, G Dang-Nhu, G Bernard-Michel, M Kuznetsov, V Molkov, B Chernyavskiy, V Shentsov,

D Makarov, R Dey, P Hooker, D Baraldi, E Weidner, D Melideo, V Palmisano, A Venestanos, and J Der Kinderen. Guidelines and recommendations for indoor use of fuel cells and hydrogen systems. *International Journal of Hydrogen Energy*, 42(11):7600 – 7607, 2017.

[Fra13a] Y Fraigneau. *Guide D'utilisation du Code SUNFLUIDH.* LIMSI-CNRS, 2013.

[Fra13b] Y Fraigneau. *Principes de Base des Méthodes Numériques Utilisées Dans le Code SUNFLUIDH Pour la Simulation des Écoulements Incompressibles et à Faible Nombre de Mach.* LIMSI-CNRS, 2013.

[FS67] R Forstrom and E Sparrow. Experiments on the buoyant plume above a heated horizontal wire. *International Journal of Heat and Mass Transfer*, 10(3):321 – 331, 1967.

[Ger92] M Germano. Turbulence: the filtering approach. *Journal of Fluid Mechanics*, 238:325–336, 1992.

[GG76] D Gray and A Giorgini. The validity of the boussinesq approximation for liquids and gases. *International Journal of Heat and Mass Transfer*, 19(5):545 – 551, 1976.

[GMS06] JL Guermond, P Minev, and J Shen. An overview of projection methods for incompressible flows. *Computer methods in applied mechanics and engineering*, 195(44):6011–6045, 2006.

[GSM+15] SG Giannissi, V Shentsov, D Melideo, B Cariteau, D Baraldi, AG Venetsanos, and V Molkov. Cfd benchmark on hydrogen release and dispersion in confined, naturally ventilated space with one vent. *International Journal of Hydrogen Energy*, 40(5):2415 – 2429, 2015.

[HCG94] H Hussein, S Capp, and W George. Velocity measurements in a high-reynolds-number, momentum-conserving, axisymmetric, turbulent jet. *Journal of Fluid Mechanics*, 258:31–75, 1994.

[Hir07] C Hirsch. *Numerical Computation of Internal and External Flows: Fundamentals of Numerical Discretization*, volume 1. Butterworth-Heinemann, 2007.

[HW65] F Harlow and JE Welch. Numerical calculation of time-dependent viscous incompressible flow of fluid with free surface. *Physics of fluids*, 8(12):2182, 1965.

[HyI] HyIndoor. Pre normative research on the indoor use of fuel cells and hydrogen systems project website. `http://www.hyindoor.eu/`.

[JL72] WP Jones and BE Launder. The prediction of laminarization with a two-equation model of turbulence. *International journal of heat and mass transfer*, 15(2):301–314, 1972.

[KBB+14] A Kotchourko, D Baraldi, P Bénard, N Eisenreich, T Jordan, J Keller, A Kessler, J LaChance, V Molkov, M Steen, A Tchouvelev, and J Wen. State of the art and research priorities in hydrogen safety. *Joint Research Centre of the European Commission (JRC)*, 2014.

[KH07] NB Kaye and GR Hunt. Overturning in a filling box. *Journal of Fluid Mechanics*, 576:297–323, 2007.

[KLN91] HO Kreiss, J Lorenz, and MJ Naughton. Convergence of the solutions of the compressible to the solutions of the incompressible navier-stokes equations. *Advances in Applied Mathematics*, 12(2):187–214, 1991.

[KM82] S Klainerman and A Majda. Compressible and incompressible fluids. *Communications on Pure and Applied Mathematics*, 35(5):629–651, 1982.

[KNW99] O Knio, H Najm, and P Wyckoff. A semi-implicit numerical scheme for reacting flow: Ii. stiff, operator-split formulation. *Journal of Computational Physics*, 154(2):428–467, 1999.

[Kol41] A Kolmogorov. The local structure of turbulence in incompressible viscous fluid for very large reynolds numbers. In *Dokl. Akad. Nauk SSSR*, volume 30, pages 299–303, 1941.

[KTB+14] R Kalter, M Tummers, J Bettink, B Righolt, S Kenjereš, and C Kleijn. Aspect ratio effects on fluid flow fluctuations in rectangular cavities. *Metallurgical and Materials Transactions B*, 45(6):2186–2193, 2014.

[LC03] J Lee and V Chu. *Turbulent Jets and Plumes: A Lagrangian Approach*. Number v. 1 in Turbulent Jets and Plumes: A Lagrangian Approach. Springer US, 2003.

[Leo75] A Leonard. Energy cascade in large-eddy simulations of turbulent fluid flows. *Advances in geophysics*, 18:237–248, 1975.

[Leo79] B Leonard. A stable and accurate convective modelling procedure based on quadratic upstream interpolation. *Computer Methods in Applied Mechanics and Engineering*, 19(1):59 – 98, 1979.

[LI73] E List and J Imberger. Turbulent entrainment in buoyant jets and plumes. *Journal of the Hydraulics Division*, 99(9):1461–1474, 1973.

[Lil62] D Lilly. On the numerical simulation of buoyant convection. *Tellus*, 14(2):148–172, 1962.

[Lin99] P Linden. The fluid mechanics of natural ventilation. *Annual review of fluid mechanics*, 31(1):201–238, 1999.

[Lin00] P Linden. Convection in the environment. *Perspectives in fluid dynamics: A collective introduction to current research*, pages 289–345, 2000.

[LLSS90] P Linden, G Lane-Serff, and D Smeed. Emptying filling boxes: the fluid mechanics of natural ventilation. *Journal of Fluid Mechanics*, 212:309–335, 1990.

[Maj84] A Majda. Compressible fluid flow and systems of conservation laws in several space variables. 1984.

[Mas] M Masoudian. Dns–buoyant jet flow. `https://sites.google.com/site/masoudianfm/`.

[Men92] F Menter. Improved two-equation k-ω turbulence models for aerodynamic flows. 1992.

[MJMB95] W Mell, A Johnson, K McGrattan, and H Baum. Large eddy simulations of buoyant plumes. *Chemical and Physical Processes in Combustion*, pages 187–190, 1995.

[MRWM13] G Maragkos, P Rauwoens, Y Wang, and B Merci. Large eddy simulations of the flow in the near-field region of a turbulent buoyant helium plume. *Flow, Turbulence and Combustion*, 90(3):511–543, Apr 2013.

[MS85] A Majda and J Sethian. The derivation and numerical solution of the equations for zero mach number combustion. *Combustion science and technology*, 42(3-4):185–205, 1985.

[MS14] V Molkov and V Shentsov. Numerical and physical requirements to simulation of gas release and dispersion in an enclosure with one vent. *International Journal of Hydrogen Energy*, 39(25):13328 – 13345, 2014.

[MTT56] B Morton, G Taylor, and J Turner. Turbulent gravitational convection from maintained and instantaneous sources. *Proceedings of the Royal Society of London. Series A, Mathematical and Physical Sciences*, 234(1196), 1956.

[Mül99] B Müller. Low mach number asymptotics of the navier-stokes equations and numerical implications, 1999.

[ND99a] F Nicoud and F Ducros. Subgrid-scale stress modelling based on the square of the velocity gradient tensor. *Flow, turbulence and Combustion*, 62(3):183–200, 1999.

[ND99b] F Nicoud and F Ducros. Subgrid-scale stress modelling based on the square of the velocity gradient tensor. *Flow, turbulence and Combustion*, 62(3):183–200, 1999.

[NJA72] P Neufeld, A Janzen, and R Aziz. Empirical equations to calculate 16 of the transport collision integrals ω (l, s)* for the lennard-jones (12–6) potential. *The Journal of Chemical Physics*, 57(3):1100–1102, 1972.

[NSC11] L Neumann, J Simunek, and F Cook. Implementation of quadratic upstream interpolation schemes for solute transport into hydrus-1d. *Environmental Modelling & Software*, 26(11):1298–1308, 2011.

[PL88] P Papanicolaou and E List. Investigations of round vertical turbulent buoyant jets. *Journal of Fluid Mechanics*, 195:341–391, 10 1988.

[Pop00] S Pope. *Turbulent Flows*. Cambridge University Press, 2000.

[PPKB08] F Plourde, M Pham, S Kim, and S Balachandar. Direct numerical simulations of a rapidly expanding thermal plume: structure and entrainment interaction. *Journal of Fluid Mechanics*, 604:99–123, 2008.

[PV05] E Papanikolaou and A Venetsanos. Cfd modelling for helium releases in a private garage without forced ventilation. *Proceedings of the Fist ICHS, Pisa, Italy*, pages 8–10, 2005.

[PVH+09] E Papanikolaou, A Venetsanos, M Heitsch, D Baraldi, A Huser, J Pujol, D Makarov, V Molkov, J Garcia, and N Markatos. Hysafe sbep-v20: Numerical predictions of release experiments inside a residential garage with passive ventilation. In *Proceeding of the International Conference on Hydrogen Safety, Ajaccio, Corsica, France*, 2009.

[Rai54] W Railston. The temperature decay law of a naturally convected air stream. *Proceedings of the Physical Society. Section B*, 67(1):42, 1954.

[Rey95] O Reynolds. On the dynamical theory of incompressible viscous fluids and the determination of the criterion. *Philosophical Transactions of the Royal Society of London. A*, 186:123–164, 1895.

[Ric22] L Richardson. *Weather Prediction by Numerical Process*. Cambridge University Press, 1922.

[RM09] M Rogers and S Morris. Natural versus forced convection in laminar starting plumes. *Physics of Fluids*, 21(8):083601, 2009.

[Rod82] W Rodi. *Turbulent buoyant jets and plumes*, volume 3. Pergamon press Oxford, 1982.

[RS61] F Ricou and D Spalding. Measurements of entrainment by axisymmetrical turbulent jets. *Journal of Fluid Mechanics*, 11:21–32, 8 1961.

[RYH52] H Rouse, C Yih, and H Humphreys. Gravitational convection from a boundary source. *Tellus*, 4(3):201–210, 1952.

[Saa03] Y Saad. *Iterative methods for sparse linear systems*. SIAM, 2003.

[Sag06] P Sagaut. *Large eddy simulation for incompressible flows: an introduction*. Springer Science & Business Media, 2006.

[SB98] M Salvetti and F Beux. The effect of the numerical scheme on the subgrid scale term in large-eddy simulation. *Physics of Fluids*, 10(11):3020–3022, 1998.

[SBMS+17] E Saikali, G Bernard-Michel, A Sergent, C Tenaud, and R Salem. Highly resolve large eddy simulations of a transitional air-helium buoyant jet in a two vented enclosure: validation against particle image velocimetry experiments. In *Proceeding of the International Conference on Hydrogen Safety, Hamburg, Germany*, 2017.

[Sch07] F Schmitt. About boussinesq's turbulent viscosity hypothesis: historical remarks and a direct evaluation of its validity. *Comptes Rendus Mécanique*, 335(9):617 – 627, 2007. Joseph Boussinesq, a Scientist of bygone days and present times.

[SGMS10] M Salvetti, B Geurts, J Meyers, and P Sagaut. *Quality and Reliability of Large-Eddy Simulations II*, volume 16. Springer Science & Business Media, 2010.

[SGS98a] M Swain, E Grilliot, and M Swain. Phase 2: Risks in indoor vehicle storage. *Addendum to Hydrogen Vehicle Safety Report: Residential Garage Safety Assessment, US*, 1998.

[SGS98b] M Swain, E Grilliot, and M Swain. Risks incurred by hydrogen escaping from containers and conduits. *Proceedings of the 1998 US DOE hydrogen program technical review meeting, Alexandria, VA (United States), 28-30 Apr 1998*, 2(NREL/CP–570-25315-Vol.2; CONF-980440–Vol.2):787–803, 1998. OSTI as DE98007508.

[SLS+95] TH Shih, W Liou, A Shabbir, Z Yang, and J Zhu. A new k-ϵ eddy viscosity model for high reynolds number turbulent flows. *Computers & Fluids*, 24(3):227–238, 1995.

[Sma63] J Smagorinsky. General circulation experiments with the primitive equations: I. the basic experiment. *Monthly weather review*, 91(3):99–164, 1963.

[SPA04] R Satti, K Pasumarthi, and A Agrawal. Numerical simulations of buoyancy effects in low density gas jets. In *42nd AIAA Aerospace Sciences Meeting and Exhibit*, page 1317, 2004.

[SSBMT17] E Saikali, A Sergent, G Bernard-Michel, and C Tenaud. Large eddy simulations of an air-helium buoyant jet in a two vented enclosure: influence of the outlet boundary condition. In *Proceeding of the 23ème Congrès Français de Mécanique, Lille, France*, 2017.

[TCC00] M Trapeznikova, N Churbanova, and B Chetverushkin. *Simulation of Gas Flows at Low Mach Number Using Parallel Computers*. 2000.

[Tra13] HL Tran. *Simulation numérique de convection naturelle d'un mélange binaire: cas d'un panache d'hélium en cavité*. PhD thesis, Université Pierre et Marie Curie-Paris VI, 2013.

[TSBMLQ13] HL Tran, A Sergent, G Bernard-Michel, and P Le Quere. Numerical simulation of the helium dispersion in a semi-confined air-filled cavity. In *Progress in safety of hydrogen technologies and infrastructure: enabling the transition to zero carbon energy. Proceedings of the 5th International Conference on Hydrogen Safety (ICHS). 9-11 Sept 2013, Brussels, Belgium*, 2013.

[TSGR61] W Tollmien, H Schlichting, H Görtler, and FW Riegels. Über ein neues formelsystem für die ausgebildete turbulenz. In *Ludwig Prandtl Gesammelte Abhandlungen*, pages 874–887. Springer, 1961.

[Tur79] J Turner. *Buoyancy Effects in Fluids*. Cambridge Monographs on Mechanics. Cambridge University Press, 1979.

[VM07] H Versteeg and W Malalasekera. *An introduction to computational fluid dynamics: the finite volume method*. Pearson Education, 2007.

[Wam78] A Wambecq. Rational runge-kutta methods for solving systems of ordinary differential equations. *Computing*, 20(4):333–342, 1978.

[Wes95] P Wesseling. Introduction to multigrid methods. *NASA technical report,*, 1995.

[WH83] M Worster and H Huppert. Time-dependent density profiles in a filling box. *Journal of Fluid Mechanics*, 132:457–466, 7 1983.

[Wil50] CR Wilke. A viscosity equation for gas mixtures. *The journal of chemical physics*, 18(4):517–519, 1950.

[Wil65] F Williams. *Combustion Theory*. Addison-Wesley series in engineering sciences. Addison-Wesley Publishing Company, 1965.

[Wil88] D Wilcox. Multiscale model for turbulent flows. *AIAA journal*, 26(11):1311–1320, 1988.

[Wor03] J Worthy. Large eddy simulation of buoyant plumes. *Cranfield University, CERES, dissertation*, 2003.

[YYB12] R Yu, J Yu, and XS Bai. An improved high-order scheme for dns of low mach number turbulent reacting flows based on stiff chemistry solver. *Journal of Computational Physics*, 231(16):5504 – 5521, 2012.

Modélisation numérique d'un jet flottant air–hélium dans une cavité avec deux évents

Abstract: Nous cherchons à modéliser numériquement un jet flottant air–hélium dans une cavité avec deux ouvertures à partir de simulations aux grandes échelles (LES) et de simulations numériques directes (DNS). La configuration considérée est basée sur une étude expérimentale menée au CEA de Saclay reproduisant une fuite d'hydrogène en environnement confiné. La dimension de la cavité a été choisie pour permettre une transition laminaire-turbulent intervenant environ à la mi-hauteur de la cavité. Cette étude porte principalement sur trois points majeurs: l'influence des conditions aux limites sur le développement du jet et son interaction avec l'environnement extérieur, la validité du modèle numérique qui est analysée en comparant la distribution de vitesse obtenue numériquement aux mesures expérimentales (PIV) et, enfin, la compréhension de la distribution air–hélium et le phénomène de stratification qui s'établit à l'intérieur de la cavité. Nous observons dans un premier temps que des conditions limites de pression constante appliquées directement au ras des évents conduisent à une sous-estimation du débit volumique d'air entrant dans la cavité et donc à une surestimation la masse de l'hélium à l'intérieur de la cavité, ce qui n'est pas acceptable dans un contexte d'évaluation du risque hydrogène. En revanche, la prise en compte, dans le domaine de calcul, d'une région extérieure à la cavité prédit correctement le flux d'air entrant. Les résultats numériques sont alors en bon accord avec les données PIV. Il a été montré que les prédictions de la DNS, par rapport à la LES, concordent mieux avec les mesures de vitesse par PIV. Le champ de concentration prédit numériquement présente une couche homogène en haut de la cavité, dont la concentration est en accord avec le modèle théorique de Linden et al. 1990. Cependant, sa position et son épaisseur ne correspondent pas au modèle. Ceci est principalement dû aux interactions directes entre le jet flottant et, d'une part, avec les limites solides de la cavité et d'autre part, avec l'environnement extérieur. L'analyse statistique concernant la production de la flottabilité de l'énergie cinétique turbulente (TKE) a permis d'identifier les limites du jet flottant.

Mots clés: Jet flottant, cavité avec évents, mélange air–helium, stratification, simulations aux grandes échelles, simulations numériques directes, conditions limites, mécanique des fluides numériques, particle image velocimetry.

CEA Saclay - DEN/DANS/DM2S/STMF/LIEFT, F-91191 Gif-sur-Yvette cedex, France,
LIMSI CNRS, UPR3251, Université Paris-Saclay, F-91405 Orsay, France,
Sorbonne Université, Collège Doctoral, ED391 SMAER, F-75006, Paris, France.

Numerical modelling of an air–helium buoyant jet in a two vented enclosure

Abstract: We present numerical results from large eddy simulations (LES) and coarse direct numerical simulations (DNS) of an air–helium buoyant jet rising in a two vented cavity. The geometrical configuration mimics the helium release experimental set-up studied at CEA Saclay in the framework of security assessment of hydrogen–based systems with an indoor usage. The dimension of the enclosure was chosen to ensure a laminar–turbulent transition occurring at about the middle height of the cavity. This study focuses mainly on three key points: the influence of the boundary conditions on the jet development and its interaction with the exterior environment, the validity of the numerical model which is analyzed by comparing the numerical velocity distribution versus the measured particle image velocimetry (PIV) ones, and finally understanding the distribution of air–helium and the stratification phenomenon that takes place inside the cavity. We observe at first that applying constant pressure outlet boundary conditions directly at the vent surfaces underestimates the volumetric flow rate of air entering the enclosure and thus overestimate the helium mass inside the cavity. On the contrary, modelling an exterior region in the computational domain better predicts the air flow-rate entrance and numerical results matches better with the experimental PIV data. It has been figured out that the coarse DNS predictions match better with the velocities PIV measurements, compared to the LES. Numerical prediction of the helium field depicts a homogeneous layer formed at the top of the cavity, with a concentration in good agreement with the theoretical model of Linden et al. 1990. However, the position and the thickness of the layer do not correspond to the theory. This is mainly due to the direct interactions between the buoyant jet and both the solid boundaries of the cavity and the exterior environment. Statistical analysis regarding the buoyancy production of the turbulent kinetic energy (TKE) served to identify the limits of the buoyant jet.

Keywords: Buoyant jet, vented enclosure, air–helium mixture, stratification, large eddy simulations, direct numerical simulations, boundary conditions, computational fluid dynamics, particle image velocimetry.

CEA Saclay - DEN/DANS/DM2S/STMF/LIEFT, F-91191 Gif-sur-Yvette cedex, France,
LIMSI CNRS, UPR3251, Université Paris-Saclay, F-91405 Orsay, France,
Sorbonne Université, Collège Doctoral, ED391 SMAER, F-75006, Paris, France.